University of Strathclyde

Strathclyde Institute of Pharmacy and Biomedical Sciences

Modelling Metabolic Switching in the Differentiating Bacterium *Streptomyces coelicolor*

Leena Nieminen

Thesis presented in fulfilment of the requirements for the degree of Doctor of Philosophy

2013

Declaration of Authenticity and Author's Rights

This thesis is the result of the author's original research. It has been composed by the author and has not been previously submitted for examination which has led to the award of a degree.

Signed:

Date:

Acknowledgements

First and foremost, I would like to thank my absolutely fantastic supervisors Paul Hoskisson, Steve Webb and Maggie Smith for all their help, support and guidance. My special thanks also go to my first supervisor Paul Hoskisson for being such a fantastic person. This project would not have been the same without your support. I would also like to thank Paul Herron and Nick Tucker for their expertise and advice.

Cheers to all my many (past and present) colleagues in the lab R5.21 and HW601 and also at the Maths department, especially Vinod, Laura, John, Tai, Vartul, Jana, Kirsty, Zhenyu, Badri and Franck. It was a pleasure to know you and to work with you all. I would also like to thank Gillian for always being there for me to offer her help (and media) at a time of emergencies.

To my family, I am eternally grateful for all your support.

Special thanks also go to Yiannis Voulgaris and Chris Baron for their help with the project. I would also like to thank D. Jakimowicz, A. Hesketh and M. Bibb for kindly providing some of the strains used in this study.

Thanks also to the many research day, symposium and conference organisers (especially SGM) who made it possible for me to present this research at 20 different occasions including events in UK, Germany and China.

This work was supported by a grant from the SULSA.

Abstract

Streptomyces are filamentous bacteria that are commonly found in soil ecosystems. During their complex life cycle *Streptomyces* produce many useful bioactive secondary metabolites. During growth in liquid cultures, filamentous, multicellular growth of *Streptomyces* can result in inefficient industrial antibiotic fermentations. *Streptomyces* form large heterogeneous aggregates in liquid culture where the morphology and metabolism of hyphae are influenced by external oxygen and nutrient profiles within a pellet. Understanding the features and emergent properties of these could significantly aid improvement of industrial-scale processes.

This thesis studies the heterogeneous nature of hyphal growth by constructing a discrete-continuum hybrid stochastic differential equation model of filamentous growth and pellet formation. The model requires relatively few values for parameterisation of which many can be derived from experiments. The model is experimentally validated and tested, through analysis of growth curve data, coupled with manual and automated image analysis. Using enhanced green fluorescent protein fusions it was possible to study the spatio-temporal localization of proteins in key cellular processes inside pellets and relate these to pellet behaviour. The model delivers realistic simulations of *Streptomyces* pellet formation and is able to predict features, such as the density of hyphae, the number of tips and the location of metabolic switch within a pellet in response to external nutrient supply, which are almost impossible to do in all but the smallest aggregates.

Using the antibiotic-producing soil bacterium *Streptomyces* as a model we have developed a flexible mathematical model platform. The model is scalable and will find utility and application in a range of branched biological networks such as fungal hyphal networks, plant root growth and angiogenesis.

Chapter 1: Introduction

Streptomyces are important natural producers of antibiotics which makes them commercially interesting organisms (Kieser *et al*. 2000). In this literature review the current challenges for commercial cultivation of *Streptomyces* are discussed. The complex life cycle of *Streptomyces* and its growth on both solid surface and submerged cultures are reviewed. Factors influencing the metabolic switch from primary to secondary metabolism are discussed and an introduction is given to mathematical modelling of hyphal growth in various organisms.

Introduction to *Streptomyces*

Streptomyces are filamentous bacteria that are most commonly found in soil ecosystems although they can also inhabit aquatic environments (Madigan *et al*. 2012). In these ecosystems *Streptomyces* participate in the carbon cycle by degrading insoluble substances, such as lignocellulose and chitin, aiding the decay of other organisms. They produce secondary metabolites of which some have antibiotic activities. Over two-thirds of naturally derived antibiotics currently in use are produced by *Streptomyces* species. Moreover some of these metabolites can act as anti-tumour agents, anti-helminthics and immunosuppressants (Bentley *et al*. 2002).

Streptomyces belong to the phylum Actinobacteria. They are characterized as filamentous, Gram-positive, high G-C% bacteria. *Streptomyces* are relatives of unicellular pathogens Mycobacteria and Corynebacteria, the causative agents of tuberculosis (*Mycobacterium tuberculosis*), leprosy (*M. leprae*) and diphtheria (*Corynebacterium diphtheriae*) (Madigan *et al*. 2012). *Streptomyces* themselves are rarely pathogenic. However, some species are know to cause infections such as *S. somaliensis* that is a known human pathogen and *S. scabies* that is a plant pathogen causing potato scab (Kieser *et al*. 2000, Sangal *et al*., 2012).

Over 600 species of *Streptomyces* have been recognised of which many produce antibiotics (Labeda, 2011). The chromosome of the model organism, *S. coelicolor* A3(2), has been fully sequenced (Bentley *et al*., 2002). The 8,667,507 base pair linear chromosome revealed the total of 7,825 predicted genes, which at the time was largest number of genes found in any bacterium (Bentley *et al*., 2002).

Streptomyces coelicolor A3(2)

S. coelicolor A3(2) produces at least four secondary metabolites with antibiotic activity; actinorhodin (ACT), undecylprodigiosin (RED), calcium-dependent antibiotic (CDA), and methylenomycin. The first one of these, actinorhodin, is an aromatic polyketide (Bentley *et al*., 2002), a red-blue acid-base indicator pigment that is either intracellular or it can be secreted in its lactone form as γ-actinorhodin (Kieser *et al*., 2000). Both undecylprodigiosin and the calcium-dependent antibiotic belong to a class of non-ribosomal peptides (Bentley *et al*., 2000, Kim *et al*., 2004). Undecylprodigiosin is a mycelium bound antibiotic (Wezel *et al*., 2000) that is often called the “red pigment” as it consists of a mixture of at least four prodiginines. The calcium-dependent antibiotic is a cyclic lipopeptide (Kieser *et al*., 2000) that is only active in the presence of calcium ions (Kim *et al*., 2004). The last one of the four antibiotics, methylenomycin, is an antibiotic that is encoded on the linear plasmid of *S. coelicolor* A3(2) SCP1 (Kieser *et al*., 2000, Bentley *et al*., 2002).

Other secondary metabolites of *S. coelicolor* A3(2) include siderophores, pigments, lipids and other molecules such as geosmin. The production of a wide range of secondary metabolites have been suggested to protect the bacteria against physical, chemical and biological stresses such as desiccation, low temperature, iron depletion and competition from other organisms (Bentley *et al*., 2002).

Developmental biology of *Streptomyces*

Streptomyces grow by forming multicellular, filamentous hyphae that undergo a complex life cycle when grown on solid surface (Figure 1.1). Growth is initiated from a single spore that goes through germination when suitable nutrients are available. The individual cells of an emerging hypha stay in contact to each other, forming multigenomic compartments. The growing hyphae form a network of vegetative hyphae also known as mycelium (Elliot *et al*., 2008). The hyphae grow by apical tip extension and branching and new cell-wall material is synthesized only at the hyphal tips. Unlike what has been seen in many rod-shape bacteria such as *Escherichia coli* and *Bacillus subtilis*, the hyphal growth of *Streptomyces* is not dependent on *mreB*, an actin homologue that can form helical cytoskeleton and orchestrate the cell elongation of the rod-shaped bacteria. Instead a coiled-coil protein, DivIVA, is involved in the tip extension, branching and cell shape of *Streptomyces* (Flärdh and Buttner, 2009).

Growth on solid substrate

On a solid substrate the growth of *S. coelicolor* vegetative hyphae continues in response to nutrient limitation by formation of aerial mycelia that, under correct conditions, can further differentiate into spores (Hoskisson *et al*., 2006). The aerial hyphae branches from substrate hyphae, breaks the surface tension of the medium and grows up into the air. To break the surface tension of the medium, *S. coelicolor* coats its aerial hyphae in a hydrophobic sheath composed of secreted proteins, chaplins and rodlins. Chaplins can be subdivided into long or short chaplins, which are both exported through the Sec (secretory) system. The long chaplins are covalently attached to the cell wall of the aerial hyphae by a sortase enzyme. The short chaplins are believed to heteropolymerize with the long chaplins to form hydrophobic filaments on the cell surface. Rodlins, on the other hand, are suggested to form a ‘basketwork of paired rodlets’ surface structure on the aerial hyphae and spores, but they are not essential for the formation of

the hydrophobic sheath and aerial mycelium (Elliot *et al*., 2003, Claessen *et al*., 2003, Flärdh and Buttner, 2009). On a rich media, a lantibiotic-like peptide, SapB, encoded by developmental gene *ramS* and regulated by *ramR*, is needed for the formation of aerial hyphae (Kodani *et al*., 2004). Ones the aerial hyphae is formed, it will, under correct growth conditions, differentiate into a chain of exospores. The aerial hyphae do not branch but will undergo synchronous septation, when each hypha is divided into 40 to 60 unigenomic compartments of the same size. Each of the compartments will contain a single chromosome and metamorphosis of the compartment will continue until mature spores chains are formed. The spores are then able to persist in the soil through nutrient depletion or dry seasons or to disperse to new, nutrient rich, environments completing the life cycle (Elliot *et al*. 2008).

Several mutants, defective in the aerial hyphae formation, have been previously constructed. Due to the lack of the fluffy appearance of the wildtype colony, these mutants have been referred to as “bald” (*bld*) phenotype (Hopwood, 1967; Merrick, 1976). Such *bld* genes can be divided into three main functional classes that include regulatory genes, genes involved in signalling and genes encoding structural elements of the aerial hyphae (Kelemen and Buttner, 1998; Chater, 2001). Some of the *bld* genes take part in extracellular signalling cascade where the formation of aerial hyphae of one mutant is restored by another when grown in close proximity on rich media. The established cascade has the gene order of *bldJ→bldK,L→bldA,H→bldG→bldC→bldD,M→ram* (Willey *et al*., 1993; Kelemen and Buttner 1998). At the start of the cascade, an extracellular oligopeptide is produced with the help of *bldJ* and most likely imported into an adjacent hypha via a multicomponent ATP-dependent transport system specified by the *bldK* locus genes. The next stage includes the transcription of *bldA* tRNA with its 3’-AAU-5’ anticodon, which is the only tRNA in *S. coelicolor* capable of reading UUA codon for leucine. The UUA codon is the rarest codon in *S. coelicolor* in which only 2% (145/7825) of the chromosomal genes contain TTA codons. The codon UUA is often positioned near the start

of the coding sequences of mRNAs and it is less represented in housekeeping genes. Many of the genes containing the TTA codon have an unknown function however, it is known that for example the pathway-specific regulator of actinorhodin, *actII-4*, and a regulatory gene for undecylprodigiosin, *redZ*, both contain the TTA codon as does the gene *bldH* (Li *et al*., 2007; reviewed in Chater and Chandra, 2006). The gene *bldH*, or otherwise known as *adpA*, is a homologue of the A-factor-dependent central regulator of *S. griseus*, that is not under γ-butyrolactone control in *S. coelicolor*. The rest of the signalling cascade includes genes *bldG*, that encodes protein known as anti-anti-σ factor, and gene *bldC*, a small protein with MerR family DNA-binding domain. The BldD is a regulatory protein that represses its own expression as well as the expression of other developmental genes such as *bldN* (ECF σ factor) and *whiG*. The σ^{BldN} is required for the transcription of one of the two promoters of *bldM* and the expression of *bldM* activates the *chp* genes encoding the chaplin proteins (reviewed in Chater and Chandra, 2006; Flärdh and Buttner, 2009).

The developmental mutants deficient in sporulation are called white (*whi*) phenotypes due to their inability to produce the grey spore pigment. Initially, the aerial hyphae elongate from the tip, laying down vegetative cross-walls. A high level of DNA replication will take place in these long compartments. The developing aerial hyphae will then arrest extension and initiate synchronous, multiple cell divisions with the help of genes *whiA* and *whiB*. This controlled cell division with sporulation septation is directed by the bacterial tubulin homologue FtsZ. The *ftsZ* expression is strongly upregulated by developmentally controlled, aerial-hyphae specific promoter (*ftsZp2*) that is not upregulated in mutants lacking *whiA*, *whiB*, *whiG*, *whiH* or *whiI*. The FtsZ then polymerizes to form a ladder like structure of helical filaments that then remodel into multiple Z-rings, distributed at ca 1.3 μm apart, that direct sporulation septation. The genes *crgA*, *whiD* and *ssgA* have been linked to the formation of these regularly spaced rings. After the formation of

sporulation septa the prespores assemble thick spore walls with the help of MreB (Flärdh and Buttner, 2009).

During the synchronous septation of aerial hyphae, the chromosomes segregate into these prespore compartments with the help of ParAB and FtsK. Another set of helical filaments along the long compartment are formed by ParA ATPase, originating from the tip towards the stem of the aerial hypha, where as the DNA-binding protein ParB binds to *parS* sites, centred around *oriC* of the linear chromosome. The filaments of ParA are believed to provide the force to move and position ParB assembled large nucleoprotein complexes at the centre of the prespore compartment so that each compartment will contain only a single chromosome. The unsegregated nuclear material is then cleared from the sites of septal formation by FtsK DNA translocase. Finally, the prespores mature and the genes related to this late-stage of sporulation are for example *sigFH* (σ^B-like stress response sigma factors) and *whiE*, where the latter specifies the synthesis of the grey polyketide spore pigment (Flärdh and Buttner, 2009).

Another σ^B-like sigma factor *sigN* has a putative target promoter of a gene *nepA*. The function of NepA is not known, however, the localization studies with *nepAp-egfp* revealed a new compartment named as sub-apical stem, that is located below the developing hypha. The sub-apical stem is suggested to lack DNA replication although its function is not fully understood (Flärdh and Buttner, 2009).

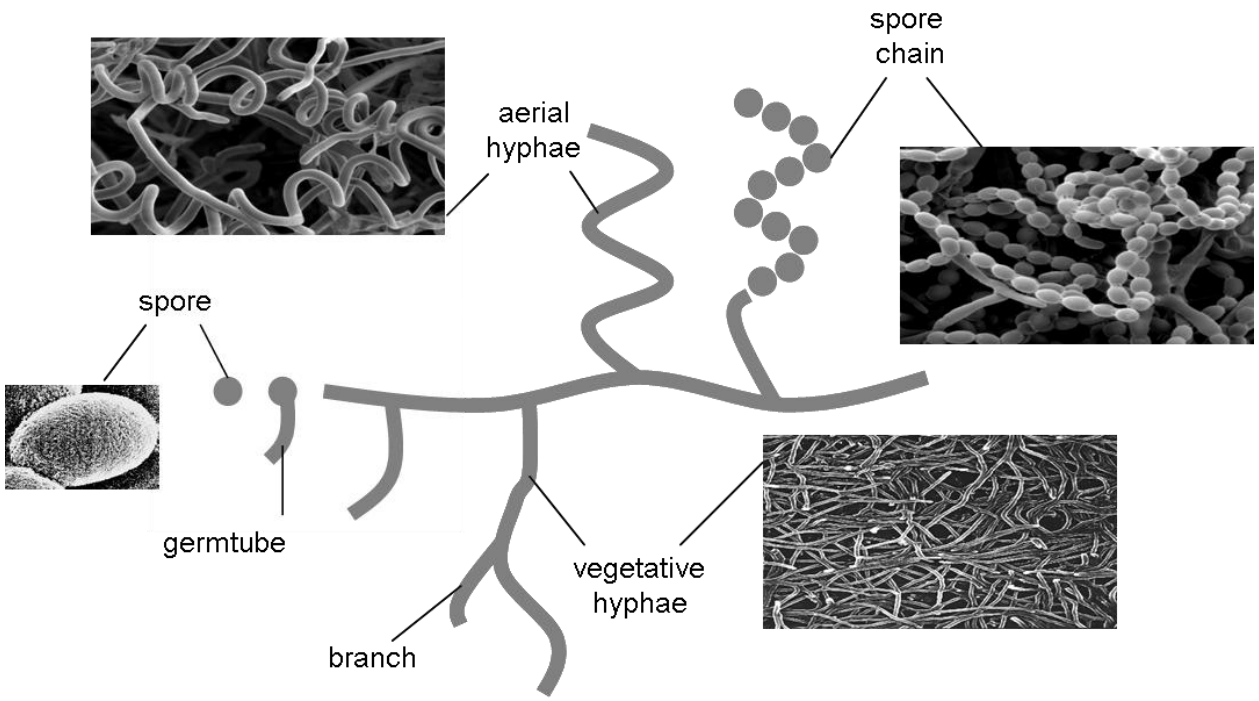

Figure 1.1: The developmental cycle of *Streptomyces*. The growth starts from a single spore by the formation of a germ tube. The emerging hyphae grow by tip extension and branching (vegetative hyphae). Under limited nutrients, the colony erects aerial hyphae that differentiate into chains of exospores. The electron microscopy images were taken by Dr P. A. Hoskisson and they illustrate the different stages of growth. The schematic illustration is an adaptation from an image published by Flärdh and Buttner (2009).

Growth in submerged culture

In liquid cultures the growth of *S. coelicolor* does not normally progress onto spore formation, however, physiological differentiation will still take place. Several other species of *Streptomyces*, however are capable of sporulation in liquid culture, such as *S. griseus* and *S. venezuelae* (Flärdh and Buttner, 2009). The growth will initiate as on solid substrate where the spore germinates and produces hyphae that will go through apical extension from the tip and achieve exponential growth by branching (Manteca *et al*. 2008). In submerged cultures no aerial hyphae will be formed, instead the vegetative filaments will grow further to form clumps and eventually pellets (Pamboukian *et al*. 2002). The pellet morphology has been directly related to generating growth conditions that promote secondary metabolite production. As the pellets get older, the cells in the centre of the pellet are known to lyse due to either cell age or the nutrient depletion that is caused by diffusion limitations of substrates within pellets. An intermediate zone has been described in older pellets that could be responsible for antibiotic production, whilst an external zone on the surface of the pellet might continue growing (Sarrà *et al.*, 1996).

Streptomyces **metabolism**

Streptomyces are aerobic, chemoorganoheterotrophic bacteria that are nutritionally versatile. They can use several carbon sources such as sugars, alcohols, organic acids, amino acids and some aromatic compounds. Growth factor requirements are rare in *Streptomyces* (Madigan *et al.* 2012).

Extracellular carbon, nitrogen and phosphate concentrations have an important regulatory effect on both primary and secondary metabolism in *Streptomyces*. A schematic presentation of simplified metabolic networks and their cellular effects are illustrated in Figure 1.2. A two-component system PhoR-PhoP senses the environmental signals and regulates the transcription of phosphate-regulated genes. The membrane sensor protein kinase, PhoR,

responds to phosphate limitation by phosphorylating the response regulator PhoP. The response regulator binds to DNA controlling transcription of, for example, *pho* regulon and actinorhodin and undecylprodigiosin biosynthesis genes. The promoter regions of genes *pstS*, *phoU*, *phoRP*, *phoA* and *phoD*, belonging to the *pho* regulon, consist of direct repeat units (DRu) of 11 nt, called PHO boxes, that act as a binding site for PhoP (Rodríguez-García *et al.* 2009).

S. coelicolor can utilize amino acids and small peptides by deamination, which produces ammonia as a by-product (Gottschalk 1986). To obtain cellular organic nitrogen, *S. coelicolor* can also assimilate ammonia with the help of glutamine synthetase (GS) (Rodríguez-García *et al.* 2009):

NH_3 + glutamate + ATP → Glutamine + ADP + P_i

Glutamine can then be used by the cell as a NH_2 donor in biosynthesis of purines, tryptophan, histidine and carbamoyl phosphate, a precursor for pyrimidine compounds. Glutamine also serves as a NH_2 donor in transamination of fructose-6-phosphate to glucosamine-6-phosphate. The latter can be used to synthesize UDP-*N*-acetylglucosamine which can further be synthesized to UDP-*N*-acetylmuramate, a precursor for peptidoglycan in bacterial cell wall (Gottschalk 1986).

In *S. coelicolor* there are two genes *glnA* and *glnII* which encode glutamine synthetase. These genes are controlled by global nitrogen activator/repressor GlnR. It has be shown by Rodríguez-García *et al.* (2009) that in *S. coelicolor* PhoP represses nitrogen metabolism genes *glnR*, *glnA*, *glnII* and *amtB-glnD-glnK* operon by binding to their promoters. Another regulator gene *glnRII* that has a similar amino acid sequence to GlnR, is controversial since it was previously found to not to be directly repressed by PhoP and its promoter does not contain any PHO boxes (Rodríguez-García *et al.* 2009). However, a recent study by Allenby *et al*. (2012) using ChIP analysis to gain *in vivo*

genomic distribution of PhoP under phosphate limited conditions identified *glnRII* as PhoP target. The latter study suggested two major roles for PhoP. Firstly, to activate phosphate recovery systems, cell wall polymer biosynthesis and cryptic polyketide biosynthesis, and secondly to repress central and secondary metabolic pathways and regulatory networks governing morphological differentiation. The logic behind these observations was explained as phosphate being essential for central metabolism (nitrogen assimilation, oxidative phosphorylation, nucleotide biosynthesis, glycogen catabolism), antibiotic production and morphogenesis. PhoP is therefore shutting down these processes until sufficient phosphate is recovered either from environmental sources or partial scavenging its own mycelium.

When glucose is used as a carbon source via glycolysis, *S. coelicolor* excretes organic acids that will gradually acidify the growth medium. These organic acids can be oxidized via the tricarboxylic acid (TCA) cycle to avoid growth-inhibitory pH levels. When the TCA cycle is being disrupted by, for example, oxygen limitation, the excretion of organic acids leads to temporal acidosis that triggers cell differentiation. When grown on solid surface, the metabolism of organic acids and the simultaneous neutralization of pH coincide with aerial hyphae formation that precedes sporulation (Viollier *et al*. 2001). The formation of aerial hyphae is associated with the production of secondary metabolites such as actinorhodin and undecylprodigiosin (Elliot *et al.* 2008). Inorganic phosphate is known to repress many secondary metabolites. For instance, actinorhodin is negatively regulated by phosphate and therefore, it can only be synthesized under phosphate-limiting conditions (Sola-Landa *et al*. 2002).

Reduction in growth rate has been noted to signal the initiation of secondary metabolism. The highly phosphorylated guanosine nucleotide (p)ppGpp participates in the growth rate control of gene expression and is also related to antibiotic production. Under nitrate limited conditions, the ribosome-associated ppGpp synthetase (RelA) is involved in the transcription of

pathway-specific regulatory gene for actinorhodin (*act*II-orf4). Other known triggers for secondary metabolism production in *S. coelicolor* include extracellular γ-butyrolactones (SCB1), members of the SARP family of regulatory proteins (AfsR etc.) and members of the LAL family (large ATP-binding regulators of the LuxR family) of transcriptional regulators. Little is known about the biosynthesis of γ-butyrolactones. The synthesis and regulation of the most characterized γ-butyrolactone, A-factor of *S. griseus*, differs from what is known about the SCB1 of *S. coelicolor*. The SARP family of regulatory proteins is only found in actinomycetes, mainly streptomycetes. It consists of both pathway-specific transcriptional activators of gene clusters that encode aromatic polyketides, ribosomally and non-ribosomally synthesized peptides, Red, Type I polyketides, and β-lactams, and pleiotropic regulators such as AfsR. The regulator AfsR plays a role in integration of various environmental signals. Membrane-associated kinases AfsK, PkaG and AfsL are all capable in phosphorylating AfsR after sensing yet unknown, environmental signals. The phosphorylated, cytoplasmic AfsR then activates the transcription of *afsS* which encodes a protein that enhances the production of Act, Red and CDA in an unknown manner. Finally, an *absA1A2* locus has been identified within the CDA cluster that encodes a two-component histidine kinase-response regulator pair that may play a pleiotropic role in the production of all four *S. coelicolor* antibiotics. It has also been suggested that the AbsA1A2 acts as a pathway-specific regulator for CDA (reviewed in Bibb, 2005).

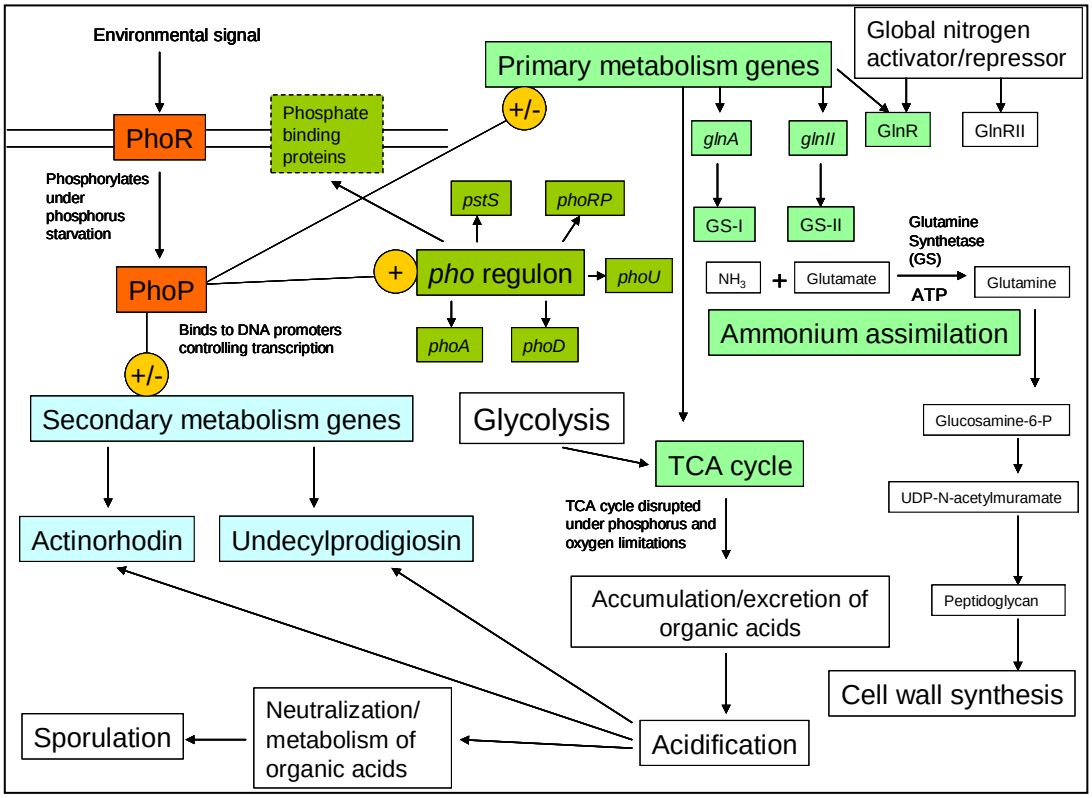

Figure 1.2: Schematic presentation of PhoR-PhoP control over primary and secondary metabolism and cell morphology (author's interpretation from previously published data, see main text). Used colour scheme: PhoR-PhoP proteins (red), transcriptional control (orange), primary metabolism genes affected (bright green), activated pho regulon translating phosphate binding proteins (dark green), secondary metabolism genes affected (blue).

Industrial production of antibiotics

Filamentous microbes, both eukaryotic fungi and prokaryotic actinomycetes, are used to commercially produce products such as antibiotics, anticancer agents, antifungicides and enzymes (Wezel *et al.* 2006). For antibiotics the market capitalization is expected to reach around 45 billion US dollars per year by 2016 (Transparency Market Research, 2012)..

Antibiotics are medium-value, medium-volume products that are produced on a scale of up to 100,000 kg per year. A typical cost for producing an antibiotic is around £60 per kg, where the majority of the cost arises from the nutrient demand and the utility and duration of the fermentation. The cost for nutrients can fluctuate significantly due to the varying global markets affecting the price and the availability of the nutrient. Therefore flexibility in primary carbon source and reliable and cheaper substrates are of importance to the pharmaceutical industry (El-Mansi *et al*. 2007). Significant cost reductions and enhanced productivity have been achieved by using more productive producer organisms and improving fermentation technology. This has especially been the case with fungal producers such as *Penicillium chrysogenum* and *Acremonium chrusogenum* (Wezel *et al*. 2006). Whereas with *Streptomyces* spp. the multi-component nature of fermentations, low titres and difficult recovery and purification methods still remain a problem for the commercial utilization. The difficulties in production have led many manufacturers to use synthetic chemistry rather than *Streptomyces* spp. to produce antibiotics on a commercial basis (Elander 2003).

The mycelial lifestyle of actinomycetes creates many challenges for the commercial production processes. The filamentous nature of the culture means that the culture broth often has complex rheology that results in difficulties in mass transfer and causes non-uniform mixing patterns (Sarrà *et al.*, 1997). The filamentous growth is often slow and may lead to the formation of large mycelial pellets that have serious oxygen and nutrient transfer problems towards the centre of the pellet. The heterogenous growth

within a pellet, may result in loss of productivity when nutrients are used for the growth of the new cells whilst old cells in the centre of the pellet end up dying. Increased mixing can be used to overcome some of these difficulties. However, the higher stirrer speeds may result in fragmentation and lysis of the mycelium making the downstream processes more complex and more expensive. *S. coelicolor* has never been used in industrial large-scale fermentations due to these growth-related difficulties (Wezel *et al*. 2006).

Pellet formation in liquid culture

Fungal pellets are either spherical or ellipsoidal consisting of masses of hyphae. The structure of fungal pellet varies from loosely packed hyphae to tightly packed, compact pellet. Four regions have been identified within the pellet. The outer layer consists of viable hyphae. Below this is a layer where signs of autolysis can be seen. When the pellet is hollow two further layers can be identified: the hyphae of the third layer shows irregular wall structure and the fourth layer at the centre of the pellet, contains no mycelia (Gow and Gadd 1995).

In *Streptomyces* the pellet is formed through germination of a single spore that grows through expanding hyphae resulting in compact network of filaments (Pamboukian *et al*. 2002). In contrast to *Streptomyces*, fungal pellets are often formed either by aggregation of spores before germination or by entrapment of spores by germ tubes. Rarer is the formation of fungal pellets through the aggregation of young mycelium. Fungal pellet formation can therefore be controlled in the bioprocess by reducing the number of spores in the inoculum. The formation of fungal pellets can also be reduced by mechanical means, such as high rates of agitation and shear forces, or by chemical ways, for example by adding anionic polymers to the culture to prevent spore aggregation (Gow and Gadd 1995).

Modelling of branched networks in biology

Branched morphological networks are ubiquitous in biology. Examples of biological networks include blood vessel network, plant root and fungal transport networks. Modelling these networks has been valuable in directing the biological understanding of these systems. However, often such models are system specific and lack flexibility. Thus an adaptable and flexible model platform for network heterogeneity would be highly desirable (Nieminen *et al*., 2013).

A typically used modelling technique is empirical kinetic based studies, which uses simple equations to describe changes of key elements in the culture. For example, kinetic studies have been used to measure the extending hyphae and mycelia, colony and population growth and cell differentiation. A key aim of the modelling is to create quantitative hypotheses that will form the basis of experimental work. The benefits from this approach are that by simulating development mathematically we may create hypothesis that will further our knowledge of mechanisms underlying the growth (Gow and Gadd, 1995). Several mathematical models have been previously produced. A selection of relevant models is reviewed next in detail (see Appendix 1 for summary of the reviewed models in table format).

Microvessel growth model with chemotaxis (1991)

Stokes *et al*. (1991) used a random walk-like method to model the motility and chemotaxis of a microvessel endothelial cell. They based their model on an Ornstein-Uhlenbeck (O-U) process (Uhlenbeck and Ornstein 1930) that was later utilized by Dunn and Brown (1987) in their discrete model to quantify random motility of a single cell. The O-U process is the simplest way of describing random motility as a persistent random walk. It defines velocity of a particle by random fluctuations (in speed and direction) in addition to a drift term to a mean velocity. The movement is only dependent on the current state of the cell and no previous states are included. Stokes *et al*. (1991)

developed a continuous version of the original model that accounted for directional bias for cell motility in a chemo-attractant gradient. Stokes and Lauffenburger (1991) extended their model to simulate the biased random walk of multiple cells, all branching simultaneously from a single parent vessel.

Hyphal growth model with internal particle movement (1992)

Yang *et al*. (1992a) created a model to determine early tip growth and the branching direction of *Streptomyces tendae,* where tip growth angles and branching angles were normally distributed. Each hypha was considered to contain discrete sections with a constant length, and growth was assumed to occur section-wise at a given hyphal extension rate. No concentration gradients of substances were taken into account in this model.

Yang *et al*. (1992b) updated this kinetic model to contain a stochastic part that allowed a correlation of branching and septation. In this model the hyphal tip extension was proportional to the formation and diffusion of key growth components within the hypha. Septation was assumed to occur within a compartment, dividing the compartment into two identical, daughter segments that contain an equal amount of nuclear material. The timing of septation was dependent on the concentration level of nuclear material. Branching sites were assumed to be normally distributed around septa.

Both of *Yang et al*. (1992a, b) models simulated pellet formation from a 3.6 µm long germ tube with realistic results. However, neither of the models took into account nutrient deprivation due to consumption within a pellet. Both models also assumed that the environmental conditions stayed constant and that no growth inhibitors were present. Although, later Yang did develop the model further to include oxygen profile and degradation of hypha within a pellet (King 1998).

Single pellet growth model with external substrates (1995)

Meyerhoff *et al*. (1995) adopted the Yang *et al*. (1992b) model and included the external substrate concentrations for oxygen and glucose. They assumed that the growth limiting substrates penetrated the pellet diffusively and that under severe deprivation conditions the pellet underwent localized decomposition. The model was also developed to include hyphal chipping effect of shear forces on the surface of the pellet.

Meyerhoff *et al*. (1995) solved the transport-reaction problem by modeling pellet in a form of spherical layers of equal thickness. Within a layer the cell and substrate concentrations stayed constant. A hyphal compartment was associated to a layer according to its origin's coordinates. Monod kinetics (Robinson and Tiedje, 1983) was applied to model growth. In this model septation process was related to the increasing length of the compartment, and nuclear material was associated with the location of the septa. Diffusion of material was assumed to be dependent on compartment-density.

The model separated between actively growing compartments and compartments with only maintenance requirements. When the glucose or oxygen concentration levels dropped below a certain value, all compartments within a layer stopped growing and started using substrates only for maintenance requirements. If the glucose or oxygen concentration dropped even further the compartments started to break down in accordance to first order kinetics (Meyerhoff *et al*. 1995).

From these simulation studies, Meyerhoff *et al*. (1995) predicted that the density of a pellet, influencing the available substrate concentrations within a pellet, did not have as big effect on pellet growth as did the substrate concentrations of the bulk medium. During the simulations the pellets did not stop growing even when glucose concentrations were low. The authors speculated whether other restriction mechanisms such as age effects were present.

Meyerhoff and Bellgardt (1995a) extended their model further to include germination, preculturing, and penicillin production. The active mycelium started to produce penicillin according to a first order rate constant once the glucose concentration dropped below a critical level of 0.4 g/l. The basic structure of a cell compartment was either type 1 compartment (with one or no tip) or type 2 compartment (with two tips). Simulations in this study were found to be realistic. However, the authors realized that the strength of this model – the detailed morphology of a single hypha, is also the weakness of the model. Simulations demanded high computer power that was not convenient when trying to model a large pellet or several pellets simultaneously. For this reason Meyerhoff and Bellgardt (1995b) developed their model further to achieve simulations of bioprocesses but with a more simplified version of the model to increase simulation efficiency (Meyerhoff and Bellgardt 1995a and b).

The new model was intended to solve the problem between the microscopic and macroscopic description of pellet formation. The pellet was divided into spherical layers. Each layer had constant cell density, growth activity, hyphal growth unit and substrate concentration. Therefore the updated model lost the description of a single hypha within a layer, instead it modeled the behavior of the biomass within a layer. Meyerhoff and Bellgardt (1995b) built their model in two parts. The first part dealt with early development of a pellet that yielded compartment densities for each layer. Once about 150-300 tips were developed the simulation continued using a spherical layered structure. All mycelium within each layer was assumed to consist of type 1 compartments with one or no tip (Meyerhoff and Bellgardt ,1995b).

Single pellet growth model with porosity of pellet affecting tip elongation (1997)

Lejeune *et al*. (1995) studied the growth of *Trichoderma reesei* in submerged cultures. They built a model based on saturation type kinetics of hyphal

apical growth, and on stochastic branching with branching probability taken to be proportional to the total length of hypha. Lejeune and Baron (1997) made further additions to their model by constraining the random walk of tips by oxygen gradient and by tracking the local porosity within the pellet. In this model oxygen was assumed to be required for growth only, according to Monod kinetics (Robinson and Tiedje, 1983), and no maintenance energy consumption was included. The oxygen balance within a pellet was based on pseudo steady-state assumption using diffusion for transportation. The porosity value of the site of apical growth or branching determined whether the new growth continued or whether it was to be annulled. The simulated pellet in three dimensional space had a fractal dimension structure determined using a box counting method. This method divided the space into cubes of various sizes. The cubes were then intersected by hyphae. The authors made further suggestions for extending the model to include the formation of hollow pellets by adding an oxygen maintenance requirement and a degradation of cells due to the oxygen depletion.

Fungal colony growth model with neighbour sensing (2004)

Meškauskas *et al*. (2004a) developed a neighbour sensing, mathematical model based on fungal hyphal growth kinetics that utilized vectors to simulate the growth of hyphal tips. The basic growth kinetics used included hyphal length, number of branches and growth rate. External factors such as gravity, light and chemicals influenced direction of growth and branching, and these factors were implemented into the model in the form of external fields.

Each virtual hyphal tip was located in virtual mycelium surroundings that consisted of different types of fields. The first field regulated branching and growth by a short distance hyphal avoidance reaction. The second field sensed the long-range interactions that were useful when describing growth in the presence of a chemical substance. Interaction between hyphae was allowed at a particular distance by a third type of interaction which was taken to be inversely proportional to the sixth degree of the distance. This enabled

simulations of a hypha growing in circle around another. The fourth and the fifth fields were introduced by assuming that short, straight line, hyphal segments formed an electric field that directed the growth (galvanotropism). The fourth field formed a parallel current that encouraged all the tips responding to this field to grow in the same direction. The fifth field determined the intensity of this galvanotropic field and influenced the orientation of the growing tips by either bringing them together or keeping them apart. The sixth and the final field influencing hyphal growth was the orientation field that allowed the formation of polarized structures such as mushroom fruit bodies (Meškauskas *et al*. 2004a).

Branching was both random according to a certain probability but it was also controlled either by the threshold value of the density field or the number of the neighboring tips. During branching, a section was divided into two, where one of the new sections continued to grow in the direction of the parent section and the second section was orientated either randomly or oriented in the direction of the tropic vector at the site of branching. Branching was controlled so that it only occured at a certain age of hyphae (Meškauskas *et al*. 2004a).

The simulations were examined in 3D space from various angles using different scales. To view the internal structure of mycelium, the visualization was displayed in slices with controllable thicknesses. The simulations were saved both as pictures and as data. An animation robot recorded the used parameters allowing the repeat of the visualization with a new population of hyphal tips (Meškauskas *et al*. 2004a). Meškauskas *et al*. (2004b) extended their model further to achieve realistic simulations of colony growth of *Phanerochaete velutina* on semi-solid substrate such as agar or soil.

From the simulation studies with this neighbor sensing model the main outcome was the discovery of population as opposed to localized driven behavior of mycelium. All the actively growing hyphae were influenced by the

same regulatory functions set by the user at any given time, and these conditions were used to simulate the formation of complex fungal fruit bodies. In other words the simulations revealed that no localized regulation is necessary for the formation of these structures (Meškauskas *et al*. 2004a).

Bioreactor circulation model (2006)

Delvigne *et al*. (2006) used a stochastic model to describe the influence of bioreactor heterogeneity on the growth and physiology of a microorganism. The model consisted of two submodels. The first submodel was a biased random walk model for microorganism circulation in scale-down bioreactor. The second submodel used a Markov chain process to describe the fluid mixing to characterize the concentration gradient within the reactor. The model was validated by comparing simulation results to the experimental data from inert and biological tracer tests. The model was used for example, to test the effect of the glucose pulse frequency to the appearance of concentration gradients within the reactor and to predict the formation of several different microbial sub-populations, differing by the extracellular substrate concentrations experienced.

Hybrid fungal growth model (2007)

Hybrid cellular automaton model was constructed by Boswell *et al.* (2007) to model fungal growth in structured environments. The model described the fungal mycelium as a discrete structure and the substrate as continuous variable. External substrate was included in the model using a hexagonal array where the substrate concentrations were assumed to be homogenous within a hexagonal cell. The hyphal network was modeled as biased random walk of tips on the vertices of a triangular lattice embedded within the hexagonal lattice of substrate. The modeled hyphal growth mimicked a straight-line growth habit of mycelial fungi, allowing the branching to occur at angles of 60°. Hyphal heterogeneity was included in the model as hyphal tip and active or inactive hyphae. The model successfully incorporated

anastomosis, translocation and acidification of environment as a result of fungal growth. The model was validated using the fungus *Rhizoctonia solani* and used to study the mycelial networks in various environments including those representing homogeneous and heterogeneous nutrient conditions and soil-like structures.

Plant root growth model (2008)

Lucas *et al*. (2008) used a Markov model to describe the branching and formation of plant root in *Arabidopsis thaliana*. The stochastic model was built on parameters obtained by a classical likelihood maximization procedure. A root was divided into zones and segments and these were given six different developmental states. To indicate possible transition from one state to another, arcs were used between states with a certain probability. The frequency of the transitions was determined from the experimental data.

Single pellet growth model with external substrate (2012)

Celler *et al*. (2012) extended the models previously done on single pellet morphology (Yang *et al*., 1992a, Meyerhoff *et al*., 1995, Lejeune and Baron, 1997). Their model combined morphological and structural model in a three-dimensional framework that included an external oxygen diffusion-reaction, shearing and collision detection during development. Celler *et al*. (2012) used *S. coelicolor* to model the relationship between antibiotic production and pellet morphology. In the model design, the hyphae was divided into three different compartments (apical, sub-apical and hyphal) and each represented a different cellular differentiation stage. The conversion of an apical to a sub-apical compartment depended on the hyphal length. The sub-apical compartment differentiated to a hyphal compartment once a certain arbitrary differentiation age had been reached. Apical extension occurred from apical compartements, new branches emerged only from subapical compartments and the hyphal compartments were responsible for secondary metabolite production. Monod kinetics were used for the local oxygen consumption and this determined the growth rate. Oxygen diffusion was modeled using the

assumption of one-dimensional radial symmetry with the boundary conditions taken to be a constant oxygen concentration in the bulk phase and zero oxygen flux at the core of the pellet. The level of external oxygen concentration also affected the probability of hyphal branching. Cross-walls were modeled to form directly before or after a branch point and breaking of hyphae due to shear forces was assumed to occur at the cross-wall locations. Collision detection was also incorporated into the model so that hyphae would not grow closer than two hyphal radii from each other. Celler *et al*., (2012) used modern visualization software in simulation outputs to illustrate the hyphal growth as regards to a DivIVA-eGFP marker.

Hyphal growth model using DivIVA-eGFP (2012)

Richards *et al*. (2012) constructed a minimal mathematical model to mimic the phenomenon seen in branch formation with experimental DivIVA-eGFP studies of *S. coelicolor*. A tip-focus splitting mechanism was suggested by the fluorescent microscopy analysis of hyphal growth and branching that showed a growing focus of DivIVA-eGFP at the hyphal tip prior to the splitting of the focus. After splitting, a new focus was left behind the elongating tip at the position of a newly emerging branch. The constructed model predicted that the tip-to-first branch distance depends on how long it takes for the apical DivIVA-eGFP foci to gather enough molecules to initiate a new branch. The parameters related to this were initial focus size, the size at which a new branch is initiated, the speed of extending tip and a binding parameter. The distance between two branches was predicted to be governed by how often foci are formed. However, the model applies a trimming rule on outputs where a tip-to-branch and branch-to-branch distances are recorded only if they appear within a certain distance.

Aims of project

The aim of this project is to study the switch from primary to secondary metabolism in *Streptomyces coelicolor*. In the pharmaceutical industry, antibiotics are produced by the bacteria grown mainly in liquid cultures. It is well known that in liquid cultures many *Streptomyces* species grow in a pellet form that is considered to be crucial for product formation. However, the pellet growth form can also create problems in bioreactors. The cell heterogeneity inside a pellet may lead to inefficiency when nutrients are used to produce biomass that does not produce antibiotics. Moreover, substrate diffusion limitations within a pellet may lead to undesired cell death. Therefore, studying the pellet formation of *Streptomyces* is key to unlocking some of the issues seen in fermentation studies. Using traditional experimental methods for this can, however, be challenging if not impossible at times. Therefore, our aim is to construct a mathematical model of pellet growth to augment experimental approaches. The mathematical model is to be constructed in close relation with measurable empirical data, with a minimum number of non-biological parameters. Model simulations are to be rigorously tested using the model organism for filamentous bacterium, *S. coelicolor*. The heterogeneous metabolism within a pellet is to be studied using fluorescent dyes and spatio-temporal expression profiles of eGFP-markers of key cellular processes. The aims of this project are summarized below:

1. Develop a mathematical model that describes the hyphal growth and metabolism which takes into account an external substrate.
2. Test and refine the model using experimental data.
3. Use the model simulations to study the emergent properties of pellet formation.
4. Study the location of metabolic transition using key protein markers in order to incorporate these in to the modeling framework.

Chapter 2: Materials and Methods

Bacterial strains, culture and storage

The bacterial strains used in this study are shown in Table 2.1. The chromosome of the model organism, *S. coelicolor* A3(2), has been fully sequenced by Bentley *et al*. (2002) The 8,667,507 base pair linear chromosome revealed the total of 7,825 predicted genes, which is one of the largest number of genes found in bacteria. (Bentley *et al*., 2002)

S. coelicolor A3(2) strain was grown on mannitol soya (MS) agar or yeast extract/malt extract (YEME) media, without any sucrose, at 30°C (see Appendix 2 for recipes). The *Streptomyces* were stored in frozen spore suspensions in 20% v/v glycerol at -80°C. The spore stocks of *Streptomyces* were prepare from a confluent growth of *Streptomyces* on MS plates and incubated until grey spore layer was visible (approximately 3-4 days). The spores were then harvested by adding sterile, 20% glycerol in distilled water onto the plate and gently rubbing the surface of the culture with a sterile cotton bud. The *E. coli* strains used in this study were grown in Luria-Broth (LB) and incubated at 37°C unless otherwise stated (see Appendix 2 for recipes). The *E. coli* strains were stored in frozen overnight (incubated for ca 16 hours) cultures at -80°C in 20% v/v glycerol. All the bacterial cultures were started using either a single colony picked from a freshly grown plate or using frozen bacteria removed from a previously made frozen bacterial stock. Liquid cultures were shaken at *ca* 220 rpm unless otherwise stated.

Plasmids and cosmids

The plasmids and cosmids used in this study are shown in Table 2.2. The concentrations for appropriate antibiotics to maintain the selection are listed in Table 2.3.

Table 2.1: Laboratory strains used in this study

Strain, plasmid or cosmid	**Relevant genotype or phenotype**	**Source or reference**
Streptomyces coelicolor		
M145	Prototrophic derivative of A3(2) strain lacking both SCP1 and SCP2 plasmids	(Kieser *et al*., 2000)
M570	Δ*relA* M600; *hyg*^{r}	(Chakraburtty and Bibb, 1997)
M680	*ΔrelA*, *ΔrshA* M600	(Sun *et al*., 2001)
M690	*ΔrshA*	Mervyn Bibb and Andrew Hesketh, John Innes Centre
J1681	*ΔbldA S. coelicolor* A3(2) strain J1501 (*hisA1, uraA1 strA1 pgl* SCP1 SCP2)	(Leskiw *et al*., 1993)
DJ542	M145 DnaN-mCherry without apramycin resistance marker	Dagmara Jakimowicz, University of Wroclaw, Poland
LN108	M145 SCO7000::eGFP (*idh-egfp*), *apra*^{r}	This study
LN205	M145 SCO4142::eGFP (*pstS-egfp*), *apra*^{r}	This study
LN301	M145 SCO4655::eGFP (*rpoC-egfp*), *apra*^{r}	This study
DJ542/RpoC-eGFP	*rpoC-egfp* translational fusion in DJ542, *apra*^{r}	This study
M570/RpoC-eGFP	*rpoC-egfp* translational fusion in M570, *apra*^{r}	This study

M680/RpoC-eGFP	*rpoC-egfp* translational fusion in M680, *apra*^{r}	This study
M690/RpoC-eGFP	*rpoC-egfp* translational fusion in M690, *apra*^{r}	This study
J1681/RpoC-eGFP	*rpoC-egfp* translational fusion in J1681 (*ΔbldA*), *apra*^{r}	This study
Escherichia coli		
DH5α	General cloning host	(Grant *et al*., 1990)
BW25113 (pIJ790)	Cloning host harbouring λRED plasmid, K-12 derivative (Δ*araBAD*, Δ*rhaBAD*)	(Datsenko and Wanner, 2000)
ET12567 (pUZ8002)	Methylation-defective cloning host harbouring RP4 (*tra*, *neo*) plasmid for intergeneric conjugation	(MacNeil *et al*., 1992)

Table 2.2: Plasmids and cosmids used in this study

Plasmid or cosmid	**Relevant genotype or phenotype**	**Antibiotic resistance**	**Source or reference**
Plasmid			
pIJ786	Contains eGFP disruption cassette with apramycin resistance marker	Apramycin Ampicillin	(Gust *et al*., 2004)
pIJ790 (λ RED)	Temperature sensitive replicon (30˚C), λ-RED mediated hyper recombination (*gam*, *bet*, *exo*) with L-arabinose inducer *araC*	Chloramphenicol	(Gust *et al*., 2004)
pUZ8002	RP4 (*tra*, *neo*), mobilizes DNA for intergeneric conjugation by coding transfer protein Tra	Kanamycin	(Paget *et al*., 1999)
Cosmid			
SCD40A.01	Harbouring *rpoC* (SCO4655) gene of interest	Carbenicillin, Kanamycin	(Redenbach *et al*., 1996)
SC8F11.26c	Harbouring *idh* (SCO7000) gene of interest	Carbenicillin, Kanamycin	(Redenbach *et al*., 1996)

SCD84.09c	Harbouring *pstS* (SCO4142) gene of interest	Carbenicillin, Kanamycin	(Redenbach *et al*., 1996)
pLN108	SC8F11.26c *idh-egfp* translational fusion	Carbenicillin, Kanamycin, Apramycin	This study
pLN205	SCD84.09c *pstS-egfp* translational fusion	Carbenicillin, Kanamycin, Apramycin	This study
pLN301	SCD40A.01 *rpoC-egfp* translational fusion	Carbenicillin, Kanamycin, Apramycin	This study

Table 2.3: Antibiotic concentrations used to maintain plasmid/cosmid selection.

Antibiotic	Stock concentration (mg/ml)	Working concentration (µg/ml)	Solvent for stock
Ampicillin	50	50	H_2O
Apramycin	100	50	H_2O
Carbenicillin	100	100	H_2O
Chloramphenicol	25	25	100% EtoH
Kanamycin	25	50	H_2O
Nalidixic acid	25	25	H_2O

Growth curve experiments

Bacterial growth curve experiments were carried out using *S. coelicolor* A3(2) strain. Two litre shaking flask incubations were started with approximately 1 x 10^5 cfu/ml bacterial spore suspension of 400 ml YEME with no sucrose. Springs were not used in the flasks to allow mycelium to pellet. The cultures were incubated at 30ºC with shaking at 220 rpm for 85 hours. Viable colony forming units (cfu) were confirmed at the start of the incubation by preparing dilution series in distilled water and plating these onto MS agar plates.

Two parallel shake flask cultures were used to generate one growth curve. Samples of 11 ml culture were collected at appropriate times from both of the cultures. At each time point pH and dry weight were measured and live/dead microscopy and sample storage was performed. From both of the cultures pH was measured using standard laboratory pH meter. Dry weight was measured in triplicate, using 5 ml of culture by vacuum-filtration onto pre-weighed, glass microfiber filters (GF/C, 4.7 cm, Whatman, UK). The filters and biomass were washed with 5 ml of distilled water and dried overnight at ca 80°C, cooled down and weighed again. The dry weight of the culture was calculated from the difference between the two weights. Samples (5 ml) of culture were also centrifuged at 4°C at 4000 rpm for 15 min and cell pellets and supernatants were stored separately at -80°C for further analysis of antibiotic production.

Fluorescence microscopy

All microscopy was performed using Nikon TE2000S inverted fluorescence microscopy. Images were captured using a Hamamatsu Orca-285 Firewire digital charge-coupled device camera.

Live/dead imaging of pellets

Live/dead microscopy was performed using Live/dead® BacLight™ bacterial viability kit (Molecular Probe, L7007, Invitrogen Detection Technologies, Leiden, The Netherlands). The BacLight™ stain contains green fluorescent SYTO9 and red fluorescent propidium iodide (PI) nucleic acid stains. SYTO9 stains all the cells where as PI only stains cells with damaged membranes. When both stains are present in the cell at the same time, only PI binds to the nucleic acid due to its stronger binding affinity. The maximum excitation/emission for SYTO-9 and PI are 480/500 nm and 490/635 nm respectively. (Molecular Probes, Invitrogen Detection Technologies, Product Information, L7007)

Microscopic slides were prepared in the dark by mixing 15 µl of culture with 15 µl of 0.0334 mM SYTO9 and 0.20 mM PI stain in distilled water. Pictures were observed using 20X objective lens. Exposure times were 20ms for bright field and FITC filter set (SYTO9) through out the growth curve analysis. For TRITC filter set (PI) the initial exposure time was 50 ms for 12 – 24 h time points and 20 ms for 37 – 85 h time points.

Imaging of eGFP tagged proteins

Images of the eGFP constructs were taken from coverslip cultures grown on solid media as described by Kieser *et al*., (2000). Coverslips were inserted diagonally into agar plates with appropriate nutrients at around 45° angle and inoculated with 5 µl of spore stock suspension. The plates were incubated at 30°C for the required time. The coverslips were removed from agar plates and the adhered mycelium on the coverslips was directly stained with fluorescent stains SYTO42 and FM4-64 according to manufacturer's instructions. Coverslips were mounted on slides and the images were taken using 100X objective lens. The exposure times were 50 ms for bright field, 100 ms to visualise eGFP under FITC filter set, and 200 ms for both

SYTO42, to visualise nucleic acids under DAPI filter set, and for FM4-64 to observe cell membranes under TRITC filter set.

Time lapse microscopy of eGFP constructs

Time lapse microscopy was performed as described earlier by Jyothikumar *et al.*, (2008). Sterile cellophane squares were inoculated with 1 µl of spore stock solution (ca 1 x 10^9 cfu/ml) and grown overnight at 30°C on minimal medium containing 5% (wt/vol) mannitol or on nutrient agar plates. The mycelium filled cellophane was then transferred into a sterile microdisc with oxygen permeable membrane (80136, ibidi Integrated BioDiagnostics, Munich, Germany) and a piece of appropriate agar was placed on top of the cellophane (Hickey *et al*., 2002). Time lapse microscopy was performed using 100X objective lens. Images were taken every 10 minutes for appropriate time with 100 ms exposure time for the eGFP using FITC filter set. A growth test was performed at the start of experiments that study the effect nutrient depletion and antibiotic treatment have on hyphal growth. In transcription foci studies, the stringent response was induced by growing bacteria under nitrate limited growth conditions where the L-asparagine in minimal medium with mannitol was replaced by sodium nitrate.

Image analysis

Pictures were analysed using IPLab scientific imaging software version 3.7 (Scanalytics, Inc., Rockville, USA). When necessary, an automated image analysis of pellets was performed for fluorescence images using iterative mode as per the software manufacturer's instructions. The resulting segmentation was manually verified to cover the area of the pellet. Computer software assisted automated measurements are detailed in Table 2.4 (IPLab Scientific Imaging Software manual, Scanalytics, Inc., Rockville, USA).

Manual measurements of an early hyphal growth in liquid cultures were taken from the bright field images. Apical length (l_1) of hyphae was measured from

the apical tip to the first branch (i.e. two of the longest parts of hyphae of a free filament). Interbranch distance (l_2) was the measurement of hyphal length between two adjacent branches. The maximum pellet diameter was measured across the hyphal clump between two tips that were the furthest apart. Total length of hyphae included all mycelium (including the hyphal length of all the branches). Branching angle (ψ) was measured between the identified apical hyphae and its branches from an angle formed at the apical hyphal side (i.e. angle closest to the nearest apical tip) (Figure 2.1 A).

Manual measurements of the pellet growth in shake flask cultures included maximum pellet diameter and total number of tips at the pellet perimeter. The manual image analysis was performed for bright field, SYTO9 and PI images taken at 12 – 61 h time points. No later time points were analysed since it was evident that majority of the pellets had lysed, and growth occurred only from the tangled hypha broken off from the original pellet. Number of tips was measured for the early time points until the pellets became too dense for counting the individual tips.

Manual measurements of *Streptomyces* grown on solid agar were mainly used to analyse the eGFP localization within the hyphae. When z-section was used in capturing these images, the individual sections were merged and deconvolution was performed as necessary, using IPLab scientific imaging software version 3.7 (Scanalytics, Inc., Rockville, USA). Multiprobe images (brightfield in grey, eGFP in green) were used to measure for example, RpoC foci length. An example of such measurements is shown in Figure 2.1 B.

Table 2.4. Description of computerized measurements (IPLab Scientific Imaging Software manual Scanalytics, Inc., Rockville, USA)

	Description
Mean	Mean intensity value of the pixels within a pellet
Area	Pellet area (1 pixel has an area of 1)
Perimeter	Pellet perimeter (1 pixel has a perimeter of 4)
Radial SD	Percentage of the mean radius of the pellet (i.e. standard deviation of the distance between the centroid and the edge of the ellipse)
Major Axis	Maximum diameter of the pellet (axis passes through the centroid of the ellipse) (µm)
Minor Axis	Minimum diameter of the pellet (perpendicular to the major axis) (µm)
Eccentricity	Value to describe how close the pellet shape is to a circle (0 for perfect circle, 1 for extreme ellipse)

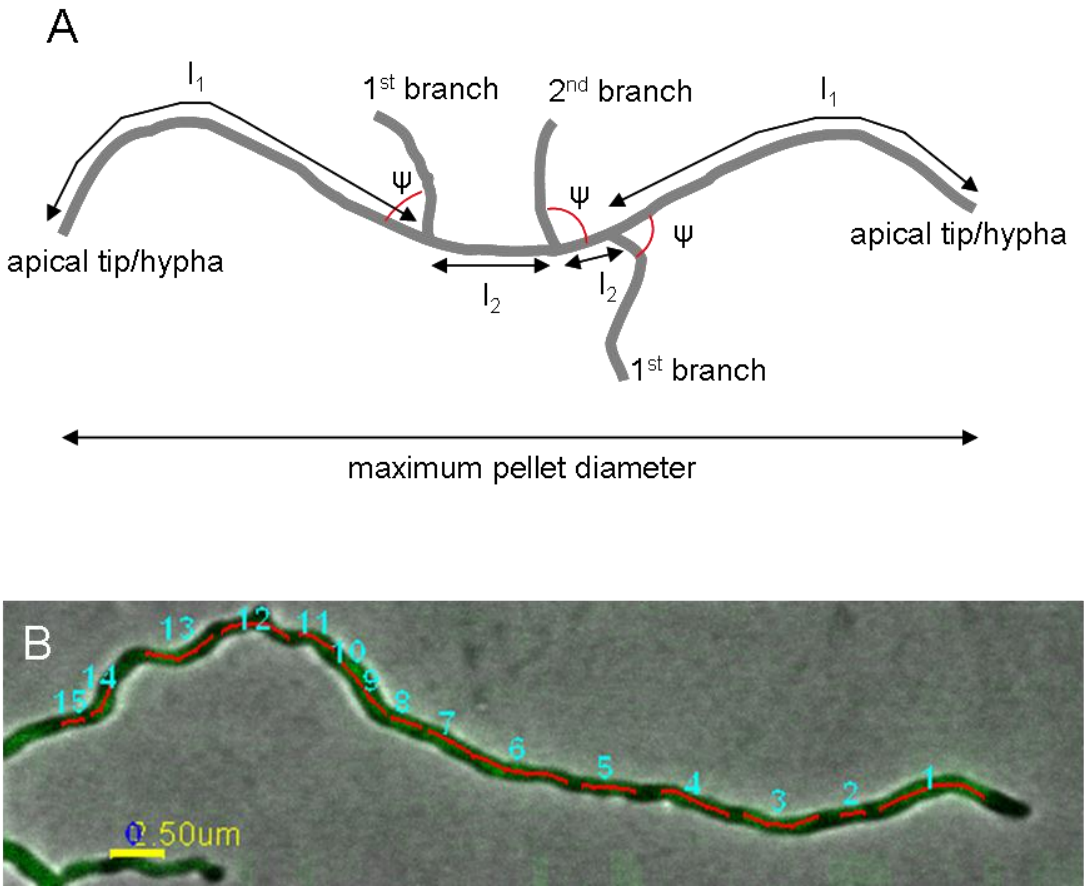

Figure 2.1: Manual measurements of hyphae. A. Diagram illustrating the apical tip and branches used to measure mycelium dimensions from free hyphae grown in shake flask cultures. Branching angle is shown as ψ, and apical (l_1) and interbranch (l_2) distances are presented. B. Typical measurements of RpoC-eGFP foci length in strain LN301 using multiprobe image (bright field in grey, eGFP in green, measured length in red). Numbers 1-15 illustrates the number of foci. A scale bar of 2.5 µm is included (in yellow).

Data analysis

Statistical analysis of the hyphal and pellet measurements was performed using Microsoft Office Excel software. The analysis included standard measures such as the average (mean), the standard deviation (Stdev) and the percentage of coefficient variation (CV%). Statistically significant difference between two data sets was calculated using unpaired two-tailed student t-test (homoscedastic). Hyphal growth unit (HGU) was calculated as the total length of hyphae divided by the total number of tips. The volume (V) of a pellet was calculated using the Equation 2.1 for prolate spheroid where a is minor axis and b is major axis.

$$V = \frac{4}{3}\pi a^2 b \tag{2.1}$$

Quantitative chemical analysis

Quantitative assays were used for samples taken during growth curve experiments to determine the substrate concentrations of phosphate and nitrogen and to monitor the antibiotic production of undecylprodigiosin and actinorhodin.

Phosphorus assay

The amount of phosphorus in the supernatants of the growth curve samples was determined. The method used was modified from Plummer (1987) to suit a 96-well plate assay. The method is based on reduction of molybdate in the presence of phosphorus that results in the formation of a blue compound that absorbance can be determined. Copper ions are added to minimize the inhibition of the reduction by bacterial extract. (Peel and Loughman, 1957)

For each assay aliquots (40 µl) of calibration standards, samples and distilled water blank were added to 96-well plate. Copper acetate buffer of pH 4 (120

µl), ammonium molybdate (20 µl) and reducing agent (20 µl) were added to each well (see Appendix 2 for recipes). Between the addition of reagents the 96-well plate was gently shaken to mix and incubated at room temperature for 10 minutes. Following the final incubation of 40 minutes at room temperature the absorbance was read at 880 nm using SpectraMAXM5 spectrophotometer. The calibration standards contained known amounts of phosphorus ranging from 2-10 µg/ml K_2HPO_4 with respect to phosphorus in distilled water. Standard curves were plotted for absorbance over concentration using Microsoft Office Excel and the phosphate concentrations of the unknown samples were determined from the calibration curves. Samples were diluted in distilled water when appropriate.

Ammonia assay

The concentration of ammonium in the growth curve supernatant samples was determined spectrophotometrically. Fawcett and Scott (1960) method was modified to be used with 96-well plates. The determination is based on the formation of indophenol blue when ammonium reacts with phenol and hypochlorite.

For each assay 5 µl aliquots of calibration standards, samples and distilled water blank were added to a 96-well plate. Sodium phenate (50 µl), sodium nitroprusside (75 µl) and sodium hypochlorite (75 µl) were added to each sample (see Appendix 2 for recipes). The plates were gently mixed and incubated at room temperature for ca 30 minutes. The absorbance was determined at 620 nm using Labsystems iEMS Reader MF spectrophotometer. The calibration standards contained 0.5-3.5 mM NH_4Cl with respect to ammonium in distilled water. Standard curves were created using Microsoft Office Excel to plot absorbance over concentration and the ammonium concentrations of the unknown samples were read from the calibration curves. Samples were diluted in distilled water when necessary.

Ninhydrin assay

The concentration of ninhydrin-positive amino group in the growth curve supernatant was determined using ninhydrin assay by Rosen (1957). The method gives a 100 % reaction yield for all amino acids except for proline and hydroxyproline.

Aliquots of 20 µl of D-Alanine calibration standards, samples and distilled water blank were added to 1 ml of ninhydrin reagent (see Appendix 2 for recipe). The samples were mixed using vortex and incubated at 37 ˚C water bath for ca 30 minutes before reading the absorbance at 570 nm using Nanodrop 2000c Spectrophotometer (Thermo Scientific). The six calibration standards ranged from 0.05 to 0.3 mg of L-Alanine in 1 ml of distilled water. The calibration curve of absorbance over concentration was plotted using Microsoft Office Excel. The concentration of amino groups in unknown samples was determined using the standard curve. The unknown samples were diluted 1:5 in distilled water prior to analysis.

Undecylprodigiosin assay

To quantify the amount of undecylprodigiosin (RED) in the growth curve cell pellets, a method described by Kieser *et al*., (2000) was used. In brief, the cell pellets were dried over night using cell freeze/dryer. From the dried mycelium, RED was extracted into 1 ml of methanol. Samples were acidified by adding HCl to a final concentration of 0.5 M prior to vortexing and centrifuging. The absorbance was measured spectrophotometrically from the supernatants at 530 nm against methanol/HCl blank using Nanodrop 2000c Spectrophotometer (Thermo Scientific). The baseline was corrected at 750 nm. The amount of RED was calculated from the absorbance readings using Beer-Lambert law;

$$A = \varepsilon c l \qquad (2.2)$$

where A is absorbance, ε is molar extinction coefficient (100500 for RED), c is the concentration of RED and l is the length of the used light path (1 cm). When necessary the samples were diluted 1:5 or 1:10 in MtOH/HCl prior to spectrophotometric analysis.

Actinorhodin assay

Extracellular γ-actinorhodin was quantified according to a method described by Kieser *et al*., (2000) from the growth curve culture supernatants. The samples were acidified to pH 2-3 by the addition of HCl. Actinorhodin was extracted into chloroform by adding ¼ volume of chloroform into the samples and vortexing gently. Samples were centrifuged and the absorbance was read from the chloroform layer using Nanodrop 2000c Spectrophotometer (Thermo Scientific) at 542 nm against chloroform blank. The concentration of γ-actinorhodin was then calculated from the absorbance readings using Beer-Lambert law (see above) with a molar extinction coefficient of 18600.

Isolation of plasmid and cosmid DNA from *E. coli* cultures

Alkaline lysis method was adapted from Birnboim and Doly (1979) and Ishhorrowicz and Burke (1981) to isolate plasmid DNA (pDNA) and cosmid DNA (cDNA) from *E.coli*. Aliquots (5 ml) of LB with the appropriate antibiotics were inoculated with an *E. coli* strain harboring the relevant plasmid or cosmid and grown overnight at 37°C with shaking at 220 rpm. Cell were harvested by centrifugation at 13000 in 1.5 ml eppendorfs and resuspended in 100 µl of ice cold solution 1 (see Appendix 2 for recipes) by pipetting and vortexing. An aliquot (200 µl) of freshly prepared solution 2 was added to each tube and the tube was inverted five times to mix the content. From here onwards the tube was stored on ice. Finally, 150 µl of ice cold solution 3 was added to the mixture and the content was mixed by vortexing the tube gently in an inverted position. The mixture was stored on ice for five minutes and then centrifuged at 13000 rpm for five minutes. The supernatant was transferred to a fresh microcentrifuge tube and 200 µl of phenol and 200 µl of

chloroform were added to the supernatant. The contents of the tube were mixed by vortexing prior to centrifuging at 13000 rpm for two minutes. The top layer was transferred to a fresh microcentrifuge tube and the phenol/chloroform extraction was repeated once as per above. The DNA was precipitated by adding two volumes (ca 700 µl) of 100% ethanol and mixing the contents of the tube by inversion and then allowed the mixture to stand for two minutes at room temperature. The tube was centrifuged for 10 minutes at 13000 rpm. The supernatant was disregarded and the pellet was dried in Speed Vacuum Concentrator (Savant) for ca 30 minutes or until dry. The pellet of DNA was resuspended in 25 - 50 µl of TE buffer and then 2 µl of DNAase-free pancreatic RNAse (20 µg/ml) was added to the suspension and the suspension was incubated at 37°C water bath for ca 15 minutes. The DNA was stored at -20°C.

For electroporation and transformation purposes, the DNA was isolated using commercial kits (Promega, Qiagen) according to the manufacturers' instructions.

Isolation of genomic DNA from *Streptomyces* cultures

Genomic DNA was isolated according to modified Kieser *et al*. (2000) method.

Small scale DNA isolation for PCR analysis

Cultures (10 ml) of YEME without sucrose were inoculated with *Streptomyces* spores and incubated at 30°C with shaking at 220 rpm for two days. Cells were harvested by centrifugation for ten minutes at 4000 rpm and the cell pellet was resuspended in 400 µl of Solution 1 of the alkaline lysis method (see Appendix 2 for recipes) and transferred to a 1.5 ml microcentrifuge tube. Aliquots (10 µl of each) of 30 mg/ml lysozyme and 5 mg/ml RNaseA were added and the mixture incubated at 37°C water bath for ca one hour. Thereafter, 10 µl of 10% SDS solution was added to the mixture and the content of the tube was mixed gently. The DNA was extracted twice by adding 250 µl of phenol, gently shaking the tube for ca five minutes, centrifuging at 13000 for five minutes and transferring the upper phase to a fresh tube on both of the times. The DNA was precipitated by adding 1 ml of 100% ethanol to the mixture and leaving the tube to stand at room temperature for ca five minutes. The nucleic acid was pelleted by centrifugation at 13000 rpm for two minutes, the supernatant removed and the pellet air dried and resuspended in 30 µl of sterile dH_2O. The DNA was stored at -20°C.

Large scale DNA isolation for Southern blot analysis

Cultures (80 ml) of YEME without sucrose in 250 ml Erlenmeyer flasks with springs were inoculated with approximately 1 x 10^7 *Streptomyces* spores and incubated at 30°C with shaking at 220 rpm for two days. Cells were harvested by centrifugation for 10 minutes at 4000 rpm, resuspended in 20 ml of Solution 1 of the alkaline lysis method (see Appendix 2 for recipes) and transferred to a 50 ml centrifuge tube. Aliquots (400 µl and 100 µl respectively) of 30 mg/ml lysozyme and 20 mg/ml RNaseA were added and the mixture incubated at 37°C for ca one hour. Cells were lysed by adding 1

ml of 10% SDS solution and mixing gently. Phenol extraction was performed three times, each time by adding 10 ml of phenol solution and then shaking the mixture gently for ten minutes prior to centrifuging at 4000 rpm for 10 minutes, always taking the aqueous layer forward. After the final extraction, 20 ml of 100% ethanol was added to the DNA sample and mixed gently. The precipitated DNA was spooled onto a sealed pipette, transferred to a fresh tube with 1 ml of 100% ethanol and centrifuged at 13000 rpm for two minutes. The supernatant was removed and the DNA pellet air dried. Finally, the DNA pellet was resuspended in 1 ml of sterile dH_2O. The genomic DNA was stored at -20°C.

Gel electrophoresis

Gel electrophoresis was performed according to the manufacturer's instructions using Biorad electrophoresis tanks. Unless otherwise stated, the gels were prepared at 0.8% agarose in 1 x TAE buffer (40 mM Tris-acetate, 1 mM EDTA) containing 10 µg/ml ethidium bromide. Gels were run at 80-100 V for 80-120 minutes in 1 x TAE buffer and visualized using Syngene GelDoc system with UV light. Standard molecular size markers were run on each gel with appropriate fragment sizes (see individual gels). Gel extraction was carried out using the UV transilluminator (UVP) on a low setting.

eGFP tagging of proteins using Redirect© technology

Proteins were translationally fused to the enhanced green fluorescent protein (eGFP) in their native chromosal location in *Streptomyces* strains (Table 2.5). The strains were constructed according to the Redirect© technology (Gust *et al.*, 2002). In brief, the insertion cassette containing the eGFP gene and apramycin resistance marker was amplified with standard PCR machine using primers with 39 nt homology extensions (see primer design below). The *Streptomyces* cosmid (Redenbach *et al*., 1996) containing the gene to be tagged was electroporated into *E. coli* BW25113 strain that had λ RED plasmid pIJ790. Then, the insertion cassette (linear DNA) was inserted into

BW25113/pIJ790 strain by electroporation where λ RED plasmid mediated its recombination to the cosmid. The correct cosmid construct was then transformed into non-methylating *E. coli* strain ET12567 harbouring non-transmissible pUZ8002 for conjugative transfer of the cosmid construct from ET12567 strain to *Streptomyces*. After successful conjugation, colonies were screened for double cross-overs ($Kanamycin^S$, $Apramycin^R$) that had gone through a homologous recombination of the eGFP cassette into the chromosome (Figure 2.2).

Table 2.5: Genes fused to eGFP.

Cosmid identification in this study	Cosmid name*	eGFP fusion to gene	SCO number of the gene	Gene product
C8F11	SC8F11.26c	*idh*	SCO7000	Isocitrate dehydrogenase
SCD84	SCD84.09c	*pstS*	SCO4142	Phosphate binding protein precursor
D40A	SCD40A.01	*rpoC*	SCO4655	RNA polymerase beta' subunit

* Cosmids received from the *S.coelicolor* cosmid library at the University of Wales Swansea (Redenbach *et al*., 1996)

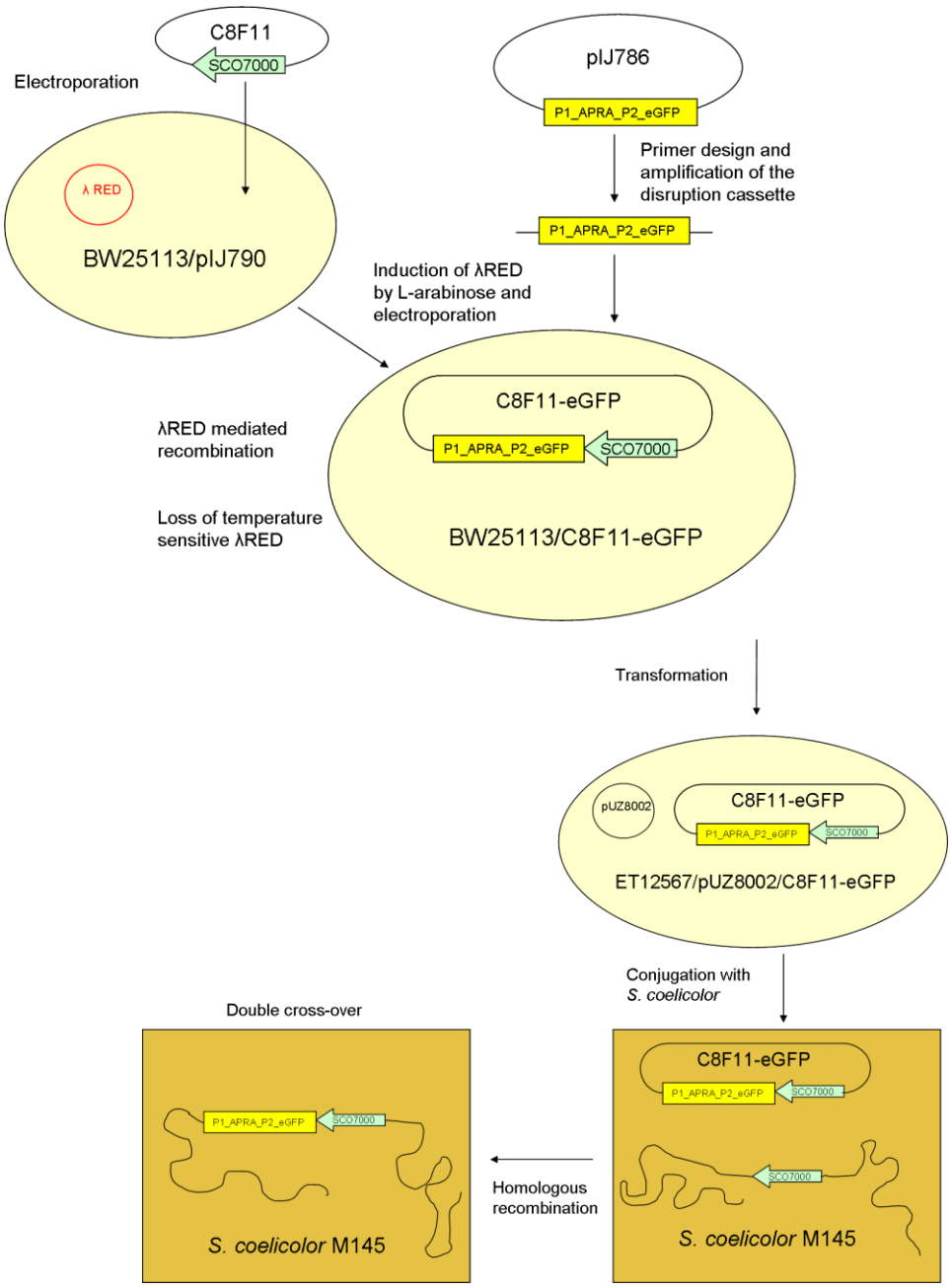

Figure 2.2: Tagging of protein SCO7000 with an enhanced green fluorescent protein (eGFP) using PCR-targeting, Redirect® technology (Gust *et al*., 2002). Amplified cassette, containing eGFP and apramycin resistance genes, was inserted into *Streptomyces* cosmid C8F11 in *E. coli* BW25113/pIJ790 strain. The cosmid construct was transformed into a methylation deficient *E. coli* ET12567/pUZ8002 strain and then transferred into *Streptomyces* strain via conjugation, where the eGFP was inserted into the chromosome via homologous recombination.

PCR primers and their design

Redirect PCR primers were designed according to Gust *et al*., 2002 using a 10 amino acid long linker sequence to enhance the correct folding of the eGFP protein, which has been used previously in eGFP tagging of proteins in *Streptomyces* by Jakimowicz *et al.* (2005). Primers to confirm the correct insertion of eGFP were designed using GeneFisher software (Giegerich *et al*., 1996) (Figure 2.3). The primers were manufactrured by Eurofins. Standard 50 µl PCR reactions were performed using GoTaq Flexi DNA polymerase (Promega) according to manufacturer's instructions. The primer sequences and the PCR conditions are shown in Tables 2.6 and 2.7 respectively.

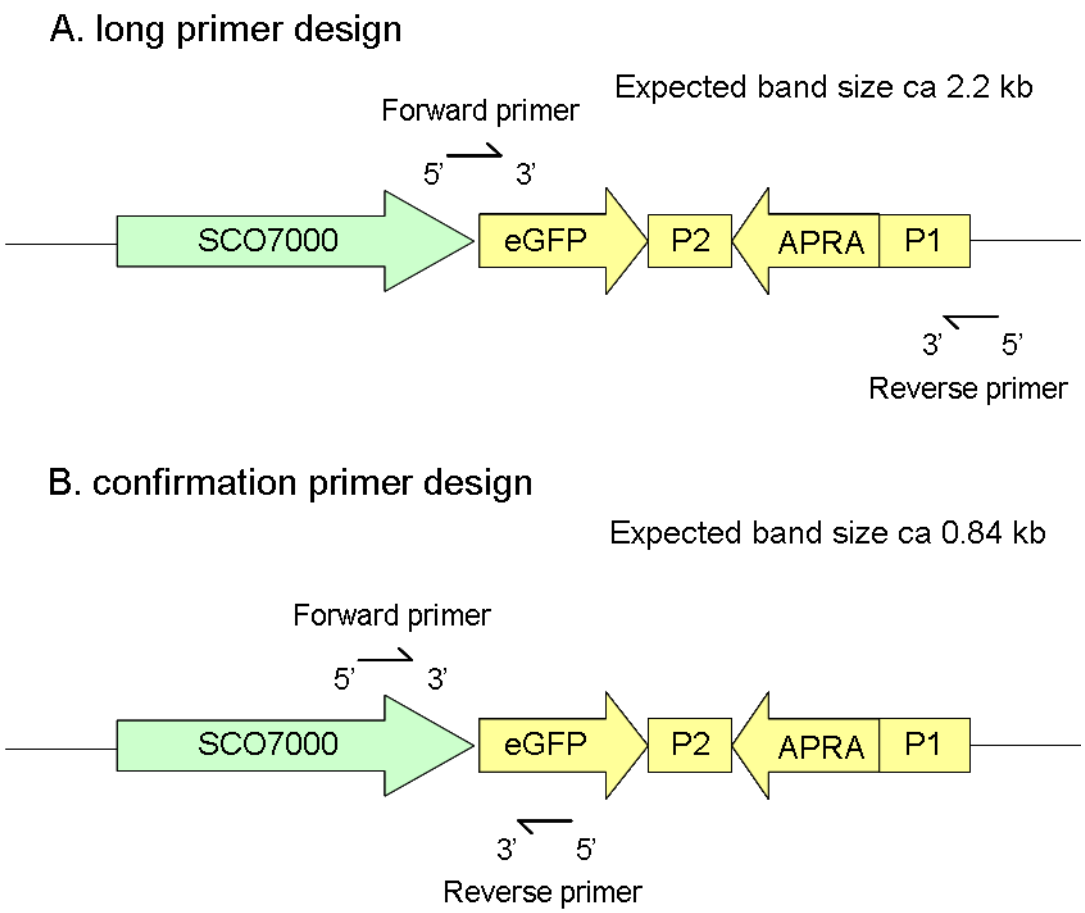

Figure 2.3: Diagram illustrating the positions of designed primers using *idh-eGFP* as an example. A. Long primer design according to Redirect protocol from Gust *et al*., (2002). B. Primers designed to confirm the successful eGFP-tagging of a protein are shown. Genes presented are SCO7000 (*idh*) and apramycin resistance cassette (eGFP-P2-APRA-P1) containing enhanced green fluorescent protein gene (*egfp*).

Table 2.6: Used primer sequences.

Oligo ID	Sequence (5' -> 3')	Tm (°C)	Source or reference
rpoC eGFP Cterm1	CCG CTG GAG GAC TAC GAC TAC GGT CCG TAC AAC CAG TAC CTG CCG GGC CCG GAG CTG CCG GGC CCG GAG GTG AGC AAG GGC GAG GAG CT	> 75	(Baron, 2009)
rpoC eGFP c term	CTC GGG GTG ACC GCC CTT CGG TCG TAT CAA GCT GCC CGC TTC CGG GGA TCC GTC GAC C	> 75	(Baron, 2009)
idh eGFP Cterm1	TCG ACC ACC TGG AAC GAG GCG CTG GCG TCC CTC GCC TGG CTG CCG GGC CCG GAG CTG CCG GGC CCG GAG GTG AGC AAG GGC GAG GAG CT	> 75	This study
Idh Rev NEW	GAA ACG GGG TGC CCG TGG GGT GCG CGG GGC TCC CGA GGA ATT CCG GGG ATC CGT CGA C	> 75	This study
pstS gfp for	ATC ACC AAG GTC CGC GAG ACC ATC TCG GGC CTG AGC TGG CTG CCG GGC CCG GAG CTG CCG GGC CCG GAG GTG AGC AAG GGC GAG GAG CT	> 75	This study
PstS gfp Rev	ACG CTG TCG GCT CCG CGC GGA GGC CGG ACC GCA CTC GGG ATT CCG GGG ATC CGT CGA C	> 75	This study
eGFP/rpoB linkF *	GGT TGT CGG GCA GCA GCA	60.5	(Baron, 2009)
eGFP/rpoB link R	GTC GGC CGC CTC CTT CCA	62.8	(Baron, 2009)
Idh-egfp check	GGC GAA GCA GAC CGA CGA	60.5	This study
pstS internalLN	GCC TGC GAC AAG GGC AA	57.6	This study

* Internal to eGFP

Table 2.7: Generalised PCR conditions

No. cycles	Temperature (ºC)	Time (minutes: seconds)
1 - Denaturation	94	2:00
28 - Denaturation	94	0:15
- Annealing	Ta	0:30
- Extension	72	1:40
1 -Final extension	72	10:00

Preparation of electrocompetent cells

Electrocompetent *E. coli* cells were prepared according to Sambrook *et al*. (1989) and Gust *et al*. (2002). Aliquots (5 ml) of LB containing the correct antibiotics were inoculated with *E. coli* and grown overnight at 37°C (30°C used for BW25113/pIJ790 strain) with shaking at 220 rpm. The overnight cultures were used to inoculate fresh 50 - 100 ml of LB or SOB with 20 mM $MgSO_4$ and with appropriate antibiotics (10 mM final concentration of L-arabinose used for BW25113/pIJ790 to induce λ RED for PCR targeting of a cosmid) in 250 ml Erlenmeyer flasks and these were grown at 37°C (30°C used for BW25113/pIJ790 strain) with shaking at 220 rpm until an OD_{600} of 0.4 - 0.6 was reached. Cells were harvested by centrifugation for 5 minutes at 2500 rpm at +4°C and resuspended gently, on ice, in 20 ml of ice cold 10% glycerol. Cells were harvested and resuspended in 10 ml of ice cold 10% glycerol as per above for a further two times. The resulting cell pellet was resuspended in ca 100-150 µl of ice cold 10% glycerol and aliquoted in 50 µl volumes into ice cold eppendorfs. The tubes were kept on ice for immediate use in electroporation.

Electroporation of *E. coli*

Electroporation of *E. coli* was carried out as per Dower *et al.* (1988) and Gust *et al*., 2002 instructions. A 50 µl aliquot of electrocompetent cells was gently mixed with 1-2 µl of the appropriate plasmid, cosmid or PCR-product (0.1 – 0.5 µg of DNA) and left on ice for 15 - 30 minutes. The mixture was then transferred to a 0.1 cm gap, ice-cold electroporation cuvette and electroporated at either 12.5 kV cm^{-1} or 18 kV cm^{-1} using Biorad MicroPulser™ electroporator. Immediately after electroporation, 1 ml of ice-cold LB medium was added to the cuvette and mixed by gentle pipetting. The culture was transferred into 5 ml Falcon tube and incubated at 37°C with shaking at 220 rpm for 60 to 180 minutes. After incubation, cells were harvested by centrifugation, resuspended in LB and spread on LB agar containing appropriate antibiotics. No salt was used in LB plates when

growing ET12567 strain. The plates were incubated 16 – 24 hours at 37°C. A sample of electrocompetent cells without added DNA was carried through the process as a negative control of antibiotic efficiency. Emerging colonies were picked from the plates to inoculate 5 – 10 ml of LB with appropriate antibiotics and incubated overnight at 37°C with shaking at 220 rpm. These cultures were stored as glycerol stocks at -80°C or used for conjugation (Kieser et al., 2000).

Preparation of chemically competent *E. coli* cells

Chemically competent *E. coli* cells were prepared according to Sambrook *et al*., 1989. Aliquots (5 ml) of LB were inoculated with DH5α strain of *E. coli* and grown overnight at 37°C with shaking at 220 rpm. The overnight culture was used to inoculate 100 ml of fresh LB media in 250 ml Erlenmeyer flask and the flask was incubated at 37°C with shaking at 220 rpm until an OD_{600} reached 0.4 - 0.6. Cells were harvested by centrifugation at 4000 rpm for 10 minutes at 4°C and resuspended gently in 30 ml of ice-cold TFB1 buffer (100 mM RbCl, 50 mM $MnCl_2$, 30 mM KAc, 10 mM $CaCl_2$, 15% glycerol, pH 5.8, sterile-filtered). The mixture was kept on ice for ca 90 minutes before harvesting the cells again as per above. The resulting cell pellet was gently resuspended in 4 ml of ice-cold TFB2 (10 mM MOPS, 10 mM RbCl, 75 mM $CaCl_2$, 15% glycerol,,pH 8.0, autoclaved). The cell suspension was then aliquoted in either 50 µl or 500 µl volumes and snap freezed in liquid nitrogen before storing at -80°C.

Transformation of *E. coli*

E. coli strain DH5α was used in transformation of chemically competent cells as per Sambrook *et al*., 1989. An aliquot (50 µl) of chemically competent cells was incubated with 1 – 5 µl of the appropriate plasmid or cosmid (1 µg – 10 µg of DNA) for 30 – 60 minutes on ice. A negative control containing only chemically competent cells with no added DNA was prepared and carried forward throughout the transformation. The cells were heat shocked at 42°C

for 2 minutes and placed at room temperature before adding 1 ml of LB or 2 x YT broth to the sample. The culture was incubated at 37°C water bath for 60 to 180 minutes. The cells were then spread onto LB agar containing the appropriate antibiotic and incubated at 37°C for overnight.

Intergenic conjugation of cosmid from *E. coli* to *Streptomyces*

A modified method from Kieser *et al*., 2000 and Gust *et al*., 2002 was used to perform the conjugation. An overnight culture of *E. coli* ET12567/pUZ8002 previously transformed with the appropriate cosmid was diluted 1:100 in LB with the correct antibiotics and grown to OD_{600} of 0.4 – 0.6 at 37°C with shaking at 220 rpm. The cells were harvested by centrifugation at 2500 rpm for 5 minutes at 4°C and washed three times in 10 ml of fresh LB. Finally, the cell pellet was resuspended in 0.5 ml of LB. Then, 10 µl of *Streptomyces* spore stock containing approximately 1 x 10^7 spores was mixed with 0.5 ml of 2 x YT and the mixture was heat shocked for 10 to 20 minutes at 50°C water bath and allowed to cool down at room temperature. The 0.5 ml *E. coli* cell suspension and the 0.5 ml heat shocked *Streptomyces* spore suspension were mixed together and and allowed to stand at room temperature for 60 to 90 minutes. The mixture was spread onto MS agar containing 10 mM $MgCl_2$, The plates were incubated at 30°C for 16 to 20 hours and then an overlay of 1 ml of nalidixic acid (500 µg/ml) and the appropriate selective antibiotic was added before continuing the incubation at 30°C. The resulting colonies were screened for double cross-over exconjugants (kanamycin^S and apramycin^R) by patching the colony onto two nutrient agar plates containing nalidixid acid and apramycin with and without kanamycin respectively. These plates were then incubated at 30°C for two days and colonies which grew on apramycin but not on kanamycin were deemed to be double cross-overs. These colonies were streaked for single colonies on MS agar for spore stock preparation. Note, if only single cross-overs (kanamycin^R and apramycin^R) obtained from nutrient agar with the correct antibiotics then colonies from nutrient agar plate with nalidixid acid and apramycin were streaked out on MS without antibiotics. After incubation at 30°C for 3 to 5 days, resulting

colonies were patched again on two nutrient agar plates containing nalidixid acid and apramycin with and without kanamycin respectively and incubated at 30°C for 2 days to screen for double cross-overs (Gust *et al*., 2002). Purified kanamycin sensitive strains were verified by PCR, sequencing and Southern blot analysis.

Southern blot

Southern blot analysis was performed as per Sambrook *et al*., 1989.

Probe preparation and labelling

Probe DNA (0.5 - 1 µg) was diluted to 15 µl of sterile, deionised water and incubated for 15 minutes at 95°C using standard PCR machine. The solution was then cooled down rapidly on ice water for approximately 10 minutes. The resulting denatured DNA was mixed with 2 µl of hexanucleotide mix (Roche), 2 µl digoxigenin (DIG) DNA labelling mix (Roche) and 1 µl Klenow fragment (Promega) and incubated overnight at 37°C. The reaction was stopped by adding 2 µl of 0.2 M EDTA.

Sample DNA digest and transfer

DNA samples were digested using appropriate restriction enzymes according to manufacturers' instructions and the fragments were electrophoresed as described previously. Unless otherwise stated, ca 2 µg of digested genomic DNA or ca 25 - 30 ng of digested cosmid DNA or ca 1 ng of digested plasmid DNA was used per lane of the gel. The DNA was transferred from the gel to Hybond N nitrocellulose membrane (Amersham) using VacuGene equipment according to the manufacturer's instructions. After transfer membrane was cross linked by exposing it to UV irradiation (Syngene transilluminator at 100%) for 2 minutes. Finally, the membrane was washed in 2 x SSC (see Table 2.8) for a further 2 minutes and either used immediately in hybridisation or stored wrapped in a clean film at -20°C.

Hybridisation and washes

For hybridisation, the membrane was wrapped in mesh and placed into a Hybaid tube containing 20 ml of preheated (65°C) standard hybridisation buffer (SHB) (see Table 2.8). The tube was placed in a rotating Hybaid oven at 65°C for 60 minutes. Meanwhile, the probe was melted at 99°C for 15 minutes and immediately placed on ice for 10 minutes. It was then added to 20 ml of SHB at room temperature. After the first incubation, the probe free SHB was removed from the tube containing the membrane and replaced with the fresh SHB containing the probe. The tube was then replaced in the Hybaid oven and left to hybridise at 65°C overnight with rotation.

Subsequently, the SHB with the probe was decanted off and the tube was washed twice by adding 150 ml of stringency buffer A (see Appendix 2 for recipes) to the tube and further incubating it for 15 minutes at 65°C. Further two washes were done using a stringency buffer B as per above. The membrane was removed from the Hybaid tube and the mesh and was rinsed in washing buffer for 30 seconds prior to washing in freshly prepared blocking solution (Roche) for 30 minutes with gentle shaking. The blocking solution was then replaced by 30 ml of antibody solution that was left to incubate for 30 minutes with gentle shaking. The unbound antibody was washed away by adding 100 ml of washing buffer for two periods of 15 minutes each. The membrane was equilibrated in 20 ml of detection buffer for 2 minutes and then incubated stagnant with 20 ml of freshly prepared colour substrate solution in the dark. Once colour was sufficiently developed, the reaction was stopped by rinsing the membrane in distilled water.

Chapter 3: Constructing a mathematical model

To assist the understanding of the pellet formation in liquid cultures, we constructed a mathematical model of hyphal growth that includes the effect of external substrate concentration and models the metabolic switch of hyphae from primary metabolism to secondary metabolism. An important aspect of the modelling work is that it is completed in parallel with the laboratory experiments, leading to a well-validated and parameterized theoretical description of streptomycete growth.

Initial framework for the model

We initiated the modeling work by creating a framework for the model based on current biological knowledge. A schematic presentation of the model framework is illustrated in Figure 3.1. The framework for the model takes into account the spatial hyphal morphology and links it to six different metabolic stages. A spore germinates in state one through formation of a tip. The tip starts to actively extend during growth and achieves exponential growth by branching. New branches continue to actively grow. It is assumed that the active hyphae formed have at least two out of three different metabolic states at any one time - metabolic activity for cellular maintenance requirements (state four) and either primary metabolism (actively growing; state two) or secondary metabolism (antibiotic production; state three). Primary metabolism is assumed to contain all requirements for active growth. In state three (secondary metabolism), cells are assumed to have stopped actively growing, although branching may still occur at a low frequency. The main metabolic requirements in this state are for production of secondary metabolites. Active hypha will become inactive (state five) over time and eventually cell death will occurs. Once at the state of cell death (state six) cells undergo lysis and will release components into the growth media. It is not clear what kind of metabolic activities inactive hypha will have if any, as the process of death and autolysis is poorly understood. The model framework suggests possible maintenance metabolism requirements and

release of components to the growth media. From experimental studies, it is also not clear if inactive hypha can return to being metabolically active hypha.

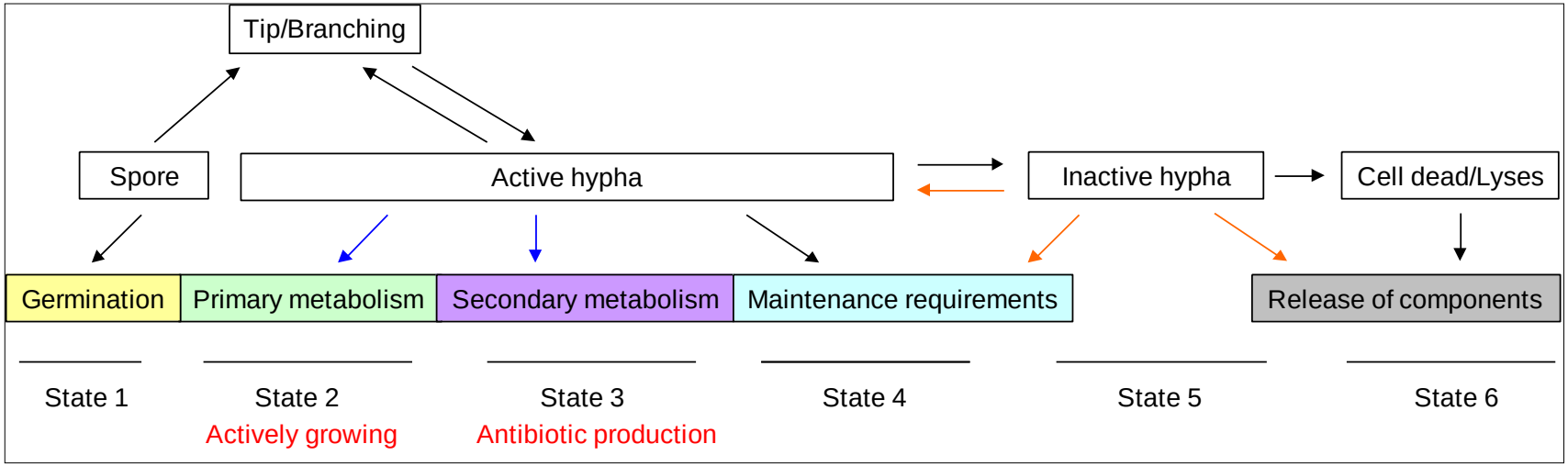

Figure 3.1: Schematic presentation of initial modeling framework. Arrows represent possible connections between developing hyphae and between six different metabolic stages. Black arrows illustrate compulsory development of the hypha. The model assumes that active hypha will have two out of possible three metabolic states occurring at one time. Maintenance requirements are present at all time in active hypha where only either primary or secondary metabolism can occur at a given time (blue arrows). Orange arrows illustrate the unknown functions of inactive hypha.

Model for early hyphal growth

Apical elongation

In filamentous organisms a cell elongates through extension of its tip (Bezzi and Ciliberto 2004). To describe the elongation of individual hyphae, we construct a 2D+ random walk model for hyphal tip movement. The assumed random walk is uncorrelated and unbiased meaning that the new direction of the tip is totally independent on the previous directions moved, and that the direction of the movement does not have any preference. The new location of the tip is therefore only dependent on its location in the previous step and its current velocity. This represents the situation in a mixed liquid medium. The model allows tip paths to cross over creating a 2D+ effect where an assumption is that the overlapping tip paths are in different 3D planes.

The hyphal growth is illustrated in Figure 3.2, where a tip is located according to its vector position ($\underline{x}$) in 2D space. Direction of the growing tip is governed by velocity ($\underline{v}$).

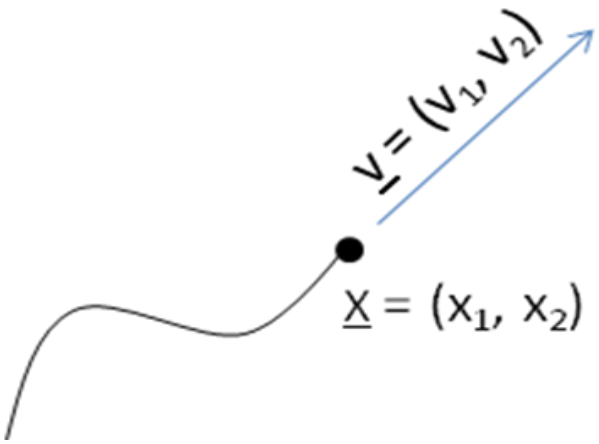

Figure 3.2: Hyphal tip movement according to its vector position (x) and velocity (v) in 2D space.

Tip position

The location of a tip over time is defined by an ordinary differential equation (3.1). where i denotes the i[th] hyphal tip with position ($\underline{x}_i$). The position varies over time (t) according to its velocity ($\underline{v}_i$):

$$\frac{d\underline{x}_i(t)}{dt} = \underline{v}_i(t). \tag{3.1}$$

Equation (3.1) was solved using Euler's method where the derivative is approximated using a forward difference approximation, namely:

$$\frac{d\underline{x}_i}{dt} = \frac{(x_i(t+dt) - x_i(t))}{dt}. \tag{3.2}$$

So that the new tip position at time t+dt is given by:

$$\underline{x}_i(t+dt) = x_i(t) + dt * \underline{v}_i(t) \tag{3.3}$$

where dt is time increment defined by the end simulation time (T) divided by total number of time increments (N).

Tip direction

The tip velocity is described by a stochastic ordinary differential equation. Previously, this approach has been used to describe the movement of endothelial cells in angiogenesis by Stokes and Lauffenburger (1991), when they described the change in tip cell velocity by a directional resistance $-\beta\underline{v}_i(t)dt$ and random fluctuation $\sqrt{\alpha}d\underline{W}_i(t)$ as shown in equation (3.4):

$$d\underline{v}_i(t) = -\beta\underline{v}_i(t)dt + \sqrt{\alpha}d\underline{W}_i(t). \tag{3.4}$$

We further amended the equation (3.4) to include the average elongation rate of hyphae (μ) and unit velocity $\hat{\underline{v}}_i(t)$, namely:

$$d\underline{v}_i(t) = \beta\left(\mu\hat{\underline{v}}_i(t) - \underline{v}_i(t)\right)dt + \sqrt{\alpha}d\underline{W}_i(t), \tag{3.5}$$

where $$\hat{\underline{v}}_i(t) = \frac{\underline{v}_i(t)}{\left\|\underline{v}_i(t)\right\|}.$$

In this type of system, the two parameters β and α are commonly referred to as drift and diffusion coefficients, respectively. The stochastic process W(t), also known as Brownian motion or a standard Wiener process, is a continuous time random process that has three requirements to satisfy (Higham and Kloeden 2008):

1. At time zero, the Wiener process is zero.
2. The Wiener process has stationary increments that are normally distributed with mean zero.
3. All the increments are independent.

Basically meaning that within a continuous time frame, succession of steps is random and that in every step the variable changes direction and value randomly. The Wiener process is solved using an independent Brownian increment shown in equation (3.6) (Higham and Kloeden 2008).

$$\Delta W \sim \sqrt{dt}N(0,1), \tag{3.6}$$

where N(0,1) is the normal distribution with mean zero. Equation (3.5) is then solved using an Euler-Maruyama scheme that approximate a numerical solution of a SDE in a similar way to Euler's method (see above) (Higham and Kloeden 2008).

Tip paths

The model allows tip paths to cross over creating a 2D+ effect where we assume that the overlapping tip paths are in different 3D planes. Therefore, the model is trying to capture some 3D effects in a simpler 2D framework. This means that crowding is not explicitly included in the model, however it is intrinsically included via the growth limiting effects of an external substrate which we describe later. The model is rigorously validated and tested using laboratory studies to overcome any geometrical limitations of the 2D+ framework.

Branching

Actinomycetes are able to grow by apical elongation and by branching (Goriely and Tabor 2003). This is an important feature of filamentous bacteria in that it allows the bacteria to grow exponentially when growth conditions are favourable. Our first attempt to model branching occurring from an apically growing tip did not create realistic simulations of early hyphal growth (data not shown). Therefore, we changed the model to allow branching to only occur at the same distance behind the apically growing tip. Our literature search supported the fact that branches emerge behind the growing tip. The distance between the apical tip and the first branch has previously been measured to be 10.94 ± 2.85 µm on average when grown on a solid surface (Jyothikumar *et al.* 2008).

In our model, the probability of branching is assumed to increase with the increasing apical length of hyphae. The length of a hypha (L_i) is defined in equation 3.7:

$$\frac{dL_i(t)}{dt} = \left\| \underline{v}_i(t) \right\| \tag{3.7}$$

where $\left\| \underline{v}_i(t) \right\| = \sqrt{v_1^2 + v_2^2}$

At each time step, the probability of branching was compared to a random number in the unit interval drawn from a uniform distribution. If the branching probability is higher than the randomly generated number, branching occurs (Note: that we only allow branching to occur if the external substrate levels are high enough for the active growth. See model development below). The probability of branching is obtained using a cumulative probability function drawn from a normal distribution (see equation 3.8):

$$\text{Probability of branching} = \frac{1}{2} + \frac{1}{2} erf\left(\frac{L_i - L_{avg}}{L_{std}\sqrt{2}}\right) \quad (3.8)$$

where L_{avg} is the average length of hyphae. This includes both interbranch length (l_2) and apical hyphal length (l_1) (During parameterisation, we used experimental data to populate the model). The standard deviation of hyphal length (L_{std}) is the standard deviations of l_{1sd} and l_{2sd}. An example of a cumulative distribution function (blue line) is shown in Figure 3.3 together with a normally distributed cumulative distribution function (dashed red line).

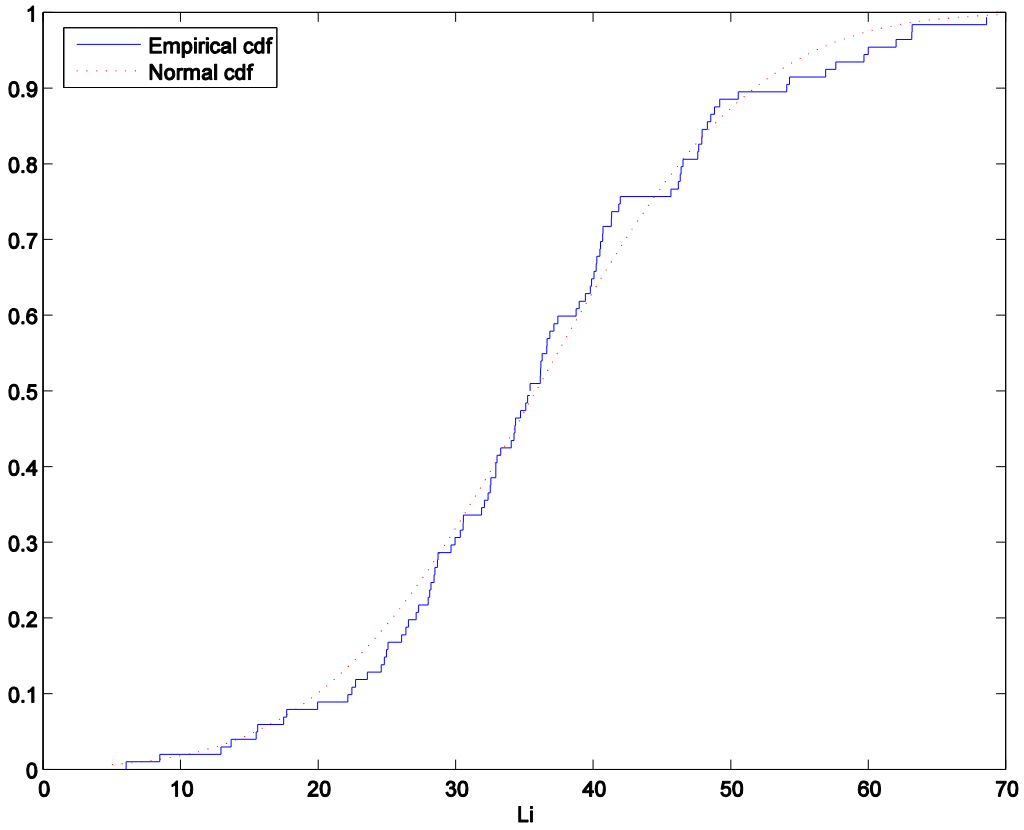

Figure 3.3: Cumulative distribution function (cdf) for branching probability of $L_i(t)$ with mean 35.8 μm and standard deviation 12.4 μm (blue line) and for normal distribution with mean zero and standard deviation one (dashed red line).

Figure 3.4 shows the subapical branching event where (I) a parent hyphae extends from position $\underline{x}_i$ with velocity $\underline{v}_i$ creating total hyphal length L_i, (II) by a certain probability a branching point ($\underline{x}_j$) is identified at an average distance of l_2 away from the germination point $\underline{x}_1$, (III) new hyphae emerges from the branching point position $\underline{x}_j$ with branching angle Ψ and average velocity $\underline{v}_{avg}$ (see Table 3.2 for experimental determination of measurements). The branching angle is taken from the parent hyphae using a normally distributed, bimodal probability distribution with means 84.0° and -84.0° and standard deviation of ±23.0 for both. (IV) Both the new and the parent hypha continue to elongate with individual velocities. The length L_i of the parent hyphae is now reset to be the distance between the latest branching point $\underline{x}_j$ and its tip position $\underline{x}_i$, whereas the length of the new hyphae L_k initiates from zero.

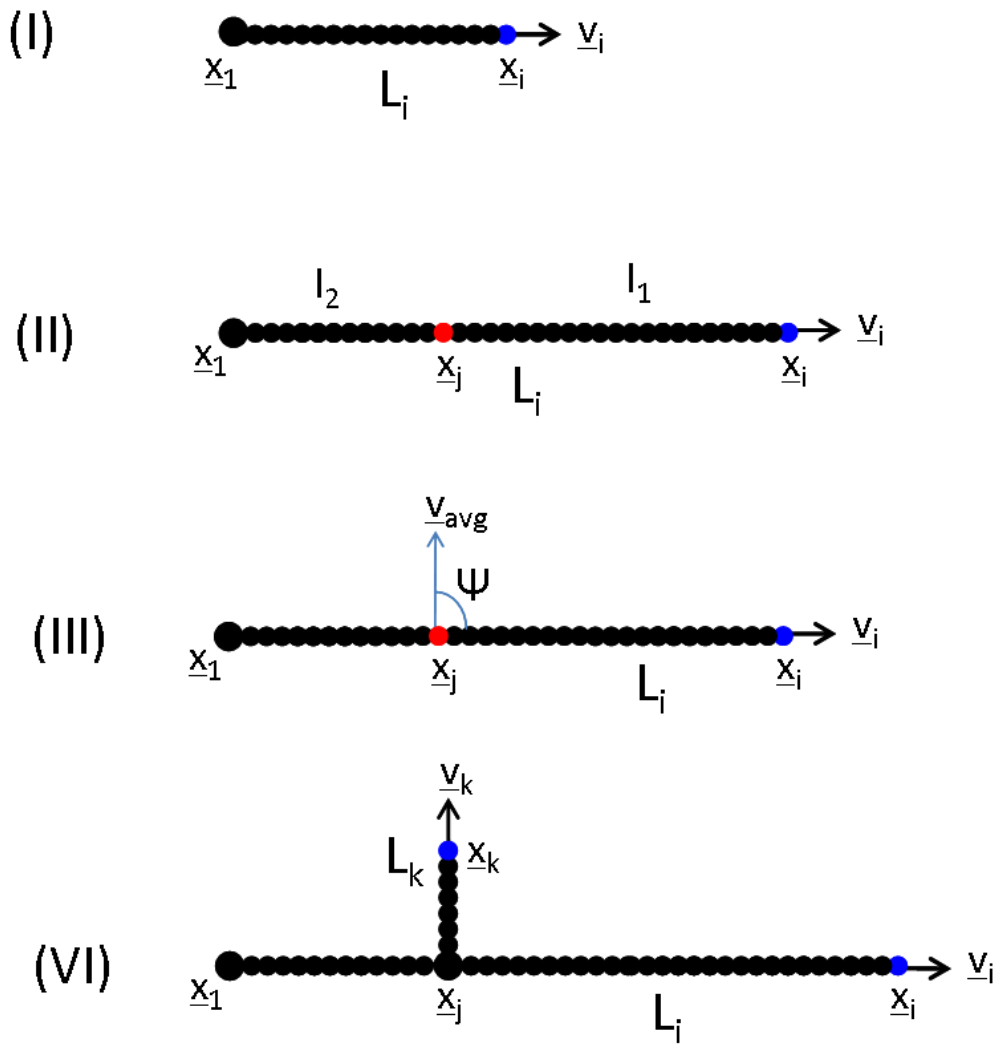

Figure 3.4: Branching event of hyphae. (I) Hyphae grows with velocity ($\underline{v}_i$) from its position ($\underline{x}_i$). The total length of the hyphae (L_i) is illustrated. (II) Once L_i reaches a certain length, a branching point ($\underline{x}_j$) is found from an average interbranch length (l_2). The average length between the tip and the apical branching point is shown (l_1). (III) Second hyphae is formed from the branching point ($\underline{x}_j$), with normally distributed branching angle (Ψ) and average velocity ($\underline{v}_{avg}$). (IV) First hyphae continues to grow with velocity ($\underline{v}_i$) and the second hyphae elongates with velocity ($\underline{v}_k$). The length L_i of the parent hypha is reset to be that from the last branching point position $\underline{x}_j$ to the tip $\underline{x}_i$ and L_k initiates from zero.

Germination

It has been studied that 63% of spores grown on solid surface produce one extending hypha and 37% produce two (Jyothikumar *et al*., 2008). In our model, growth is assumed to occur in both directions from a spore. No growth arrests are included in the model, as has been observed experimentally in majority of the cases studied (Jyothikumar *et al*., 2008).

Parameterising and calibrating the early hyphal growth model

We performed an experiment where we examined early hyphal growth (6-28 h following germination) that provided numerical data to parameterise the model for hyphal growth in the absence of external substrate effects. To match the model description, this experiment was designed to take into account early hyphal growth only. At early stages of growth, all hyphal filaments are assumed to be in a homogenous, nutrient sufficient environment, where there is no growth limiting factors present affecting growth. Furthermore, the measurements of hyphae at the early stages of the growth curve are relatively easy due to individual hyphae not being tangled together and not overlapping each other.

The culture was started with spore suspension resulting in a final concentration of 1 x 10^5 cfu/mL of YEME. Samples were taken at 6 h, 8 h, 10 h, 12 h, 14 h and 28 h. To ensure nutrient availability and to monitor growth, dry weight, pH, phosphorus and ammonia measurements were taken at every time point (see Figure 3.5). At the 28 h time point the culture appeared pink, indicating that the antibiotic production of the cell bound antibiotic, undecylprodigiosin had started (Kieser *et al.,* 2000).

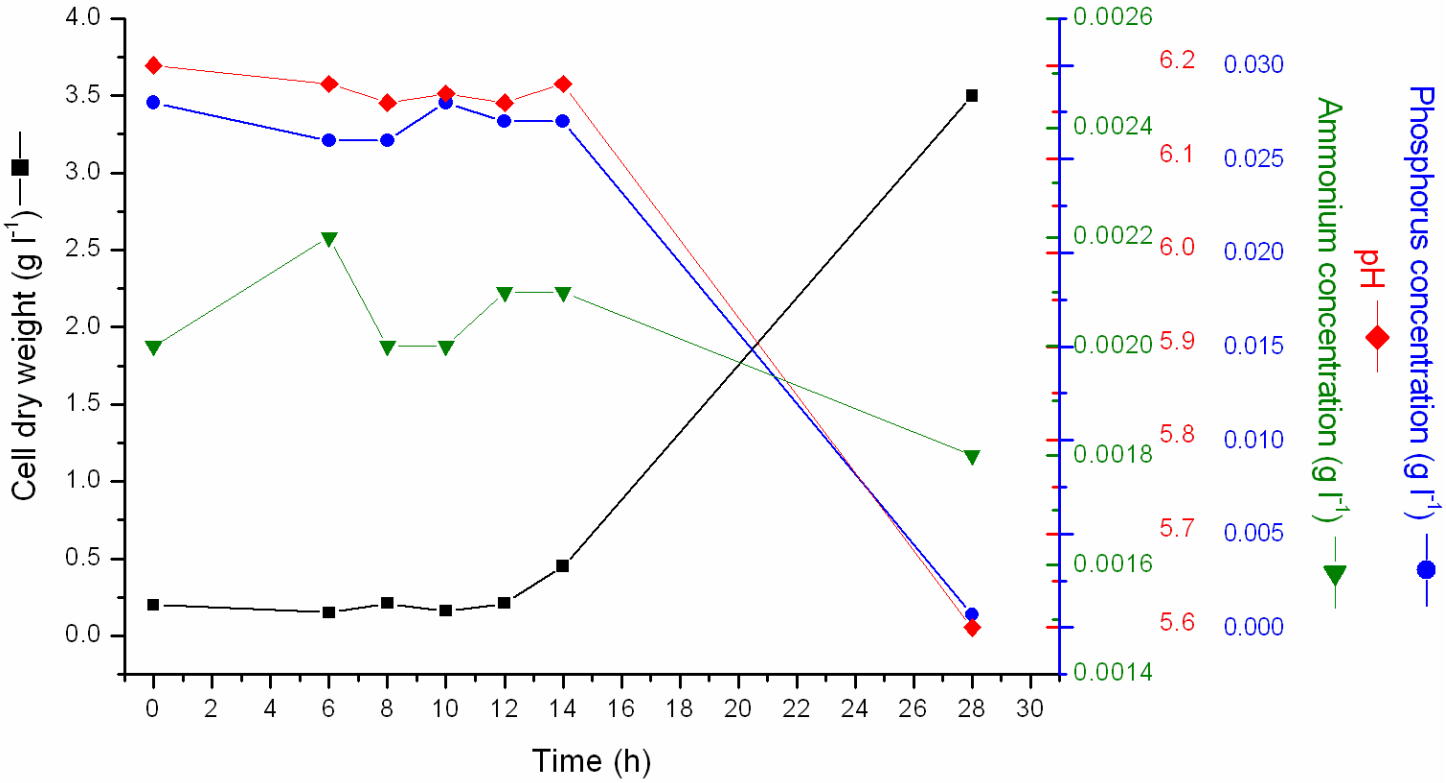

Figure 3.5: Ammonia, phosphorus and pH variation during early hyphal growth. Growth curve time points are shown between 0 – 28 h.

Image and data analysis

Pictures of growing hyphae were taken at time points of 6 – 14 h when the nutrients were still in excess. Due to hyphal clump formation, only the pictures from 6 – 12 h were possible to measure. The measurements were performed manually from the bright field micrographs. The mean, standard deviation (stdev), coefficient of variation (CV%) and number of measurements (n) for total length of hyphae, number of tips, HGU (see Chapter 2 for calculation), interbranch distance, apical length, branching angle and maximum pellet diameter are shown in Table 3.1. Only the 10 h time point measurements were chosen to parameterise the model, since only at this time point, the number of measurements (n) for interbranch distance and branching angle were statistically satisfactory. All the parameters used for simulations are summarized in Table 3.2.

Table 3.1: Manual measurements of early hyphal growth.

Measurement		Mean	Stdev	CV%	n
Total length of hyphae (µm)	6 h	1.5	0.7	44.6	250
	8 h	31.0	21.9	70.8	34
	10 h	80.0	54.0	67.5	41
	12 h	121.3	44.1	36.4	3
Number of tips	6 h	2.0	0.0	0.0	250
	8 h	2.5	1.3	50.8	34
	10 h	4.2	2.2	51.3	41
	12 h	6.0	2.6	44.1	3
HGU	6 h	N/A	N/A	N/A	N/A
	8 h	12.1	5.2	43.3	34
	10 h	18.1	5.4	30.0	41
	12 h	21.3	7.3	34.4	3
Max. pellet diameter (µm)	6 h	N/A	N/A	N/A	N/A
	8 h	25.1	12.2	48.7	32
	10 h	50.1	20	40.0	44
	12 h	84.1	46.8	55.6	7
Apical length (µm)	6 h	N/A	N/A	N/A	N/A
	8 h	N/A	N/A	N/A	N/A
	10 h	28.5	8.5	29.7	46
	12 h	N/A	N/A	N/A	N/A
Interbranch distance (µm)	6 h	N/A	N/A	N/A	N/A
	8 h	4.5	2.1	47.3	4
	10 h	7.3	3.9	54.1	48
	12 h	5.2	2.7	52.4	7
Branching angle (º)	6 h	N/A	N/A	N/A	N/A
	8 h	92.3	20.9	22.7	6
	10 h	84.0	23.0	27.4	65
	12 h	90.8	13.6	15.0	6

N/A not analysed. Note, initial velocity was calculated from average maximum pellet diameters between 10 h and 8 h time points taking into account hyphal growth in two directions.

Table 3.2. Parameters used for early hyphal growth.

Parameter	**Symbol**	**Value**	**Reference**
Simulation time interval	T	4 h	this study
Number of Brownian steps	N	100	n/a
Diffusion coefficient	α	10	n/a
Drift coefficient	β	10	n/a
Average apical length	l_1	28.5 μm	this study
Average interbranch length	l_2	7.3 μm	this study
Standard deviation of apical length	$l_1$sd	8.5 μm	this study
Standard deviation of interbranch length	$l_2$sd	3.9 μm	this study
Average branching angle	ψ	84.0 deg	this study
Standard deviation of branching angle	ψ_{sd}	23.0 deg	this study
Average hyphal velocity *	v_{avg}	6.3 μm/h	this study

n/a not analysed.

* Note, initial velocity was calculated from average maximum pellet diameters between 10 h and 8 h time points taking into account hyphal growth in two directions.

Validation of diffusion and drift coefficients for early hyphal growth

Of the 11 parameters used in the model at this stage, only three cannot be measured directly from laboratory experiments. The first one of these parameters, the number of Brownian steps, was set to be 100 for 4 h time interval. This was found sufficient for convergence of the Euler-Maruyama scheme used to numerically solve the stochastic differential equation. The best values for the other two parameters, diffusion and drift coefficients, were then determined empirically using comparisons of a number of model simulations of equivalent measurements from early hyphal growth experiments allowing for visual inspection of the simulations to see which behaved most like *Streptomyces*.

The simulation results for different diffusion and drift coefficient values are shown in Figure 3.6, where subplots (A)-(D) show the diffusion coefficient (α) varying from 0.1-1000, when the drift coefficient (β) is taken to be constant at 10. The bottom row (subplots (E)-(H)) illustrate the difference between the drift coefficient values (β) when they range from 0.01-100, when the diffusion coefficient (α) is taken to be constant at 10.

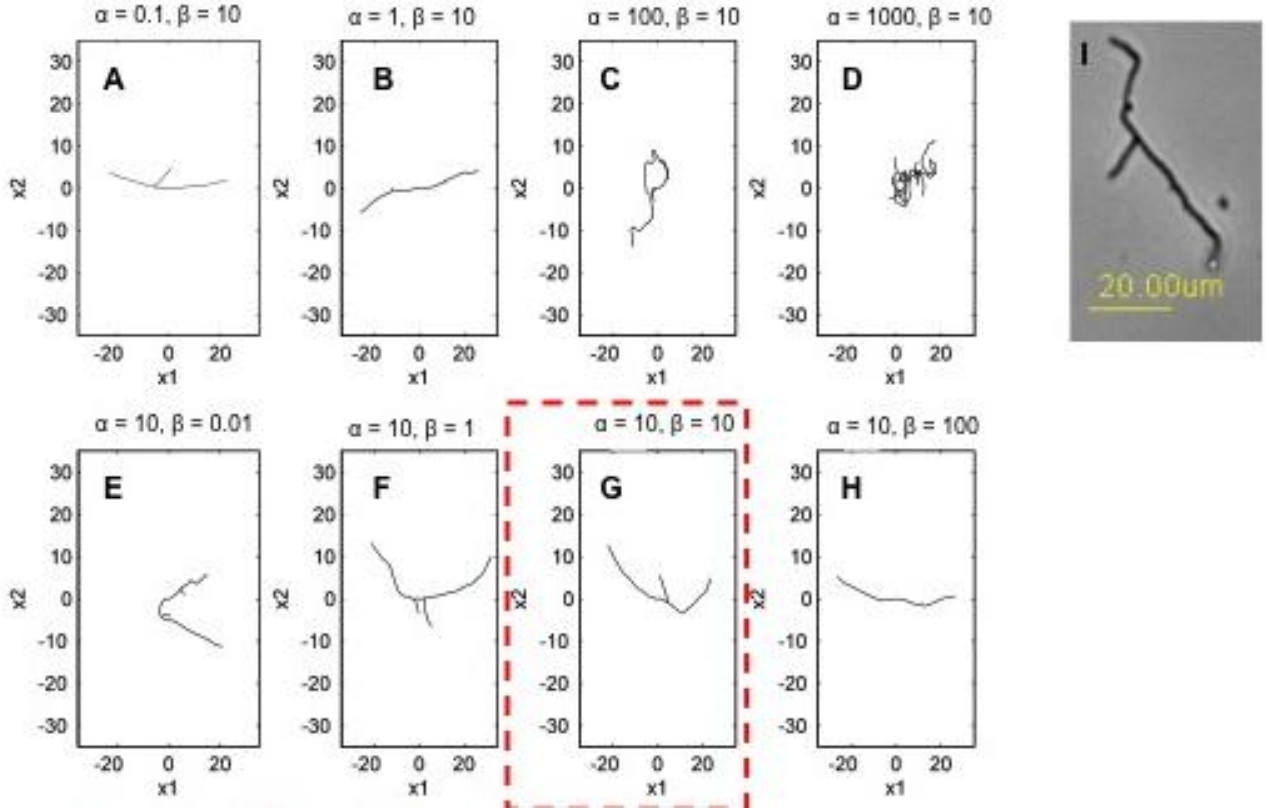

Figure 3.6: Simulation results for early hyphal growth using different drift and diffusion coefficient values. (A-D) diffusion coefficient varying from 0.1-1000, drift coefficient is fixed at 10. (E-H) drift coefficient ranging from 0.01-100 when diffusion coefficient is fixed at 10. The remaining parameters are as per Table 3.2. (I) Corresponding phase-contrast image of *S. coelicolor* early hyphal growth. The dashed red box shows the simulation results for α and β values used in further simulations.

The difference in average velocities in the simulations in Figure 3.6 are shown in Figures 3.7 and 3.8. The Figure 3.7 illustrates how the stochastic term, including both the diffusion coefficient and Brownian motion, creates random fluctuations of whose magnitude depends on the value of the diffusion coefficient. It is straight forward to see that the greater the diffusion coefficient the larger the random noise observed in the simulations.

In Figure 3.8 the average hyphal velocities for different drift coefficient values are compared. It is shown that with large drift coefficient values the resistance to random fluctuation is higher.

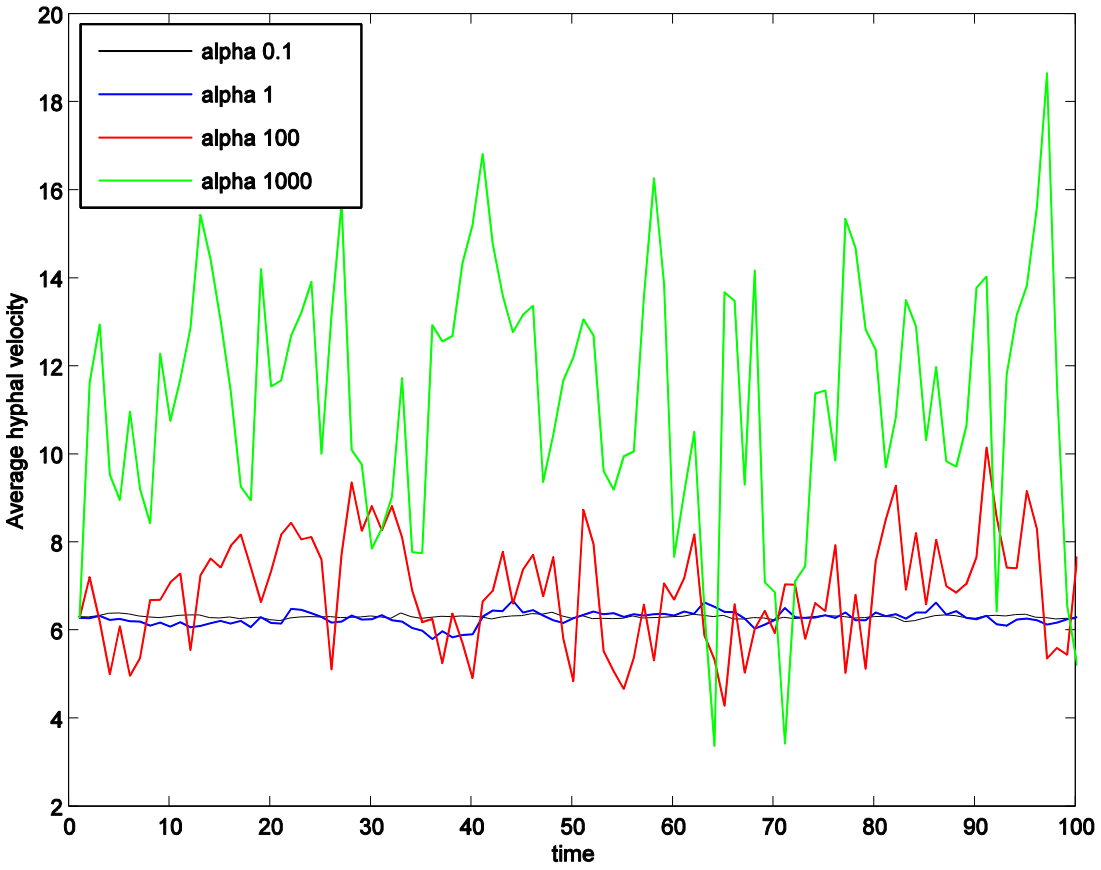

Figure 3.7. The random fluctuation in average hyphal velocity with different diffusion coefficient (alpha) values. See simulations A-D of Figure 3.6 for hyphal morphology.

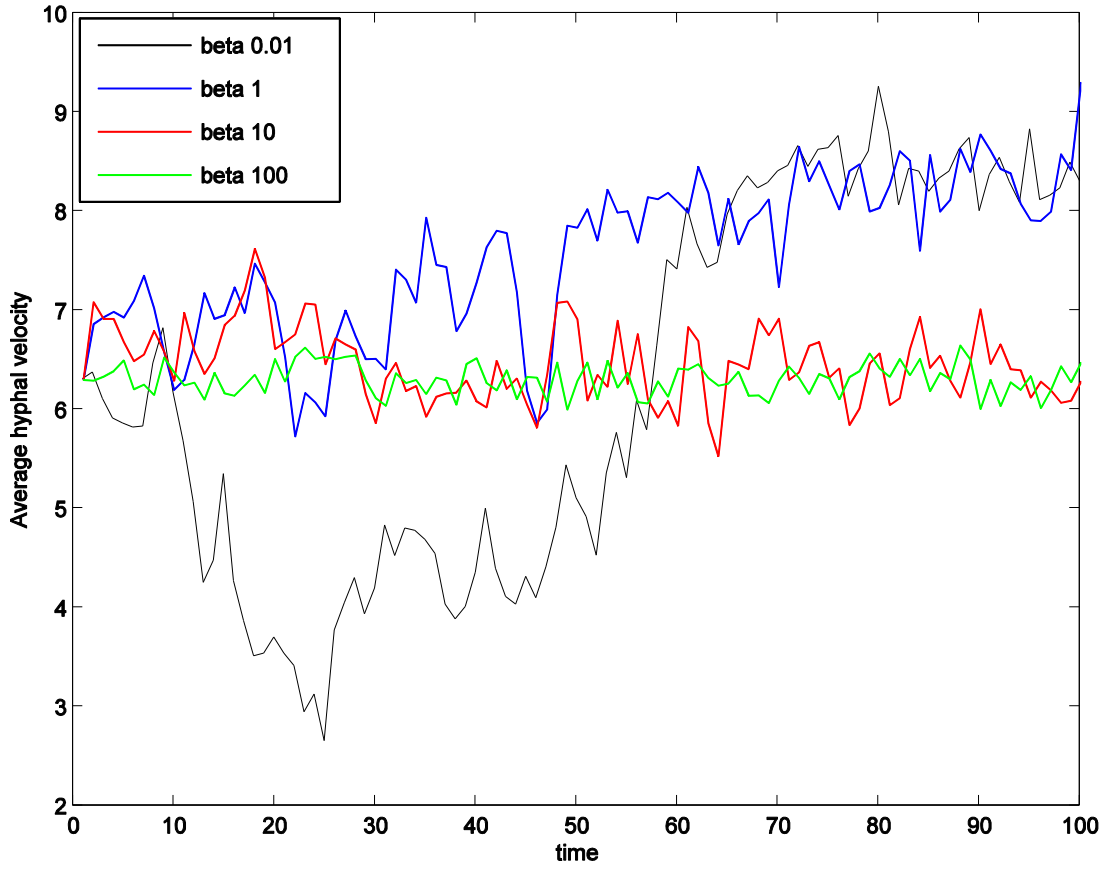

Figure 3.8. The effect on average hyphal velocities by varying drift coefficient (beta). See also simulations shown in Figure 3.6 (E-H).

To further assess the effect of α and β in the model, we show numerical calibrations of alpha and beta (Figure 3.9). In particular, values for maximum pellet diameter and number of tips from five parallel simulations were compared to measurements from microscopic pictures (see Table 3.1). Six different simulations are run for different alpha (0.1-10) and beta (0.01-1000) values. The simulation results are presented as averages with error bars showing the minimum to maximum values. The results from the laboratory experiments are shown as yellow lines for mean (continuous line) and standard deviation (dashed line). From the comparison of the maximum pellet diameter it can be seen that the low alpha and high beta values reduce the variation between the minimum and maximum values of pellet size. To keep the minimum and maximum values within the scope of the experimental standard deviations and still maintain as high random variation as possible, only the alpha values of one and 10 and beta values of 0.01-10 are taken forward. When comparing the effect alpha and beta have on the number of the tips in the simulations, it is shown that only with the value 10 for both alpha and beta the variation between simulations stays within the observed biological variations. This value for alpha and beta was also acceptable when testing the effect on the maximum pellet diameter. Therefore, the alpha and beta were set at the value of 10.

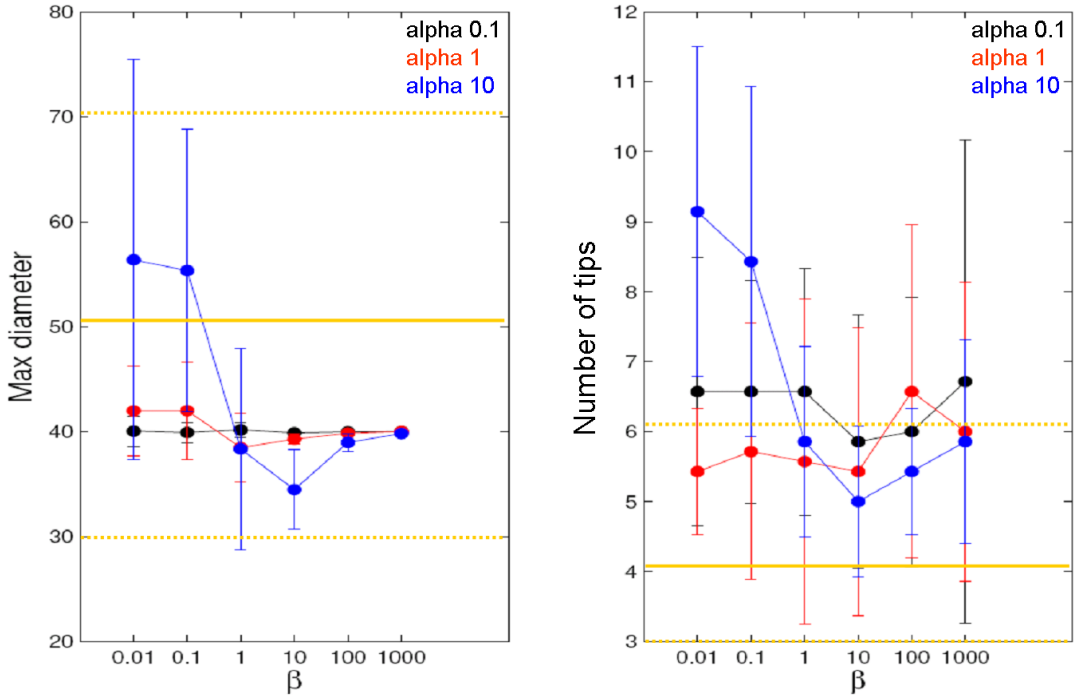

Figure 3.9: Calibration of diffusion and drift coefficients for early hyphal growth. Both the maximum diameter of hyphae and the number of tips are simulated by varying the drift coefficient (β) from 0.01-1000 and diffusion coefficient (α) between 0.1 (black), 1 (red) and 10 (blue). The error bars show the minimum to maximum values of 5 simulations where the dots denote average values. The constant yellow line shows the mean value from the laboratory experiment (see Table 3.1) with upper and lower standard deviations denote by the dashed yellow lines. Note that the lower standard deviation for the number of tips is below the displayed y-scale.

Model with an external substrate

In shake flask (Batch) cultures, cells grow in a constantly changing environment where nutrient and oxygen levels can vary due to consumption, diffusion, cell lysis and degradation processes (Hoskisson and Hobbs, 2006). Aerobic bacteria require several substrates for growth, the main requirements being oxygen, carbon, phosphorus and nitrogen (with smaller contributions from other micronutrients such as iron, sulphur, etc.). As a result of consumption, the depleted nutrients may become growth limiting factors (Taylor and Pirt, 1977). Nutritional starvation is known to be one of the triggers for secondary metabolite production (Nieselt *et al*. 2010, Bibb, 2005).

The dynamic, external substrate was incorporated into the model using a reaction-diffusion equation, where the diffusion term is described by Fick's law which, in spatial 2-dimensions, has the form,

$$\frac{\partial c}{\partial t} = \left(\frac{\partial^2 c}{\partial x^2} + \frac{\partial^2 c}{\partial y^2} \right) D_c - d_c c \tag{3.8}$$

where $c(\underline{x},t)$, $\underline{x} = (x,y)$ is the substrate concentration (mmol/l), D_c is the diffusion coefficient ($\mu m^2/h$) and d_c is the rate of consumption (h^{-1}). According to Fick's law, the substrate diffuses from high to low concentrations (Murray 1993). If there is no consumption present, the change in the substrate levels is governed only by the diffusion term, and the substrate levels would then be expected to tend to a homogenous solution.

The second order derivatives in the partial differential equation (3.9) are solved using a central differences approximation namely,

$$\frac{\partial^2 c_{i,j}}{\partial x^2} = \frac{c_{i+1,j} - 2c_{i,j} + c_{i-1,j}}{\Delta x^2} \quad \text{and} \quad \frac{\partial^2 c_{i,j}}{\partial y^2} = \frac{c_{i,j+1} - 2c_{i,j} + c_{i,j-1}}{\Delta y^2} \tag{3.9}$$

where the 2D domain is characterized by $\underline{x}$ = (x,y) in [-L,L] x [-L,L]. A typical value for L is taken to be in the region of 200 μm. However, this parameter has to be adjusted to be large enough so that the growing pellet does not reach the domain's boundary within the time scale of the simulation. The 2D domain is partitioned into mesh points of x..x_N and y..y_N, and a uniform spacing of Δx and Δy is assumed. We use $c_{i,j}$ to denote $c(x_i,y_j)$.

The growth rate of the hyphae (hours^{-1}) defines the time scale of interest. Compared to this time scale, the diffusion (D_c) and the consumption (d_c) rates are very fast (order of seconds). We make use of these differences and write equation (3.9) as:

$$\frac{1}{D_c}\frac{\partial c}{\partial t} = \frac{\partial^2 c}{\partial x^2} + \frac{\partial^2 c}{\partial y^2} - \frac{d_c}{D_c}c \tag{3.10}$$

Furthermore, by realising that $O(1/D_c) << 1$ and $O(d_c) \sim O(D_c)$, we come to the following leading order expression,

$$0 = \frac{\partial^2 c}{\partial x^2} + \frac{\partial^2 c}{\partial y^2} - \bar{d}_c c \tag{3.11}$$

where $\bar{d}_c$ = d_c/D_c. The equation (3.11) can then be solved using finite-differences approximation described above and, by a little re-arranging, it can be written as:

$$c_{i+1,j} + c_{i-1,j} + \alpha^2\left(c_{i,j+1} + c_{i,j-1}\right) - c_{i,j}\left(2 + 2\alpha^2 + \bar{d}_c\Delta x^2\right) = 0 \tag{3.12}$$

where $\alpha^2=\Delta x^2/\Delta y^2$. Thus giving a system of N^2 coupled algebraic equations, with N^2 unknowns that we solve using Matlab.

The boundary conditions on the spatial domain are fixed for the substrate concentration that is detected in media in the absence of any cells. Initially a homogeneous concentration is assumed throughout the matrix. Note that the

hyphal consumption rate (d_c) is taken to be a function of hyphal occupancy, which we denote by $\mu_h(x,y)$. This is calculated by interpolating each of the hyphal branches to the underlying grid (see Figure 3.10), and counting the number of hyphae of different metabolic states in each grid cell.

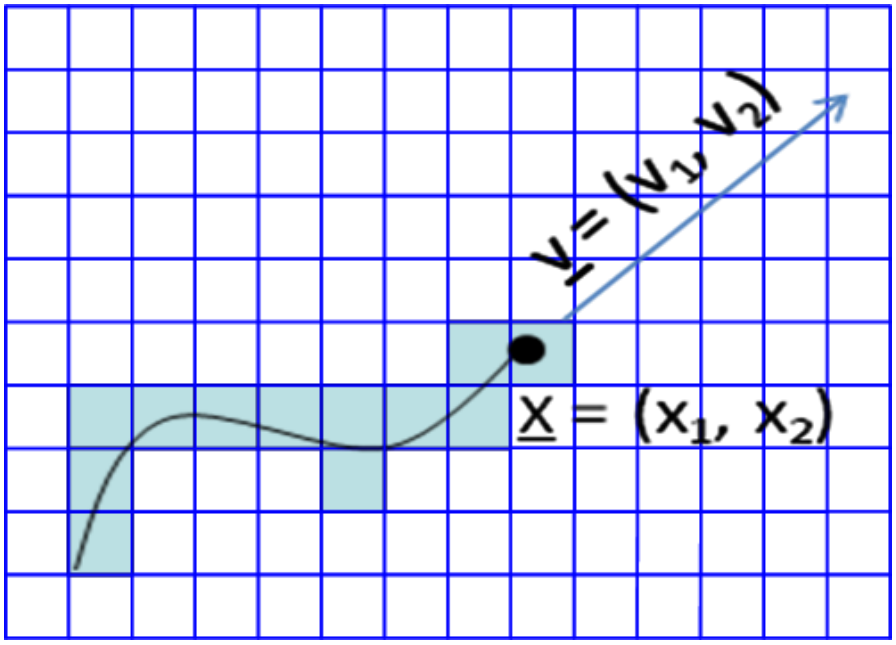

Figure 3.10: Hypha's substrate consumption on the grid. Initially homogenous substrate concentration was assumed across the grid. As the hypha grows, it occupies squares on the grid (shaded). Hypha within the occupied squares consume substrate according to the metabolic state of the hypha and the number of hyphae present in the square.

To incorporate the metabolic state of the hyphae into the model (see Figure 3.1 for a schematic illustration of metabolic states), it was assumed that the external substrate concentration depletes due to the consumption and diffusion limitations. Nutrient limitation results in the hyphae switching from an actively growing state to an antibiotic producing state, in keeping with the accepted model for activation of antibiotic biosynthesis (Bibb, 2006). As the concentration depletes even further the hyphae either die directly, or before dying, the hypha goes through a period where only maintenance energy is required. In this state, the hypha does not grow nor produce antibiotics yet it still has some level of substrate consumption before it dies. From this maintenance energy-only requirement state the hyphae are still able to recover active growth or antibiotic producing states depending on fluctuations of external substrate concentration levels (described by equation 3.8). The demand for substrate by the cells is assumed to decrease as the hyphae metabolism changes from actively growing to antibiotic producing and additionally to the maintenance energy-only requirement state. Once a hyphae becomes dead in the model, no consumption occurs nor is it possible for the hypha to recover any previous metabolic states. Cell lysis and the presence of growth inhibiting substances were not taken into account in the model, as it is impossible to parameterise the quantity of nutrients released following lysis using current methodology.

With above assumptions, the substrate consumption rate in each grid cell (i,j), i,j $\in$ [1,N] is defined as

$$d_c^{\,i,j} = d_c^{\,b} B^{i,j} + d_c^{\,a} A^{i.j} + d_c^{\,m} M^{i,j} + d_c^{\,d} D^{i,j} \qquad (3.13)$$

where $B^{i,j}$, $A^{i,j}$, $M^{i,j}$ and $D^{i,j}$ are the numbers of actively growing, antibiotic producing, maintenance only and dead hyphae, respectively, in grid cell (i,j). The parameters $d_c^{\,b}$, $d_c^{\,a}$, $d_c^{\,m}$ and $d_c^{\,d}$ are the assumed substrate consumption rates for different the metabolic states of hyphae (see Table 3.3).

Model simulation with an external substrate

The simulation results shown in Figure 3.11 give realistically looking hyphal arrangements for pellets, where the external substrate concentration depletes towards the core of the pellet, which is also where the highest hyphal density is observed. The model simulation predicts the metabolic state of the hyphae within a pellet, based on our assumptions. The actively growing hyphae are predicted to be at the outer edges of the pellet. Within those, there are the parts of the hyphae that produce antibiotics. Under the conditions used in these simulations and the time scale used, no dead hyphae were observed, however, at the core of the pellet the hyphae still have maintenance energy requirements for substrate.

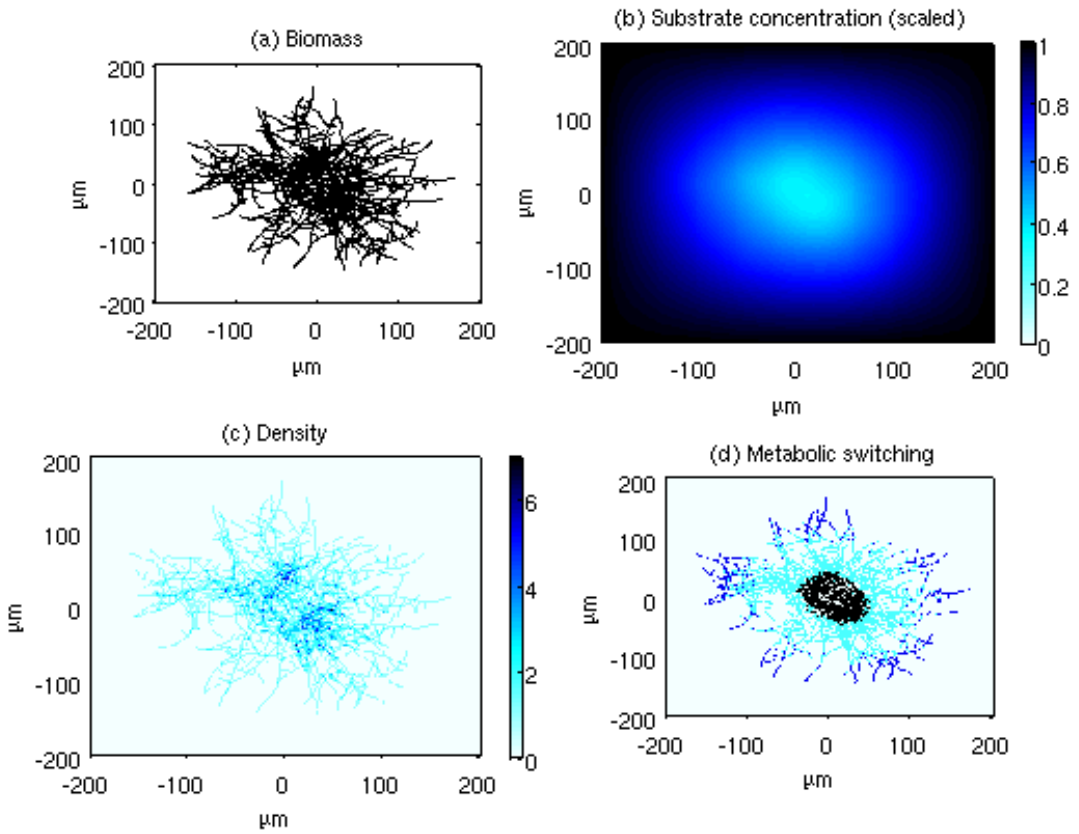

Figure 3.11. Model simulations for pellet growth under substrate limitations. (a) Hyphal arrangement at the end of the exponentially growing phase. (b) Depletion of substrate due to consumption and diffusion. (c) Hyphal density within a pellet. (d) Prediction of the metabolic state of hyphae within a pellet: actively growing hyphae (dark blue), antibiotic producing hyphae (cyan), hyphae with only maintenance requirements (black), dead hyphae (light blue). Note that within this simulation time scale no dead hyphae is seen. See Tables 3.2 and 3.3 and Figure 3.13 for the parameters used in the simulation.

The effect of diffusion and drift coefficients on pellet

The diffusion coefficient (α) and drift coefficient (β) parameters, validated previously for early hyphal growth (see above), are tested further with fully developed pellet simulations with external substrate. The alpha and beta values included are the ones that produced most realistic looking early hyphal growth simulations (see Figure 3.6, subplots B, C, F, G and H). The simulation results for the pellet morphology and its metabolic state are shown in Figure 3.12 together with a bright field image of a fully developed pellet. The dashed red box illustrates the simulation result using the previously validated alpha and beta value of 10. From the comparison between the simulations and the microscopy image, it can be concluded that the simulations with either value 10 for both alpha and beta or value 10 for alpha and one for beta give the best illustrations of the pellet morphology. Since the value 10 for alpha and beta also produced the best fit between the model and the experimental data during early hyphal growth (see above), the alpha and beta values were kept unchanged at value 10 in further simulations in this study.

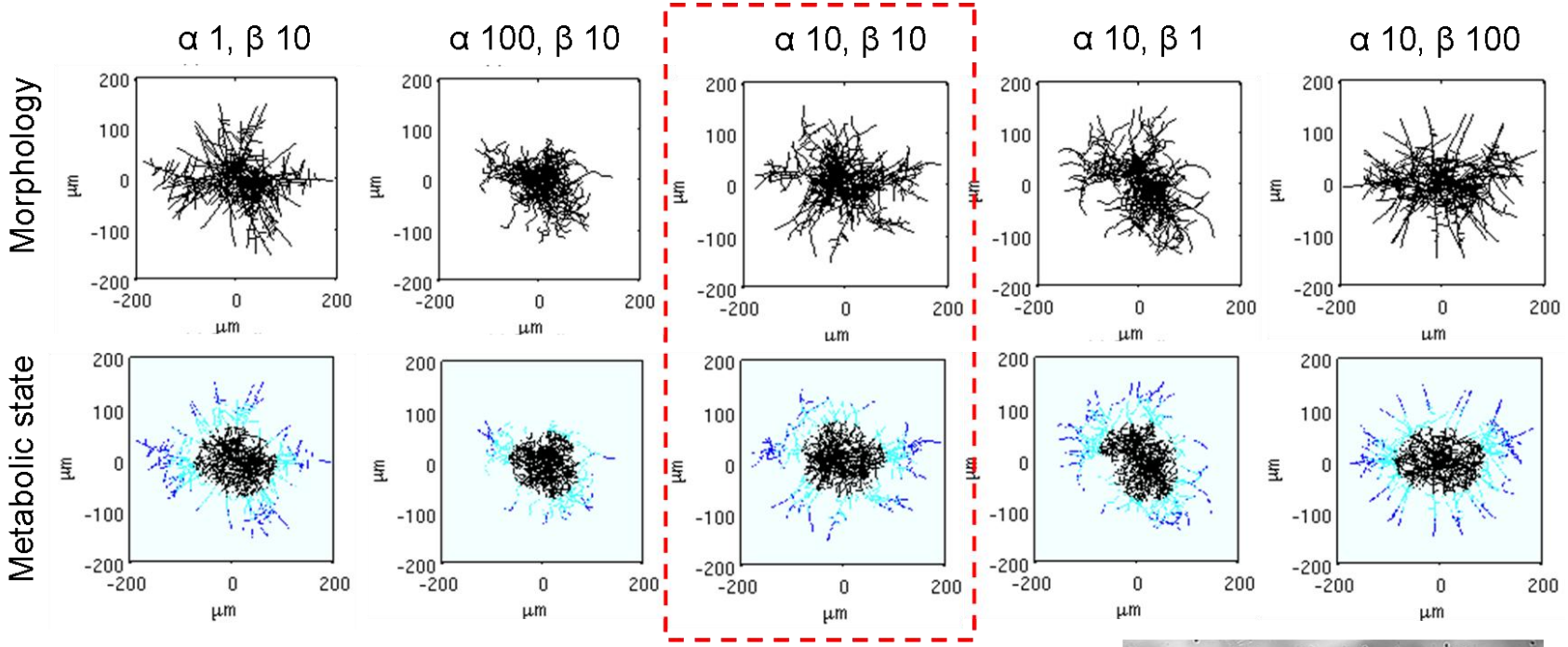

Figure 3.12: Simulation results for pellet growth using different diffusion (α) and drift coefficient (β) values. The pellet morphology (top row) and its metabolic state (bottom row) are shown. The dashed red box illustrates the simulation result using diffusion and drift coefficient values that were previously validated for early hyphal growth. A bright field image of a pellet is shown in the left with a yellow scale bar of 100 µm.

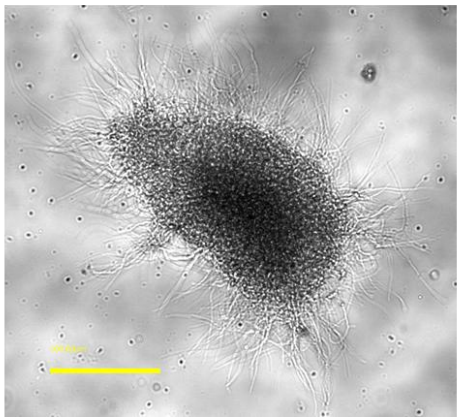

Parameterising oxygen consumption

To model the external oxygen consumption, we used the parameters shown in Table 3.3 and Figure 3.14.

To simplify the calculations, the diffusion coefficient D_{O2} for oxygen was assumed to be the same in media as it is in water. Therefore, the effects of dissolved substrates and micro-organisms were not taken into account in the calculations. The oxygen diffusion coefficient was calculated using Wilke and Chang 1955 correlation (see equation 3.13). The correlation gives the result in cm^2/s units that were then converted to $\mu m^2/h$ for the model.

$$D_{o_2} = 7.4x10^{-8} \frac{T\left(\psi_{H_2O} M_{H_2O}\right)^{1/2}}{\mu \nabla_{O_2}^{0.6}}, \qquad (3.14)$$

where $T =$ absolute temperature = 303 K

$\psi_{H_2O} =$ parameter for solvent water = 2.26 (Reid *et al*. 1977)

$M_{H_2O} =$ molecular weight of water = 18.02 g/mol

$\mu =$ viscosity of water at 30°C = $7.978*10^{-4}$ Pa · s (Weast, 1969)

= 0.7978 centipoise

$\nabla_{O_2} =$ the molar volume of oxygen = 25.6 cm^3/g (Welty *et al*. 1984).

Table 3.3: Parameters used in simulations of oxygen consumption.

Parameter	Symbol	Value	Reference
O_2 diffusion coefficient	D_{O2}	9.216 x 10^6 $\mu m^2/h$	this study
O_2 concentration in media	c_{O2}	0.1975 mmol/l	this study
O_2 consumption rate* – actively growing cells	$\bar{d}_c{}^b$	1 x 10^{-5} μm^{-2}	this study
O_2 consumption rate* – antibiotic producing cells	$\bar{d}_c{}^a$	70% of $\bar{d}_c{}^b$	this study
O_2 consumption rate* – cells with only maintenance requirements	$\bar{d}_c{}^m$	50% of $\bar{d}_c{}^b$	this study
O_2 consumption rate* – dead cells	$\bar{d}_c{}^d$	0	this study

* Consumption rate rescaled by diffusion rate.

The concentration of oxygen in media ($c_{O2)}$ was determined by Ioannis Voulgaris, SIPBS, University of Strathclyde using a dissolved oxygen probe (Mettler Toledo, UK). The sensor was calibrated in water with air gas at saturation levels for the 100% reading and oxygen free nitrogen for the 0% reading. The mean of triplicate measurements came to 84.26% of dissolved oxygen in YEME, without any sucrose, at 30°C. Using the value of 7.5 mg/l as dissolved oxygen concentration in water at 30°C and 760 mmHg (Lewis 2006) as the measure for 100% saturation, the oxygen saturation in media was calculated as 84.26%/100% x 7.5mg/l giving the dissolved oxygen concentration of 6.32 mg/l in media. This was converted to correct units (mmol/l) using the mass formula $n = m/M_{O2}$.

We calculate the rescaled consumption rate ($\overline{d}_c{}^b$) by taking into account the single cell dry weight, a grid voxel's volume, the external oxygen concentration ($c_{O2)}$, the oxygen consumption rate (d_c) and the oxygen diffusion coefficient (D_c). Since the mass of an average cell of *Streptomyces* is not known; this is because the cell dimensions in filamentous organisms are hard to define (Shahab *et al*. 1996), assumption was made to base the cell dry mass on the *E. coli* cell dry weight. The size of an *E. coli* cell depends on nutrients and the type of the strain. For this study, only the largest *E. coli* DSM 613 cell volume was taken into account, and this was found to be 1172 fg for a 3.5 μm^3 large *E. coli* cell (Loferer-Krosbacher *et al*. 1998). To calculate the hypothetical cell volume for *Streptomyces coelicolor*, we exploited the fact that a single nucleus is associated with 1.9 µm hyphal length in vegetative hyphae and a hyphal diameter is known to vary between 0.5-1 µm (Prosser and Tough 1991). Therefore, the *Streptomyces* single cell dimensions were assumed to be cylindrical with length of 1.9 µm and diameter of 1 µm, giving a volume of the cell of 1.49 μm^3. Then by assuming that an *E. coli* cell of 1.49 μm^3 weighs the same as *Streptomyces* 'cell' of 1.49 μm^3, we calculated a *Streptomyces* cell dry weight of 500 fg (1172/3.5 x 1.49).

The consumption rate of oxygen was then estimated to be 6.5 mmol g^{-1} h^{-1} for actively growing hyphae. According to Melzoch *et al.* (1996) continuous culture studies, at this rate, *Streptomyces coelicolor* M145 does not produce antibiotics, yet its consumption rate for specific glucose is high. By applying the above values for the rescaled oxygen consumption rate calculations ($\overline{d}_c = d_c/D_c$), we were able to come to an oxygen consumption rate of ca 1 x 10^{-6} μm^{-2}.

We ran simulations where the rescaled oxygen consumption rate was varied (see Figure 3.13) and compared the metabolic state of the pellet to experimental data (see Chapter 4). It was noted that with the value 1 x 10^{-6} μm^{-2} the pellet appears dense and fully metabolically active in the simulations. This does not correspond with the live/dead staining of pellets where the centre of the pellet stains red indicating the presence of membrane damaged cells i.e. cells that are unlikely to be metabolically active (see Chapter 4). Therefore, the rescaled consumption rate in simulations was adjusted to be 1 x 10^{-5} μm^{-2}. The one order of magnitude higher rescaled oxygen consumption rate gives simulations that better correspond with the microscopic images of live/dead stained pellets. We found this difference in the model parameter acceptable since the single cell dry weight is based on assumptions, and some of the data used in the calculations is from 3D studies (continuous culture studies), yet our model only takes into account 2-dimensions.

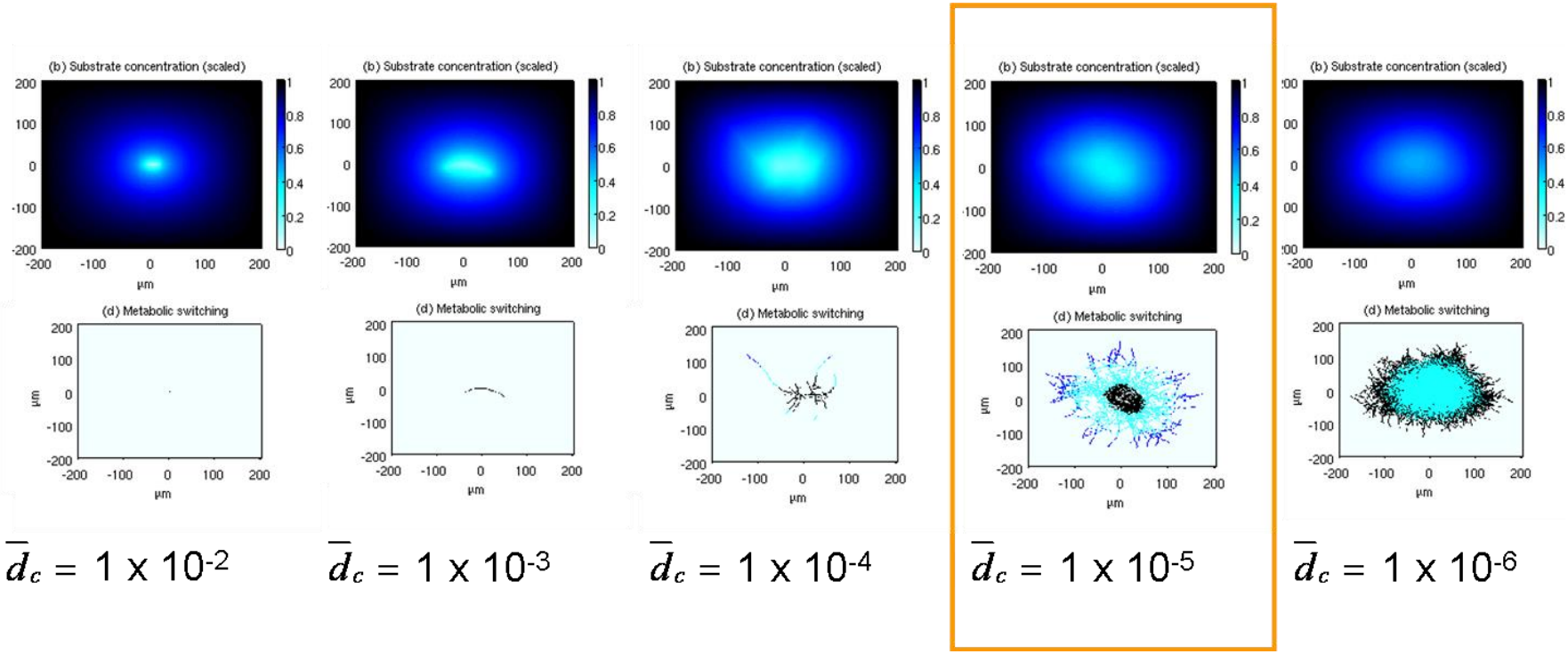

Figure 3.13: Simulations with varying rescaled oxygen consumption rate ($\bar{d}_c$ from 1 x 10^{-2} to 1 x 10^{-6}). The top row shows the external oxygen concentration distribution and the bottom row the corresponding hyphal growth. Different metabolic states of hyphae are illustrated as dark blue for actively growing state, cyan for antibiotic producing state and black for maintenance requirement only state. The box (in orange) highlights the chosen parameter value that best fits observed growth morphologies.

Assumption was also made that the antibiotic producing hyphae and the maintenance energy-only requirement hyphae have lower oxygen consumption rates compared to the actively growing hyphae. The data from Melzoch *et al.* (1996) supports this assumption. The rescaled consumption rates for oxygen in antibiotic producing hyphae was assumed to be 70% of the actively growing hyphae's consumption rate and for maintenance requirements only hyphae this value was assumed to be 50% (Melzoch *et al.*, 1996; Paul Hoskisson, personal communication). No oxygen consumption was assumed to occur in dead hyphae.

We estimated the effect of the external oxygen concentration on the metabolic state of the hypha by using data from Melzoch *et al*. (1996) (see Figure 3.14). At 90-100% of initial oxygen concentration, all hypha were modelled to be in an actively growing state. When the oxygen levels dropped due to the consumption, the probability of hyphae to switch from an actively growing state to an antibiotic producing state increased. When the external oxygen levels were between 50-60% of the initial concentration, all the hyphae were producing antibiotics. Antibiotic production stopped when less than 40% of the initial oxygen concentration was present and the cells died when less than 15% of the initial oxygen concentration level was available. The maintenance energy-only requirements state occurred at the oxygen level of 15-46%. These parameters can vary according to the used culturing conditions, for example, studies with *Saccharopolyspora erythraea* showed that it produced erythromycin A best when the dissolved oxygen level was above 40% (Chang-fa *et al*., 2009). In previous studies of *S. fradiae*, the cellular growth and tylosin production was severely reduced when dissolved oxygen level dropped below 25% (Chen and Wilde, 1991). Also, Ozergin-Ulgen and Mavituna (1998) performed a study of *S. coelicolor* A3(2) in a batch bioreactor where the cells died when the dissolved oxygen level was below 10%. These studies all suggest that our assumptions and simulations reflect the situation occurring within real *Streptomyces* hyphae.

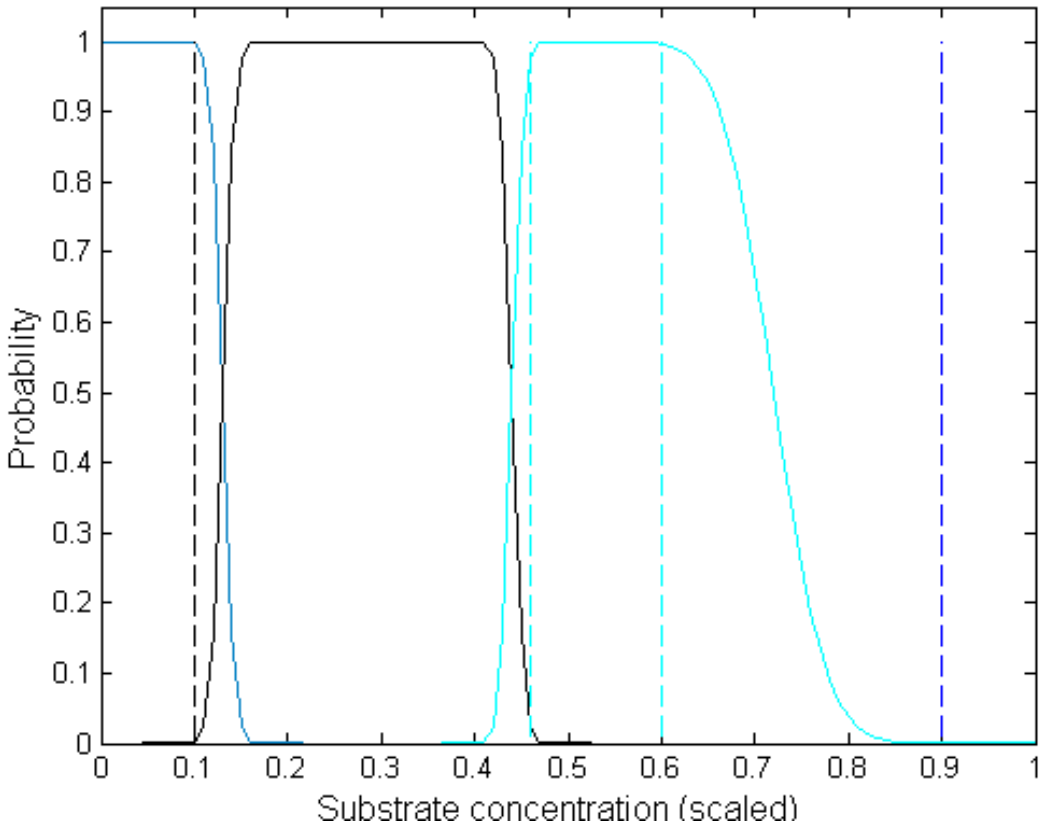

Figure 3.14: Thresholds for external oxygen concentration affecting metabolic state of the hypha. A scaled substrate concentration of value one corresponds to the oxygen concentration determined from the media before any consumption has occurred. At this concentration, all cells are actively growing. As the oxygen concentration drops due to the consumption, the probability of cells switching from actively growing state to antibiotic producing state increases (curve in cyan). All cells are at antibiotic producing state when the external concentration of oxygen is between 50-60% of the initial concentration. The probabilities for maintenance requirements only state and dead cells are shown in black and light blue respectively.

Parameter sensitivity of rescaled oxygen consumption rates

Data in Melzoch *et al*., (1996) can also be used to fine tone the parameters for oxygen consumption. From Melzoch *et al*., (1996) continuous culture study, we can estimate different levels of oxygen consumptions depending on the used dilution rate. At dilution rates 0.13 h^{-1}, 0.115 h^{-1} and 0.104 h^{-1}, the actinorhodin production rate is less than 30 µg/g.h. The respective oxygen consumption rates are 7.45 mmol/g.h, 6.5 mmol/g.h and 5 mmol/g.h. Since almost no antibiotic is produced at these dilution rates we utilise these three oxygen consumption rates separately as 100%. The oxygen consumption rate for antibiotic production is taken to be 2.5 mmol/g.h, using dilution rate of 0.06 h^{-1} , at which the level of actinorhodin production is the maximum of 415 µg/g.h. The oxygen consumption rate for the maintenance requirements only hyphae is taken to be 2.0 mmol/g.h (lowest dilution rate of 0.045 h^{-1}, no actinorhodin production). Taken the above numbers together, this leads us to three different estimates of the oxygen consumption rates for the antibiotic producing hyphae and the maintenance energy requirement only hyphae (see Table 3.4). In Figure 3.15 the simulations of the different rescaled oxygen consumption rates shown in Table 3.4 are presented.

Table 3.4: Estimated oxygen consumption rates from Melzoch *et al.*, (1996) continuous culture study.

	5 mmol/g.h as 100%	6.5 mmol/g.h as 100%	7.45 mmol/g.h as 100%
Rescaled consumption rate of oxygen in antibiotic producing hyphae	50%	38.5%	33.6%
Rescaled consumption rate of oxygen in maintenance requirements only hyphae	40%	30.8%	26.8%

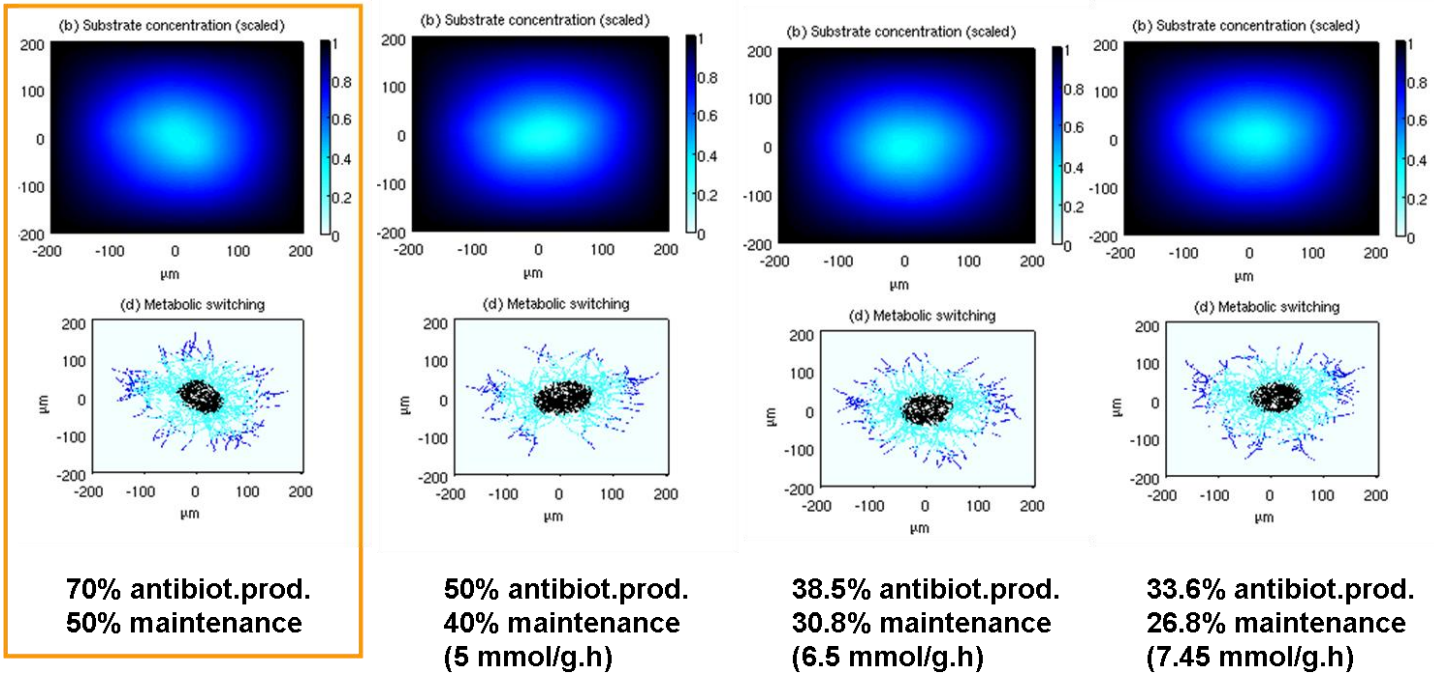

Figure 3.15: Comparison of simulations using different rescaled oxygen consumption rates for antibiotic producing hyphae and maintenance requirements only hyphae. The percentages were estimated from Melzoch *et al*., (1996) continuous culture studies (at 5 mmol/g.h, 6.5 mmol/g.h and 7.45 mmol/g.h oxygen consumption rates almost no actinorhodin was produced). The top row illustrates the external oxygen concentration levels and the bottom row shows the resulting metabolic states of the hyphae for active growth (dark blue), antibiotic production (cyan), maintenance only requirements (black) and dead cells (light blue). Note, no dead cells are present in the simulations. No difference is seen in simulations when compared to the original estimates of 70% and 50% (Paul Hoskisson, personal communication) (original simulation shown in orange box).

Model simulation with oxygen as substrate

To be able to better assess the model, various parameters are monitored in the model simulations, such as maximum pellet diameter, pellet area and pellet perimeter. These values can be validated against the laboratory experiments. However, other measures for example hyphal growth unit, number of tips and proportion of tips are not attainable from in fully developed pellets in laboratory experiments. However, we can quantify these from the model simulations. The frequency of distribution of the interbranch distances, branching angles and elongation rates are also monitored. All of these measurements are shown in Figure 3.16 for the model simulation using parameters discussed above (see Tables 3.2 and 3.3 and Figure 3.14).

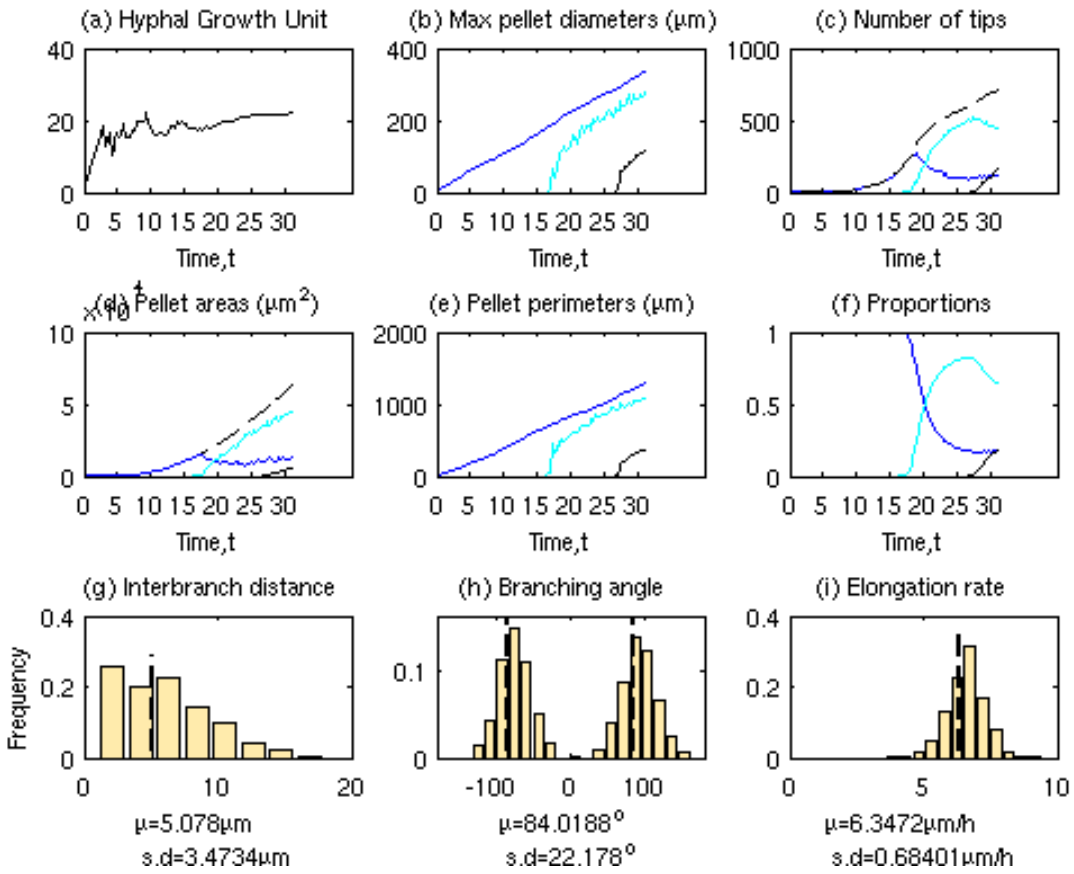

Figure 3.16. Pellet growth simulation measurements under oxygen limitation. For parameters used in this simulation see Tables 3.2 and 3.3 and Figure 3.14. The simulation time denoted is the time after germination. Hyphal growth unit (a) is the total length of hyphae divided by the total number of tips. Pellet area (d) is shown on y-axis as 0-10 x 10^4 μm^2 and includes internal spaces. (f) shows the proportions of tips of different metabolic states. Note that within this simulation time scale no dead hyphae is seen. Colour codes for the different metabolic states are: actively growing hyphae (dark blue), antibiotic producing hyphae (cyan), hyphae with only maintenance requirements (black) and dead hyphae (light blue). The dashed black line illustrates the total number of measurements of interest. The mean (µ) and the standard deviation (s.d.) are shown for the interbranch distance, the branching angle and the elongation rate data.

Summary and conclusions

To understand hyphal elongation or pellet formation of filamentous organisms, several mathematical models have previously been constructed (see Chapter one). Some of these models do take into account external substrate and metabolic state of cells, however only a few attempt to include antibiotic production. The model framework suggested in this study includes spatial heterogeneity in both hyphal growth, modelled as a discrete random walk model, and an external substrate, modelled via a continuous reaction-diffusion equation. This discrete model framework is able to predict the location of antibiotic producing cells in a pellet without having to compromise on the structure of a single hypha. The hyphal elongation and branching both have a random aspect to them and the antibiotic production is modeled due to depletion of the external substrate concentration. No length increment subtraction was needed to localize the antibiotic producing hyphae. The model allows 2D+ effect for elucidating the hyphal density inside the pellet. This model has the advantage that it is constructed from a few parameters that can be determined from experimental data. This tight link between mathematics and biology and the low number of unknown parameters makes the model extremely well validated with an extremely strong predictive potential that is applicable to a wide range of branched networks in biology such as angiogenesis in organs and tumor (Jones and Sleeman, 2006), transport networks in fungi (Smith *et al*., 1992; Boswell *et al.*, 2002) and amoebae (Bebber *et al*., 2007) and the development of root systems in plants (Dupuy *et al*., 2010).

Chapter 4: Experimental validation of the model

To test and validate the model developed in Chapter 3 laboratory based experiments were designed. A case study using growth curve experiments was carried out in order to numerically analyse and validate the model outputs and also to gain further insight into the pellet development linking this to *Streptomyces* biology.

External nutrient profiles

Shake flask cultures were started with spore suspension resulting in a final concentration of 2 x 10^5 cfu/ml in YEME. Incubation (without any springs or baffles in the flasks) was continued until the culture was in stationary phase. To show the relationship between bacterial growth and nutrient depletion a range of parameters were measured throughout growth, such as dry weight, pH, phosphorus, ammonium and amino acid concentrations.

The growth curve experiments in YEME medium showed that *S. coelicolor* entered log-phase at 14 h after the start of the incubation. At mid-log phase (around 22 h) the culture had turned from yellow to pink indicating the onset of the red-pigmented antibiotic, undecylprodigiosin. Cultures entered stationary phase at 37 h post-inoculation (see Figure 4.1 for the total length of incubation and Figure 4.2 for the exponential growth phase). Monitoring the concentration of nutrients within the culture showed that phosphorus concentration dropped dramatically after 14 h of incubation and remained low (< 5 µg/ml) from 20 h onwards. The pH of the culture was 6.4 at 16 h. It then decreased to 6.0 at 22 – 24 h and then continued to increase until the end of the growth curve (8.3 at 85 h). The increase seen in pH is related to the excretion of ammonium due to de-amination of amino acids from the medium (Hoskisson *et al*., 2003).

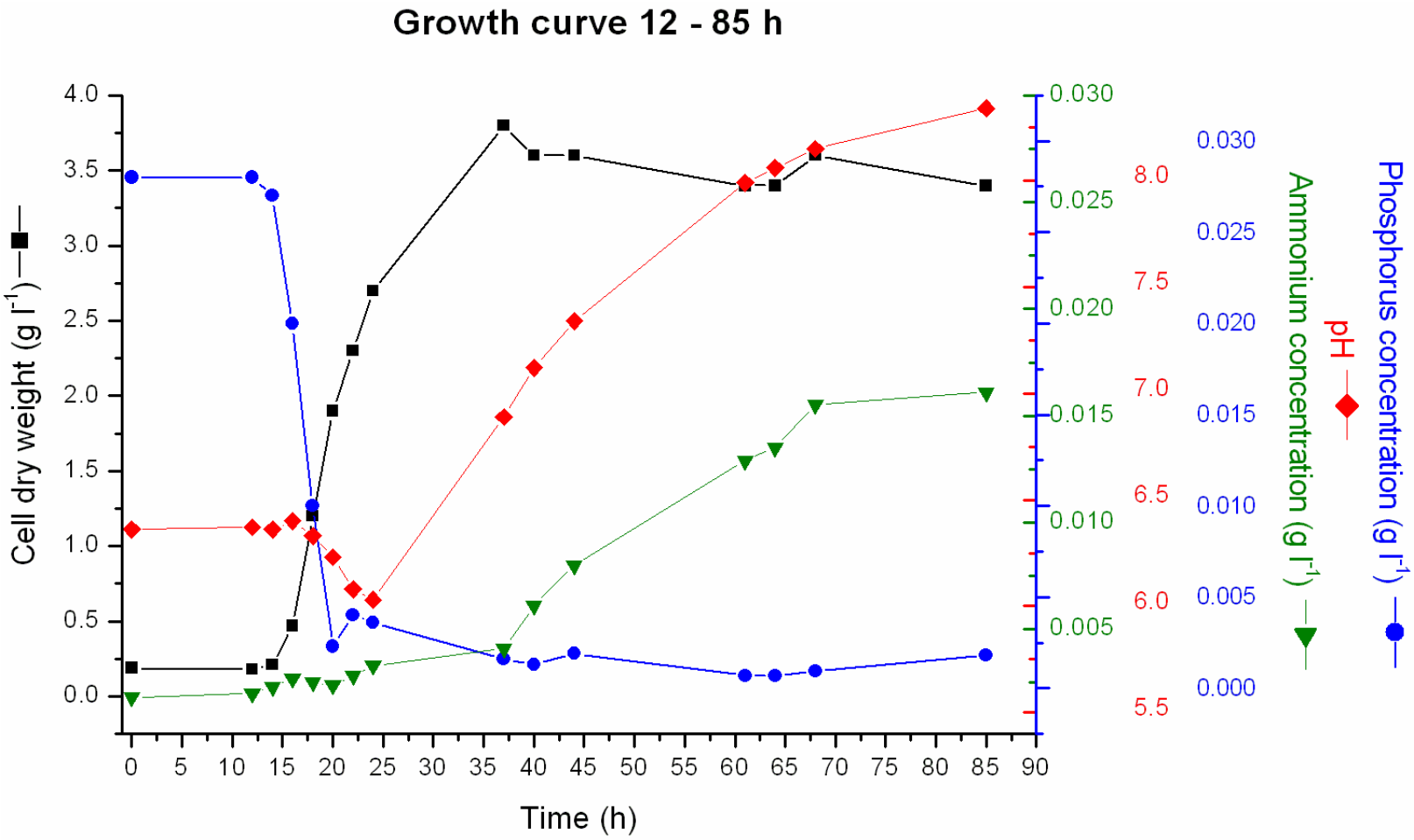

Figure 4.1: Shake flask growth curve (12 – 85 h). Cell dry weight (g l^{-1}; black squares), ammonium (g l^{-1}; green triangles), phosphorus (g l^{-1}; blue circles) and pH (red diamonds) concentrations were determined.

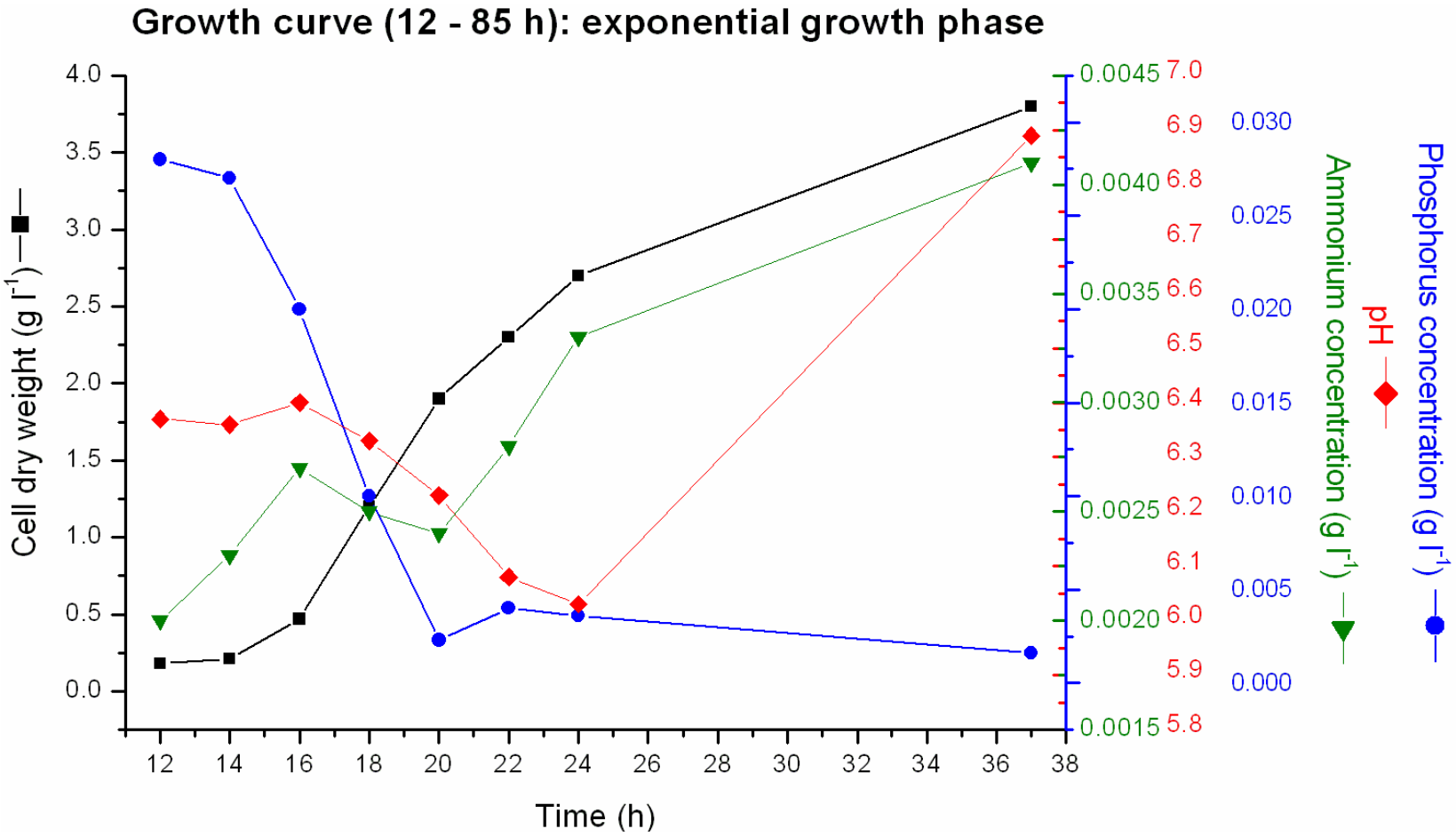

Figure 4.2: Exponentially growing phase of the shake flask growth curve (12 – 85 h). Cell dry weight (g l^{-1}; black squares), ammonium (g l^{-1}; green triangles), phosphorus (g l^{-1}; blue circles) and pH (red diamonds) levels are monitored.

It is known that ammonium is excreted when bacteria utilizes amino acids as a source of nitrogen (Voelker and Altaba, 2001). To test the level of amino acids in the culture, we performed ninhydrin assay that detects all amino acids except proline and hydroxyproline. The ninhydrin-positive amino group concentration is shown in Figure 4.3, where it can be seen that the amino acid concentration decreased during the growth but that there were still amino acids present at the end of the incubation period (85 h).

At the start of the incubation (12 – 16 h), the concentration of amino acids increased. This is likely to be the result of proteases secretion that break down the peptides present in the peptone component of the YEME into amino acids. The first drop (18 h) in amino acid concentration coincided with the fast exponential growth observed in the cell dry weight, indicating heavy amino acid consumption. At the onset of antibiotic production (22 h) until the end of the exponential growth (37 h), the amino acid concentration increased. In order to adapt to the low phosphate concentration, *S. coelicolor* is known to induce the production of extracellular hydrolytic enzymes and scavenging uptake systems that allow the cell to recover phosphate from organic sources (Allenby *et al*., 2012). At stationary phase (37 h onwards), the concentration of amino acids gradually declined indicating the consumption of amino acids at the time when most of the amino acids in the organic matter have already been made available.

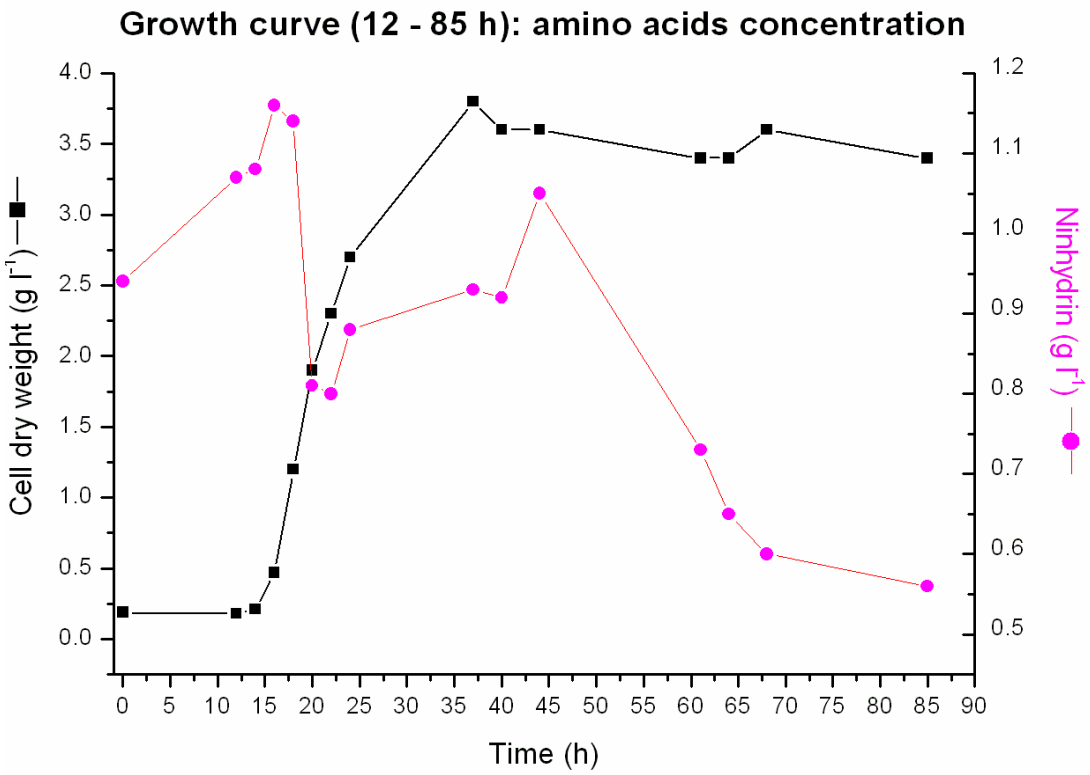

Figure 4.3: The concentration of ninhydrin-positive amino groups as the indicator for amino acids during shake flask culture (12 - 85 h). The amino acids concentration (g l^{-1}) is shown as circles (magenta). (The course of the growth curve was monitored using cell dry weight (g l^{-1}; black squares).

Antibiotic production and cell heterogeneity

In the mathematical model, we assume cell heterogeneity within a pellet. To study the development of a pellet and to illustrate this heterogeneity, we obtained *Bac*Light™ stained fluorescence images of pellets over the course of the shake flask culture (see Figures 4.1, 4.2 and 4.3 for the growth curve in question). The BacLight™ stain contains green fluorescent SYTO9 and red fluorescent propidium iodide (PI) nucleic acid stains. According to the manufacturer, SYTO9 is a membrane permeable stain that can enter live cells and stain DNA green in the absence of PI. The manufacturer claims that the PI is a membrane impairment and therefore is being excluded from the healthy cells. It is noted that alternative to the membrane impermeability theory, PI might be excluded from the live cells by active efflux pumps. In the presence of PI, only PI will stain DNA due to its stronger binding affinity (Stocks, 2004). In Figure 4.7 the development of tangled hypha to dense pellet is shown together with the cell dry weight and undecylprodigiosin (RED) production. The production of RED initiated at the mid-log phase at ca 22 h. The concentration of cell associated RED then increased until the start of the stationary phase when a small decrease was detected before a further increase. Cell heterogeneity within a pellet was assessed by the SYTO9 green areas, showing cells with intact cell membrane potential i.e. live cells, and by propidium iodide (PI) red areas, illustrating cells with impaired cell membrane potential that are likely to be dead or at the very least metabolically inactive (Stocks, 2004; Hoskisson P.A. personal communication). It is noted, that the red areas started to spread from the core of the pellet, eventually covering the whole pellet. Some parts of the hyphae already stained red at 12 hours even though the pellets were not properly formed before the 14 hours time point. The SYTO9 stained images showed hollow pellets from 37 h onwards (end of log-phase) indicating a decrease in the number of live cells. At the 61 h time point, the majority of the pellets contained only red cells, and the pellets began to lyse shortly after. At the end of the growth curve (85 h), only the tangled hyphae, released from

the dense, dead pellets, remained active and formed the basis of new pellet regrowth.

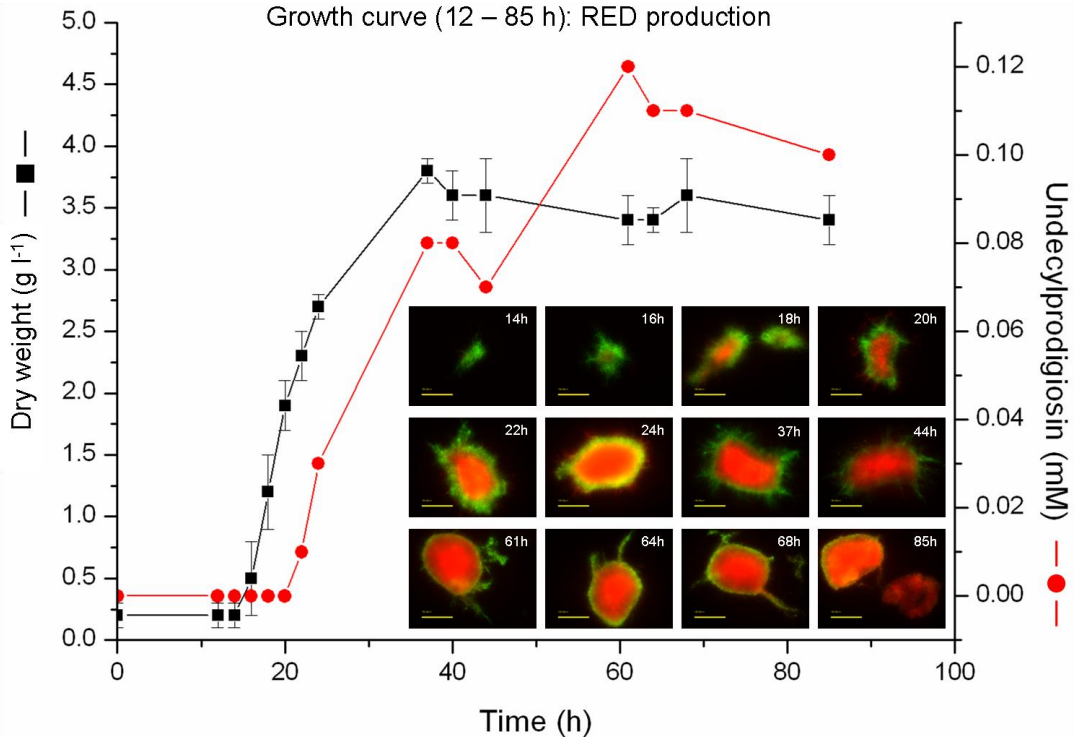

Figure 4.7: Pellet development during the growth curve (12 – 85 h) experiment. The heterogeneity of cells within pellets is illustrated using live/dead staining. Green areas correspond to SYTO9 dyed cells with intact cell membrane. Red areas show cells that are stained with propidium iodide, representing cells with impaired cell membrane potential that are likely to be dead. The course of the growth curve was monitored using cell dry weight (g l^{-1}; black squares, shown as average ± standard deviation) and the production of antibiotics is determined as undecylprodigiosin production (mM; red circles). The yellow scale bar in the fluorescence images is 100 µm.

From the live/dead microscopy analysis it is shown that a pellet contains both active and inactive hyphal parts. Stocks and Thomas (2001) carried out fermentation studies with *Saccharopolyspora. erythraea* where they used *Bac*Light™ staining. Their studies implied that fragmentation of hypha coincides with the appearance of hyphal regions of permeabilised membranes. However, Stocks and Thomas (2001) could not locate the first appearance of red hyphal parts in the fragmented hyphae. The results shown in this study imply that the red stained regions of hypha are located mainly at the centre of the pellet. The appearance of the mycelium with impaired cell membranes (also present at the early stages of the growth curve) could be down to a substrate(s) limitation (oxygen, phosphorus) within the pellet, or down to the natural cell death occurring at the older parts of the hypha.

The concentration of another antibiotic, γ-actinorhodin (excreted the lactone form of actinorhodin), was determined (see Figure 4.8). The spectrophotometric assay was performed at 542 nm as per materials and methods. However, a related peak was observed at 532 nm and the combined absorbance of both 542 nm and 532 nm is also shown. The concentration of the combined absorbance of 542 nm and 532 nm followed the trend of γ-actinorhodin concentration. Gamma-actinorhodin concentration was first noticed at mid-log phase at ca 22 h at micromolar level. The γ-actinorhodin concentration in the culture supernatant stayed between 1 – 2 μM between 24 h to 68 h. The concentration then increased rapidly to 4.4 μM at 85 h.

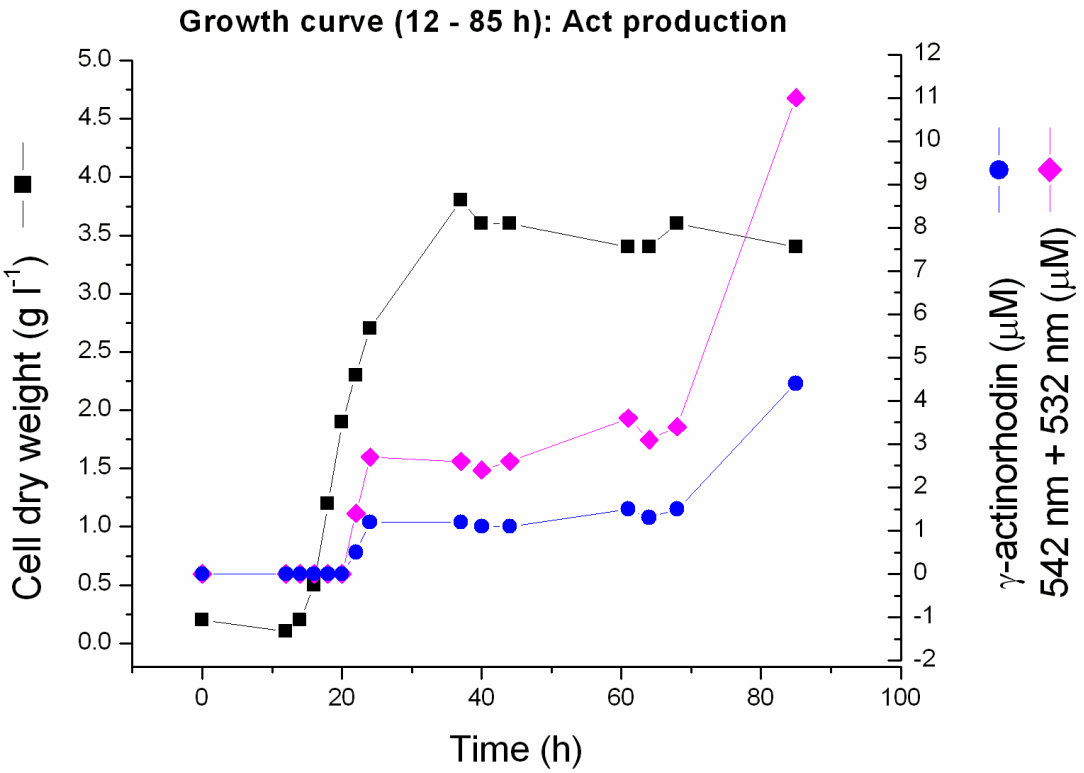

Figure 4.8: The concentration of γ-actinorhodin over the course of a growth curve (12 – 85 h). The duration of growth curve was monitored using cell dry weight (g l^{-1}; black squares) and the excreted lactone form of actinorhodin was determined at 542 nm (μM; blue circles). During the spectrophotometrical analysis, a related peak was observed next to the 542 nm at wavelength of 532 nm. The substance concentration was calculated using the combined absorbance from 542 nm and 532 nm and the molar extinction coefficient of γ-actinorhodin (μM; pink diamonds).

Image and data analysis (manual measurements)

To describe the pellet development in a quantitative manner, we manually measured the maximum pellet diameter during the growth curve experiment. The average maximum pellet diameter in bright field and SYTO9 and PI stained fluorescence images are presented in Table 4.1 and illustrated in Figure 4.9. Average maximum pellet diameter for both bright field and SYTO9 pictures showed a similar growth curve, although SYTO9 measurements were consistently lower than the corresponding bright field measurements. The diameter of the PI area also followed the trend of the bright field and the SYTO9 measurements with only few variations. The average diameter of the pellet, dyed with PI, dropped at the 16 h time point. This drop is thought to be caused by the change in the slide preparation when the time between the preparation of the slide and the imaging was reduced. The time delay between microscopic slide preparation and the start of taking the pictures was kept to minimum from the 16 h time point onwards. At the 24 h time point, the average maximum diameter of PI pellets was higher than the average maximum pellet diameter of SYTO9. After this time point the exposure time for PI pictures was dropped from 50 ms to 20 ms. As a possible consequence, at 37 h, the average maximum pellet diameter of the PI dropped back to below the SYTO9 measurements. Interestingly, both the bright field and SYTO9 images showed a drop in average maximum pellet diameter growth at the 22 h time point. This time point correlates with the start of the undecylprodigiosin production. At the 37 h time point, when the culture entered the stationary phase, a simultaneous drop was seen in the average maximum pellet diameter in bright field, SYTO9 and PI images. We observed a difference in maximum pellet diameter between the bright field and SYTO9 stained images. From manual measurements it was shown that the bright field images of pellets were on average ca 28% larger than the corresponding SYTO9 dyed images.

We also monitored the number of tips at the pellet perimeter. The number of tips continued to grow until 16 h. After this time point the pellets had grown in

size so that it had became difficult to count the individual hyphae. As a consequence the number of tips dropped at 18 h. Therefore, the number of tips was not measured after this time point.

Table 4.1: Manual measurements of average maximum pellet diameter for growth curve time points 12 – 61 h.

Time point (h)	Bright field (µm)	SYTO9 (µm)	PI (µm)	Average number of tips	n*
12	113	73	61	11	31
14	182	118	101	20	53
16	224	149	84	51	10
18	233	149	131	34	10
20	308	229	202	N/A	10
22	288	221	211	N/A	10
24	299	227	246	N/A	10
37	444	341	266	N/A	10
40	391	272	204	N/A	10
44	373	285	230	N/A	10
61	390	326	313	N/A	10

* n = Number of measurements

N/A = Not analysed

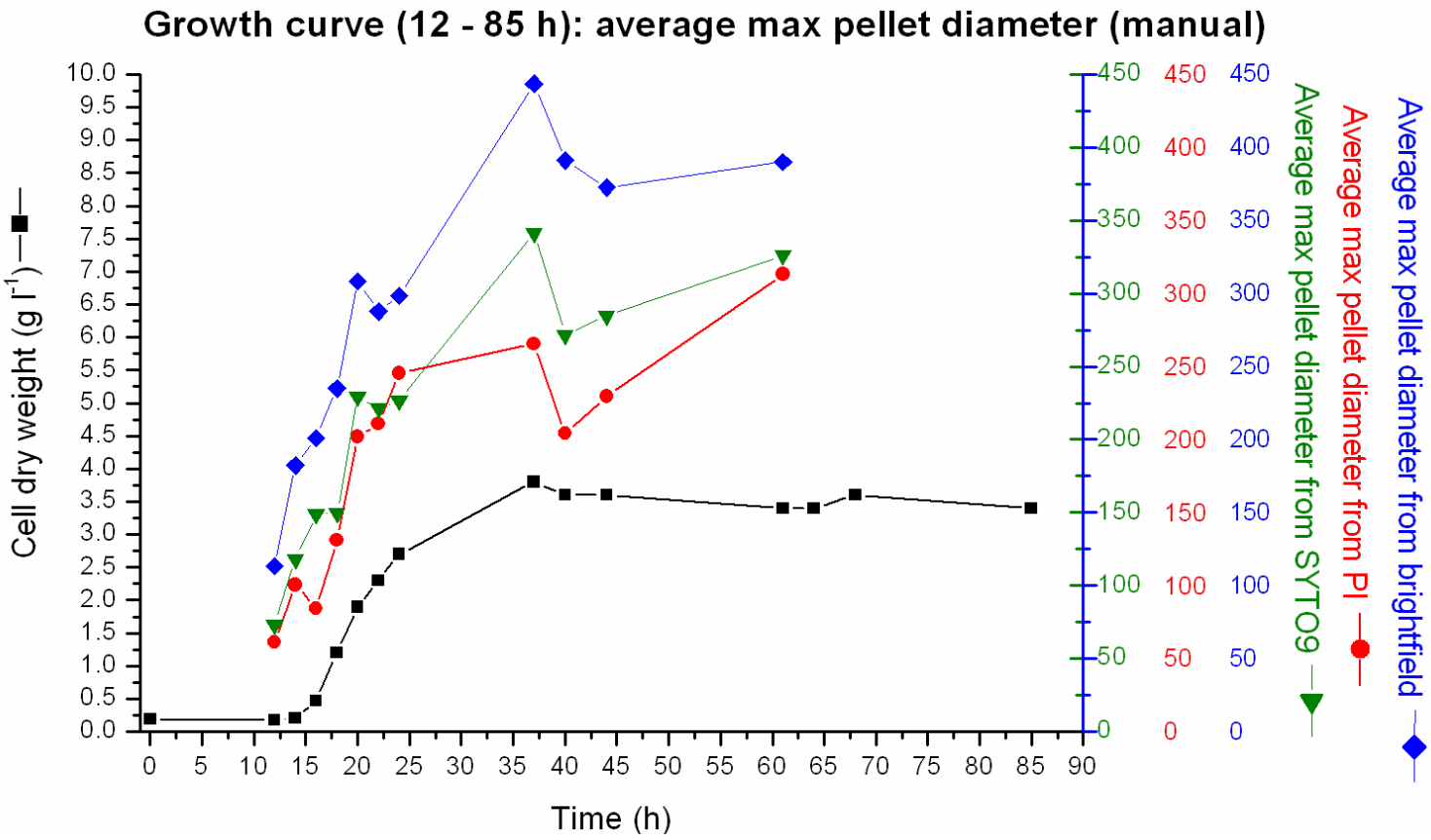

Figure 4.9: Manual measurements of average maximum pellet diameter from growth curve (12 – 85 h). The average maximum (max) pellet diameters (µm) were measured manually from brightfield (blue diamonds) and fluorescent images of SYTO9 (green triangle; live cells) and propidium iodide (PI, red circles; likely to be dead cells). The course of the growth curve was monitored using cell dry weight (g l^{-1}; black squares).

Further data analysis (manual) for the 12 h time point

To identify any possible trends in pellet development between pellet size and the number of tips and between the size of live and dead maximum pellet diameters, further analyses were performed for the manual measurements of microscopic pictures taken at the 12 h time point. The maximum pellet diameters (brightfield, SYTO9 and PI) were sorted in ascending order according to the total number of tips. The data is shown in Figure 4.10. No clear correlation was seen between the total number of tips and the pellet diameter.

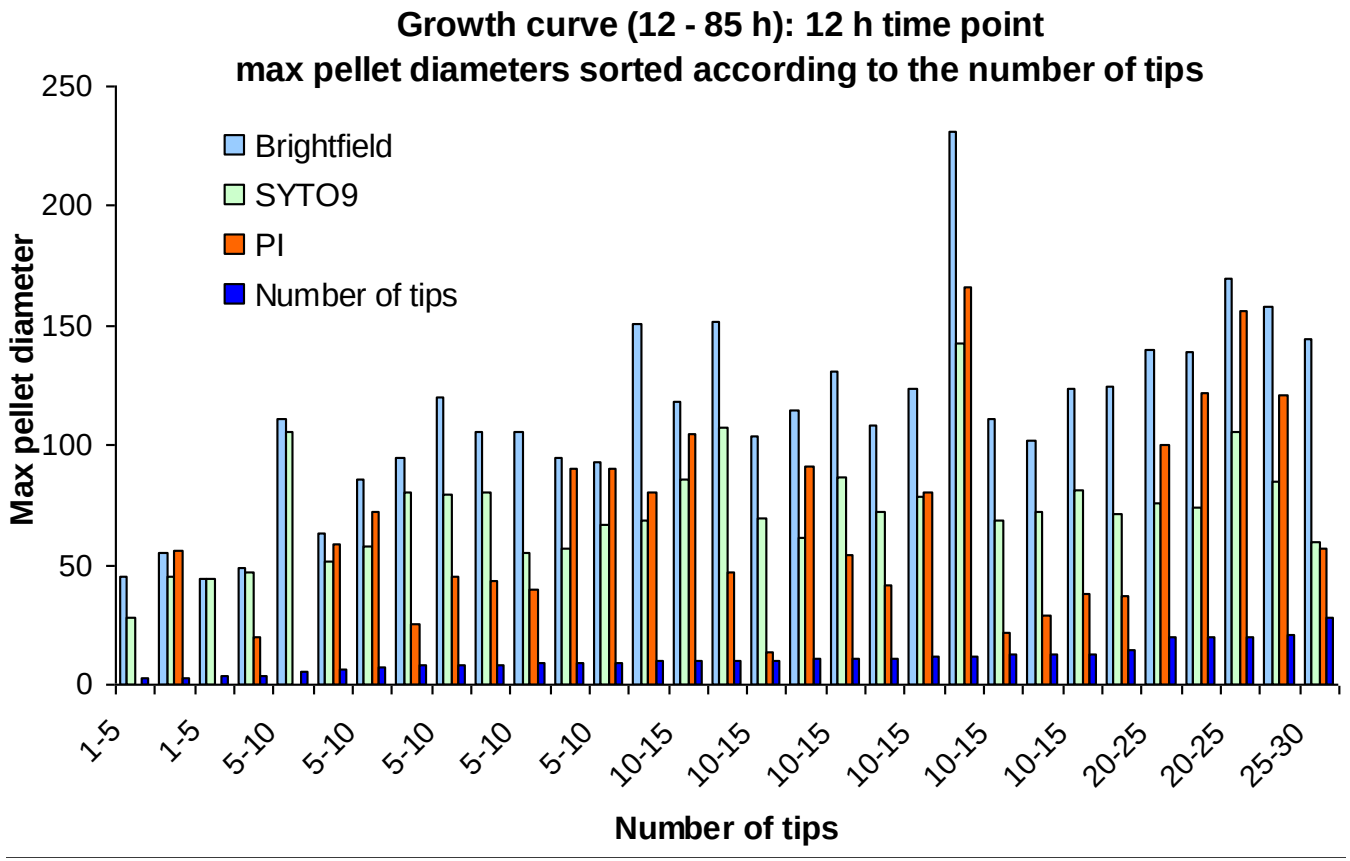

Figure 4.10: Maximum pellet diameters versus number of tips. The maximum (max) pellet diameters (μm) from brightfield and SYTO9 and propidium iodide (PI) fluorescent images were sorted according to the number of tips at the pellet perimeter at the 12 h time point. The measurements of max pellet diameter and the number of the tips were made manually. The data was sorted in ascending order according of the total number of tips using Microsoft Excel.

Image and data analysis (automated)

To increase the confidence of the statistical analysis of pellets and to gain additional measurements of pellet morphology, such as the pellet area, perimeter and minor axis, we performed an automated image analysis, where we were able to measure between 30 - 71 pellets per time point. The automated measurements for SYTO9 and PI pictures are shown in Table 4.2 and Table 4.4 respectively. The respective coefficients of variation (CV%) are shown in Tables 4.3 and 4.5.

The average major and minor axis and the average area and perimeter of the pellet increased through out the growth curve (12 - 37 h). However, the pellet growth for these measurements slowed down after 20 h in SYTO9 and after 22 h in PI pictures. The average intensity of SYTO9 doubled over the 2 h time period at the 12 h and 16 h time points. After the 16 h time point the average SYTO9 intensity started decreasing showing a small increase at the 24 h time point. The average PI intensity followed this trend with a time delay. Both the average eccentricity and radial SD decreased through out the growth curve with exception at the 24 h time point when a small increase was seen in both SYTO9 and PI pictures.

Table 4.2: Average of measurements from the automated data analysis for growth curve (12 – 85 h) with SYTO9 dye (see Chapter 2 for description of different measures). Note only exponentially growing phase time points are included.

Time point	12h	14h	16h	18h	20h	22h	24h	37h
Mean	240	507	631	1266	988	905	1115	520
Area	4235	4864	9603	15608	23627	25468	27077	30859
Perimeter	1094	561	845	745	1056	1044	1042	1516
Radial SD	41	27	25	22	20	21	26	23
Major Axis	71	104	140	170	219	222	242	266
Minor Axis	34	57	83	101	134	141	136	154
Eccentricity	0.85	0.80	0.79	0.78	0.76	0.75	0.80	0.75
n*	30	53	67	71	66	44	50	60

* n = Number of measurements

Table 4.3: Coefficient of variation (CV%) for the data from automated data analysis for growth curve (12 – 85 h) with SYTO9 dye (see Chapter 2 for description of different measures). Note only exponentially growing phase time points included.

Time point	12h	14h	16h	18h	20h	22h	24h	37h
Mean	32	56	34	47	37	30	37	25
Area	52	109	150	145	71	75	73	46
Perimeter	110	41	108	50	37	33	34	39
Radial SD	32	29	30	37	33	32	31	39
Major Axis	30	41	65	51	33	31	31	29
Minor Axis	34	45	72	56	32	37	35	28
Eccentricity	18	15	17	15	16	17	15	19
n*	30	53	67	71	66	44	50	60

* n = Number of measurements

Table 4.4: Average of measurements for the automated data measurements for the growth curve (12 – 86 h) with PI dye. Note only exponentially growing phase time points are included.

Time point	12h	14h	16h	18h	20h	22h	24h	37h
Mean	257	314	395	609	936	818	879	637
Area	1526	3986	7047	11322	13895	15905	14381	18853
Perimeter	451	663	744	871	832	993	861	961
Radial SD	36	26	22	21	18	18	23	20
Major Axis	69	95	112	140	164	171	161	181
Minor Axis	32	53	70	88	102	112	96	114
Eccentricity	0.86	0.79	0.75	0.74	0.75	0.72	0.77	0.75
n*	28	52	66	68	64	48	64	61

* n = Number of measurements

Table 4.5: Coefficients of variation (CV%) for the automated data measurements for the growth curve (12 – 86 h) with PI dye. Note only exponentially growing phase time points are included.

Time point	12h	14h	16h	18h	20h	22h	24h	37h
Mean	11	37	46	79	36	39	69	33
Area	70	100	142	160	83	79	123	39
Perimeter	58	46	67	48	37	35	48	24
Radial SD	25	36	40	40	31	35	42	34
Major Axis	35	40	54	50	36	35	42	25
Minor Axis	49	41	56	60	33	38	50	22
Eccentricity	13	16	18	19	17	20	19	16
n*	28	52	66	68	64	48	64	61

* n = Number of measurements

The variation observed in Tables 4.3 and 4.5 is relatively large. At the end of the exponentially growing phase (31 h), both the SYTO9 and PI pellet areas had relatively high coefficient variations (CVs) of 46% and 39% respectively. Therefore, we analysed the data using the histograms shown in Figure 4.11. The frequency histogram for stained pellet areas of both SYTO9 and PI were at the end of the exponentially growing phase (31 h after 6 h germination) is presented. From a total of 60 measured SYTO9 stained pellets measured, four pellets were small (<10,000) and three were large (>60,000) suggesting that only a few pellets contributed to this large distribution.

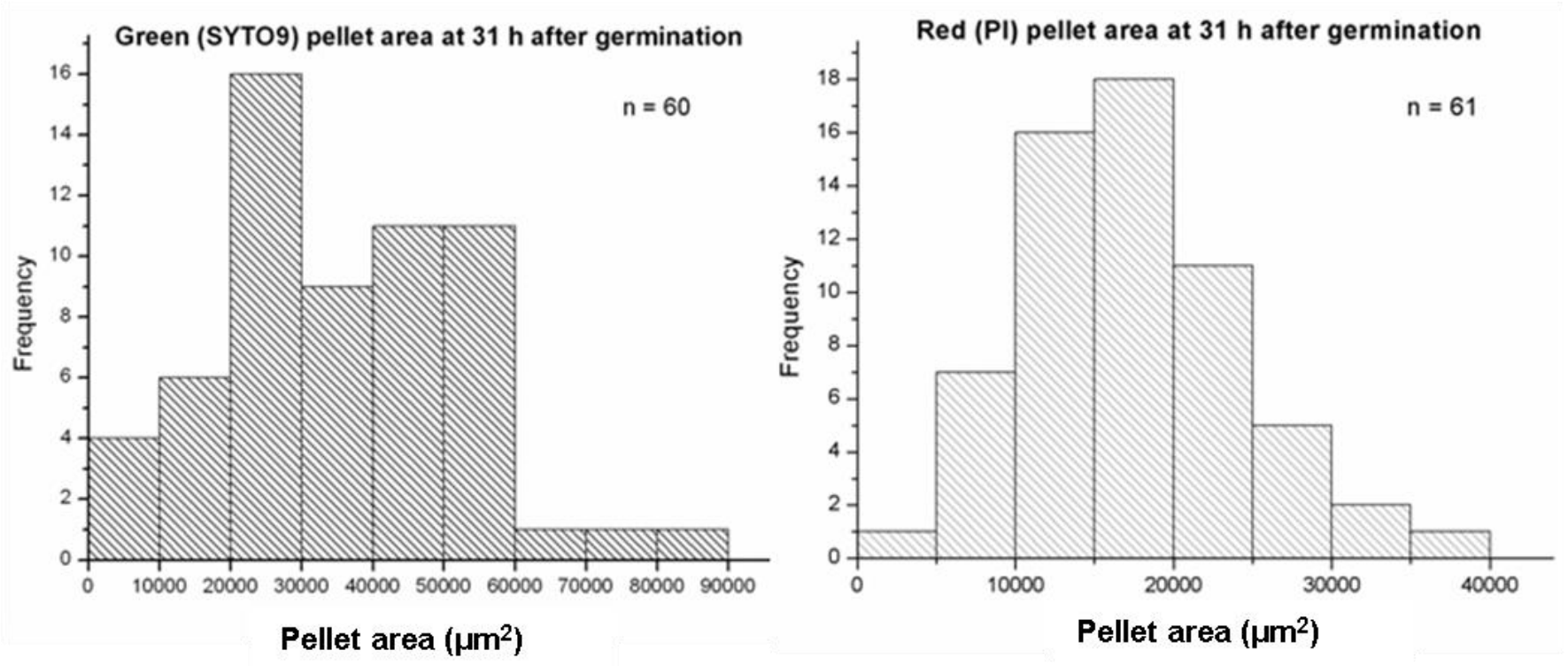

Figure 4.11: Frequency histograms of the SYTO9 and propidium iodide (PI) dyed pellet areas (μm^2) at the end of exponentially growing phase (31 h excluding 6 h germination time).

Average maximum pellet diameter

The average maximum pellet diameter was 270 µm for the SYTO9 fluorescence image analysis at the end of the exponential growth phase. By comparing manual measurements between SYTO9 fluorescence and bright field images, it was seen that the average maximum pellet diameter in SYTO9 dyed images were 65.6% (CV 20.5) and 75.8% (CV 8.1) of the average maximum pellet diameter in bright field images for time points 6-12 h and 14-31 h after germination respectively (Table 4.6). Consequently, the average maximum pellet diameter measured from SYTO9 fluorescence images gives results that are 35% and 24% smaller than the actual pellet for 6-12 h and 14-31 h after 6 h germination respectively. If the average value of 270 µm was corrected to represent the actual maximum pellet diameter, then the average maximum pellet diameter would be around 356 µm. The difference seen in measurements between the fluorescence and the bright field images of pellet development may be explained by the fact that pellets are dense, therefore the fluorescence from the centre is higher than the fluorescence from the individual tips and this may result in low levels of fluorescence from the tips not being detected.

Table 4.6: The ratio of maximum pellet diameter in SYTO9 fluorescence images compared to phase-contrast images (manual measurements)

Time after germination[1] (h)	Ratio of max pellet diameter (%)	n
6	67.2	31
8	64.9	53
10	66.3	10
12	63.8	10
14	74.4	10
16	76.6	10
18	75.4	10
31	76.7	10

[1] Germination time 6 h

Pellet population

Representative statistics of pellet population

The mean value for the SYTO9 average pellet area at the end of log-phase was 37,000 μm^2 and the mode was between 20,000-30,000 μm^2. This raised the question as to whether the mean, the mode or the median was more representative measure for the data. In Figure 4.12 the mean, the mode, the median and minimum and maximum values of the SYTO9 stained pellet's major axis measurements are compared. The comparison was carried out for the major axis data since its CV was lower than the others (29%) making it a more reliable measure to take forward. It was observed that the mean and the median were almost identical and they both fit in the variation seen in the mode. Therefore, all the three statistical measures (mean, mode, median) are equally sufficient to represent the dynamics of the population.

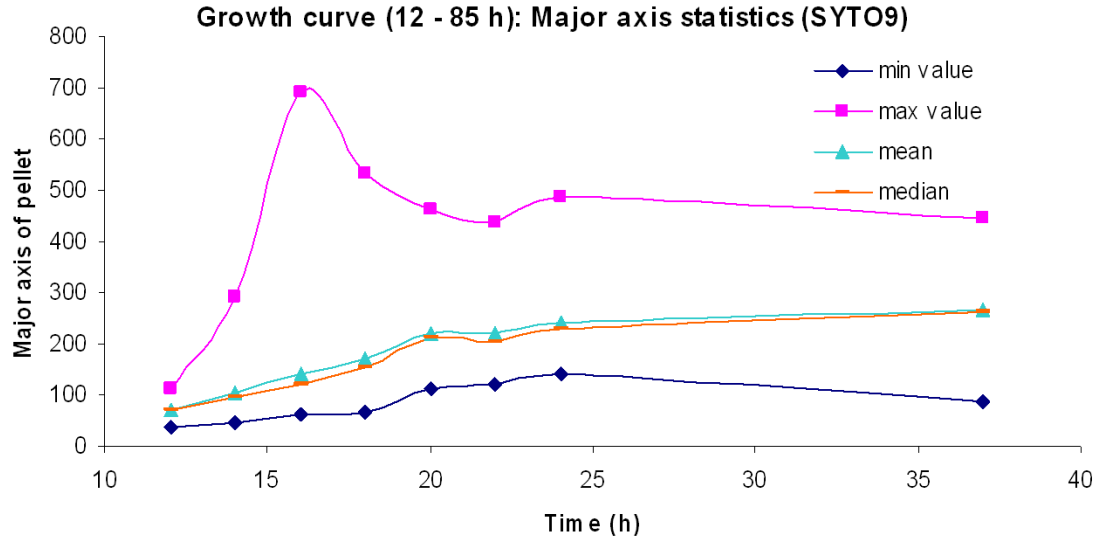

Time point (h)	12	14	16	18	20	22	24	37
min value	36	45	61	66	111	121	140	86
max value	114	293	692	533	464	437	487	446
mean	72	104	140	170	219	222	242	266
mode	67 - 83	80 - 116	61-140	124-183	199-287	147 - 226	189 - 239	240 - 291
median	71	94	120	153	214	205	231	261

Figure 4.12: Comparison between mean, mode, median and minimum and maximum values of the major axis of the pellet. The major axis (µm) of the SYTO9 stained pellets are from the automated image analysis of the growth curve (12 – 85 h) experiment. The mean (light blue triangles), median (orange lines) and the minimum (dark blue diamonds) and maximum (pink squares) values are illustrated in the diagram (top). The table at the bottom compares the above to the median (bottom row).

A putative second pellet population

A recent study using flow cytometry on liquid-grown *Streptomyces* cultures identified two parallel yet distinct populations of pellets. The first pellet population had a constant average maximum pellet diameter of around 260 µm where as the second pellet population consisted of larger mycelia whose diameter varied according to the strain, the age of the culture and medium composition (van Veluw *et al*., 2012) The frequency histogram in Figure 4.11 for SYTO9 stained pellet areas might indicate a second pellet population (first peak at 20,000-30,000 μm^2, second peak at 40,000-60,000 μm^2). Therefore, in Figure 4.13 we studied histograms of major axis at 14 h (phosphate abundant, no antibiotic production), 20 h (phosphate limited, no antibiotic production), 22 h (phosphate limited, start of antibiotic production) and 37 h (end of log-phase) of both SYTO9 and PI dyed pellets. The modes of the histograms varied from below 100 µm to over 250 µm (over 200 µm for the PI) as the time progressed. Therefore, for the 14 h, 20 h and 22 h time points, it is unlikely that a population with a constant mean major axis of 260 µm existed. This might be a consequence of different culturing conditions (volume of flask/media, use of spring or baffles, starting inoculum, rpm, viscocity) or sampling intervals (van Veluw *et al*. 2012; first time point was at 24 h). Larger pellets (major axis >> mode), however, were present at all four time points in our growth curve experiment. At 37 h (i.e. 31 h after germination), however, the SYTO9 major axis histogram had a mode approximately around 250 µm, and 8 out of 60 pellets (13 % of the total) had a major axis between 350 - 450 µm, which might indicate a putative second pellet population, and be in agreement with the data published by van Veluw *et al*. (2012).

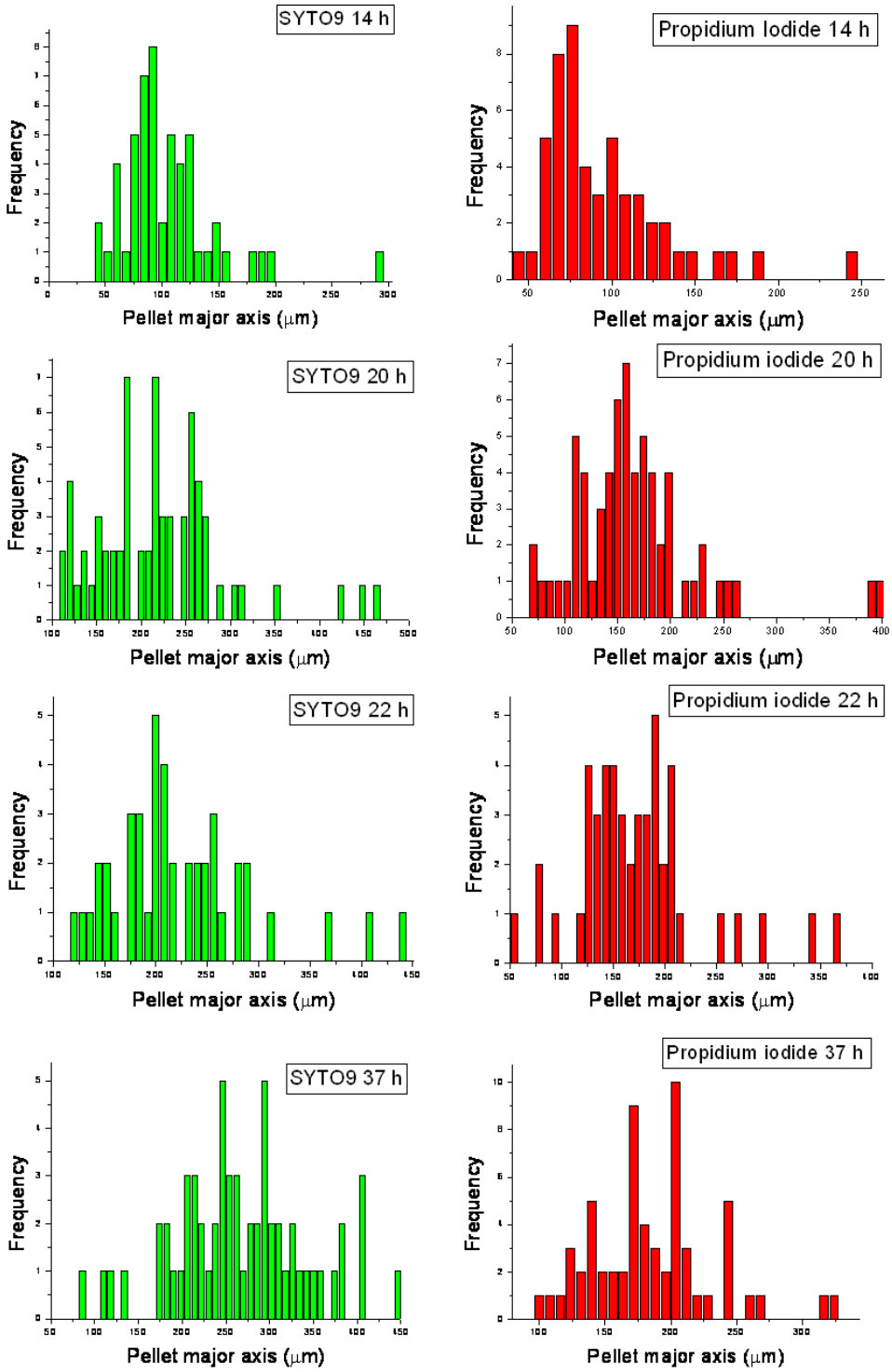

Figure 4.13: Comparison of the major axis histograms for SYTO9 and propidium iodide stained pellets. The time points were 14 h (phosphate abundant, no antibiotic production), 20 h (phosphate limited, no antibiotic production), 22 h (phosphate limited, start of antibiotic production) and 37 h (end of log-phase).

Hyphal density within a pellet

From the automated SYTO9 fluorescence measurements presented in this study, it can be seen that the average mean intensity of pellets first increased between 12 – 18 h time points and then decreased until 22 h, at which point the undecylprodigiosin production started. A second increase in fluorescence intensity was seen just between the 22 - 24 h time period, and a second drop is seen at 24 h onwards when the culture is coming to an end of the log-phase (see Figure 4.14). The PI fluorescence intensity curve follows the trend of the SYTO9 curve with a small time delay for the appearance of the first peak (seen at 20 h instead of at the18 h time point).

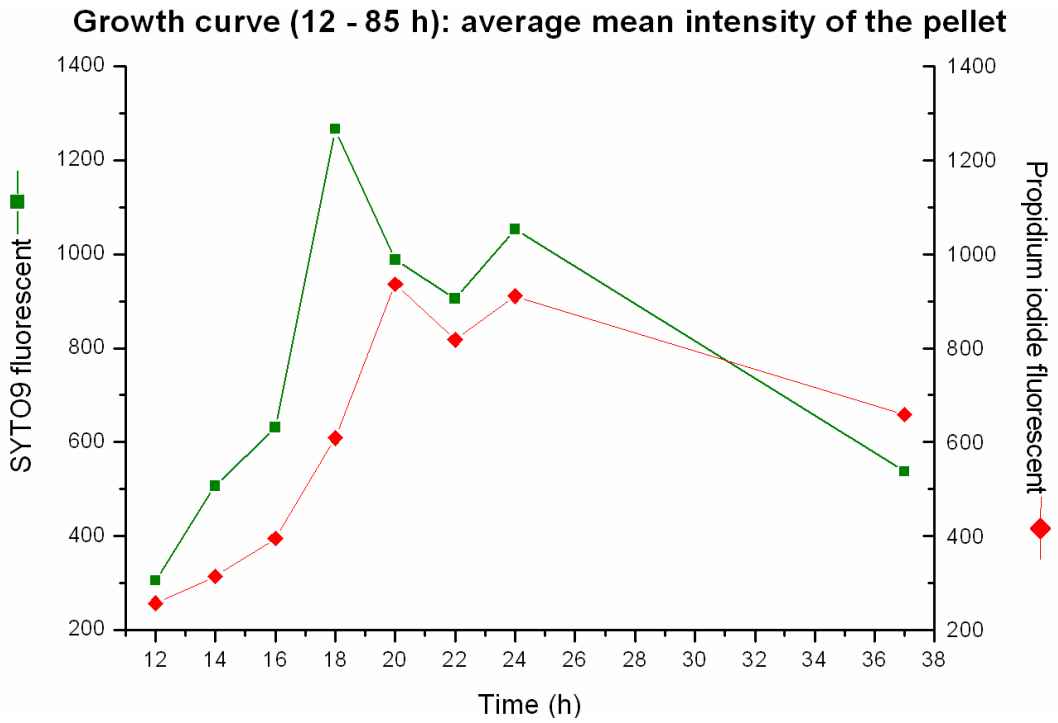

Figure 4.14: The average mean intensity of pellets during exponential growth. *Bac*Light™ live/dead staining illustrates the metabolic states of live cells (SYTO9, green squares) and likely to be dead cells (propidium iodide, red diamonds). The measurements were made from growth curve (12 – 85 h) experiment.

Using current laboratory techniques it is very difficult to gain knowledge of the hyphal density within a pellet, this highlights the use of modelling to determine such parameters. We utilised the dry weight and the theoretical pellet volume in order to shed light into the pellet density variation over time. We compared the increase seen in pellet volume (calculated from the major and minor axis using the automated image analysis data, see Chapter 2 for pellet volume calculation) to the increase in dry weight at each time point. Using this kind of comparison, it was hypothesised that both the pellet volume and the dry weight would increase simultaneously. However, this was not the case (see Figure 4.15). Interestingly, between 16-20 h the dry weight increased at equal levels of 20%. However, the pellet volume increased 9% at 16 - 18 h and, three times higher, 27 % at the 18 - 20 h time period. At the following time of 20-24 h, the dry weight yet again increased by ca 10% on both occasions, where as the pellet volume first increased only 6% and then again at a three times higher rate, 18%, at 22 - 24 h. The difference seen at the 16 - 18 h time period, when the dry weight increased by 20% and the pellet volume increased only by 9%, suggests the formation of branches. This would increase the pellet weight but not the pellet volume. The timing of this also coincides with the doubling of the mean average intensity in SYTO9 stained pellets supporting the hypothesis of branch formation internal to the pellets. Also, at this 16 -18 h time period the pH started to decrease indicated interruptions in TCA cycle possibly due to phosphorus limitations. The second low increase in pellet volume seen at the 20 - 22 h time period coincided with the observed onset of antibiotic production indicating a possible lag in hyphal growth during the switch from primary to secondary metabolism.

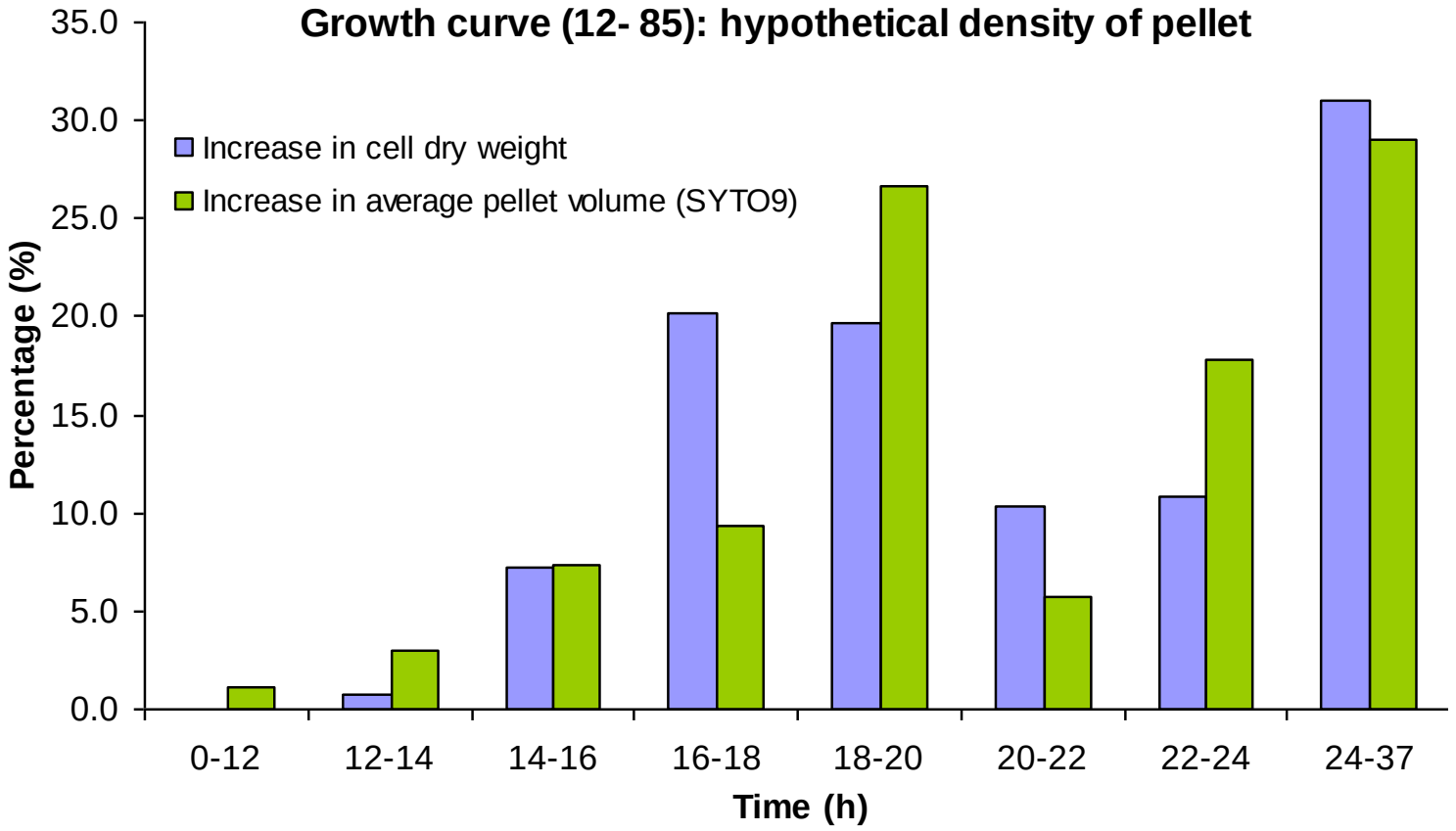

Figure 4.15: Comparison between the increase seen in theoretical volume of the pellet and the cell dry weight. The average major and minor axis of SYTO9 stained pellets from growth curve (12 -85 h) exponential growing phase was used to calculate the theoretical pellet volume (μm^3). The increase (%) in average pellet volume (green) was compared to the increase (%) seen in cell dry weight (blue) between each time point.

Validation of the model: Computer model simulation versus laboratory experiment

The laboratory based experiments now enable a direct comparison with the computer model to mimic the hyphal growth from a single cell to a fully developed pellet and show the hyphal morphologies at 6h, 12h, 18 h and 31 h after the germination period (see Figure 4.16). The parameters used for the simulation are shown in Tables 3.2 and 3.3 and in Figure 3.14. Since no time lag is incorporated into the model for spore germination, the time shown is from the emergence of a germ tube, which in the experiments was following approximately 6 hours of incubation. It can be seen that the pellet formation starts from a single hyphae that through branching and elongation eventually forms a dense pellet. The actively growing hyphae are present first, followed by antibiotic producing hyphae and, later on, by maintenance requirements only hyphae.

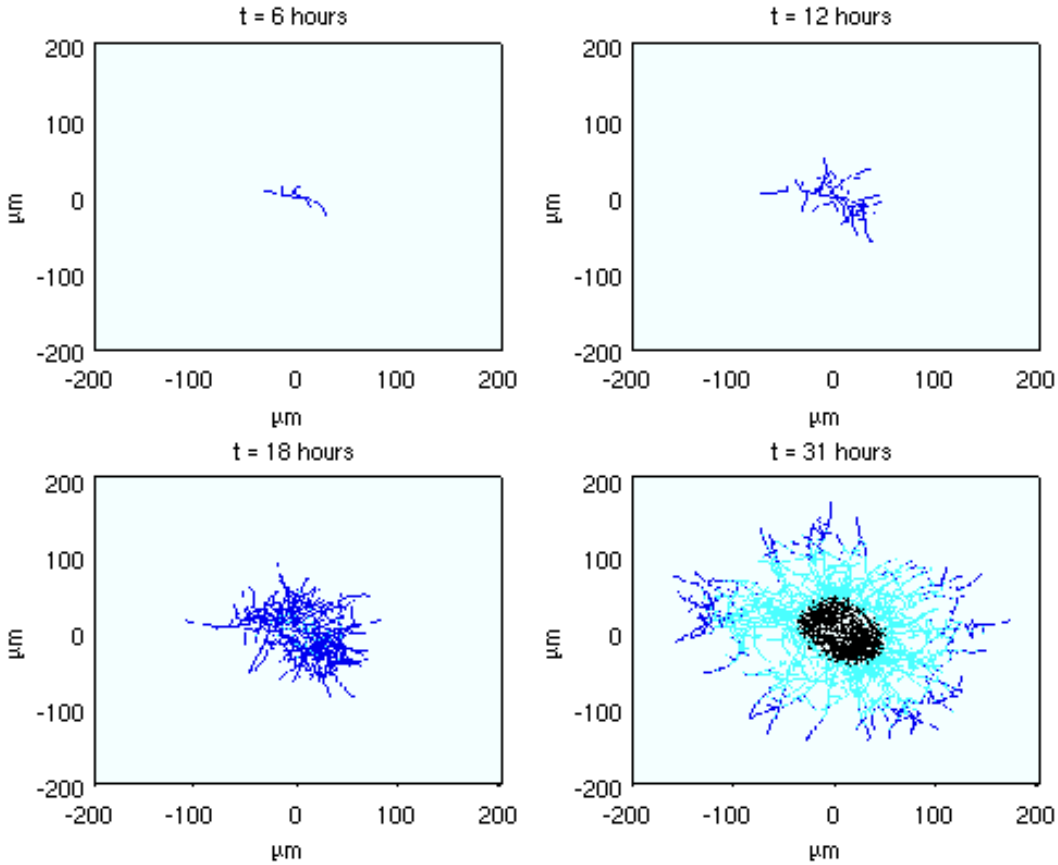

Figure 4.16. Pellet development and hyphal heterogeneity over time under oxygen limitations. Parameters used for the simulation are shown in Tables 3.2 and 3.3 and in Figure 3.14. Pellet development shown at 6 h, 12 h, 18 h and 31 h after germination. The metabolic states of hyphae are actively growing hyphae (dark blue), antibiotic producing hyphae (cyan), hyphae with only maintenance requirements (black) and dead hyphae (light blue). Note that within this simulation time scale no dead hyphae are seen.

The measurements of maximum pellet diameter, pellet area and pellet perimeter were determined in both the laboratory experiment and the model simulation and these are compared to each other in Table 4.7. The results from the laboratory experiment are from SYTO9 dyed pellets at the end of the exponentially growing phase (31 h after 6 h germination), and they are presented as minimum to maximum measurements. The simulation results are from the end of 31 h simulation using parameters in Tables 3.2 and 3.3 and in Figure 3.14. It is noted that the pellet dimensions from the simulations fit within the biological variation observed at the end of exponential growth. The corrected value for the experimental, average maximum pellet diameter is ca 356 µm, and the corresponding value to this from the simulations is 363 µm. Therefore, the model correlates very accurately to the experimental data when comparing the pellet diameter for the parameter set shown in Table 3.2 and 3.3 and in Figure 3.14. The experimental data for the pellet area gave a mode between 20,000-30,000 μm^2 and an average of ca 37,000 μm^2 (see Figure 4.11). If this average is corrected to represent the bright field images of pellets (+24%) then it becomes around 46,000 μm^2. This is still slightly smaller than the average of 59,600 μm^2 received from the simulations and this difference might reflect the fact that there are more growth limiting factors present in the experiment than just oxygen. The average pellet perimeter of 1250 µm in the simulations is again close to the experimental median of 1670 µm.

Table 4.7: Comparison between the pellet measurements from the laboratory experiment and the model simulation at the end of the exponentially growing phase (31h after germination). The wet results are from SYTO9 died pellets (n=60). Five simulations were run with parameter values shown in Tables 3.2 and 3.3 and in Figure 3.14. The range shown is from minimum to maximum.

Measurement	**Laboratory experiments**	**Model simulations**
max pellet diameter (μm)	90 – 450	340 – 380
pellet area (μm^2)	250 – 90,000	55,200 – 62,800
pellet perimeter (μm)	260 – 3,600	1,140 – 1,350

In Figure 4.17 the simulation data of maximum pellet diameters during exponential growth are presented (using the parameters summarized in Tables 3.2 and 3.3 and in Figure 3.14). The different metabolic states of the hyphae are illustrated as blue for actively growing hyphae, cyan for antibiotic producing hyphae and black for hyphae with only maintenance requirements for oxygen. We find no dead hyphae present in this simulation. The diameters continue growing until the end of the exponentially growing phase (31 h after 6 h germination period). The appearance of a metabolic switch from actively growing to antibiotic producing hyphae starts at ca 15 h after germination, which is the time we observed the antibiotic production in the wet experiment (compare to Figure 4.7 and 4.8). Up until this time (15 h) the maximum pellet diameter increases at the same level in both simulation and in experiments. After the onset of RED production, the pellet growth slows down in experiments most likely due to the substrate (in this case phosphate) limitations. This cessation of pellet growth is not observed in the pellet simulation that might reflect the need for incorporating other growth limiting factors than just oxygen in to the model.

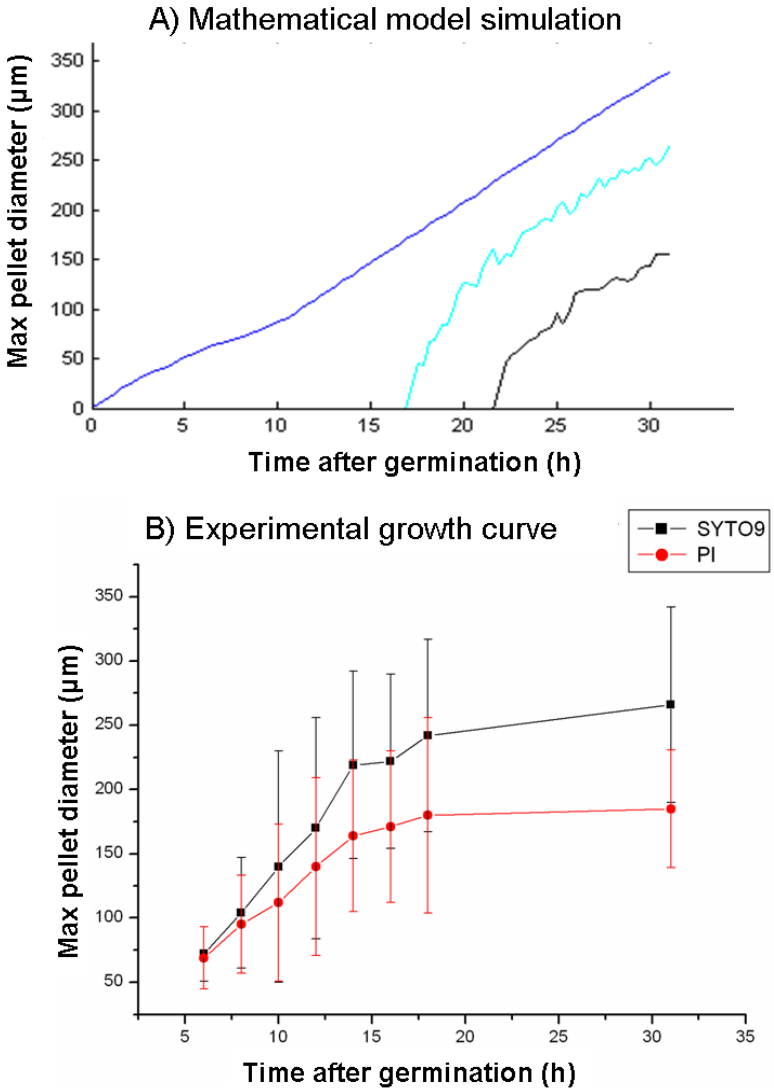

Figure 4.17: Simulation results of maximum pellet diameters compared to the corresponding experimental data. A. The metabolic states as included in the simulation: actively growing hyphae (dark blue), antibiotic producing hyphae (cyan) and maintenance requirements for oxygen only hyphae (black). Note that there are no dead hyphae found in this simulation. The parameters used are summarized in Tables 3.2 and 3.3 and in Figure 3.14. B. The average of the maximum pellet diameters (± standard deviation) in the growth curve experiment (see Table 4.2). The *Bac*Light™ live/dead staining illustrates the different metabolic states where SYTO9 corresponds to fully metabolically active hyphae (black squares) and PI represents hyphae with damaged membranes that are likely to be dead (red diamonds). The time excludes a 6 h germination period.

Summary and conclusions

The model was used to elucidate the effect that oxygen has on hyphal morphology and metabolism as a growth limiting substrate. Comparison of the model to the experimental data confirmed that the current model is a proof of concept of approach and even with a single substrate, gives a good comparison to the experimental data. The model accurately predicts the time of the appearance of antibiotic producing cells and the size dimensions of the pellet at the end of exponential growth. An interesting phenomenon is the lack of dead hyphae in the simulation. The live/dead staining experiment indicated the presence of hyphae that has a compromised cell wall and is therefore likely to be dead. However, it has previously been reported by Davey and Hexley (2010) that stressed *Saccharomyces cerevisiae* membranes are permeable to propidium iodide. Their studies indicate that, irrespective of the stress applied, around 7 % of the stressed cells that took up PI were able to repair their damaged membrane and remain viable. This raises an important question of what hyphal portion of the *Streptomyces* aggregate is still viable after being stained red with PI. If the answer is none, then it is likely that other growth limiting nutrients such as phosphorus, nitrogen and carbon, contribute to the observed cell death, and it is therefore important to include these nutrients in any future modelling approaches.

From the results presented in this study, it can be concluded that phosphorus has a major role over *Streptomyces* metabolism (Sola-Landa *et al*., 2003). The phosphorus exhaustion was observed at mid-log phase (around 20 - 22 h) and it coincided with the onset of antibiotic production and the start of the slower growth rate seen in the average pellet diameter. Voelker and Altaba (2001) discussed that under phosphate exhaustion the teichoic acids of the cell wall get broken down to recover phosphate from the cell wall to continue growth. It is evident from the literature that phosphate has control over primary and secondary metabolism. Stocks and Thomas (2001) reported that mid-growth phase and end-growth phase fragmentation is a common phenomenon in actinomycetes grown in both defined and complex media.

They studied the breaking force of hypha in both glucose and nitrogen-limited fermentations. Their data showed that once glucose got exhausted the culture entered the stationary phase. The strongest hyphae were observed at this stage. In nitrogen-limited fermentations, the growth continued after nitrate had been exhausted (at mid-log phase) although with a slower growth rate. The hyphal diameter and the breaking force of hypha decreased after mid-log phase. The nitrate-limited culture also entered the stationary phase once glucose was exhausted. Since phosphate has control over nitrogen and carbon metabolism and cell wall synthesis, it could be concluded for future modeling purposes that phosphate exhaustion results in alterations of the cell wall synthesis and ultimately a slower pellet extension rate. The mathematical model constructed in this thesis can serve as a basic model platform that can be updated as required. The addition of multiple substrates to this model platform is straightforward and a feasible way forward for further modeling studies of *Streptomyces*.

Chapter 5: Model analysis with enhanced green fluorescent protein

The model developed in Chapter 4 predicts the location of antibiotic producing cells and maintenance energy requiring only cells within the framework of a pellet. If the simulations of the model are taken and compared to laboratory experiments, such as in Figure 5.1, a good correlation can be seen with the predictions. A phase-contrast (A) and fluorescence (B) images of a pellet is compared to model simulations (C and D) of pellet at the end of the exponentially growing phase. In model simulation C, the green colour corresponds to live cells and red colour illustrates the cells surrounded by less than ca 50 % of the external oxygen present at the start of the incubation. In D, the different metabolic states of hyphae are shown as actively growing hyphae (blue), antibiotic producing hyphae (cyan) and maintenance energy-only demanding cells hyphae (black) where oxygen is the limiting substrate. Simulation predicts that the antibiotics are produced at pellet periphery just within the perimeter of the pellet. The core of the pellet is predicted to contain maintenance energy-only demanding cells and no dead cells.

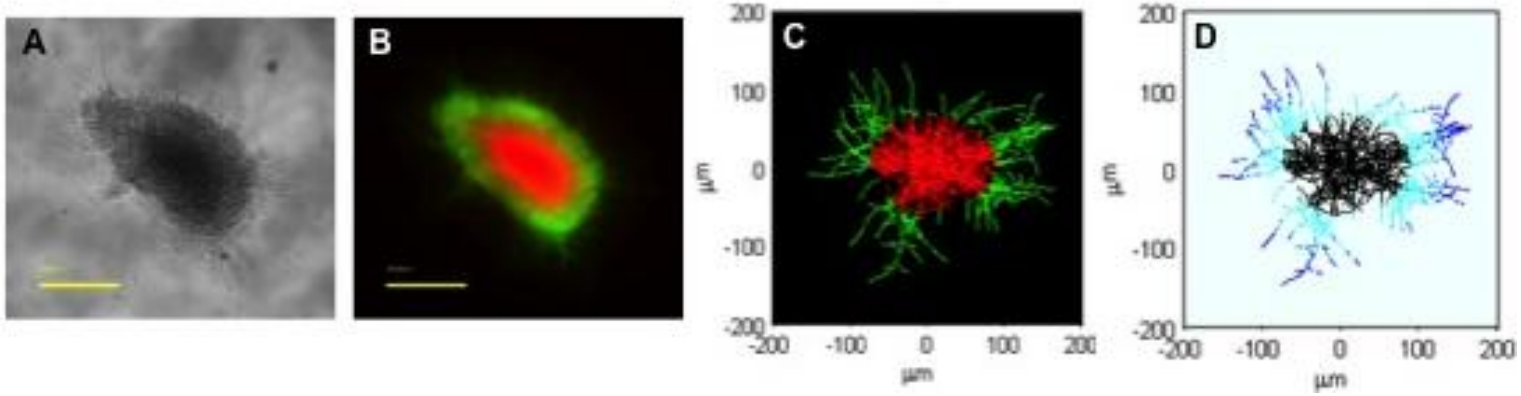

Figure 5.1: Microscopy images of Streptomyces coelicolor pellet (A, B) compared to model simulations (C, D). A. Phase-contrast image of a pellet at the end of exponential growth phase. B. Fluorescence image of the pellet using green SYTO9 (live cells) and red propidium iodide (likely dead cells) nucleic acid stains. C. Model simulation of a live/dead pellet at the end of the exponentially growing phase. Green colour corresponds to live cells and red colour illustrates the cells surrounded by less than ca 50 % of the external oxygen present at the start of the incubation. D. Different metabolic states of hyphae within a pellet at the end of the exponentially growing phase predicted by the computational model. Blue colour at the outskirts of the pellet marks the actively growing hyphae. Cyan colour corresponds to hyphae producing antibiotics. Black colour, at the core of the pellet, illustrates metabolically inactive hyphae with only maintenance demands for oxygen.

To test the model prediction of the metabolic states within the pellet, we constructed three *S. coelicolor* strains each carrying an enhanced green fluorescence protein (eGFP) gene in their genomes to elucidate the spatio-temporal localization of key metabolic proteins. Translational fusions of eGFP were made to isocitrate dehydrogenase (*idh*), to phosphate binding protein precursor (*pstS*) and to RNA-polymerase beta'-subunit (*rpoC*). A short description of the rational for choosing each of the three proteins is given below.

Isocitrate dehydrogenase is involved in Tricarboxylic acid (TCA) cycle, where it catalyzes the oxidative decarboxylation of isocitrate producing α-ketoglutarate and CO_2 while converting $NADP^+$ to NADPH (or NAD^+ to NADH) (Zhang *et al*., 2013). Idh in *Streptomyces coelicolor* is a monomeric protein with a molecular weight of around 80 kDa. It shares only a very distant sequence similarity with the dimeric Idh from *E. coli*. The TCA cycle provides the cells with energy and biosynthetic precursors for cell growth. Under certain growth conditions the carbon flow is directed to the glyoxylate bypass, growing anapleurotically, by-passing the TCA cycle in order to efficiently supply precursors for gluconeogenesis and more importantly in this case, the synthesis of polyketide antibiotics such as actinorhodin (Taylor, 1992). Recent proteomic studies of *S. coelicolor* suggest that Idh is one of the most abundant central carbon metabolic enzymes during exponential growth (Thomas et al., 2012). Therefore, as Idh-eGFP is involved in the TCA-cycle it is a good indicator for primary metabolic activity.

Phosphate binding protein precursor *pstS*, a gene that is part of the high-affinity phosphate transport system PstSCAB in *Streptomyces*. The promoter of *pstS* is repressed by high phosphate concentration. During promoter activity studies with *S. coelicolor*, the expression of *pst*S increased after 24 h incubation of pregerminated spores and reached to its maximum at 36 h (Sola-Landa *et al*., 2005). The protein, PstS, is a native glycoprotein of molecular weight of ca 40 kDa (Wehmeier *et al*., 2009).High level of

phosphate within culture is known to repress the PhoP-PhoR regulon, which includes pstS and also respresses antibiotic synthesis (Sola-Landa *et al*., 2005: Bibb 2005). Such that under phosphate limitation, PhoP-PhoR activate the pho regulon, including *pstS*. Therefore PstS-eGFP would make a useful reporter for activation of the pho regulon and the activation of antibiotic biosynthesis.

RNA-polymerase beta'-subunit, *rpoC*, is one the five different subunits (β, β', α, ω and σ present in two copies) of RNA polymerase in *Bacteria*. The RNA-polymerase holoenzyme (RNAP binds together with the sigma factor, recognizes the promoter site and initiates transcription (Browning and Busby, 2004; Madigan *et al*., 2012). RNAP tagged with eGFP therefore represents transcriptionally active cells and can act as a reporter for the spatial and temporal dynamics of transcription. The localization of RpoC-eGFP can therefore represent sites of transcriptional activity as discrete foci or RNAP unbound to DNA as more disperse fluorescence.

Genome organization of the genes of interest

The positions of i*dh*, *pstS* and *rpoC* in *S.coelicolor* genome are shown in Figure 5.2 as annotated on the StrepDB database (Bentley *et al*., 2002; Bishop *et al*., 2004). Isocitrate dehydrogenase gene (*idh*) is located near the right end of the linear genome at start position of 7771060 and it is adjacent to genes SCO6999, a hypothetical protein, and SCO7001, a putative integral membrane protein. The gene *pstS* codes for phosphate binding protein precursor and it is located at the middle of the *S. coelicolor* genome at start position of 4556707. The adjacent genes to *pstS* are SCO4141, a phosphate ABC transport system permease protein, and SCO4143, putative mutT-like protein. The third gene of interest, *rpoC*, codes for DNA-directed RNA-polymerase beta' chain. The start position of rpoC is 5081644 and it is adjacent to genes SCO4654 and SCO4656, DNA-directed RNA polymerase beta chain and putative integral membrane protein respectively. The predicted length of the proteins are 739 aa for Idh, 370 aa for PstS and 1299 aa for RpoC.

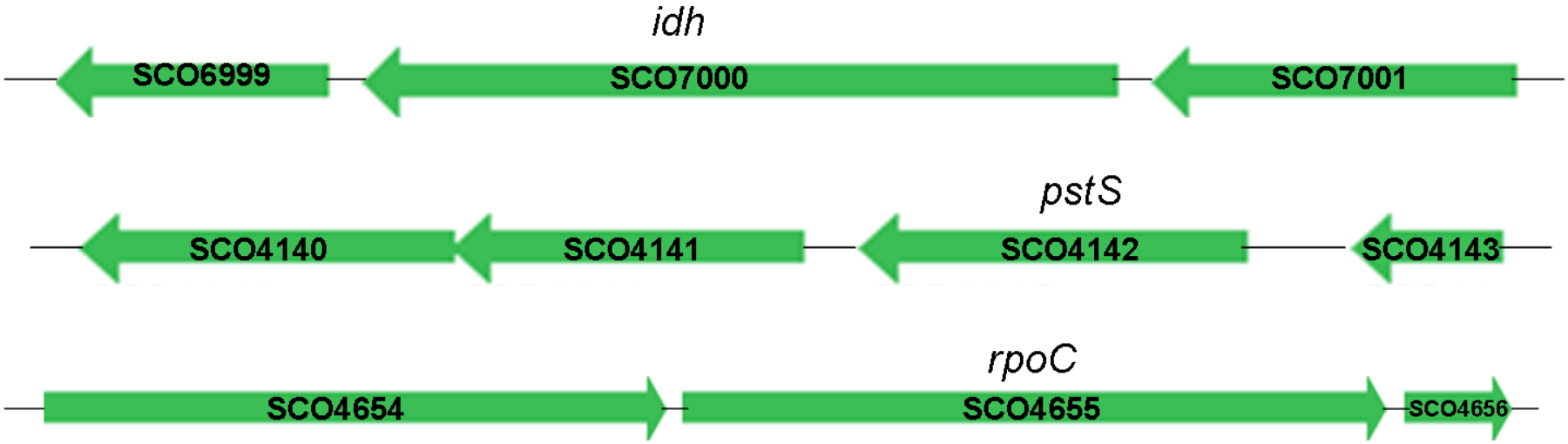

Figure 5.2: The genomic orientation of the genes *idh* (SCO7000), *pstS* (SCO4142) and *rpoC* (SCO4655). Gene annotation and modified image as per StrepDB database (Bentley *et al*., 2002).

eGFP tagging of the genes of interest using the redirect cassette, pIJ786

Due to the complexities of *Streptomyces* genetics, it is standard to make all genetic manipulations in *Escherichia coli*, and then conjugate the constructs in to Streptomyces. The eGFP fusions in this study were created using the ReDirect procedure of Gust *et al*., (2003). The template plasmid pIJ786, containing the gene encoding eGFP along with an apramycin resistance marker, was used as a PCR template for creating the eGFP fusions. The plasmid was cut with restriction enzymes HindIII and EcoRI and the resulting fragment of 2144 bp which was purified using appropriate gel purification kit according to manufacture's instructions (see Figure 5.3 for in silico illustration). The gene fragment was PCR-amplified using appropriate long primers and PCR-conditions listed in Materials and Methods Table 2.6 and 2.7. Gel purified PCR-product was then used to transform *E.coli* BW25113/pIJ790 harboring the cosmid of interest.

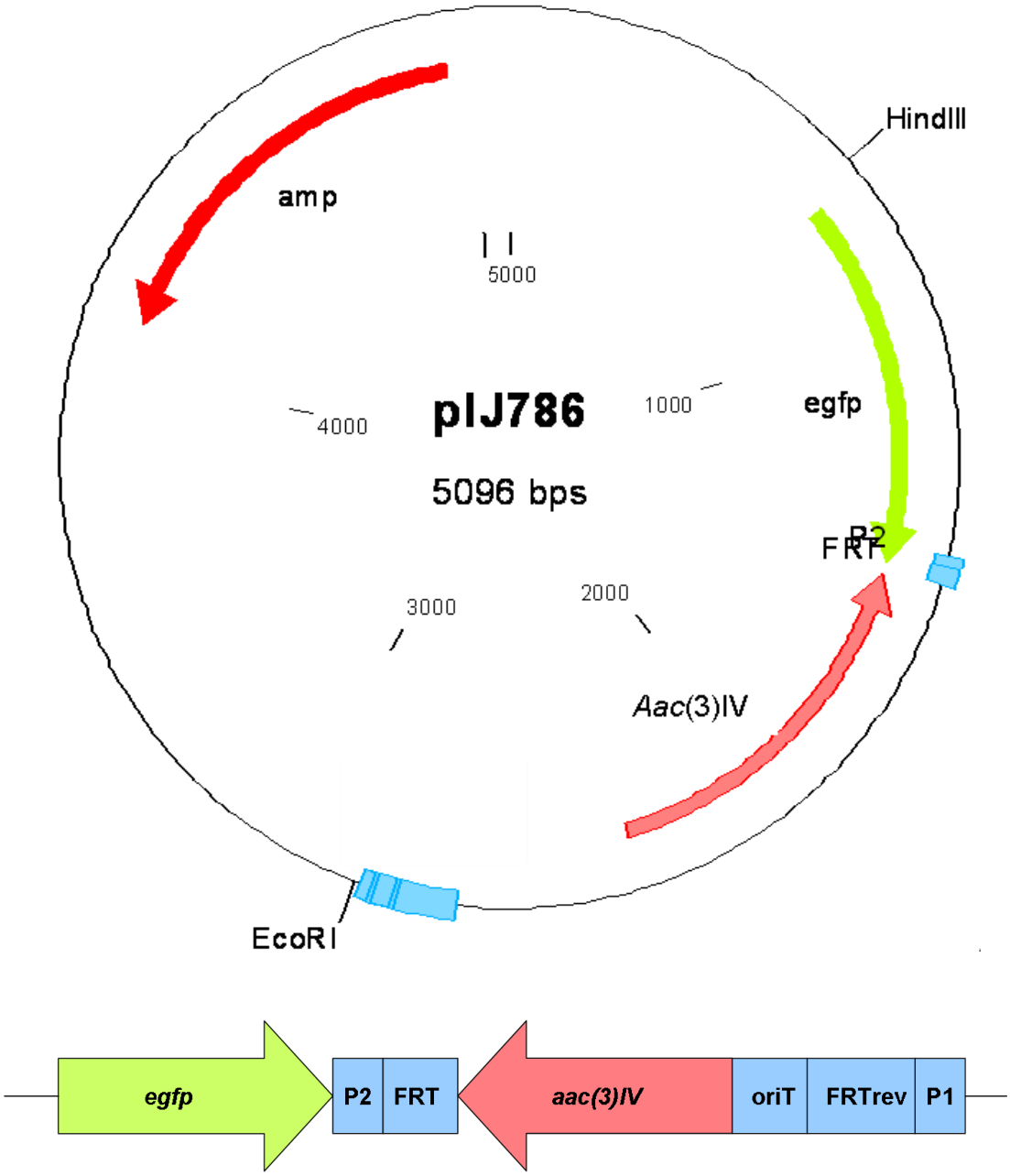

Figure 5.3: Map of plasmid pIJ786 (5096 bp). Genes of interest are illustrated as enhanced green fluorescence protein (*egfp*; green), apramycin resistance gene (*aac*(3)IV; light red) and ampicillin resistance gene (*amp*; dark red). A fragment (2144 bp) cut with restriction enzymes *Hind*III and *Eco*RI is illustrated below and it includes RK2 origin of transfer (OriT), left and right priming sites (P1 and P2), FLP binding sites (FRT and FRTrev) for FLP-mediated excision of insertion cassette (not used in this study).

Long primer design

Two long primers for each eGFP-fusions were designed according to Gust *et al*. (2002) with a linker sequence in forward primer. The forward primer (59 nt) consisted of 39 nt sequence matching the coding strand at the end of the gene of interest. The stop codon was changed from TGA to TGG. Ten amino acid linker sequence (CTG CCG GGC CCG GAG CTG CCG GGC CCG GAG) was placed between the gene of interest and the eGFP cassette to maximise the likelihood that the fused eGFP would be functional (Jakimowicz *et al*., 2005). After the linker, the forward primer finished with 20 nt long sequence matching the start of the eGFP cassette (from pIJ786) with respect to the correct reading frame of the gene of interest. Reverse primer (58 nt) had 39 nt matching the *S.coelicolor* complementary strand adjacent to the gene of interest and 19 nt matching the end of the priming site 1 (P1) on the eGFP cassette (from pIJ786).

Cosmid construction and verification and screening for double-crossovers

Wild-type cosmids containing the genes of interest were received from the *S.coelicolor* cosmid library at the University of Swansea (Redenbach *et al*., 1996). The wild-type cosmids C8F11, D40A and SCD84 were transformed into BW25113/pIJ790. Transformation with the linear PCR-amplified eGFP cassette with flanking regions to the gene of interest and BW25113/pIJ790/wild-type cosmid was performed according to the protocol of Gust *et al*., 2002. The resulting cosmid constructs were isolated using standard DNA isolation kit and the cosmid constructs were transformed into DH5α before isolating the cosmid DNA again and verifying to correct cosmid construction using restriction enzyme digests. The cosmid constructs were transformed into ET12567/pUZ8002 that was then used in intergenic conjugation of the construct cosmid from *E. coli* to *Streptomyces*. The resulting primary exconjugant colonies were screened for double crossovers (apramycin resistant, kanamycin sensitive). Finally, spore stocks were prepared and genomic DNA was isolated from the putative double crossover isolates LN108 (*idh-eGFP*), LN205 (*pstS-eGFP*) and LN301 (*rpoC-eGFP*).

In silico maps of the supercos-1 backbone and the *S. coelicolor* genomic insertion were created using CloneManager program. The virtual cosmids were then used to select the appropriate restriction enzymes for digestions and to predict the band sizes to be detected in wild-type and eGFP-insertion cosmids. The predicted fragment sizes to confirm the correct orientation of the wild-type cosmids and the successful insertion of eGFP-cassette into the relevant cosmid are shown in Figures 5.5, 5.9 and 5.12. All cosmid constructs successfully integrated the eGFP-cassette. Virtual cosmid maps were also used for the prediction of band sizes to be detected in wild-type and eGFP-fused strains. The predicted band sizes and the restriction enzyme digests showing the diagnostic bands for the eGFP-fusion are also shown in Figures 5.5, 5.9 and 5.12. All three *Streptomyces* strains LN108 (idh), LN205 (pstS) and LN301 (rpoC) were confirmed to contain the eGFP-fusion. Note that there was an extra band of around 8 kb present in all *Xho*I

digests. Further analysis was carried using *Xho*I to digest pIJ786 (ca 5 kb). Figure 5.6 confirms that the ca 8 kb band is a contamination of the *Xho*I restriction enzyme stock since the contamination band is present in both the digest of pIJ786 and in the negative control containing only the mastermix and the restriction enzyme.

Whole cosmids pLN108, pLN205 and pLN301, containing the eGFP insertion, were labelled with digoxigenin (DIG) and used as a probe in Southern blot analysis. With this approach, the specific site of the eGFP-fusion could be confirmed and the separate strains could be differentiated by the band pattern observed on each blot. Southern blots shown in Figures 5.7, 5.10 and 5.13 confirmed the successful eGFP-fusions to the genes *idh*, *pstS* and *rpoC* in strains LN108, LN205 and LN301 respectively. The highlighted bands are diagnostic to the eGFP-insertion in the expected region. Note that an extra band of around 9 kb was present in genomic DNA of both LN108 and M145 but not in the corresponding cosmid DNA (see Figure 5.7). This 9 kb band was most likely a result of unspecific binding. There was also unspecific binding of the whole cosmid probe to the 1 kb DNA ladder. An extra band of ca 6 kb was seen in LN205 genomic DNA in Figure 5.10 where it was most likely the uncut fragment of 4.5 kb and 1.8 kb fragments together. In Figure 5.13, the fragments of 0.9 kb, 0.9 kb, 2.3 kb and part of the 3.9 kb band were specific to the supercos-1 backbone and therefore were not present in the genomic DNA. The fragments of 6.6 kb, 13.2 kb, >2.0 (part of the 3.9 kb) and >19.4 kb (part of the 19.4 kb) were present in the wild-type M145 genomic DNA as expected. In LN301 genomic DNA there were additional two bands of 5.1 kb and >6.6 kb. The 5.1 kb fragment is diagnostic for the *rpoC-eGFP* fusion.

Finally, the successful eGFP-insertions were also confirmed by PCR-amplifying the region containing the end of the gene of interest and the start of the eGFP-insertion. The used primers were eGFP/rpoB linkF and eGFP/rpoB link R (*rpoC-eGFP*), Idh-egfp check and eGFP/rpoB linkF (*idh*-

eGFP), and pstS internalLN together with eGFP/rpoB linkF (*pstS-eGFP*). The resulting PCR-products were then sequenced at GATC Biotech (UK) and the sequences aligned against the virtual sequence of cosmids LN108, LN205 and LN301 using Clustal Omega version 1.1.0 (Sievers *et al*., 2011). Figures 5.8, 5.11 and 5.14 show the sequence alignments for LN108, LN205 and LN301 respectively. The sequences amplified from the *Streptomyces* strains LN108, LN205 and LN301 were all identical to their virtual sequence counterparts.

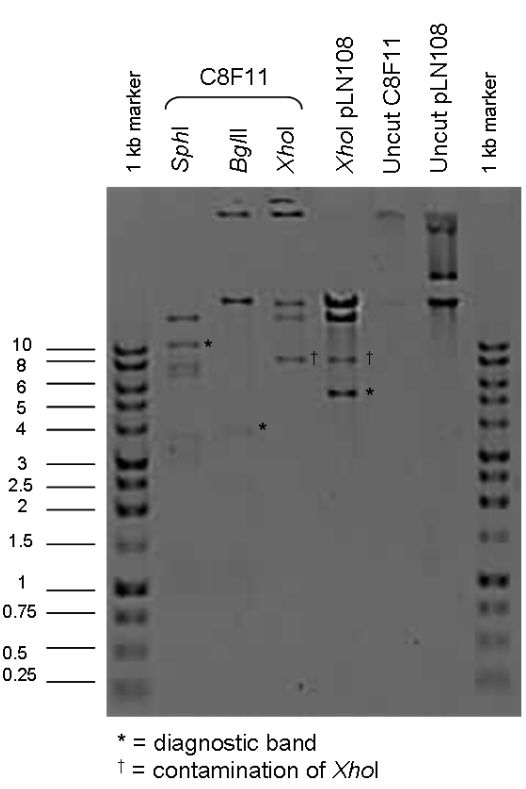

	C8F11 orientation A (bp)	C8F11 orientation B (bp)	pLN108 (bp)
*Sph*I	16211	16211	
	8843	**9771**	
	8049	7121	
	6404	6404	
	3387	3387	
	3003	3003	
	2797	2797	
	1280	1280	
	1135	1135	
	1085	1085	
	471	471	
	243	243	
	72	72	
	39	39	
*Bgl*II	45515	47210	
	5308	**3613**	
	2196	2196	
*Xho*I		35893	32846
		16527	16527
		-	**5173**
		599	599

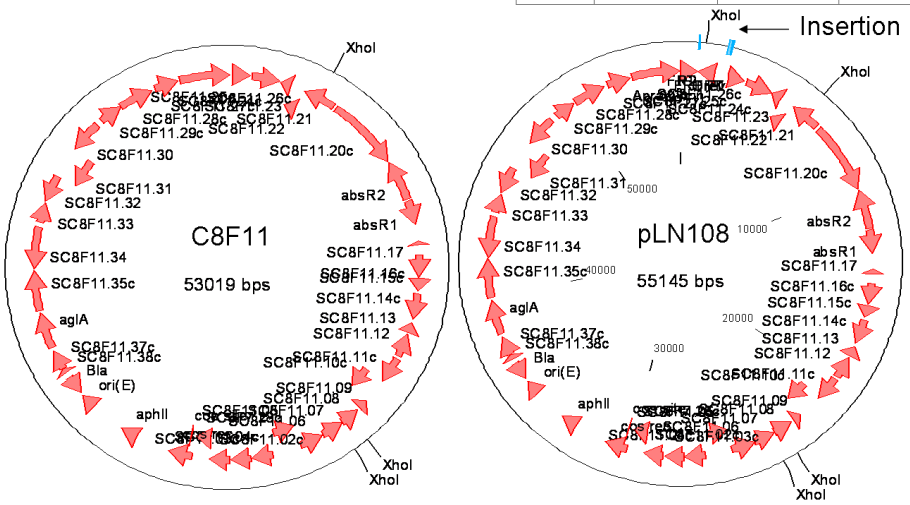

Figure 5.5: Restriction enzyme digest of cosmid DNA identifying the in silico orientation of supercos backbone in C8F11 (*Sph*I and *Bgl*II digests) and showing the successful insertion of eGFP-cassette in pLN108 (*Xho*I digest). Gel: 0.8% agarose, 80 V. Expected fragment sizes (bp) are shown on the right hand side (diagnostic fragments in bold). Note: *Xho*I digests had contamination band at ca 8 kb (see Figure 5.6). The cosmid maps of wild-type C8F11 and *idh-egfp* fusion pLN108 cosmids are shown at the bottom.

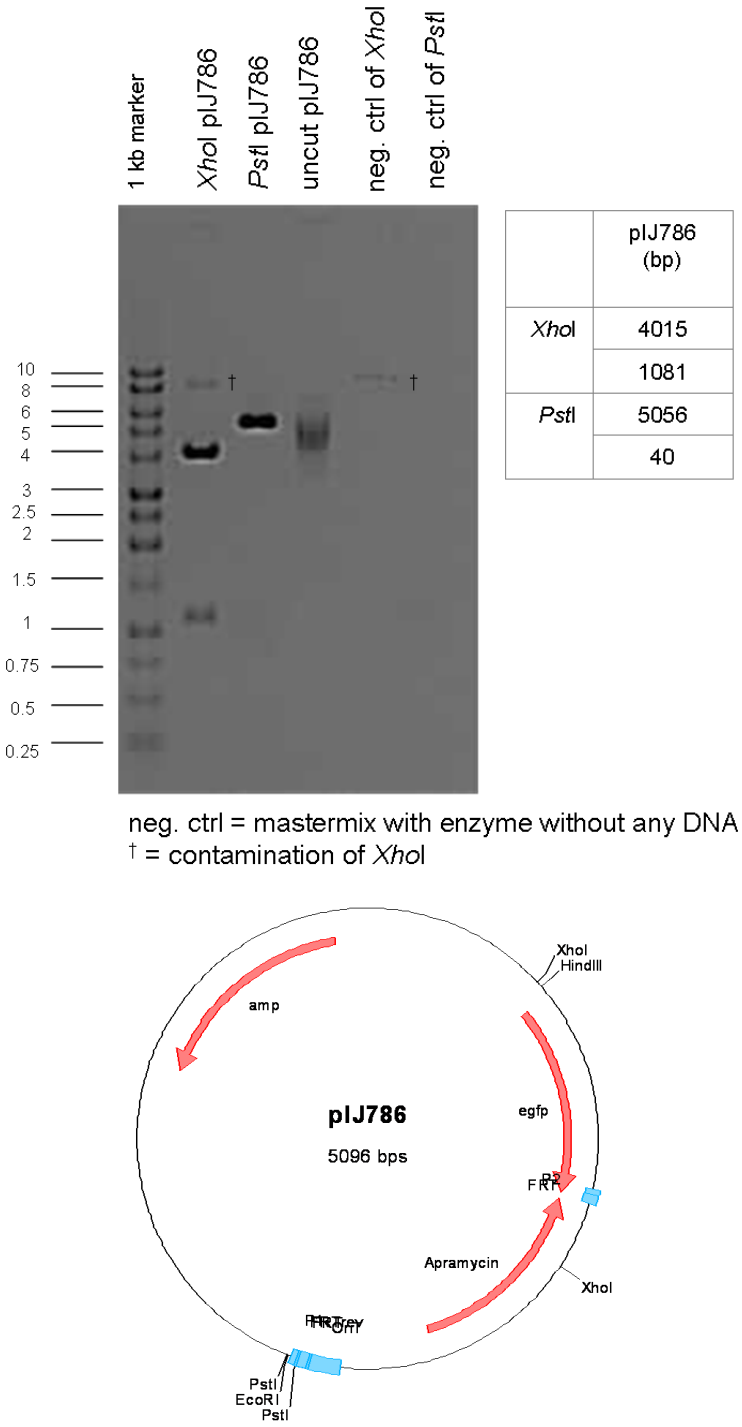

Figure 5.6: The restriction digest of pIJ786 illustrating the contamination of *Xho*I enzyme. Expected fragment sizes (bp) for *Xho*I and *Pst*I digests of pIJ786 and the cosmid map of pIJ786 are shown. Mastermix together with the enzyme, with no added DNA, was used as negative controls. The contamination band of ca 8 kb is present in both the *Xho*I digest and in *Xho*I negative control.

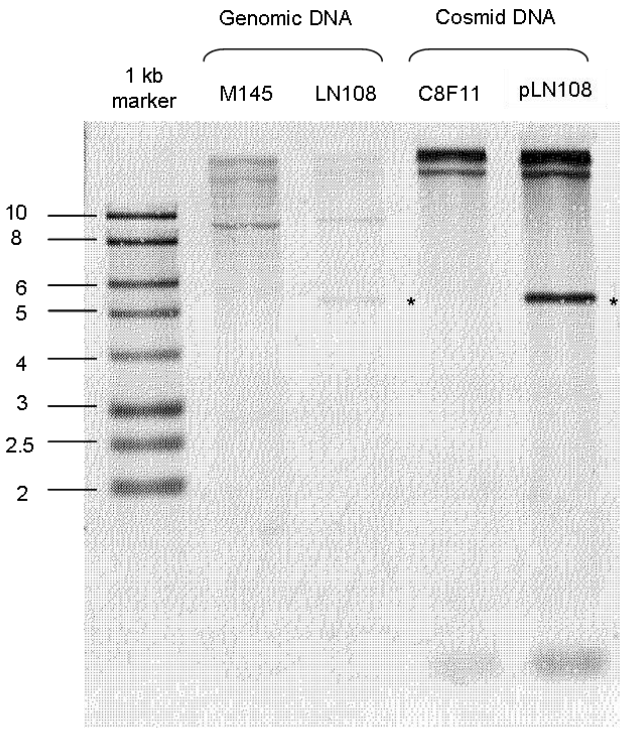

	C8F11 orientation B (bp)	pLN108 (bp)
*Xho*I	35893	32846
	16527	16527
	-	**5173**
	599	599

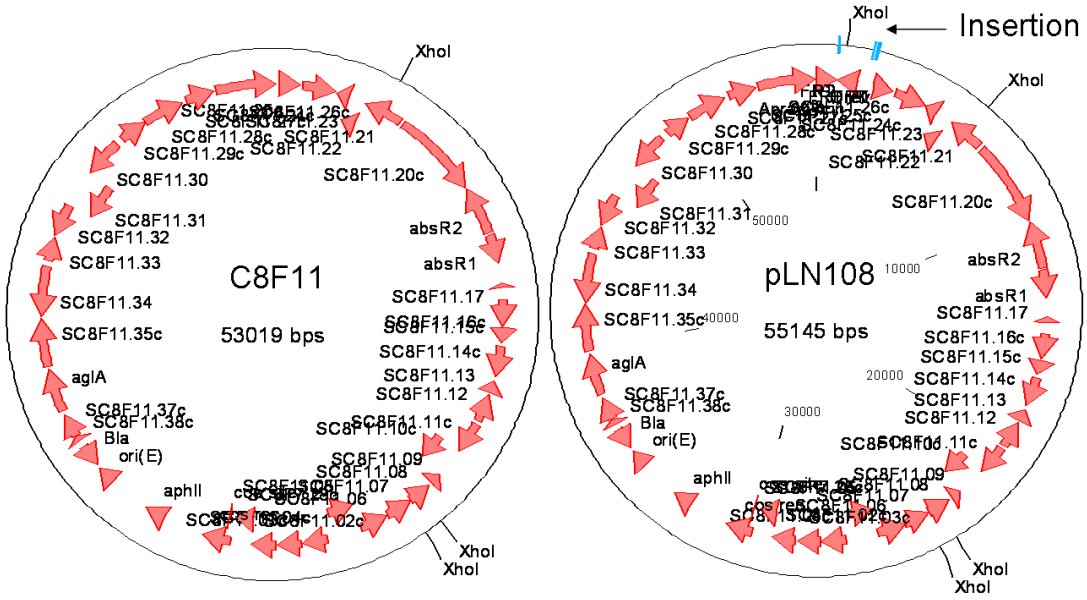

Figure 5.7: Southern blot analysis of genomic fusion of eGFP to isocitrate dehydrogenase (*idh*). Band sizes (bp) for *Xho*I digests of C8F11 and pLN108 are shown on right. The band size diagnostic for eGFP-insertion is shown in bold. The wild-type C8F11 and *idh-egfp* fusion pLN108 cosmid maps are shown at the bottom.

Figure 5.8: Sequence alignment of virtual cosmid pLN108 and sequenced PCR-product of LN108 strain to confirm successful eGFP-fusion to isocitrate dehydrogenase (*idh*). The virtual sequence shows the end of the gene *idh* (blue), ten amino acid linker sequence (orange), the start of eGFP (green) and the two primer binding sites for primers Idh-egfp check and eGFP/rpoB linkF (pink). The alignment was done using Clustal Omega version 1.1.0 (Sievers *et al*., 2011).

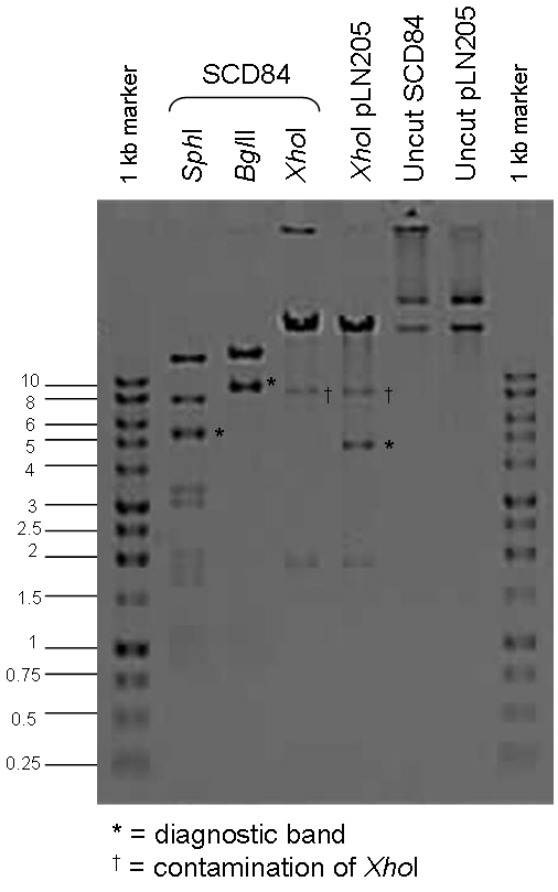

	SCD84 orientation A (bp)	SCD84 orientation B (bp)	pLN205 (bp)
*Sph*I	15025	13303	
	7350	7350	
	5004	**5316**	
	3594	5004	
	3190	3190	
	2900	2900	
	1981	1981	
	1761	1761	
	1636	1636	
	1085	1085	
	897	897	
	849	849	
	72	72	
*Bgl*II	13765	14593	
	12898	13765	
	10008	8673	
	8673	**8313**	
*Xho*I		43529	41187
		-	**4468**
		1815	1815

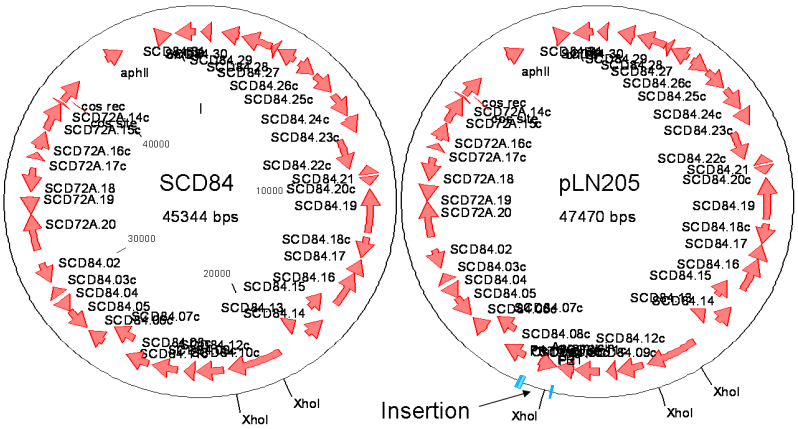

Figure 5.9: Restriction digests of cosmid DNA identifying the in silico orientation of supercos backbone (*Sph*I and *Bgl*II digests) in wild-type SCD84 and the confirmation of successful insertion of eGFP-cassette to gene *pstS* in pLN205 (*Xho*I digests). Gel: 0.8% agarose, 80 V. Expected fragment sizes (bp) are shown on the right hand side where the diagnostics bands are highlighted in bold. Note: see Figure 5.6 for explanation on the contamination band seen in *Xho*I at ca 8 kb. The cosmid maps are shown at the bottom.

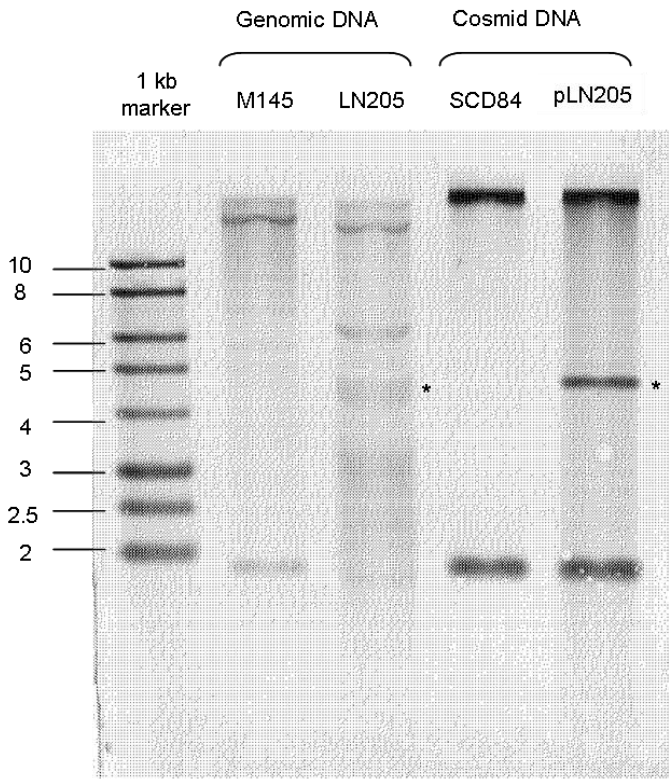

	SCD84 orientation B (bp)	pLN205 (bp)
*Xho*I	43529	41187
	-	**4468**
	1815	1815

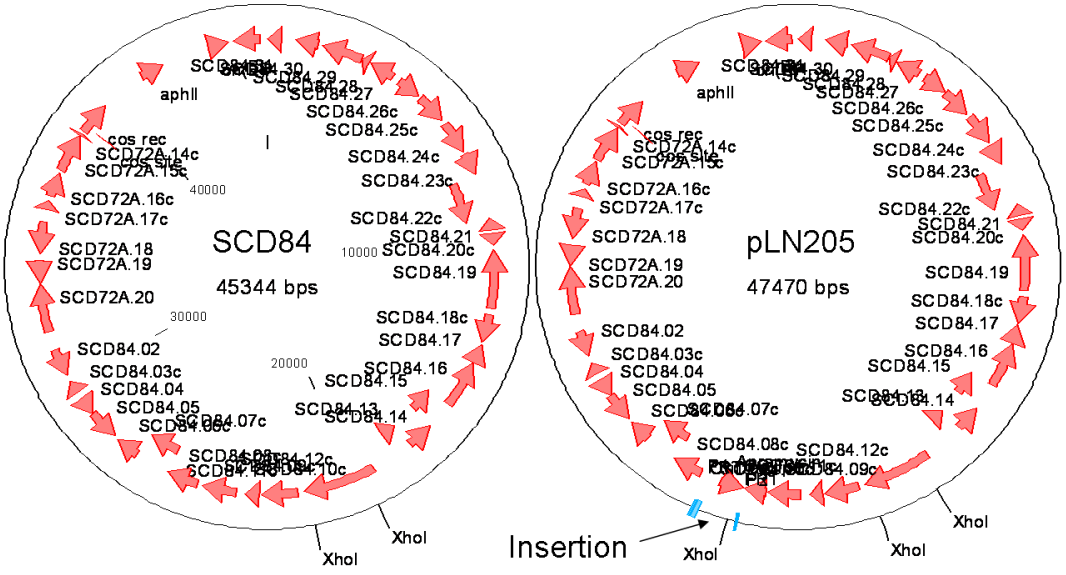

Figure 5.10: Southern blot analysis of eGFP fusion to phosphate binding protein precursor (*pstS*) in LN205 strain compared to wild-type M145 strain. Band sizes (bp) for *Xho*I digests of wild-type cosmid SCD84 and cosmid harbouring *pstS-egfp*-fusion pLN205 are shown at right hand side. The diagnostic fragment size for eGFP-insertion is shown in bold. The cosmid maps showing the *Xho*I cutting sites are shown at the bottom.

```
virtual_pLN205          CCGGACGCCGCCGGCGCCTACCCGCTGGTCCTGGTGACGTACGAGATCGCCTGCGACAAG
LN205                   ------------------------------------------------------------

virtual_pLN205          GGCAACAAGGCGGACACCCTGCCCGCCACCAAGTCCTTCCTGAACTACATGGCCTCGGAG
LN205                   -----------------------------------AGTCTTCTGNVTNCTGGCCTCGGAG
                                                           . ** * :. .: .**********

virtual_pLN205          GACGGCCAGGGCCTGCTGGCGGACGCCGGCTACGCCCCGATGCCCACCGAGATCATCACC
LN205                   GANGGCCAGGGCCTGCTGGCGGACGCCGGCTACGCCCCGATGCCCACCGAGATCATCACC
                        ** ************************************************************

virtual_pLN205          AAGGTCCGCGAGACCATCTCGGGCCTGAGCTGGCTGCCGGGCCCGGAGCTGCCGGGCCCG
LN205                   AAGGTCCGCGAGACCATCTCGGGCCTGAGCTGGCTGCCGGGCCCGGAGCTGCCGGGCCCG
                        ************************************************************

virtual_pLN205          GAGGTGAGCAAGGGCGAGGAGCTGTTCACCGGGGTGGTGCCCATCCTGGTCGAGCTGGAC
LN205                   GAGGTGAGCAAGGGCGAGGAGCTGTTCACCGGGGTGGTGCCCATCCTGGTCGAGCTGGAC
                        ************************************************************

virtual_pLN205          GGCGACGTAAACGGCCACAAGTTCAGCGTGTCCGGCGAGGGCGAGGGCGATGCCACCTAC
LN205                   GGCGACGTAAACGGCCACAAGTTCAGCGTGTCCGGCGAGGGCGAGGGCGATGCCACCTAC
                        ************************************************************

virtual_pLN205          GGCAAGCTGACCCTGAAGTTCATCTGCACCACCGGCAAGCTGCCCGTGCCCTGGCCCACC
LN205                   GGCAAGCTGACCCTGAAGTTCATCTGCACCACCGGCAAGCTGCCCGTGCCCTGGCCCACC
                        ************************************************************

virtual_pLN205          CTCGTGACCACCCTGACCTACGGCGTGCAGTGCTTCAGCCGCTACCCCGACCACATGAAG
LN205                   CTCGTGACCACCCTGACCTACGGCGTGCAGTGCTTCAGCCGCTACCCCGACCACATGAAG
                        ************************************************************

virtual_pLN205          CAGCACGACTTCTTCAAGTCCGCCATGCCCGAAGGCTACGTCCAGGAGCGCACCATCTTC
LN205                   CAGCACGACTTCTTCAAGTCCGCCATGCCCGAAGGCTACGTCCAGGAGCGCACCATCTTC
                        ************************************************************

virtual_pLN205          TTCAAGGACGACGGCAACTACAAGACCCGCGCCGAGGTGAAGTTCGAGGGCGACACCCTG
LN205                   TTCAAGGACGACGGCAACTACAAGACCCGCGCCGAGGTGAAGTTCGAGGGCGACACCCTG
                        ************************************************************

virtual_pLN205          GTGAACCGCATCGAGCTGAAGGGCATCGACTTCAAGGAGGACGGCAACATCCTGGGGCAC
LN205                   GTGAACCGCATCGAGCTGAAGGGCATCGACTTCAAGGAGGACGGCAACATCCTGGGGCAC
                        ************************************************************

virtual_pLN205          AAGCTGGAGTACAACTACAACAGCCACAACGTCTATATCATGGCCGACAAGCAGAAGAAC
LN205                   AAGCTGGAGTACAACTACAACAGCCACAACGTCTATATCATGGCCGACAAGCAGAAGAAC
                        ************************************************************

virtual_pLN205          GGCATCAAGGTGAACTTCAAGATCCGCCACAACATCGAGGACGGCAGCGTGCAGCTCGCC
LN205                   GGCATCAAGGTGAACTTCAAGATCCGCCACAACATCGAGGACGGCAGCGTGCAGCTCGCC
                        ************************************************************

virtual_pLN205          GACCACTACCAGCAGAACACCCCCATCGGCGACGGCCCCGTGCTGCTGCCCGACAACCAC
LN205                   GACCACTACCAGCAGAACACCCCCATCGGCGACGGCCCCGTGCTGCTGCCC---------
                        **************************************************
```

Figure 5.11: Confirmation of successful eGFP-fusion by sequence alignment of virtual cosmid harbouring *pstS-egfp*-fusion, pLN205, and sequenced PCR-product of LN205 strain. The virtual sequence illustrates the end of the phosphate binding protein precursor gene, *pstS* (blue), ten amino acid linker sequence (orange), the start of eGFP (green) and the two primer binding sites for primers pstS internalLN and eGFP/rpoB linkF (pink). Clustal Omega version 1.1.0 (Sievers *et al*., 2011) was used to perform the alignment.

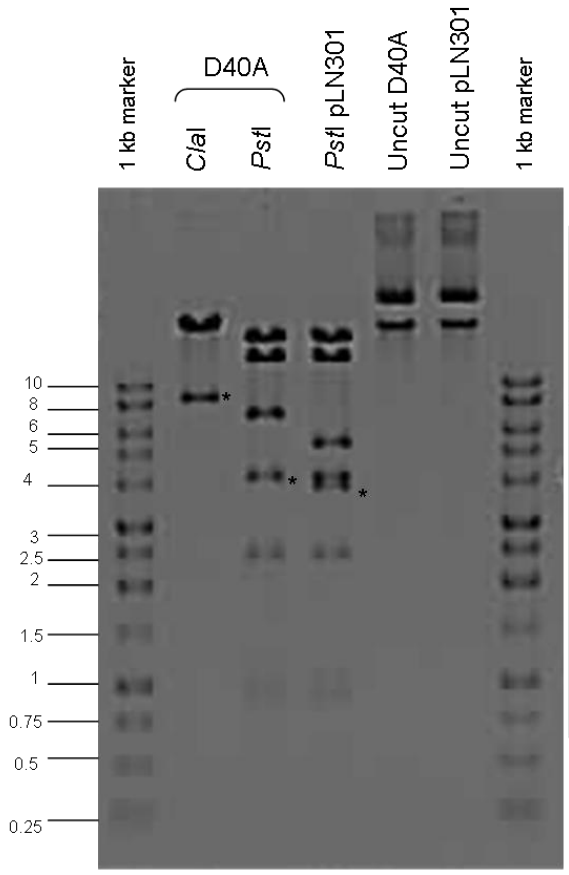

	D40A orientation A (bp)	D40A orientation B (bp)	pLN301 (bp)
*Cla*I	32572	39313	
	14710	**7969**	
*Pst*I	20528	19401	19401
	13160	13160	13160
	6615	6615	**5095**
	2815	**3942**	3942
	-	-	**3645**
	2357	2357	2357
	923	923	923
	884	884	884

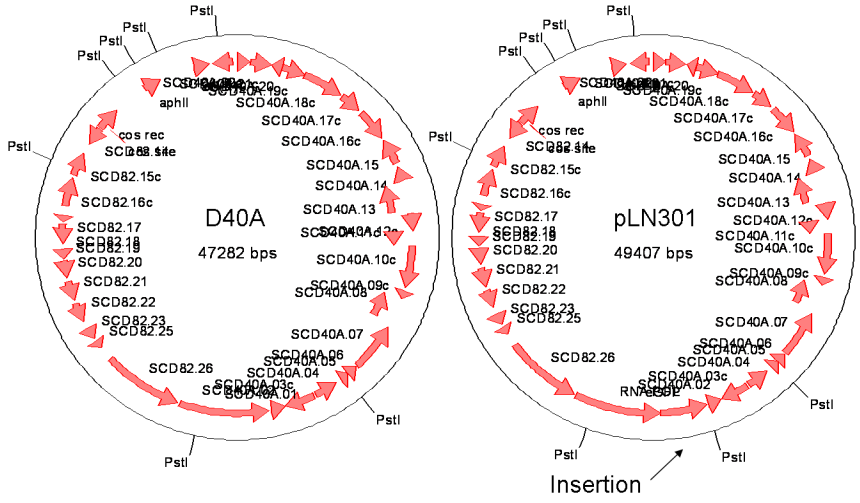

Figure 5.12: Restriction digest of cosmid DNA determining the orientation of supercos backbone in wild-type cosmid D40A (*Cla*I and *Pst*I digests) and showing the insertion of eGFP-cassette to RNA-polymerase beta' subunit, *rpoC*, in pLN301 (*Pst*I digest). Gel: 0.8% agarose, 80 V. Expected band sizes (bp) for digests are shown on the right hand side (diagnostic bands in bold). The virtual cosmid maps are shown at the bottom.

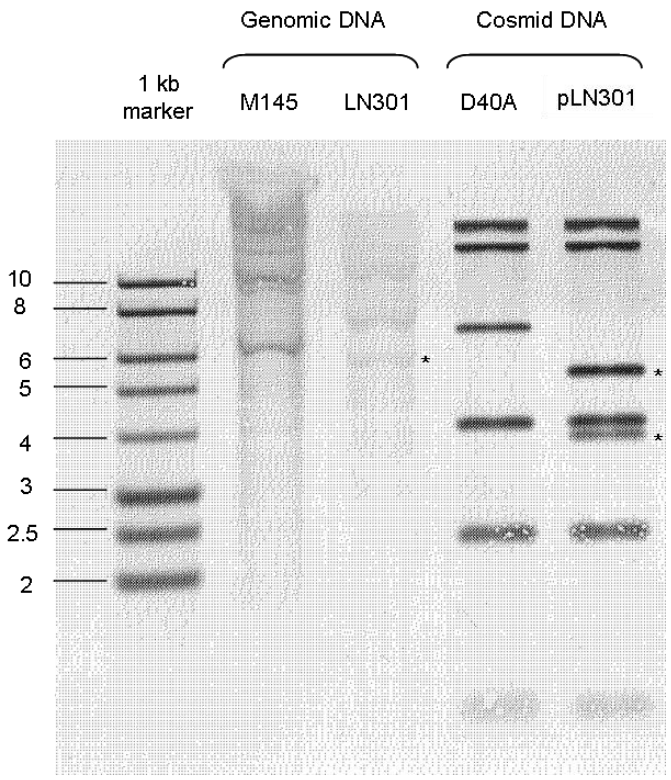

	D40A orientation B (bp)	pLN301 (bp)
*Pst*I	19401	19401
	13160	13160
	6615	**5095**
	3942†	3942†
	-	**3645**
	2357†	2357†
	923†	923†
	884†	884†

* = diagnostic band

† = band specific to supercos-1 backbone

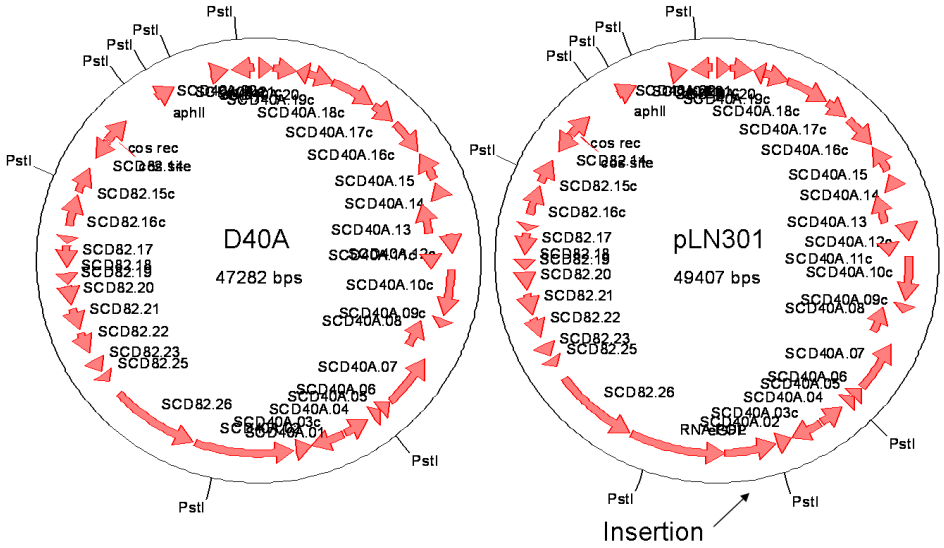

Figure 5.13: Southern blot analysis of eGFP fusion to RNA-polymerase beta' subunit, *rpoC,* in LN301 strain compared to wild-type M145 strain. Band sizes (bp) for *Pst*I digests of wild-type cosmid D40A and cosmid harbouring *rpoC-egfp*-fusion pLN301 are shown on right where the diagnostic fragment size for eGFP-insertion is shown in bold. The virtual cosmid maps illustrating the cutting sites of *Pst*I restriction enzyme are shown at the bottom

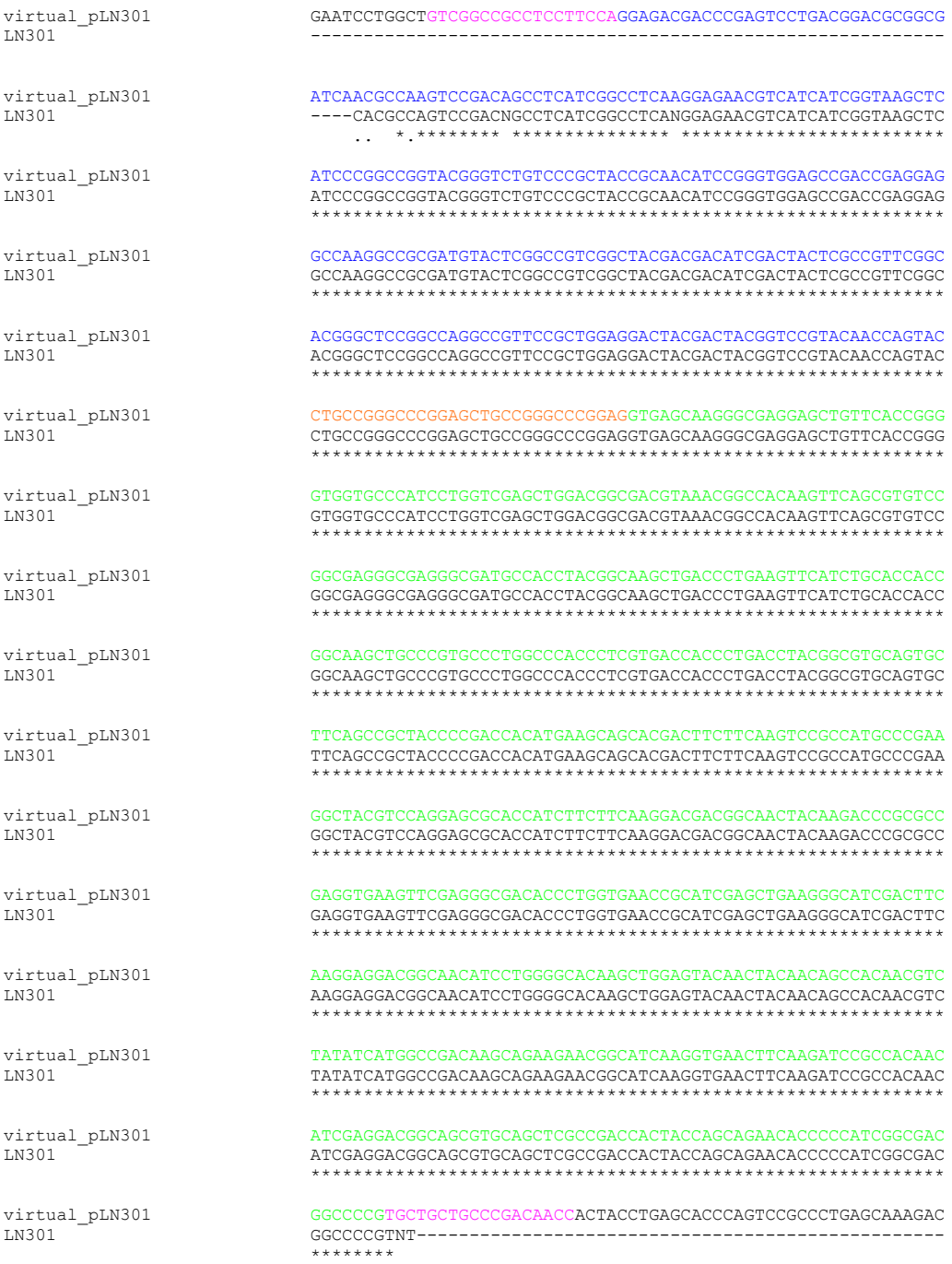

Figure 5.14: The eGFP-fusion to RNA-polymerase beta' subunit (*rpoC*) was confirmed by sequencing. The virtual cosmid pLN301 and sequenced LN301 strain were compared. The end of the gene *rpoC* (blue), ten amino acid linker sequence (orange), the start of eGFP (green) and the two primer binding sites for primers eGFP/rpoB link R and eGFP/rpoB linkF (pink) are shown. Alignment was performed using Clustal Omega version 1.1.0 (Sievers et al., 2011).

Antibiotic production and sporulation of eGFP-strains

To test the eGFP-insertion in strains LN108 (*idh-egfp*), LN205 (*pstS-egfp*) and LN301 (*rpoC-egfp*) does not alter the antibiotic production and sporulation of the *Streptomyces*, we streaked out spores onto plates containing R2YE, minimal medium supplemented with mannitol (MM+Man) and mannitol soya flour (MS). The resulting growth was then compared to the wild-type M145 growth. The plates were incubated at 30°C for 3 days and then at room temperature for over a week. Images of the plates at different times are shown in Figure 5.15. On R2YE plate all strains appeared first orange (2 days) and then mainly dark blue with few additional red colonies (3 days). All three strains also sporulated similarly on both MS and R2YE plates (ca one week). On MM + Man plate, the production of antibiotics was slower and faint pink colour, that later on turned into pink, was observed after ca one week of incubation. The colour formation was mainly similar in all four strains. Slightly darker colour was observed in strain LN301 and fainter colour in strain LN205 after over a week of incubation.

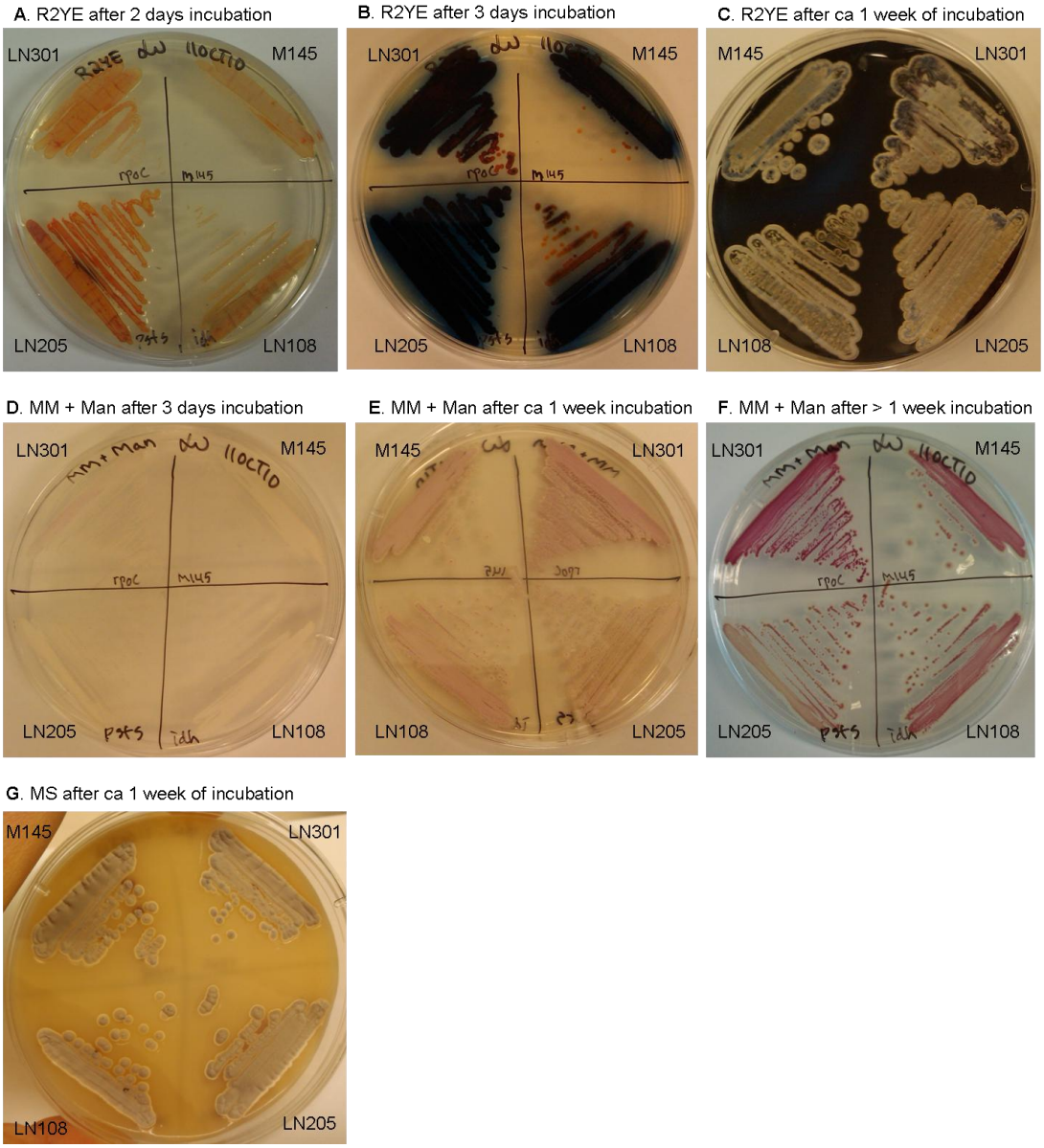

Figure 5.15: Antibiotic production (A-F) and sporulation (C, G) of eGFP-strains LN108 (*idh-egfp*), LN205 (*pstS-egfp*) and LN301 (*rpoC-egfp*) compared to the wild-type M145. Medium R2YE is shown on top row (A-C) and minimal medium supplemented with mannitol (MM + Man) is shown on the middle row (D-F). Mannitol soya flour (MS) medium, illustrating the sporulation, is shown at the bottom (G). Note: the incubation temperature for the first three days was 30°C and room temperature thereafter.

Microscopy of eGFP-strains

The spatio-temporal localization of eGFP-tagged proteins in strains LN108, LN205 and LN301 was tested using fluorescence microscopy. The localization of eGFPs was analysed in both solid and liquid cultures for strains LN108 and LN205. More detailed analysis of RpoC-eGFP in strain LN301 is provided in the next chapter.

When grown on solid, the Idh-eGFP was located in vegetative hyphae, aerial hyphae and spores in 2-3 days old culture of strain LN108 (see Figures 5.16 and 5.17). No fluorescence was detected in wild-type strain M145 using the same FITC filter settings as for Idh-eGFP. The nucleic acids and cell membranes were stained with fluorescence dyes SYTO42 and FM4-64 respectively. No specific pattern of Idh-eGFP localization was observed in vegetative hyphae where eGFP-fluorescence was detected in all parts of hyphae. During development of aerial hyphae, when compartments are clearly visible and the nucleic acids have already taken the shape of a spore, the Idh-eGFP still showed almost uniform distribution along the aerial hyphae, where as in the more mature spore chain, the Idh-eGFP localization was more defined into a spore-like shape.

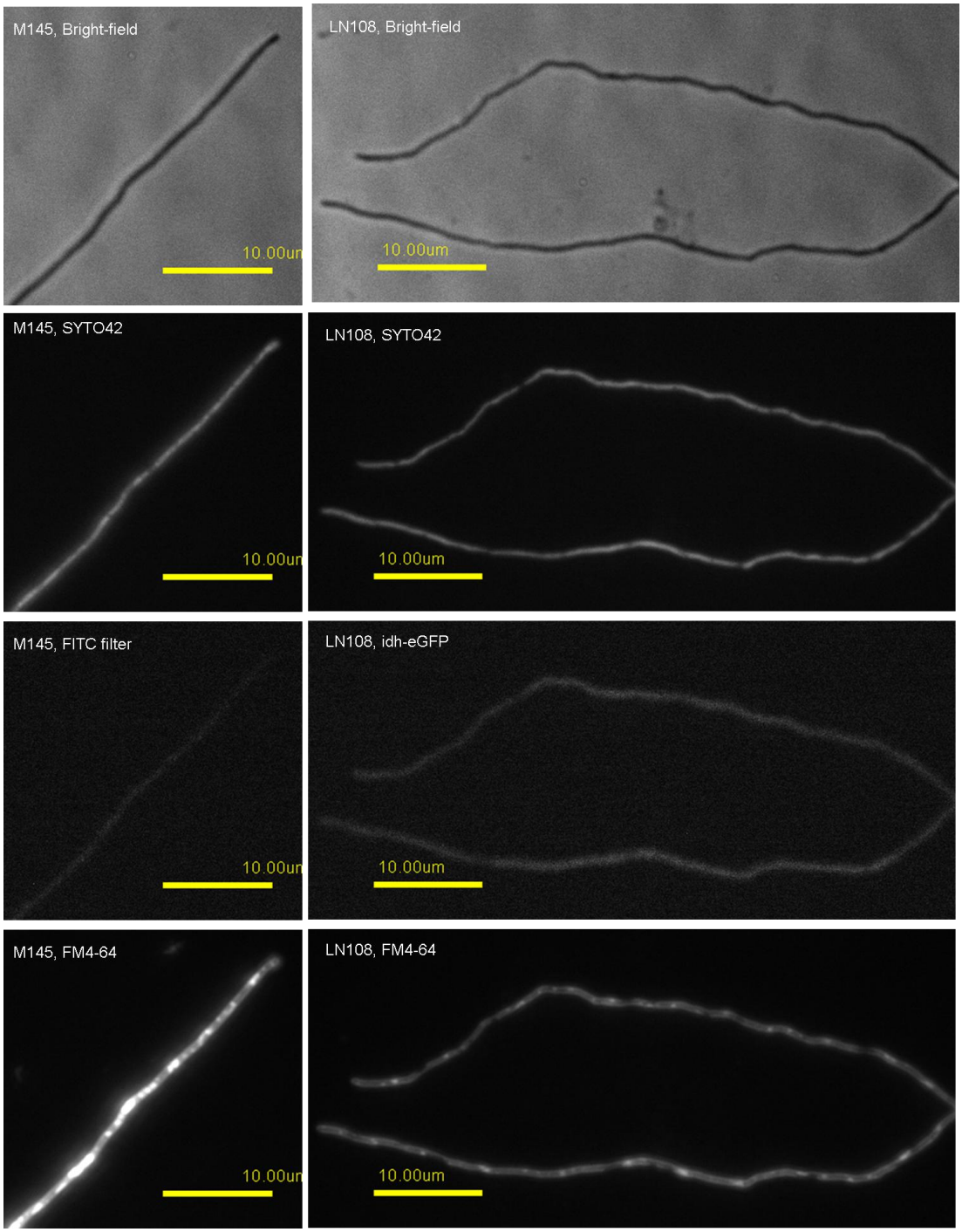

Figure 5.16: The Idh-eGFP in strain LN108 is located in all parts of vegetative hyphae with no specific localization pattern. Nucleic acids and cell membranes were stained with SYTO42 and FM4-64 respectively in both LN108 and its wild-type strains M145. The used scale bar is 10 µm. Deconvolution performed to z-section images. Exposure time for idh-eGFP was 100 ms.

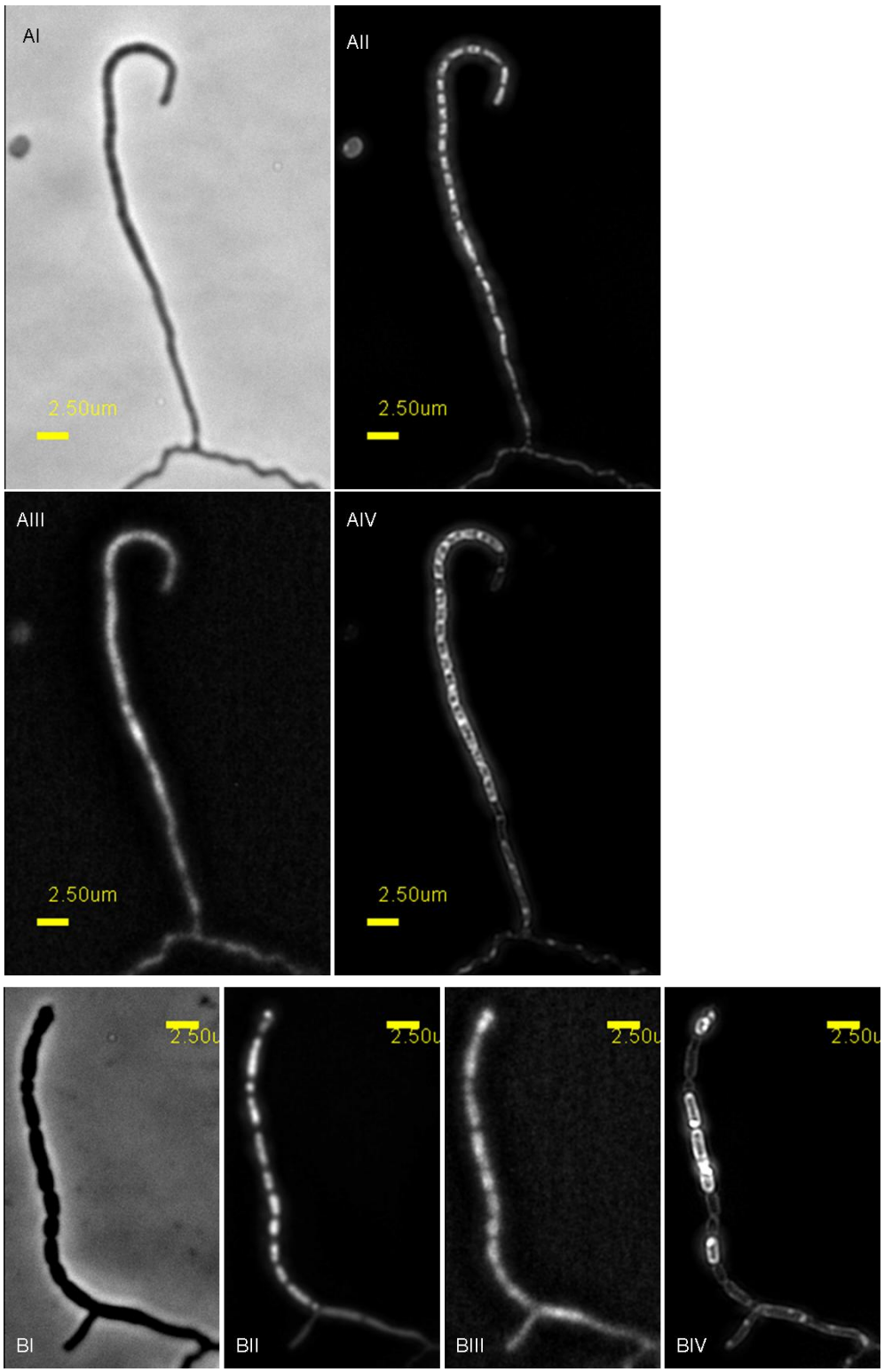

Figure 5.17: Aerial hyphae (A) and a spore chain (B) of strain LN108 illustrating the localization of idh-eGFP (III, z-section, 100 ms exposure time). Images show bright-field (I), nucleic acids stained with SYTO42 (II) and cell membranes dyed with FM4-64 (IV). Scale bar is 2.5 µm.

In liquid cultures (started with 1 x 10^5 cfu/ml in 400 ml culture) of strain LN108 (*idh-egfp*), we were able to observe the fluorescence protein in pellets before the start of antibiotic production. Figure 5.18 shows the localization of Idh-eGFP in pellets. *Streptomyces* were grown in YEME without sucrose and the images were taken before the onset of antibiotic production. The Figure 5.18 shows bright field (AI, BI and CI) and the corresponding fluorescence (AII, BII and CII) images for LN108 (A) and the wild-type M145 (B, C). Note that there is no detectable autofluorescence seen despite of the large variation noticed in pellet size. The fluorescence covered the whole pellet in LN108 indicating that Idh is found in all parts of vegetative hyphae.

To make parallel measurements of the Idh-eGFP and the viability of the hyphae within a pellet, we included propidium iodide (PI) staining for pellets. Unfortunately, the spectrum of PI overlapped with the eGFP spectra and since the intensity from the dye was very high compared to the intensity of the Idh-eGFP, the resulting fluorescence images of eGFP and PI were identical to each other. However, even though we were not able to distinguish the eGFP fluorescence from the fluorescence signal of PI when used on its own, we successfully performed the live/dead staining using SYTO9 and PI together. The live/dead staining for LN108 (D) and M145 (E) indicated the presence of non-viable hyphae at the centre of the pellets (see Figure 5.18). This result suggests that fluorescence attributable to isocitrate dehydrogenase (*idh-egfp*) is present in hyphae that are likely to be dead or metabolically inactive.

We were not able to study the localization of Idh-eGFP in pellets after the antibiotic production had started (i.e. cultures turned red) due to increased levels of autofluorescence (see Figure 5.19). An interesting observation was, however, that two wild-type M145 pellets of the same size were noticed to autofluorescence at two very different intensity levels.

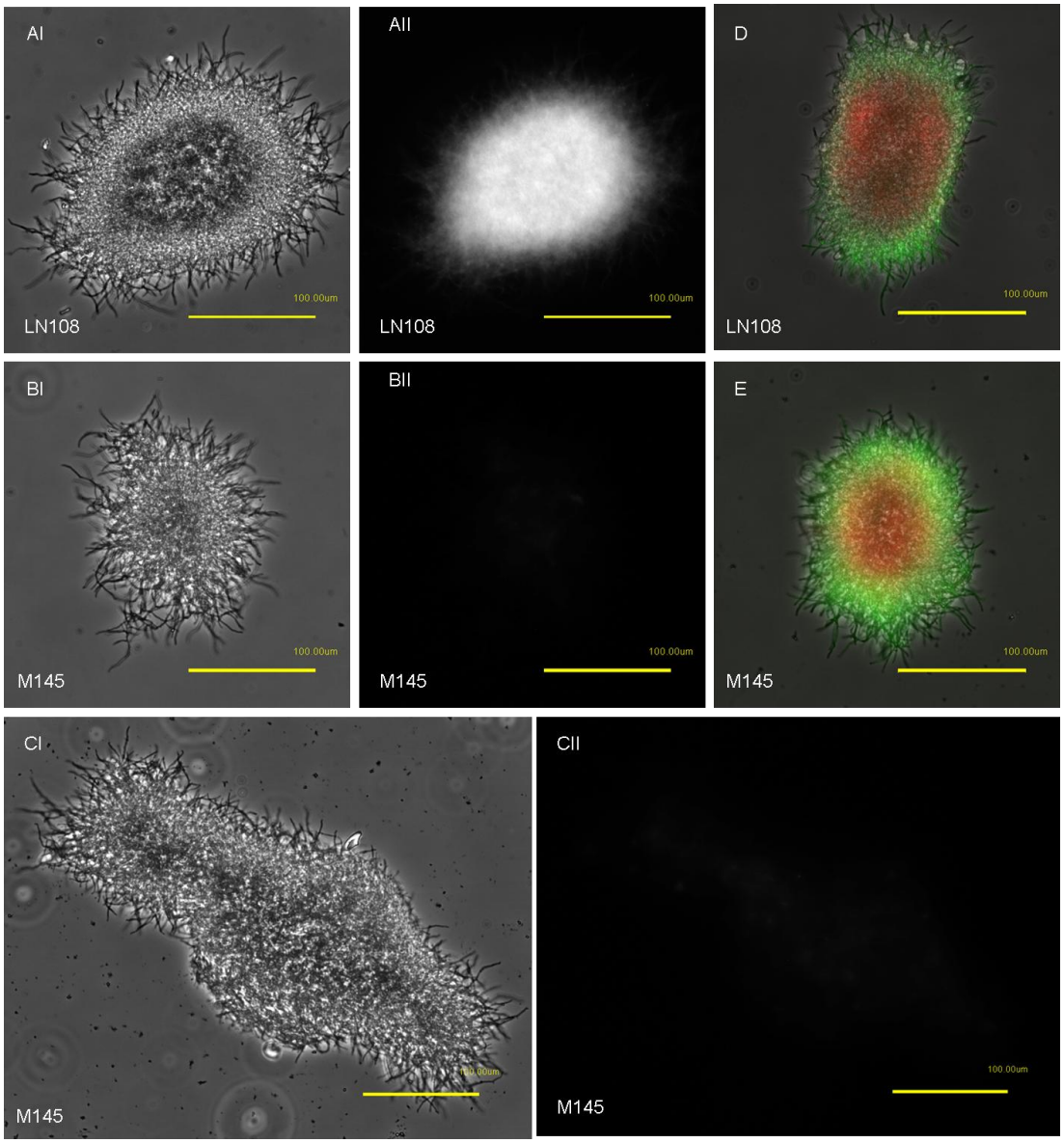

Figure 5.18: The localization of idh-eGFP in pellets before the start of the antibiotic production. Bright-field (I) and eGFP fluorescence (II, exposure time 5000 ms) images of LN108 (A) and wild-type M145 (B, C) were compared. The idh is located in all parts of vegetative hyphae. The live/dead staining of LN108 (D) and M145 (E) showed the presence of unviable hyphae at the centre of pellets at the time of sampling (23 h). The scale bar is 100 µm.

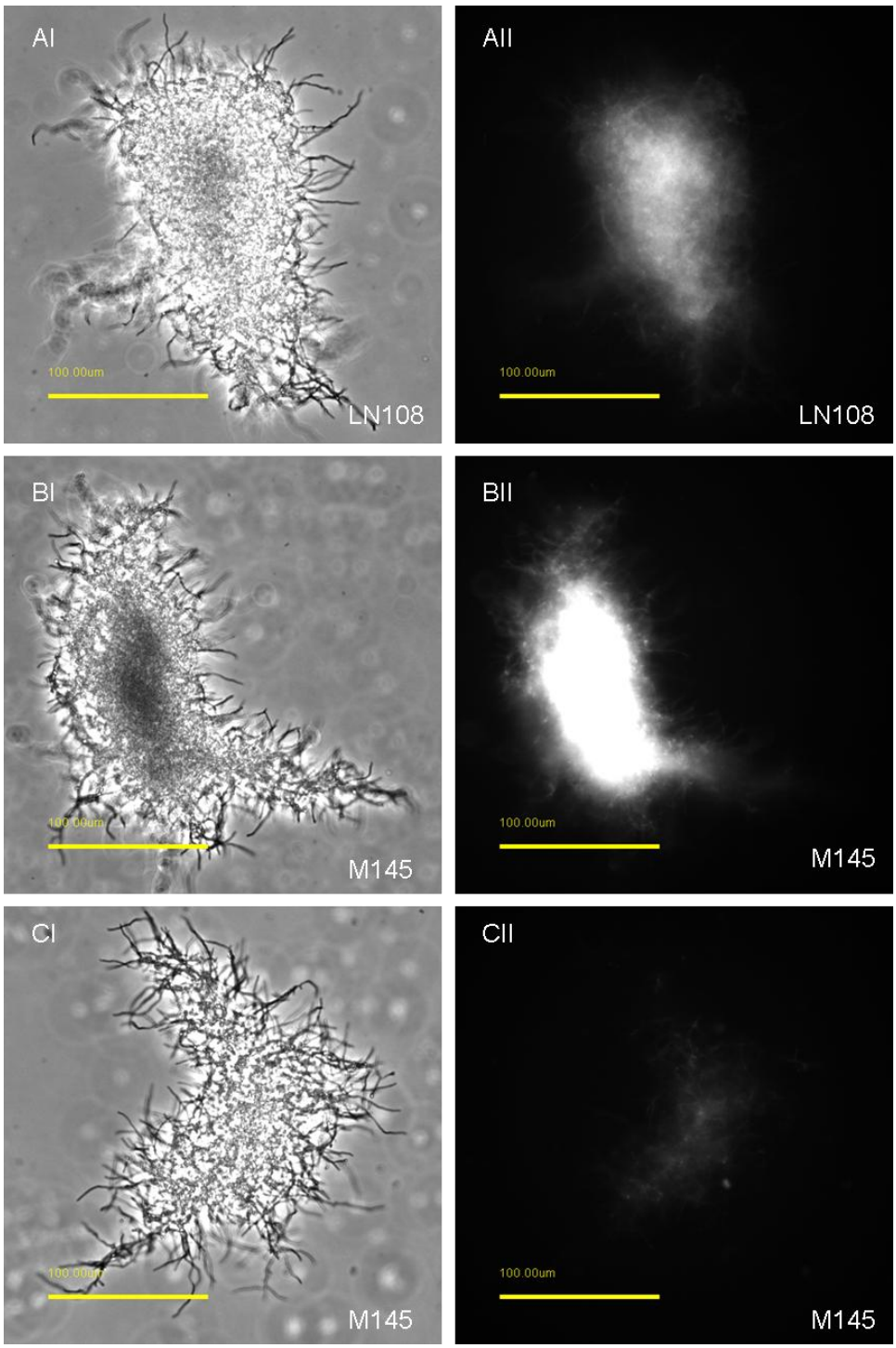

Figure 5.19: Pellets after the onset of antibiotic production (20 h). The localization of idh-eGFP in strain LN108 (A) was not detectable due to the increased autofluorescence levels as seen in some wild-type M145 pellets (B, C). Bright-field images (I) and fluorescence images (II, exposure time 500 ms) are shown. Scale bar is 100 µm.

Fluorescence microscopy was used to study the fluorescence pattern of strain LN205 (*pstS-eGFP*) grown on plates under different nutritional conditions in order to identify the location of phosphate starved hyphae. The tested growth conditions were minimal medium with both low and high phosphate concentrations, R2 medium with both low and high phosphate concentrations and MS. The used low concentration of phosphate was 10 µM and high phosphate concentration was 5 mM as per Sola-Landa *et al*. (2003). As with LN108 (*idh-egfp*) autofluorescence interfering with the detection of protein localization can be an issue with these experiments.

On minimal medium with low phosphate concentration, uniformly spread, low intensity fluorescence was detected in all parts of hyphae with couple of brighter spots seen in the subapical parts of hyphae in strain LN205 when grown for two and three days at 30°C (see Figure 5.20). The level of autofluoresence in wild-type strain M145 was noticeable after three days of incubation.

When grown on minimal medium with high phosphate concentration, short brighter areas were noticed at a location of ca 45 µm and 56 µm behind the tip (see Figure 5.21). Note that after 3 days of incubation the autofluorescence levels increased to a level where eGFP-fluorescence was not distinguishable from the background.

After three days incubation on R2 medium with low phosphate concentrations both brighter fluorescence spots in some parts of hyphae and uniform, lower intensity of fluorescence along the hyphae, were detected in both the mutant and the wild-type strains (see Figure 5.22). Note that after two days of incubation on the same medium the autofluorescence levels were high and no difference was seen in the fluorescence images between the mutant and the wild-type strain.

Where as, when the LN205 and M145 strains were grown for two days on R2 medium with high phosphate concentration brighter almost evenly spread spots were noticed along the hyphae of LN205 together with some background fluorescence (see Figure 5.23). Note that there was no brighter spots observed in this culture after three days of incubation and that the autofluorescence levels were interfering with the detection.

Strains LN205 and M145 were also grown on MS but there was no difference seen in the fluorescence levels between the wild type and the mutant strain after two days of incubation.

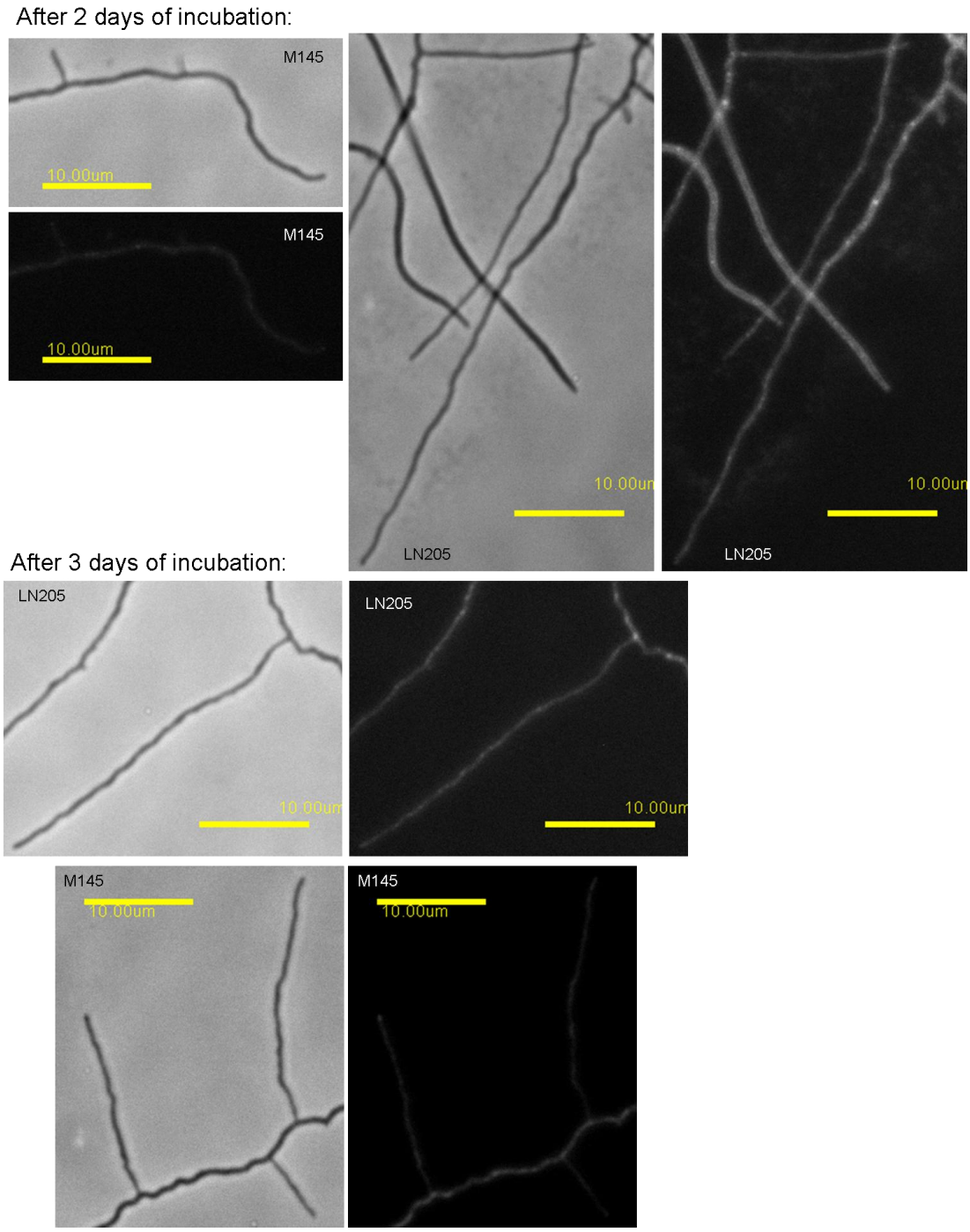

Figure 5.20: Strain LN305 (PstS-eGFP) grown on minimal medium with low phosphate concentration (10 µM). Bright-field and fluorescence (500 ms) images of strains LN305 compared to wild-type M145 after two and three days of incubation. The fluorescence images are comparable to each others on each day. Scale bar is 10 µm.

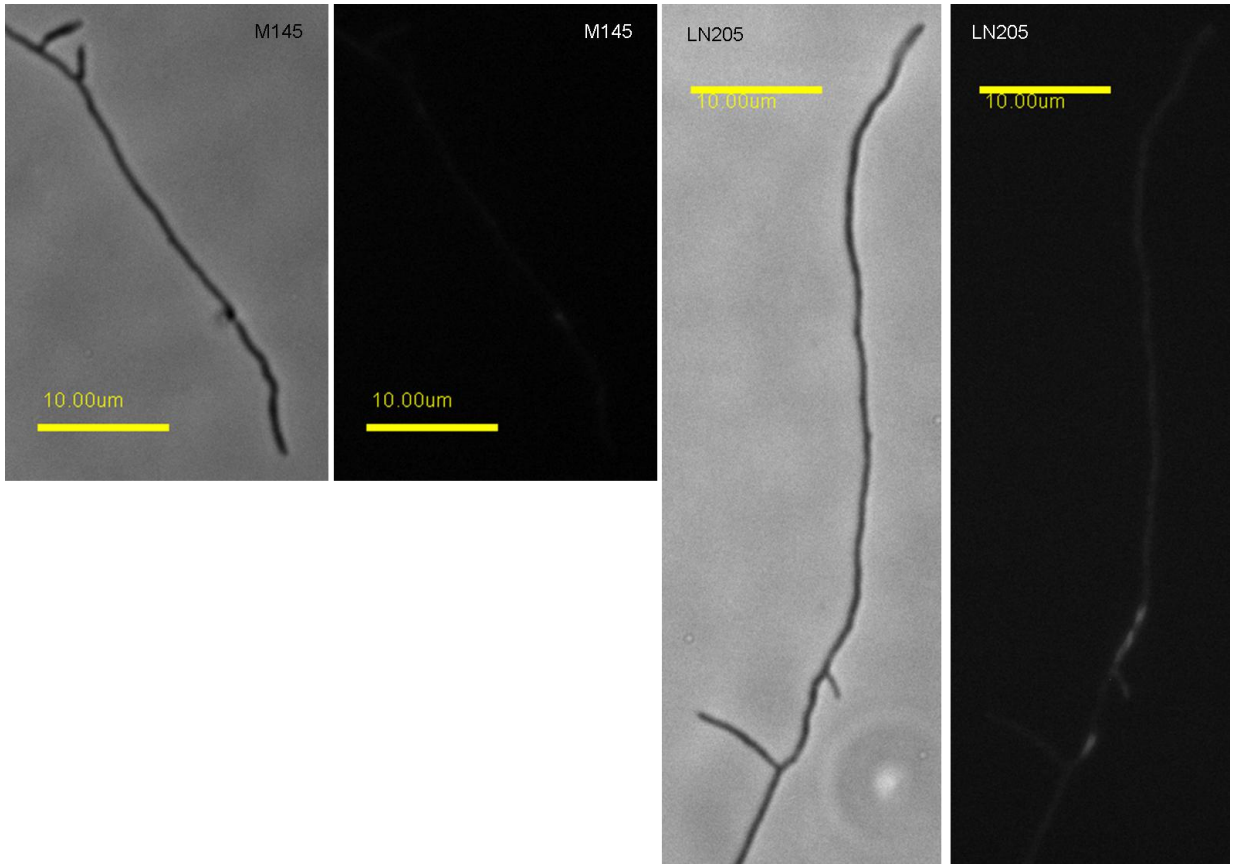

Figure 5.21: Strain LN305 (PstS-eGFP) grown on minimal medium containing high phosphate concentration (10 mM) after two days of incubation. When compared to the wild-type M145, the eGFP fluorescence image (500 ms) of LN305 hyphae had bright areas at ca 45 µm and 56 µm away from the tip indicating putative localization of PstS-eGFP. The used scale bar is 10 µm.

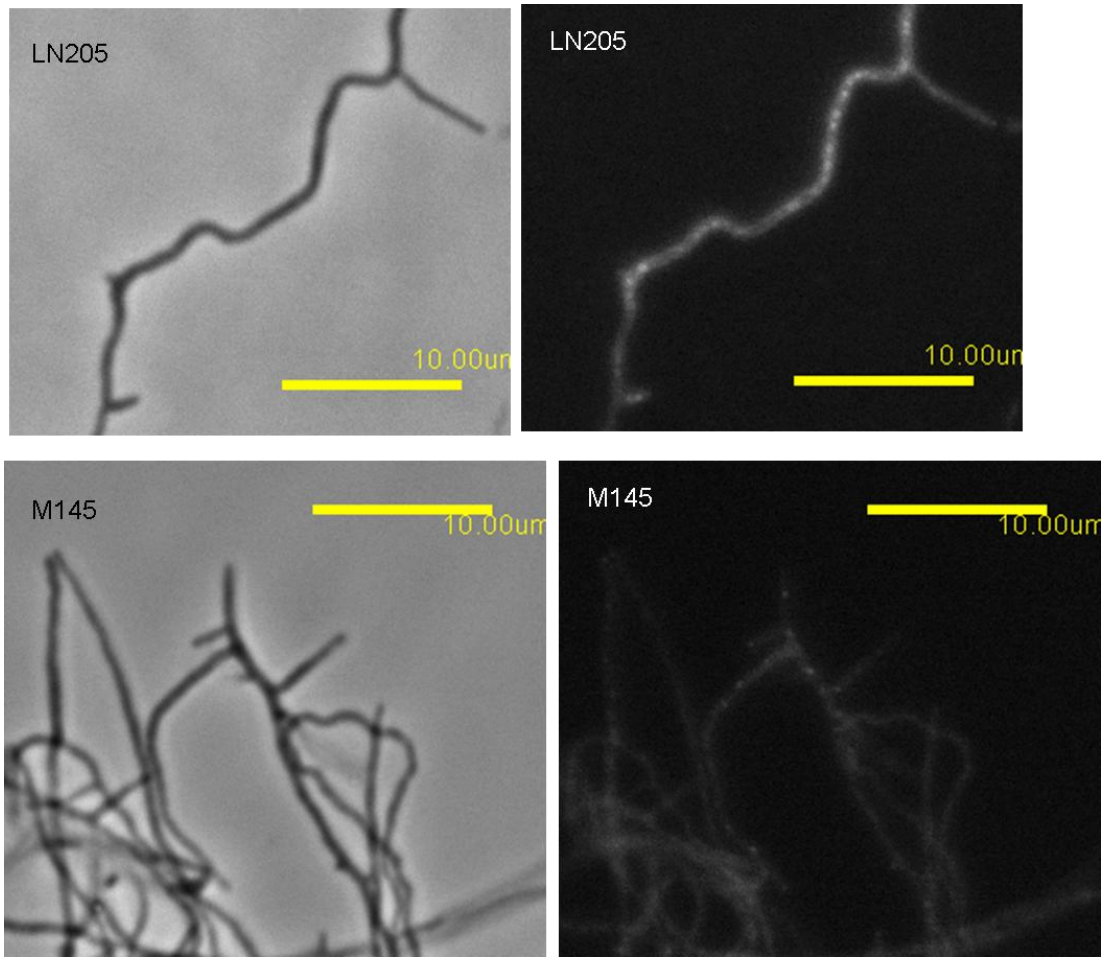

Figure 5.22: Wild-type (M145) and LN305 (PstS-eGFP) strains grown on R2 medium with low phosphate concentration (10 μM) for three days. Bright-field and fluorescence (500 ms) images are shown. Brighter spots within the hyphae were noticed in fluorescence images of both the wild-type and the mutant strains. Scale bar 10 μm.

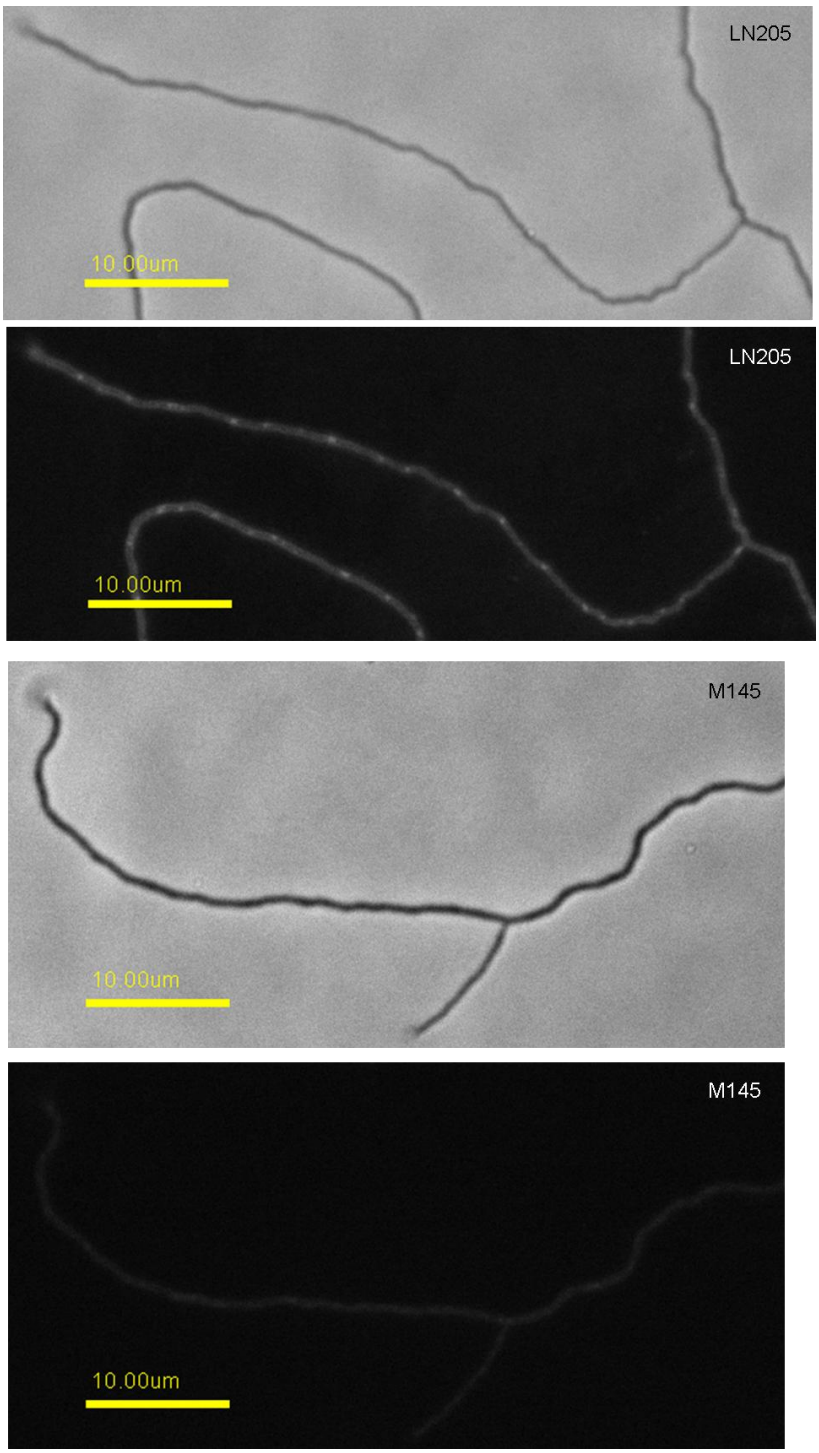

Figure 5.23: Fluorescence images (500 ms) of strain LN305 (PstS-eGFP) compared to wild-type M145 after two days of incubation on R2 medium with high phosphate concentration (10 mM). The used scale bar is 10 µm.

The localization of PstS-eGFP inside a pellet was also studied in order to identify the location of phosphate starved hyphae and the metabolic switch from primary to secondary metabolism. LN205 was grown on YEME without any sucrose. The culture was started with approximately 5 x 10^6 cfu/ml in 10 ml of culture in 100 ml flasks without any springs. The images were taken after 18 h of incubation at 30°C with 220 rpm when the culture was observed to show faint red colour. All the images that were taken from the LN205 pellets at this time point showed the same fluorescence pattern of bipolar, subapical fluorescence localization (see Figure 5.24, FITC filter set with 5000 ms exposure time). When the culture was incubated for further three hours to establish full antibiotic production (21 h, the colour of the culture was red), this fluorescence pattern had disappeared and the whole pellet fluorescent brightly. The simultaneous live/dead staining of pellets showed the size of the pellet area that is likely to be metabolically inactive. Taken together this suggests that the metabolic switch initiates at the periphery of the propidium iodide stained, red fluorescence areas of the pellets.

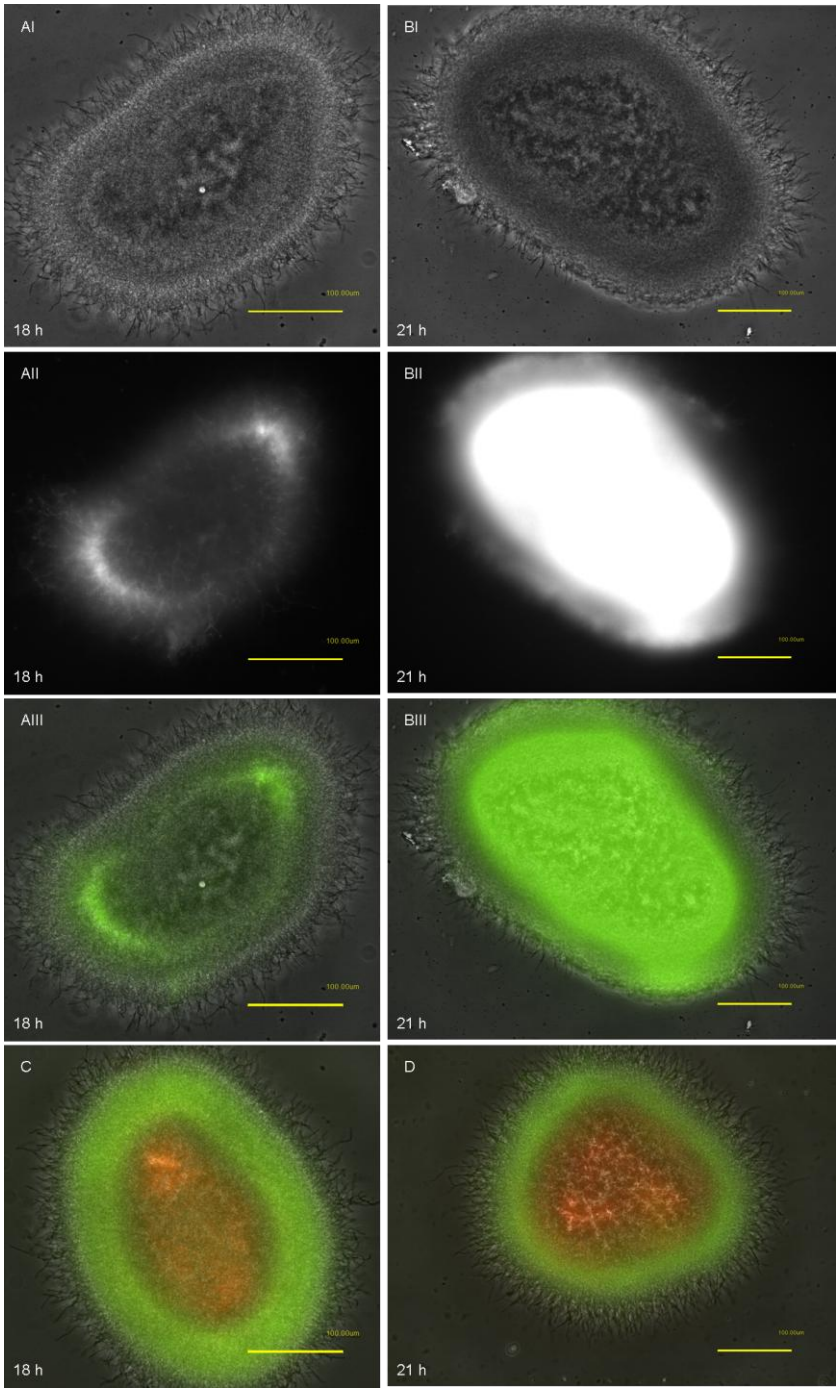

Figure 5.24: Pellets of strain LN205 (PstS-eGFP) at the onset of antibiotic production (18 h, faintly reddish culture) and after antibiotic production has started (21 h, red culture). The pellets A and B are illustrated as bright-field (I), FITC filter set for eGFP (II, 5000 ms exposure time) and multiprobe images of the bright-field and FITC (III). Live/dead stained pellets at the two time points are showed in images C and D.

To determine the location of transcription activity within hyphae, strain LN301 (*rpoC-eGFP*) was viewed under fluorescence microscopy stained with fluorescence dyes of SYTO42 (nucleic acids) and FM4-64 (cell membrances). In Figure 5.25 the bright field (I) and the fluorescence images show the nucleic acids (II), rpoC-eGFP (III) and cell membranes (IV) in vegetative hyphae of both LN301 and wild-type M145 strains. The localization of the RpoC-eGFP followed the pattern of nucleic acids rather than the cell membranes as would be expected. The fluorescence from rpoC-eGFP was patchy along the hyphae. No RpoC-eGFP fluorescence was detected at the sites of high cell membrane content. RpoC-eGFP was not detected at the hyphal tip. Further, in to depth analysis of LN301 growth on solid is presented in Chapter 7.

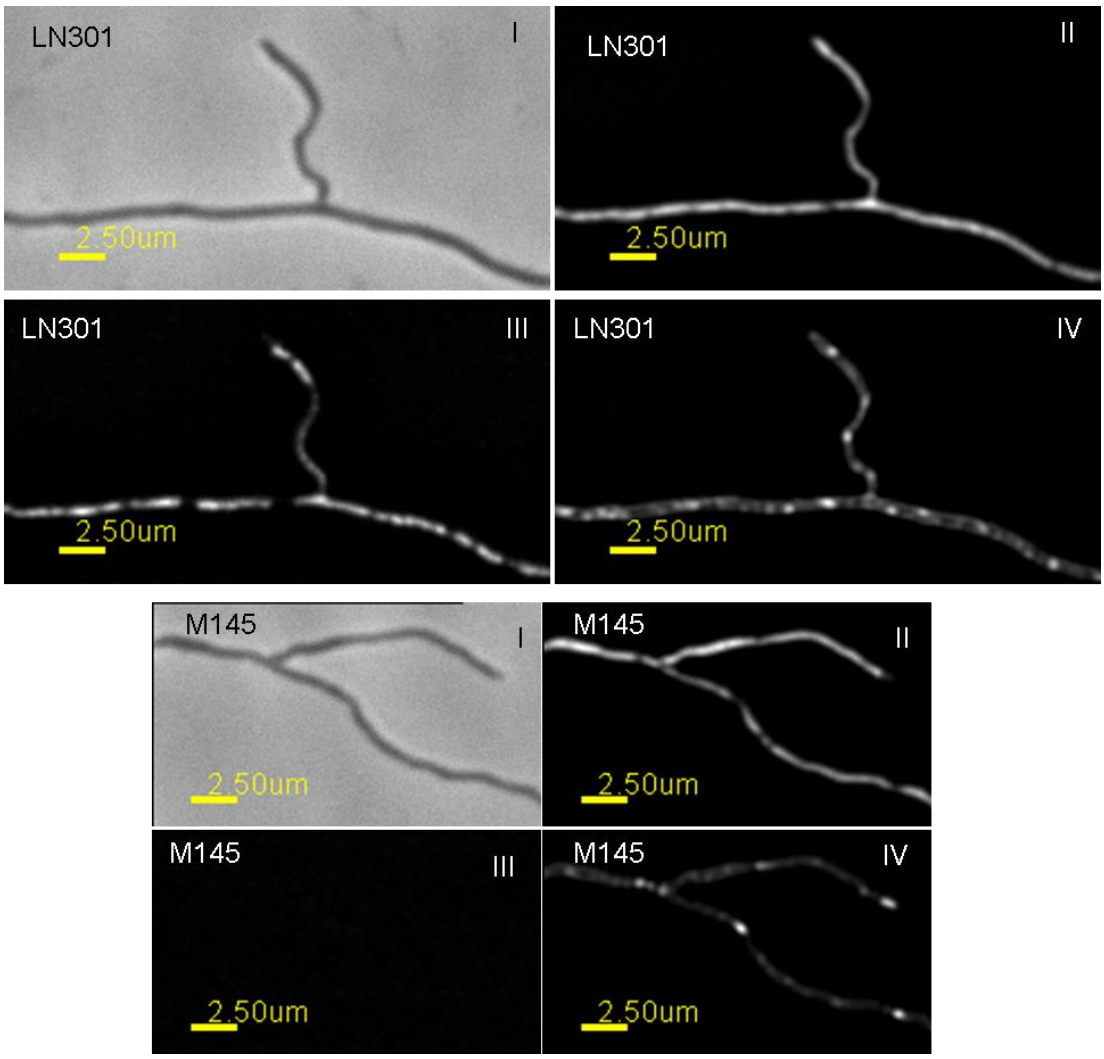

Figure 5.25:. The localization of transcription in vegetative hyphae of strain LN301 (*rpoC-eGFP*) is illustrated. Bright field (I) and fluorescence images of RpoC-eGFP (III, 100 ms exposure time) in mutant and wild-type M145 strains are shown. The nucleic acids (II) and cell membranes (IV) were visualized using fluorescence dyes SYTO42 and FM4-64 respectively. Deconvolution performed on z-section images. The used scale bar is 2.5 µm.

The location of transcription in pellets before the onset of antibiotic production was tested in shake flask cultures using LN301 strain. The culture was started with 5 x 10^6 cfu/ml in 50 ml of culture in 250 ml flasks (without any strings). Samples were taken after 23 h of incubation at 30°C at 150 rpm when the culture was still yellow indicating that the production of undecylprodigiosin had not yet started. The bright-field and fluorescence images (200 ms exposure time) of the strain LN301 and the wild-type M145 are presented in Figure 5.26. The whole pellet of LN301 was observed to fluorescence brightly indicating that the RpoC-eGFP is present in all parts of the pellet.

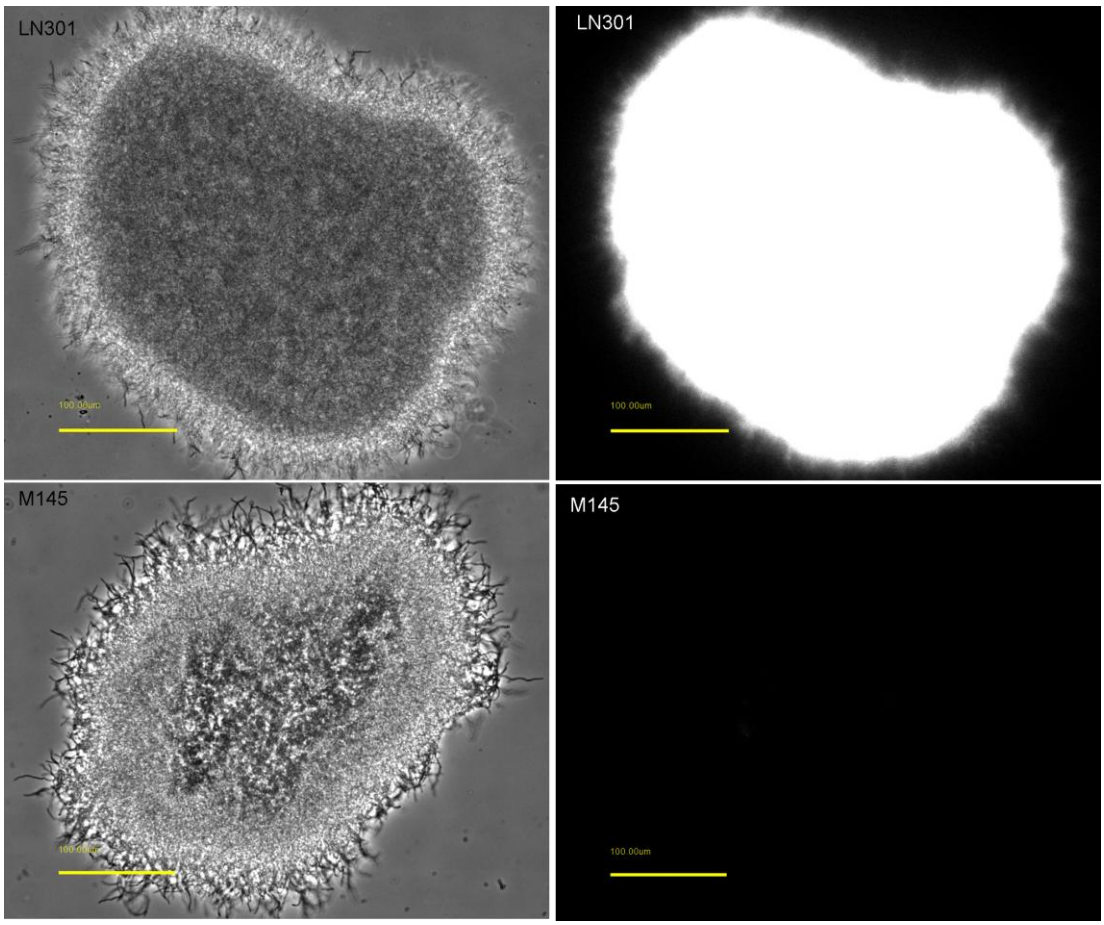

Figure 5.26: The localization of RpoC-eGFP within a *Streptomyces* pellet. Bright-field and fluorescence images (exposure time of 200 ms) of pellets of strains LN301 (rpoC-eGFP) and wild-type M145 are presented. The imaging was performed before the onset of antibiotic production (yellow culture) after 23 h incubation in shake flask cultures. The used scale bar is 100 µm.

Summary and conclusions

Typical model simulation predicts that the core of the pellet contains hyphae with only maintenance requirements for oxygen. The simulation does not contain any dead hyphae. We tested this prediction using two genes, *idh* and *rpoC*, translationally fused to eGFP. The Idh-eGFP served as an indicator for the primary metabolism through its involvement in TCA-cycle and the RpoC-eGFP illustrated the location of RNA-polymerase indicating the sites of transcription. Both Idh-eGFP and RpoC-eGFP were found in almost all parts of hyphae. Until the onset of antibiotic production, both Idh-eGFP and RpoC-eGFP were observed in all parts of the pellet despite of the presence of membrane compromised hyphae seen in the live/dead staining. To gain more insight into this discrepancy more experimental work is needed, for example enzyme activity assays or protein half-life studies. Unfortunately, we were not able to follow the Idh-eGFP nor the RpoC-eGFP localization in pellets after the onset of antibiotic production since the level at which the hyphae autofluorescence increased dramatically at this point making it impossible to distinguish the fluorescence of the eGFP from the autofluorescence.

The model simulation presented at the start of this Chapter (Figure 5.1) also predicts that the location of the antibiotic producing hyphae is at the periphery just below the surface of the pellet. We used translational fusion of eGFP to phosphate binding protein, PstS, in order to test this hypothesis. The gene *pstS* is expressed under phosphate limited conditions. Phosphate limitation is known to preceed the onset of secondary metabolite production. The protein, PstS-eGFP was therefore used in this study as an indicator for metabolic switch. In the experiment, fluorescence was noticed to initiate at bipolar locations beneath the pellet surface. High autofluorescence levels were unfortunately interfering with this experiment and therefore, further experiments such as Western blot are need to confirm that the bipolar, subapical fluorescence seen in the pellets at the onset of antibiotic production is actually from *pstS-eGFP* expression.

The putative, spatio-temporal PstS-eGFP expression doesn't fully support the model prediction on the location of antibiotic producing hyphae within a pellet. The model predicts that the antibiotic producing cells first emerge at the centre of the pellet and localizes at the periphery, below the surface, only afterwards. The PstS-eGFP experiment suggests that the initial location of the metabolic switch is at the periphery of the core of the pellet, that fluorescent red when stained with propidium iodide. However, the model simulation is based on one substrate (oxygen) and refinement of the location of the secondary metabolism cells may happen if further nutrients are incorporated to the model.

Chapter 6: Analysis on model predictions

In chapter 4 a model was constructed of *Streptomyces* pellet growth and metabolism which was validated with experimentally derived parameters and tested using indicators of specific metabolic activity such as the live/dead staining of pellets and eGFP-tagging of key cellular proteins. So far we have used the model to predict the location of the metabolic switch inside the pellet. In this chapter, we concentrate on utilizing the model further to gain predictions on *Streptomyces* biology and pellet formation.

Oxygen concentration at the green/red interface

Using the model simulations the fluctuating, external oxygen levels inside a pellet were studied. In Figure 6.1, a typical, multiprobe fluorescence image of a LIVE/DEAD® *Bac*Light™ stained pellet at the end of the exponential growth phase (A) is presented. The metabolic state of these green and red stained pellet areas is currently not known. We assume that the red pellet area consists of dead cell or possibly cells with only maintenance energy requirements for oxygen (i.e. a very low rate of metabolism), due to impairment of the proton motive force across the membrane. The green area is assumed to contain both the actively growing and the antibiotic producing cells. The simulation results in Figure 6.1 show the green/red pellet (B) using the above assumptions and the corresponding external oxygen concentration profile (C).

To predict the external oxygen concentration surrounding cells located at the interface of live/dead stained areas (referred to as green/red interface from now on), a number of simulations were run using different values of external oxygen concentration for the switch from green (alive) to red (likely to be dead) areas and measuring the resulting red area. The red areas in simulations are then compared to the average red area seen in experimental data, where the average red area was observed to be 1.71×10^4 μm^2 at the end of log phase (measured from TRITC filter set fluorescence images, see

Chapter 4). Using this comparison the current model predicts that the shift seen in experiments from green to red occurs when external oxygen concentration drops to ca 50-55% (giving a red area of around 1.53 - 1.89 x 10^4 μm^2, see Table 6.1). Note that the oxygen percentage is scaled to the total carrying capacity of oxygen in media.

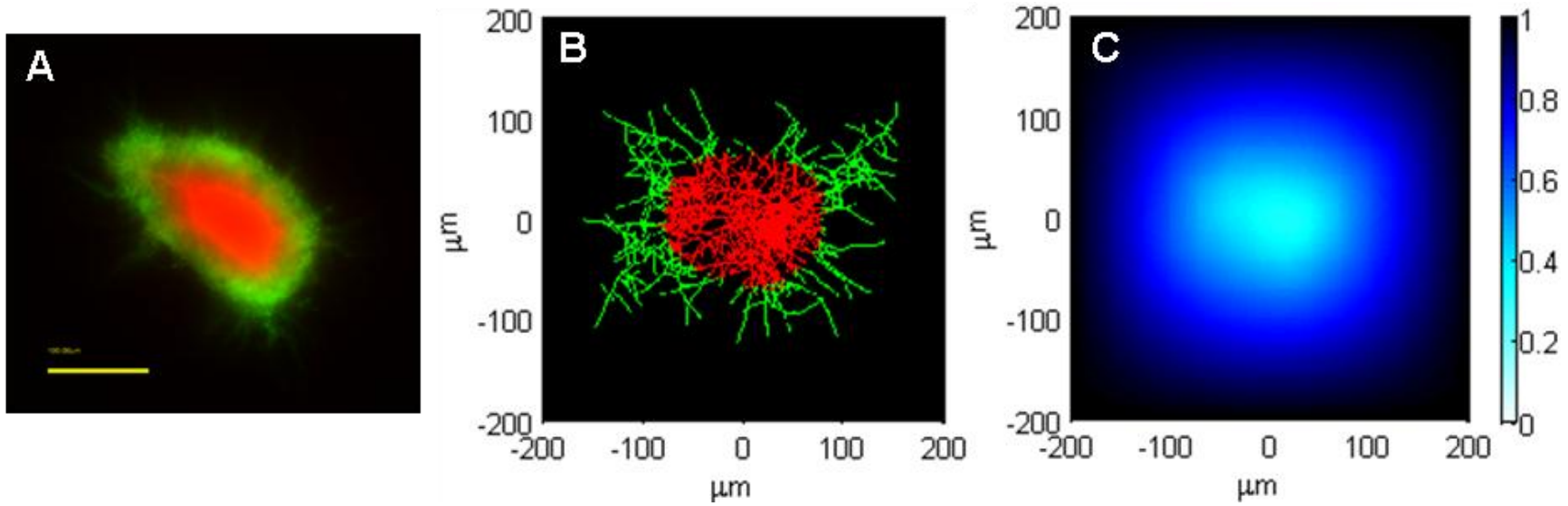

Figure 6.1: Model prediction of the oxygen concentration at the green/red interface compared to the experiment profile. A. Multiprobe fluorescence image of a typical LIVE/DEAD® *Bac*Light™ stained pellet at the end of the exponential growth (31 h after 6 h germination period). Green colour corresponds to SYTO9 dyed (alive) cells and red colour indicates propidium iodide stained hyphae (likely to be dead). The used scale bar is 100 µm. B. Model simulation of live/dead stained pellet at the end of the log-phase when the red area (1.81×10^4 µm^2) matches the average area of propidium iodide stained cells in experimental data (1.71×10^4 µm^2). C. External oxygen concentration in the model simulation. The scaled external oxygen concentration at the green/red interface inside a pellet is predicted to be 54% in this simulation experiment. The remaining parameter values are as per Tables 3.2 and 3.3 and Figure 3.14.

Table 6.1: The average area of propidium iodide (PI) stained cells in experimental data (1.71 x 10^4 μm^2) is used to predict the oxygen concentration level at the green/red interface.

External O_2 concentration[1] at the interface of green/red areas in the simulations (%)	Average red (PI) area in simulations (x 10^4 μm^2)
40%	0.62
45%	1.04
50%	1.53
51%	1.45
52%	1.56
53%	1.66
53.5%	1.78
54%	1.81
55%	1.89
60%	2.48
65%	2.89

[1] Percentage scaled to the total carrying capacity of oxygen in media

Simulations were run assigning the predicted value of 54% for the external oxygen concentration at the green/red interface and observed the simulated pellet formation. Figure 6.2 shows the simulation results at 6 h, 12 h, 18 h and 31 h (time after 6 h germination period). It is observed that the red hyphae is absent from the simulations during the first three time points. When compared to the corresponding time points of the growth curve experiment (see Chapter 4, Figure 4.7 and 4.20B), it was noticed that in the experiment the red stained hyphae already existed in some parts of hyphae as early as 6 h and at the pellet core at 10 – 12 h onwards (time after germination). This discrepancy in pellet formation between the model simulation and the experimental data could be a result of a number of things. Assuming that the fault does not lie in the use/design of the model i.e. in the used parameter values, in the way oxygen diffusion is modelled to occur inside the pellet or in the 2D+ pellet density solution, the inconsistency could be a consequence of a biological matter such as cell death/membrane damage caused by nutrient limitations or natural cell death due to ageing of hyphae; aspects that are currently not included in the model. Further work is needed to properly assess this dilemma. For the purposes of this thesis, the model predictions made from here onwards concentrate on the end of the log-phase.

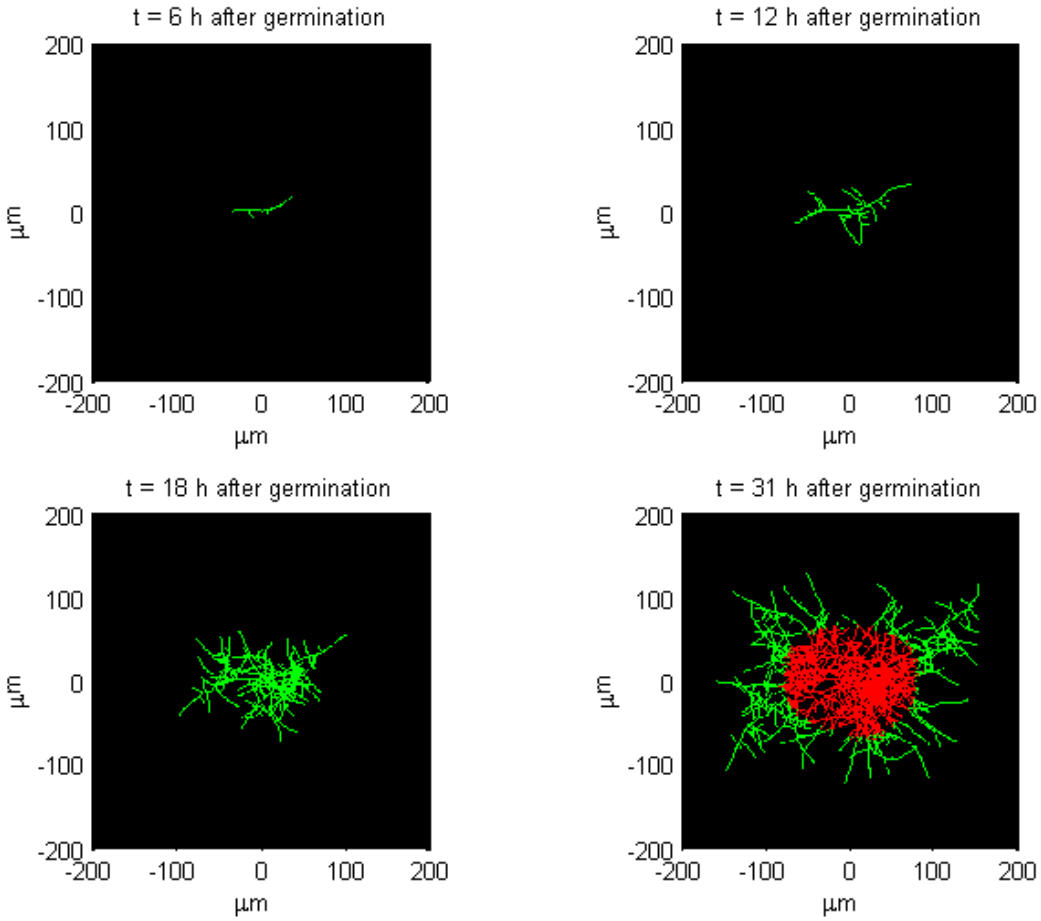

Figure 6.2: Model simulation of pellet formation during exponential growth. Green area is assumed to have oxygen consumption of an active hyphae (active growth or secondary metabolite production) and red area corresponds to inactive hyphae that still has some maintenance requirements for oxygen. The rest of the parameters are as per Tables 3.2 and 3.2 and Figure 3.14.

Branching pattern influences pellet metabolism

To find the effect that different branching patterns have on features such as pellet morphology, oxygen consumption and metabolism, simulations were run varying parameters for apical (first branch point) and inter-branch distances as previously measured for *S coelicolor* by Jyothikumar *et al*. (2008) and by Allan and Prosser (1983) (see Table 6.2). In Figure 6.3, the simulations show that just by altering branching frequency can have significant effects on pellet morphology. The model prediction of pellet morphology using frequent branching parameters shows the appearance of satellite pellets that are likely to break off from the original pellet under experimental conditions. A reassuring conclusion about the good fit between the model behaviour and empirical work is that the high hyphal density co-localises with increased branching frequency. The denser pellet areas also have higher oxygen consumption. The simulation prediction of the metabolic state of hyphae suggests that less frequent branching pattern creates larger and less dense pellets that consume less oxygen and stay fully metabolically active.

Table 6.2: Parameter values for frequent and less frequent branching patterns.

Frequent branching[1]		
Parameter	**Symbol**	**Value**
Average apical length	l_1	10.94 μm
Average interbranch length	l_2	7.63 μm
Standard deviation of apical length	l_1sd	2.85 μm
Standard deviation of interbranch length	l_2sd	6.68 μm
Less frequent branching[2]		
Parameter	**Symbol**	**Value**
Average apical length	l_1	35.2 μm
Average interbranch length	l_2	9.91 μm
Standard deviation of apical length	l_1sd	1.12 μm
Standard deviation of interbranch length	l_2sd	0.52 μm

[1] as previously measured by Jyothikumar *et al*. (2008).

[2] as previously measured by Allan and Prosser (1983).

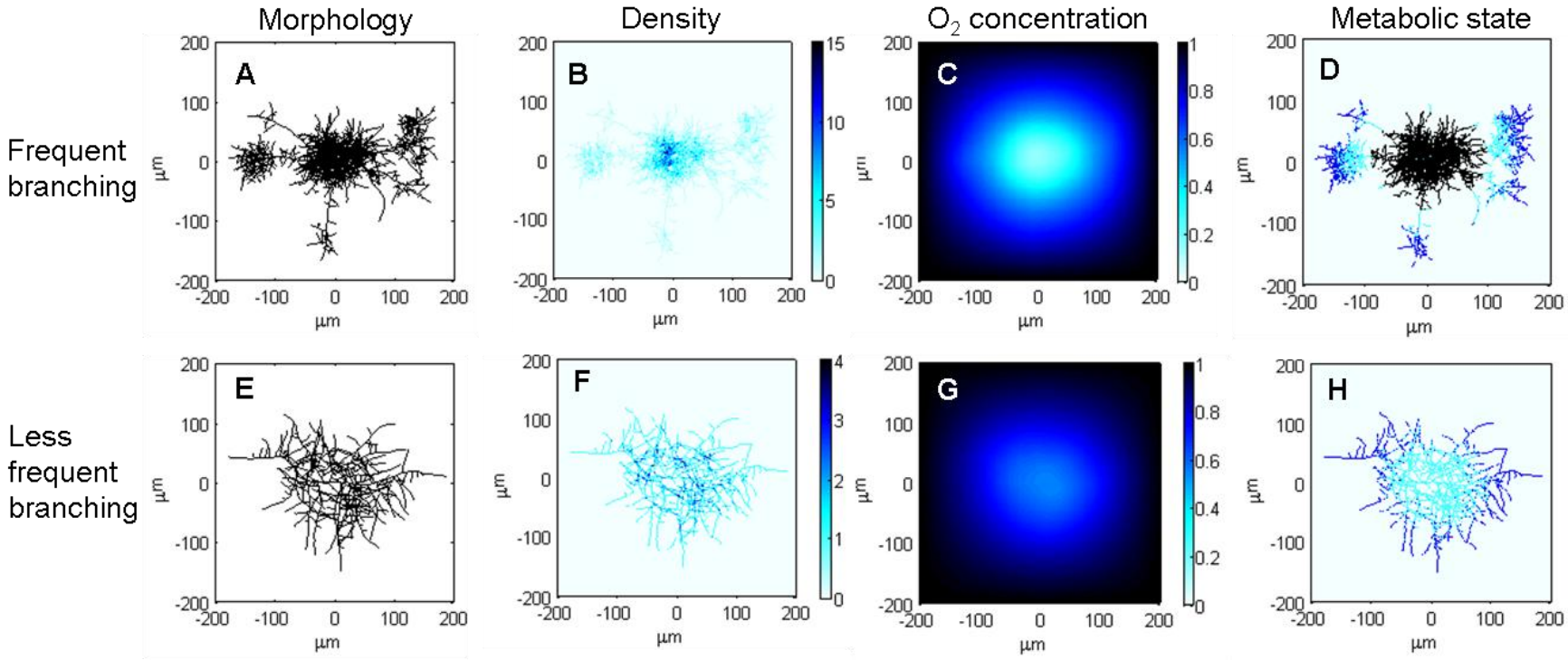

Figure 6.3: Simulation comparison between two different branching patterns. Pellet morphology (A, E), hyphal density (B, F), external oxygen concentration (C, G) and predicted metabolic state of pellet areas (D and H, where blue is actively growing hyphae, cyan is for antibiotic producing hyphae and black is for inactive hyphae with only maintenance requirements for oxygen) are shown for frequent branching (top row) and for less frequent branching (bottom row) as previously measured by Jyothikumar *et al*. (2008) and by Allan and Prosser (1983) (see Table 6.2). The remaining model parameters are as per Tables 3.2 and 3.3 and Figure 3.14.

Average hyphal velocity

In the model the hyphae currently elongate according to an average velocity of 6.3 μm/h, based on experimental values. To find out the effect of different elongation rates to pellet morphology, we ran multiple simulations using average velocity values of 2.5 μm/h (-60%), 4.4 μm/h (-30%), 8.2 μm/h (+30%), 10 μm/h (+60%) and 12.6 μm/h (+100%), where the value in brackets corresponds to a percentage difference from our initially assumed average velocity. The Figure 6.4 shows that by decreasing velocity the pellets appear smaller with delayed antibiotic production. If the velocity is increased significantly, the overall pellet morphology is affected, with the pellet growing quicker and antibiotic producing cells appearing earlier. However, even though, as the main body of the pellet stays approximately the same size a few long, unbranched hyphae emerge from the main body. This simulation outcome reveals two unexpected aspects of our model. Firstly, to avoid premature abortion of the simulation, the spatial domain required increasing such that the hyphal tips did not hit the boundary. The larger domain boundary affected the oxygen distribution resulting in an artificial oxygen gradient appearing outside the pellet. This resulted in the lack of oxygen near the pellet surface making it impossible for most of the hypha to continue elongating. The long hypha seen in the simulations, are a result of the only few hyphal tips still reaching the area where adequate oxygen concentration for growth is present. Secondly, the single, elongating hyphae appear unbranched even though the branching frequency is assumed to increase with the increasing hyphal length. In the model, when a branching event occurs, the new branching point is calculated from the previous branching point. Since the previous branching point does not change, the new branch will try to emerge at approximately the same position. If this position is already in the area of inadequate external oxygen concentration for growth, the branching event is going to be unsuccessful. Therefore, it is noted that under limited oxygen concentration, the current model is favouring unsuccessful branching events.

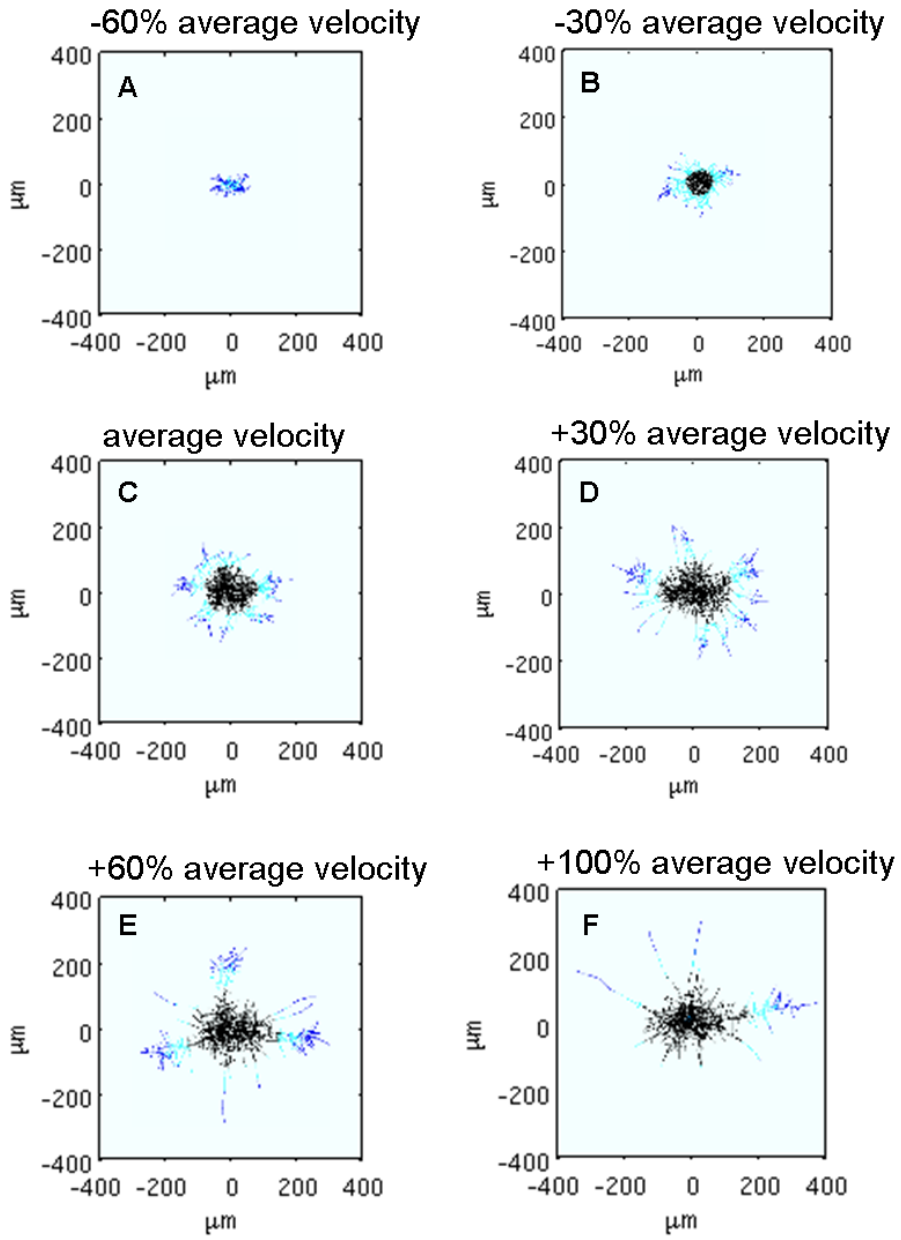

Figure 6.4: The effect of average velocity to pellet morphology and metabolism. Simulations showing an average tip elongation rate of -60 % (A), -30 % (B), 0 % (C), +30 % (D), +60% (E) and +100% (F) of the experimentally observed value (6.3 µm/h) are presented. To accommodate the increased velocities, the domain sizes were increased to 500 µm x 500 µm, 600 µm x 600 µm, 800 µm x 800 µm in (D), (E) and (F), respectively. Note: the images were manually adjusted to show 800 µm x 800 µm domain size to allow a comparison between the different cases. The rest of the parameters are shown in Tables 3.2 and 3.3 and in Figure 3.14.

Examples of model applications

As an example of how the model could allow us to gain quantitative insight into processes that are very difficult or impossible to obtain experimentally, we utilize the model without stirring effect, with parameter values of 1×10^{-5} μm^{-2} for rescaled oxygen consumption and 54% for the calibrated, external oxygen concentration at the green/red interface. In Figure 6.5, the frequency of successful (blue) and unsuccessful (red) branching events during simulations is shown. At the start of the growth curve, most of the branching events are successful with increasing frequency. Successful branching then declines rapidly following the onset of antibiotic production.

The data from the velocity simulations in Figure 6.4 could also be used further. We plot HGU at the end of log phase versus average tip velocity and the time of maximum successful branching versus these calculated HGUs (see Figure 6.6). Again, using the calculated HGUs, we can observe the relationships between end pellet diameters and areas of the different metabolic regions versus HGU. Note that the different states of metabolism resemble growth curve characteristics with lag phase, exponential growth and stationary/death phases. We also plot the maximum rates of oxygen consumption in these simulations versus the calculated HGUs. Not only can these plots be used for prediction purposes but also they highlight that an optimal value of average tip velocity for exponential growth exists and could be utilised in the design of industrial processes through the application of rational process design.

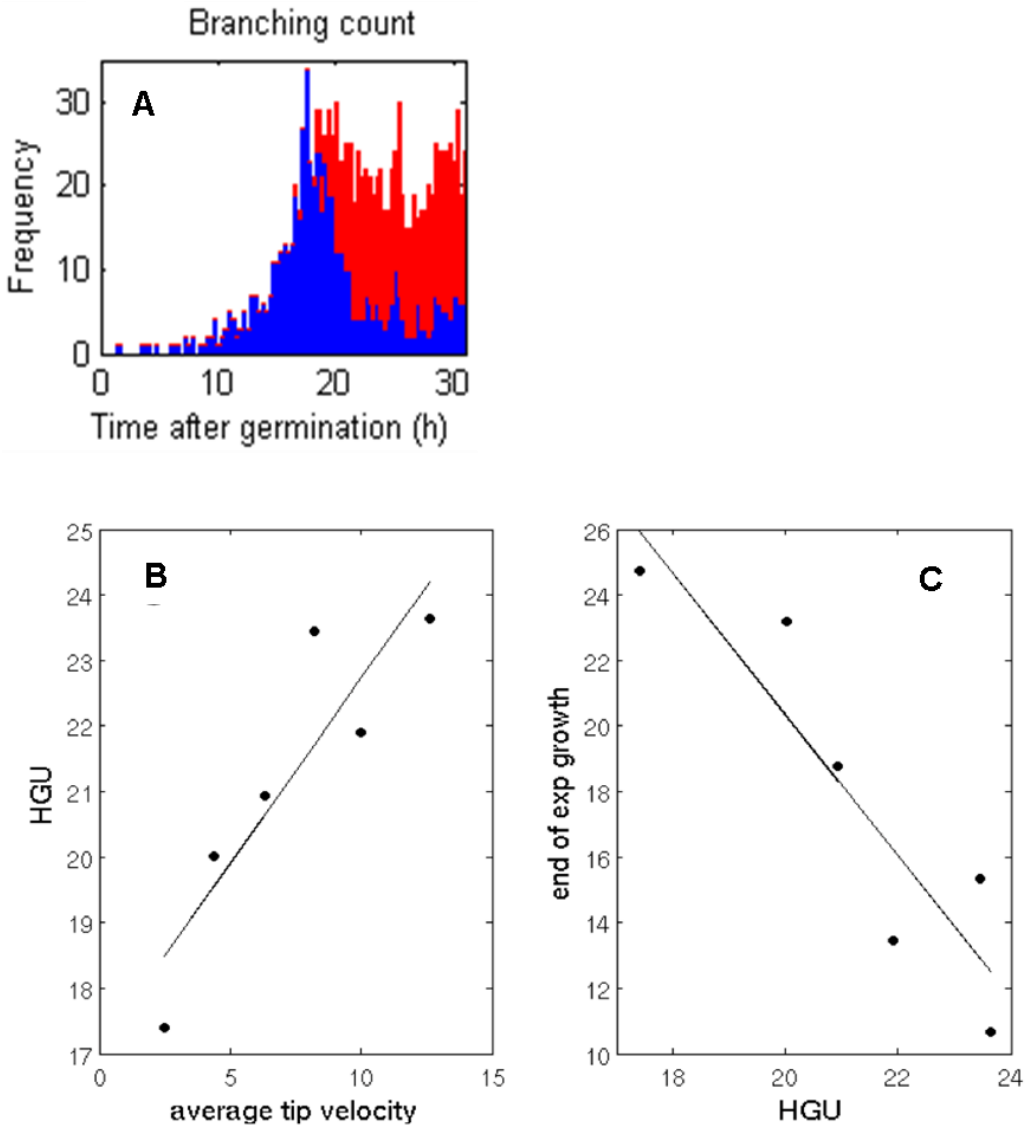

Figure 6.5: Simulation results showing successful branching count and the utilization of regression lines. A. The frequency of successful (blue) branching events is shown compared to the frequency of unsuccessful (red) ones. B and C. Regression lines can be utilized to determine the HGU and the time of maximum successful branching based on average tip velocities of 2.5 µm/h (-60%), 4.4 µm/h (-30%), 6.3 µm/h (±0), 8.2 µm/h (+30%), 10 µm/h (+60%) and 12.6 µm/h (+100%). %). Simulations are run with the 'old' branching rules (see main text for details), using 1 x 10^{-5} μm^{-2} for rescaled oxygen consumption and 54% for the external oxygen concentration at the green/red interface. The remaining model parameters are presented in Tables 3.2 and 3.3 and in Figure 3.14.

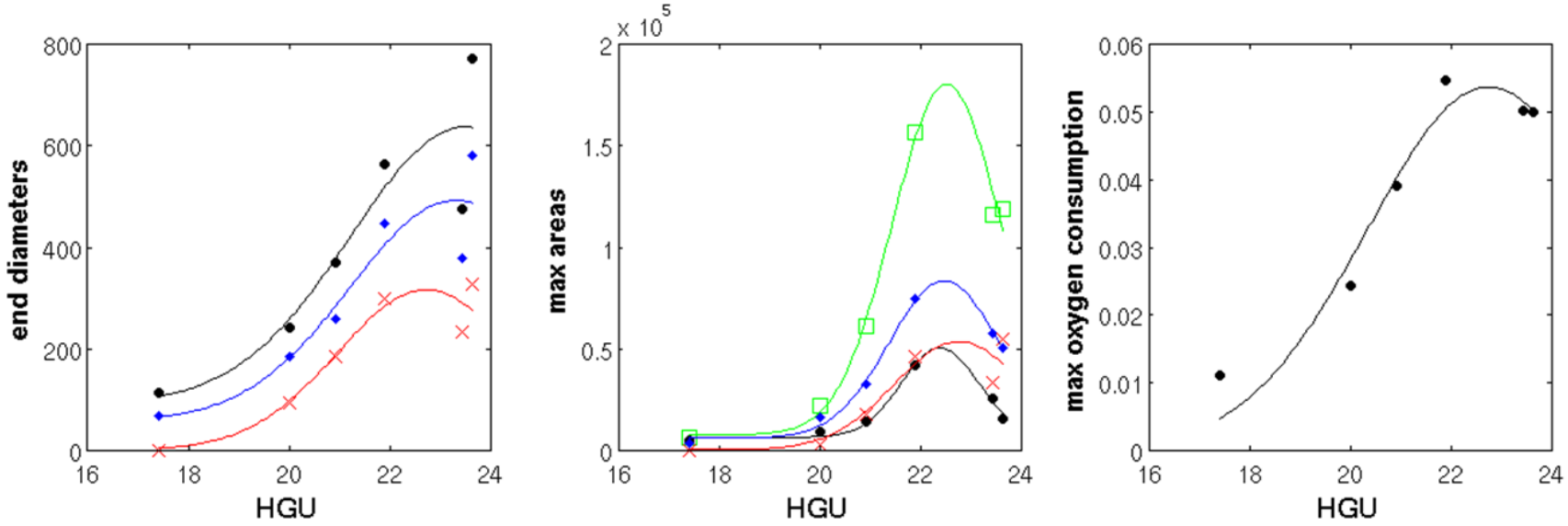

Figure 6.6: Model predictions using different average tip velocity simulations. The relationships between end diameters and areas of the different metabolic regions and the maximum rates of oxygen consumption versus the calculated HGUs are shown. The simulations are run with the 'old' branching rules with the rescaled oxygen consumption and the external oxygen concentration at the green/red interface as 1 x 10^{-5} μm^{-2} and 54% respectively. The average tip velocities are 2.5 µm/h (-60%), 4.4 µm/h (-30%), 6.3 µm/h (±0), 8.2 µm/h (+30%), 10 µm/h (+60%) and 12.6 µm/h (+100%). The metabolic state of the hyphae is indicated for actively growing cells (black circles), antibiotic producing cells (blue diamonds), maintenance requirements only cells (red crosses) and the total area of pellet (green rectangles).

Model updates – branching rule and stirring effect

In shake flask cultures where the culture is going through constant movement, it is very unlikely that substrate gradients appear outside the pellet. Therefore, to prevent the formation of an oxygen gradient, external to the pellet (such as that predicted in Figure 6.4), and to assess the appearance of the single unbranched hyphae in high velocity simulations, the model was updated further by changing the branching rule and by adding the stirring effect of external oxygen.

First, we explore the effects of varying the branching rules in the model without stirring. The branching event is revised in two, equally plausible, ways. First option is to calculate the branching distance from the tip instead of the last branching point using a normal distribution function of average apical length (l_1) and its standard deviation ($l_1$sd). The second option calculates the position of the new branching point using a flat distribution function derived from the apical and interbranch distance measures (l_1, l_2, $l_1$sd, $l_2$sd), where a uniform distribution is assumed around the mean, between the values of l_1 and l_2 (Figure 6.7, see parameter values in Table 3.2 and 3.3 and in Figure 3.14). The high velocity simulations (+100%) using these three different branching event solutions are compared in Figure 6.8. Both unbranched, long single hyphae and branched hyphae forming satellite pellets are observed in all three branching event simulations. A higher number of satellite pellets are observed in the model updates than in the initial model. No dramatic difference is noticed between the two branching event updates in this simulation. The two model updates differ, however, from the initial model in that they both create less dense pellets with a delay seen in the onset of metabolic switch as observed from the tracking of the tips. The total number of tips at the end of exponential growth between the three branching event models is more or less the same.

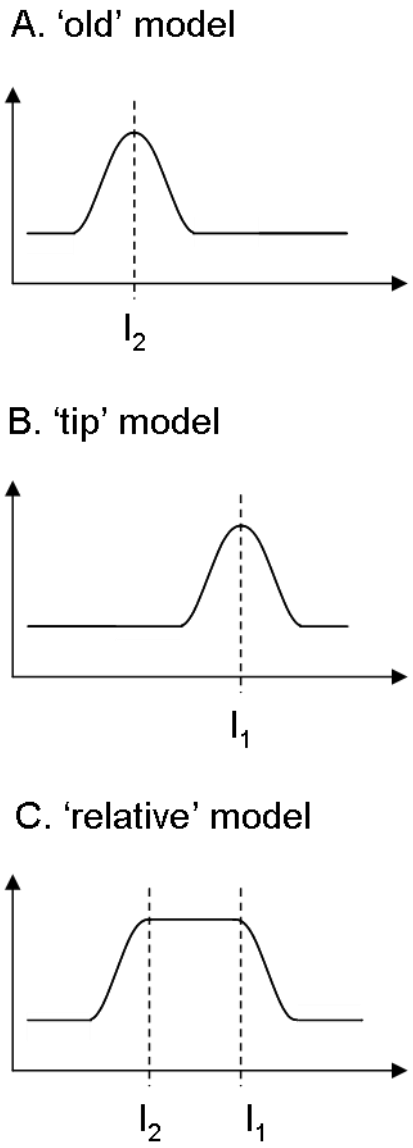

Figure 6.7: Schematic illustration of three different branching rules. A. ‘old’ model with new branching point calculated using the interbranch distance (l2) and its standard deviation ($l_2$sd). B. ‘tip’ model where the new branch emerges using a normal distribution function of average apical length (l_1) and its standard deviation ($l_1$sd). C. ‘relative’ model calculates the position of the new branching point using a flat distribution function derived from the apical and interbranch distance measures (l_1, l_2, $l_1$sd, $l_2$sd), where a uniform distribution is assumed around the mean, between the values of l_1 and l_2.

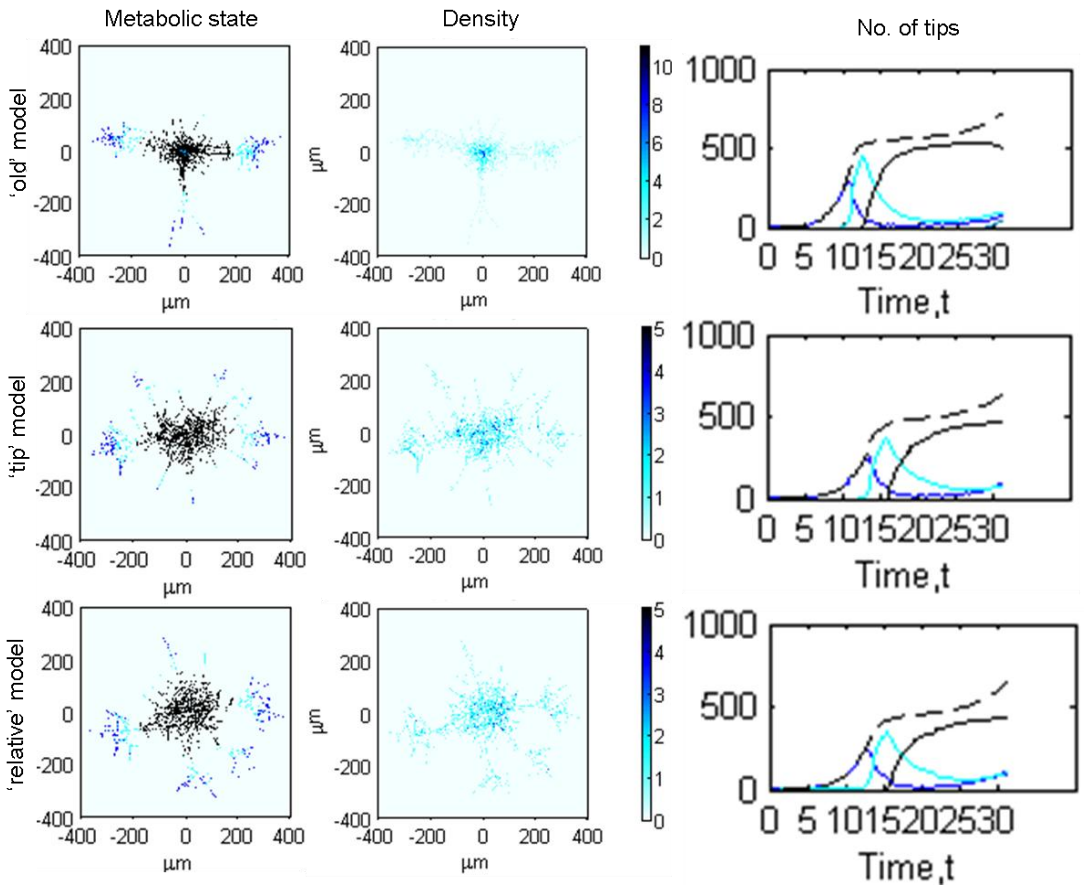

Figure 6.8: The effect different branching rules have on pellet morphology and metabolism in high average velocity (+100%) simulations. The pellet simulations (metabolic state, density) are at the end of the exponential growth. Metabolic state and the number of tips illustrate actively growing hyphae (dark blue), antibiotic producing hyphae (cyan), maintenance requirements only (black) and dead hyphae (light blue). The total number of tips is shown as black dashed line. The rest of the model parameters are shown in Tables 3.2 and 3.3 and Figure 3.14.

In order to establish how much the oxygen gradient observed around the pellet plays a role in the formation of the long unbranched and branched hyphae in high velocity simulations, we update the model further to include a stirring effect for the external oxygen outside the pellet. The stirring is modelled by assuming an inner domain at the periphery of the pellet. The inner domain connects from tip to tip located at the outskirts of the pellet. Outside of this inner domain, the oxygen concentration is assumed to be equally dispersed and above a minimum level. Inside of the inner domain the oxygen diffusion (and consumption) is modelled to occur as described previously (Figure 6.9).

Figure 6.10 shows the simulation comparison between average hyphal velocity and high (+100) average hyphal velocity using the model updates where the distance to the new branching point is calculated from the tip and the stirring effect for of external oxygen is included. The oxygen concentration simulation with high velocity shows that with the stirring effect, the gradient is only within the pellet area, with an approximately homogeneous oxygen concentration externally to the spheroid due to the stirring. Note that by including the stirring effect in the model, the base rate (average velocity 6.3 μm/h) simulations resulted in creation of a pellet that consisted of actively growing hyphae only (image not shown). Even when the rescaled oxygen consumption rate ($\overline{d}_c^b$) is increased from 1 x 10^{-5} to 1 x 10^{-4} (as shown in Figure 6.7) the pellet appeared fully metabolically active at the end of the exponential growth phase. Importantly, with an increased average velocity (+100%) the pellet shape stays the same (no long, single unbranched or branched hypha as in Figure 6.4) and that the pellet appears larger yet not denser. However, in this case three metabolic states of hyphae (active growth, antibiotic production, maintenance only) are observed and the pellet diameter is 742 μm and red pellet area is 4.4 x 10^4 μm^2 at the end of the exponential growth phase. Note that the high velocity in this simulation comparison magnifies the pellet growth beyond the biological variance seen in Figure 4.14 and Table 4.8.

Interestingly, a resemblance was noticed between the pellet simulations of the stirring model, using 1 x 10^{-4} μm^{-2} as rescaled oxygen consumption rate, and the initial model, using 1 x 10^{-6} μm^{-2} as rescaled oxygen consumption rate, when the average velocity was the base value of 6.3 μm/h (compare Figures 6.10 and 3.13). Note that the rescaled oxygen consumption rate of 1 x 10^{-6} μm^{-2} is the original value estimated from experimental data (see Chapter 3). It therefore seems that the initial model, using the experimental oxygen consumption rate estimation, is able to produce simulations that are convergent with the stirring model with a higher oxygen consumption rate. This new finding motified us to run simulations using the initial model (with no stirring effect) with the experimental estimate of 1 x 10^{-6} μm^{-2} as a rescaled oxygen consumption rate but with the calibrated value of 54% for the external oxygen concentration at the green/red interface. The resulting simulation gives a red pellet area of ca 0.5 x 10^4 μm^2 with a pellet diameter of 376 μm at the end of the log phase (image not shown). When the external oxygen value at the green/red interface was increased to 64%, the resulting red pellet area at the end of logarithmic phase was ca 1.5 x 10^4 μm^2 which is close to the experimental value of 1.71 x 10^4 μm^2. The corresponding pellet diameter is 334 μm which also fits within the biological variance seen in experiments (compare to Table 4.8).

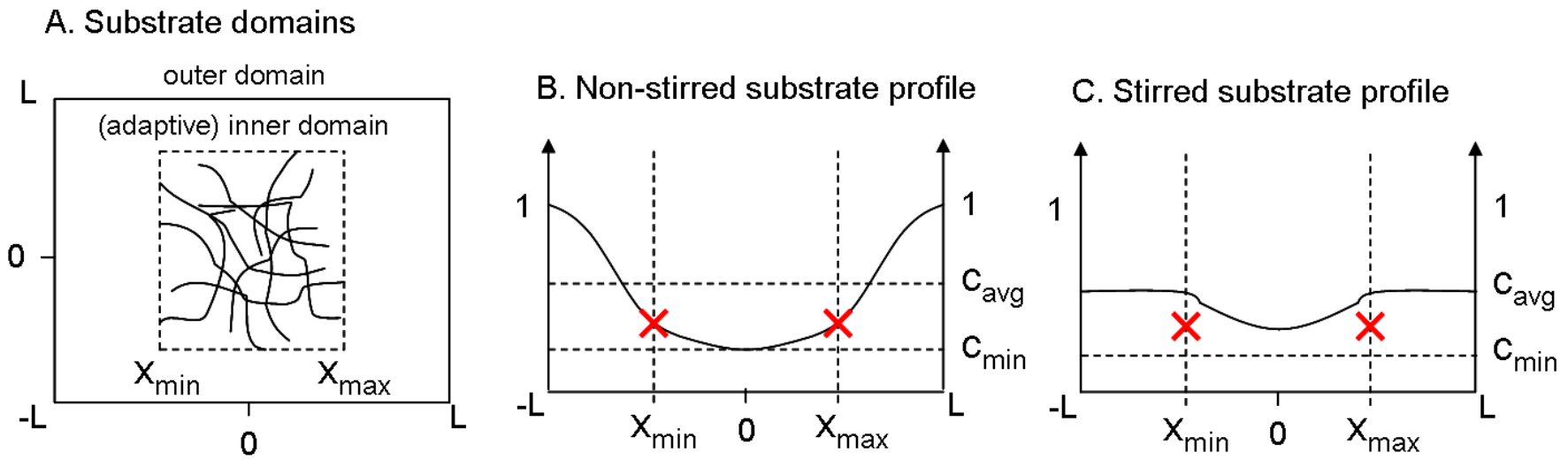

Figure 6.9: Schematic illustration of the stirring effect. A. Substrate (c) domains showing the inner (adaptive) domain at the outskirt of the pellet (x_{min}, x_{max}) and the outer domain –L x L. B. Substrate concentration profile of the old model (without stirring effect). Note, the substrate gradient appearing outside the inner domain. C. Substrate concentration profile of the stirring effect. Outside the inner domain the substrate concentration is constant at an average value (c_{avg}). Inside the inner domain the substrate concentration is above the minimum concentration (c_{min}).

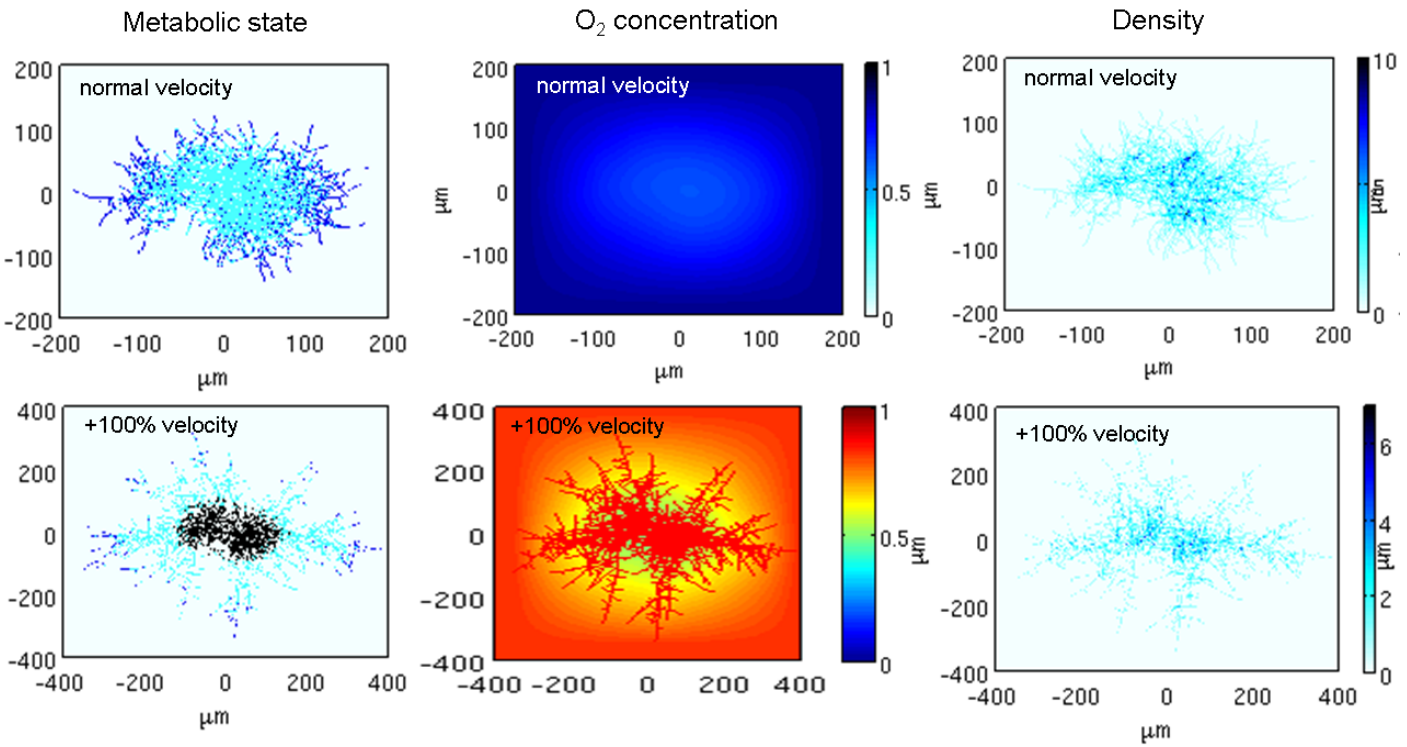

Figure 6.10: Simulation comparison of hyphal velocity affecting the pellet metabolism at the end of log-phase as modelled with updated stirring effect. Metabolic state illustrates actively growing hyphae (blue), antibiotic producing hyphae (cyan) and maintenance requirement only hyphae (black). The oxygen concentration profile for the high velocity (+100) simulation also shows the location of hyphae. The model used for the simulations calculates branching distance from the tip and includes stirring. The scaled oxygen consumption rate ($\overline{d_c}^b$) is 1 x 10^{-4} in the simulations. The rest of the parameters are as shown in Tables 3.2 and 3.3 and Figure 3.14.

The updated parameter values (i.e. 1 x 10^{-6} μm^{-2} as rescaled oxygen consumption rate and 64% for the external oxygen concentration at the green/red interface) were then used to further assess the difference between the three different branching rule models (see Figure 6.9) (Note, no stirring effect was included here). From here onwards, these three branching models are referred to as ‘old’ (branching distance calculated from the last branching point), ‘tip’ (branching distance calculated from the tip) and ‘relative’ (branching distance calculated relative to both apical and interbranch distances). It is noticed (See Figure 6.11) that the ‘old’ simulation produces a very dense pellet with a large number of tips. The antibiotic production also appears earlier in this simulation than what is observed in the simulations of the other two branching models. Both the ‘old’ and ‘relative’ models produce maintenance requirements only cells within the simulation time, with branch-old model showing a higher number of them.

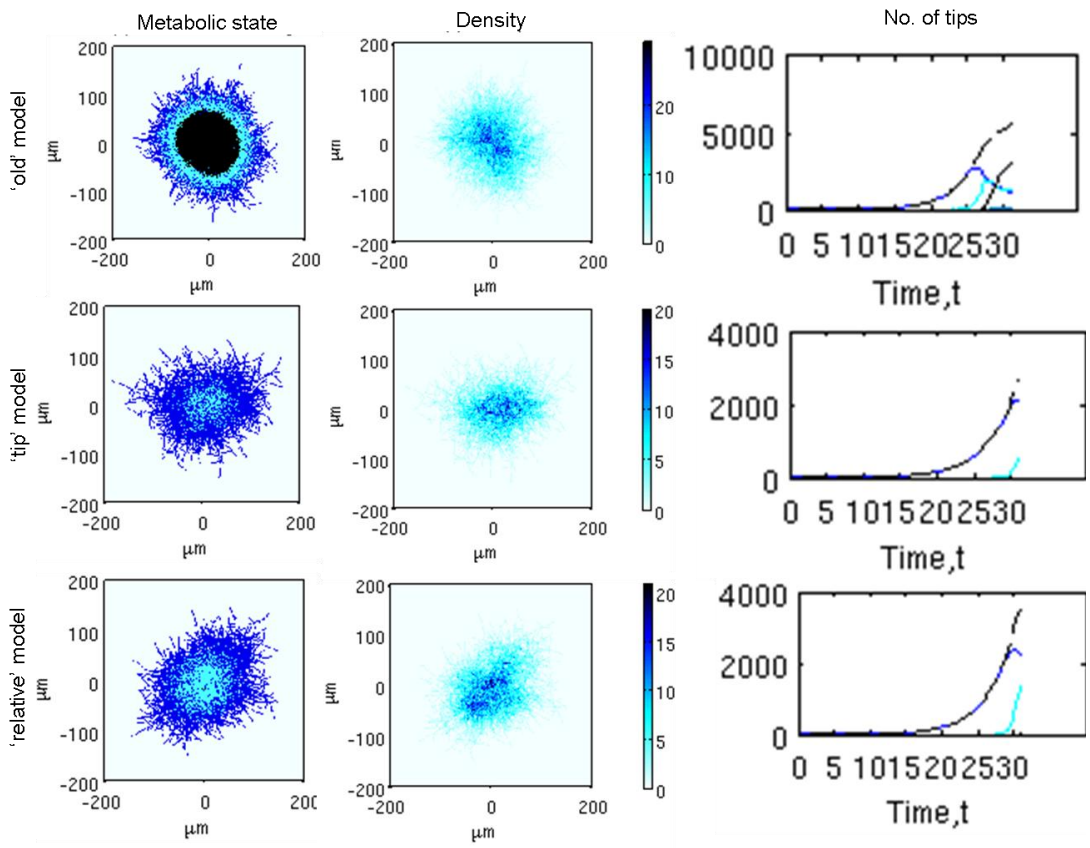

Figure 6.11: Simulation results comparing three different branching models 'old', 'tip' and 'relative' (without stirring effect) using experimental estimates for rescaled oxygen consumption (1 x 10^{-6}) and for the recalibrated, external oxygen concentration at the green/red interface (64%) (rest of the parameters as per Tables 3.2 and 3.3 and Figure 3.14). The metabolic states of hyphae are illustrated as blue for active growth, cyan for antibiotic production and black for maintenance requirements only, for metabolic state and number of tips simulations.

To draw further biological insight into measurements such as HGU and the area for antibiotic producing cells inside a pellet at the end of log phase, we run simulations using the different branching rule models with varying apical and interbranch distances. At first, the simulations are run with the apical and inter-branch lengths as measured in this study at a 10 h time point of the growth curve experiment, in which we see a long apical branch distance and short inter-branch distance which we will refer to as the standard parameters (see Table 3.2). To start with, we use the branching models without the stirring effect but with parameter values of 1 x 10^{-6} μm^{-2} for the rescaled oxygen consumption and 64% for the recalibrated, external oxygen concentration at the green/red interface (see Figure 6.12) (Note, that the resulting pellet morphologies are presented in previous Figure 6.11). The results show that all the three branching models give an HGU of around 20-23 μm for standard branching parameters but the 'tip' model creates smaller antibiotic production area than the other two branching models. The standard deviations for the simulation outcomes are shown. Unfortunately, with these parameter values, the time to run one simulation increases tremendously due to the larger number of tips being present. Therefore, to gain some insight we then changed the parameter values of rescaled oxygen consumption and external oxygen concentration at the green/red interface back to 10^{-5} μm^{-2} and 54% respectively. This time, the antibiotic producing areas are more or less the same size between the three branching models with the standard branching distances, where as the HGU varies between ca 21-25 um (see Figure 6.13).

In Figure 6.13, the HGU and the pellet area of antibiotic producing cells are also presented for the apical and inter-branch lengths associated with the less frequent branching patterns (L) and for parameter values associated with the frequent branching (F) (see Table 6.2 for the parameter values). Interestingly, the 'old' model shows the smallest antibiotic producing area with frequent branching pattern where as the 'relative' model has the smallest area using less frequent branching pattern. The size of the antibiotic

producing area did not change in ‘tip’ model between the different branching pattern parameters. The simulation results for HGU were compared to experimentally determined HGU. The HGUs in the experiments were 32.63 ± 1.6 µm for less frequent (Allan and Prosser,1983) and 18.1 ± 5.4 µm for the standard branching. For less frequent and standard branching the simulated HGUs are ca 29-31 µm and ca 21-25 respectively. The HGU values in simulations resemble the values seen in experiments. Further analysis of the simulation results show, as expected, that increasing branching frequencies in the models reduces the HGUs. This monotonic form, however, is not repeated in any of the models when comparing the sizes of the pellet areas producing antibiotics. The size of the area of antibiotic producing cells differs depending on which branching pattern parameters and branching rule models used.

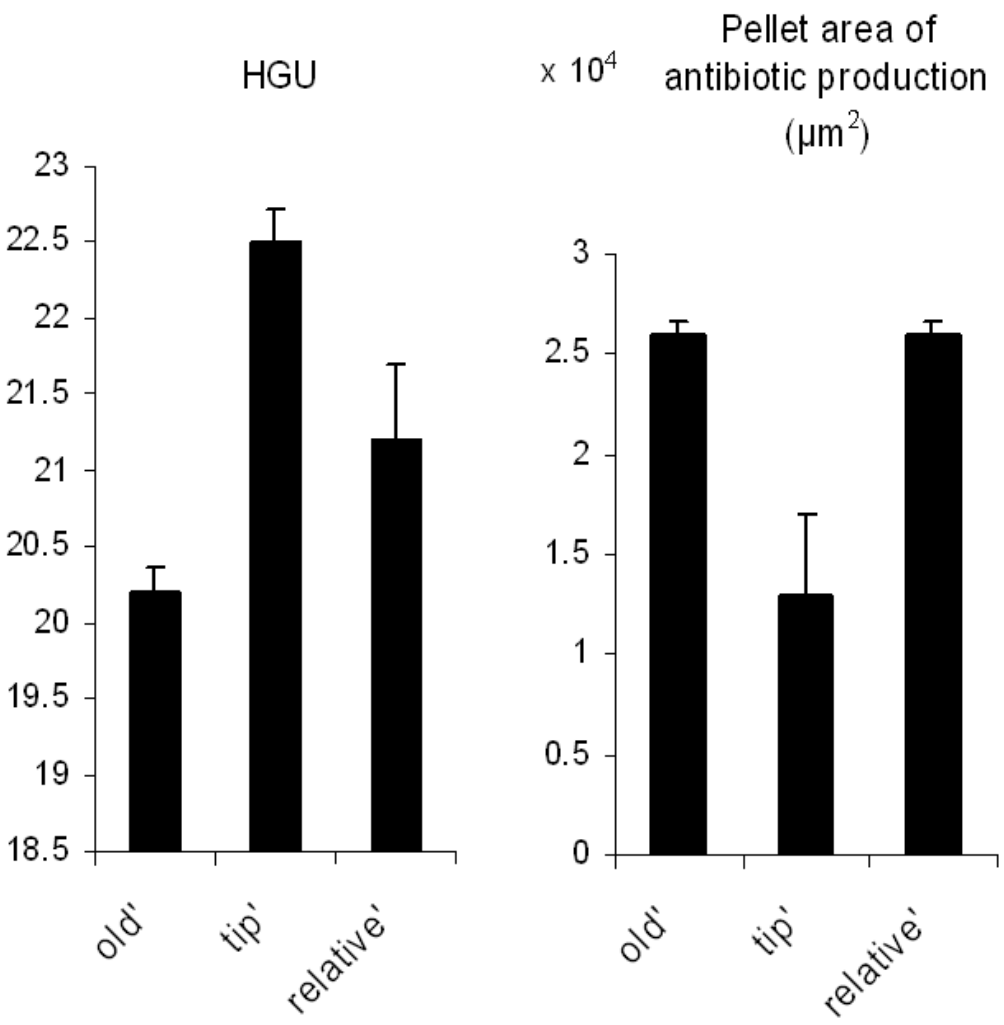

Figure 6.12: Simulations comparing the three branching rule models ('old', 'tip', 'relative'). Simulation results are from the end of log phase using 1 x 10^{-6} μm^{-2} for the rescaled oxygen consumption and 64% for the external oxygen concentration at the green/red interface and standard branching pattern (see Tables 3.2 and 3.3 and Figure 3.14 for rest of the parameters). Three different branching rule models: branching distance calculated from last branching point ('old'), from the tip (brangh_tip) or relative for both apical and interbranch distances ('relative') (see text for further information). The bars show standard deviation.

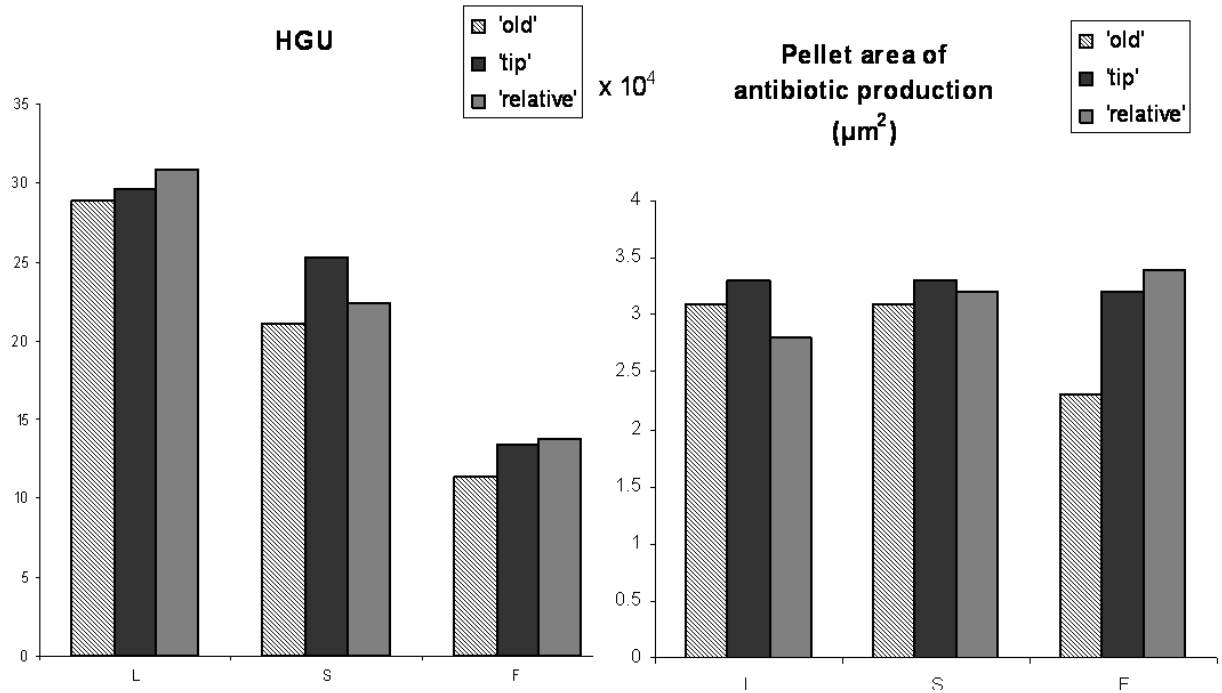

Figure 6.13: Three branching rule models compared to each others using three branching patterns. The simulation results show HGU and antibiotic producing pellet area at the end of log phase using 1 x 10^{-5} μm^{-2} for rescaled oxygen consumption and 54% external oxygen concentration at the green/red interface. Three different branching patterns are less frequent (L), standard (S) and frequent (F) branching (see Table 6.2 for used parameter values). The branching rule models are the following: branching distance calculated from last branching point (‘old’), distance calculated from the tip (brangh_tip) or distance calculated relative to both apical and interbranch distances (‘relative’) (see text for further information). The rest of the parameters are shown in Tables 3.2 and 3.3 and Figure 3.14.

Summary and conclusions

In this chapter, we have explored the robustness of the model behaviours for varying parameter estimates. Unexpected aspects of the model were identified (such as external oxygen gradient and increased unsuccessful branching) and the model design was revised by altering the branching rules and by adding a stirring effect to the external oxygen concentration. It was noticed that the original model with the rescaled oxygen consumption rate, estimated from experimental data, reflected the stirring effect simulations. The comparison between the different branching pattern simulations highlighted the importance of hyphal density to pellet morphology and metabolism. Variance was observed in the model outputs such as the HGU and the area of antibiotic production, between the different branching rule models using the different branching pattern parameters. Another issue relating to the model design also rose from the discrepancy noticed in the pellet development over time seen between the model simulations and the growth curve experiment, which is likely to affect the size of the antibiotic producing pellet areas at the end of the growth curve simulations. Further biological analysis of the model is needed to properly assess these issues.

Chapter 7: Transcription in *S.coelicolor*

To study transcription in live *S.coelicolor* with a view to incorporation of the dynamics in to a future model, we translationally fused eGFP to the RNA polymerase beta-subunit (*rpoC*) in its native chromosomal location. The fusion was confirmed by sequencing and by Southern blot and the functionality of eGFP was confirmed by fluorescence microscopy (see Chapter 5).

RNAP is localized at the sites of DNA and is absent from the tip

Fluorescence microscopy images of the eGFP fusion were taken from strain LN301 grown on cover slips over two days at 30°C and then stained with fluorescent dyes to illustrate DNA (SYTO42) and cell membranes (FM4-64). Figures 7.1 and 7.2, show that the transcription complexes are co-localized with nucleic acids rather than with the cell membranes. It was noticed that the fluorescent signal from RpoC-eGFP did not localize at the hyphal tips. Moreover, the fluorescent signal from the nucleic acids was located closer to the tip than RpoC-eGFP.

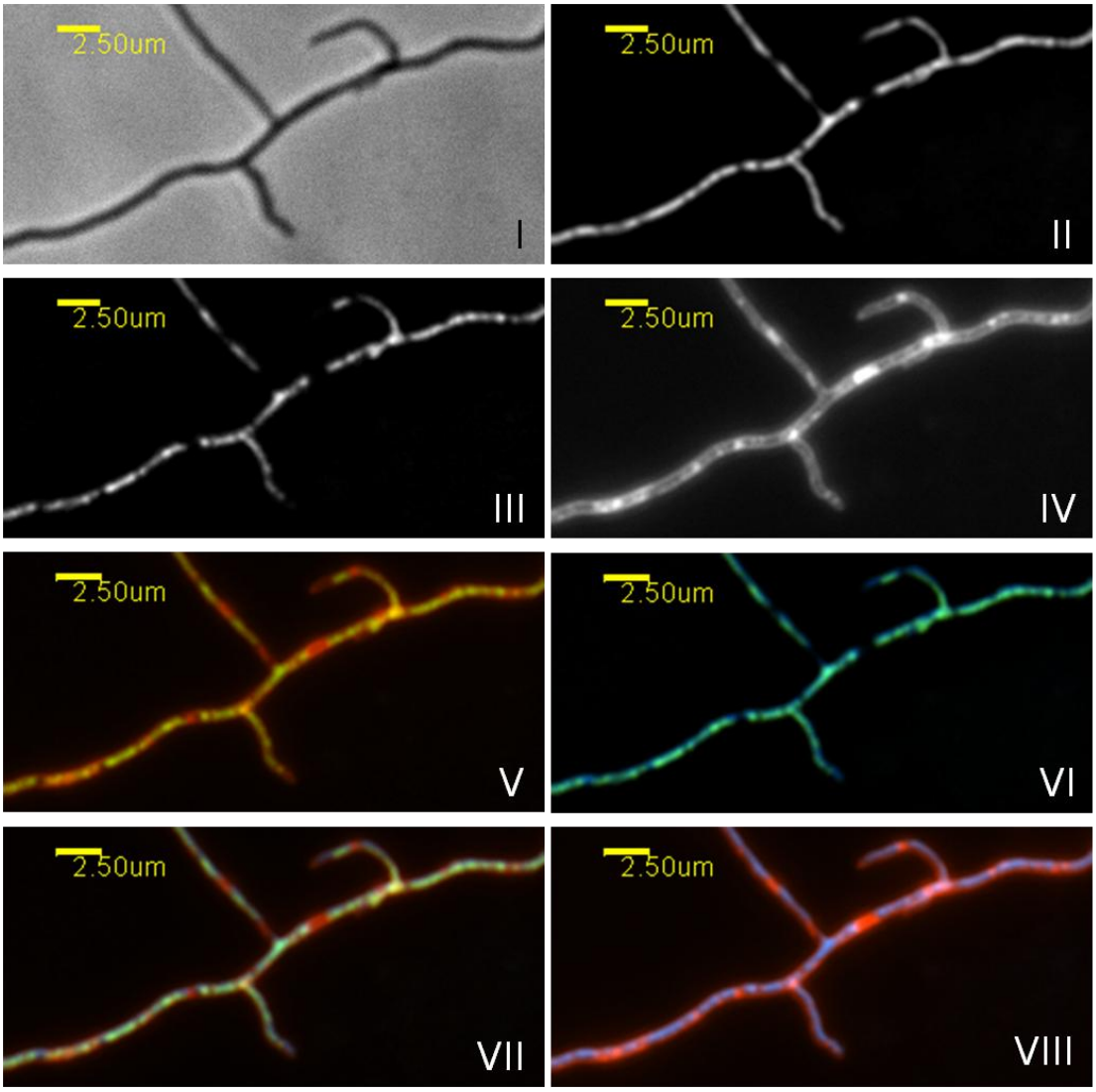

Figure 7.1: Localization of RpoC-eGFP in vegetative hyphae of strain LN301. A phase contrast image of hyphae (I) and fluorescence images of nucleic acids (II), RpoC-eGFP (III) and cell membranes (IV) are shown. Multiprobe images of RpoC-eGFP with cell membranes (V), RpoC-eGFP with nucleic acids (VI), RpoC-eGFP with both nucleic acids and cell membranes (VII) and just cell membranes with nucleic acids (VIII) are also illustrated. The colours in multiprobe images correspond to green for RpoC-eGFP, blue for nucleic acids and red for cell membranes. The nucleic acids and cell membranes were stained with SYTO42 and FM4-64 respectively. Deconvolution was performed on z-section images. Scale bar of 2.5 µm is shown.

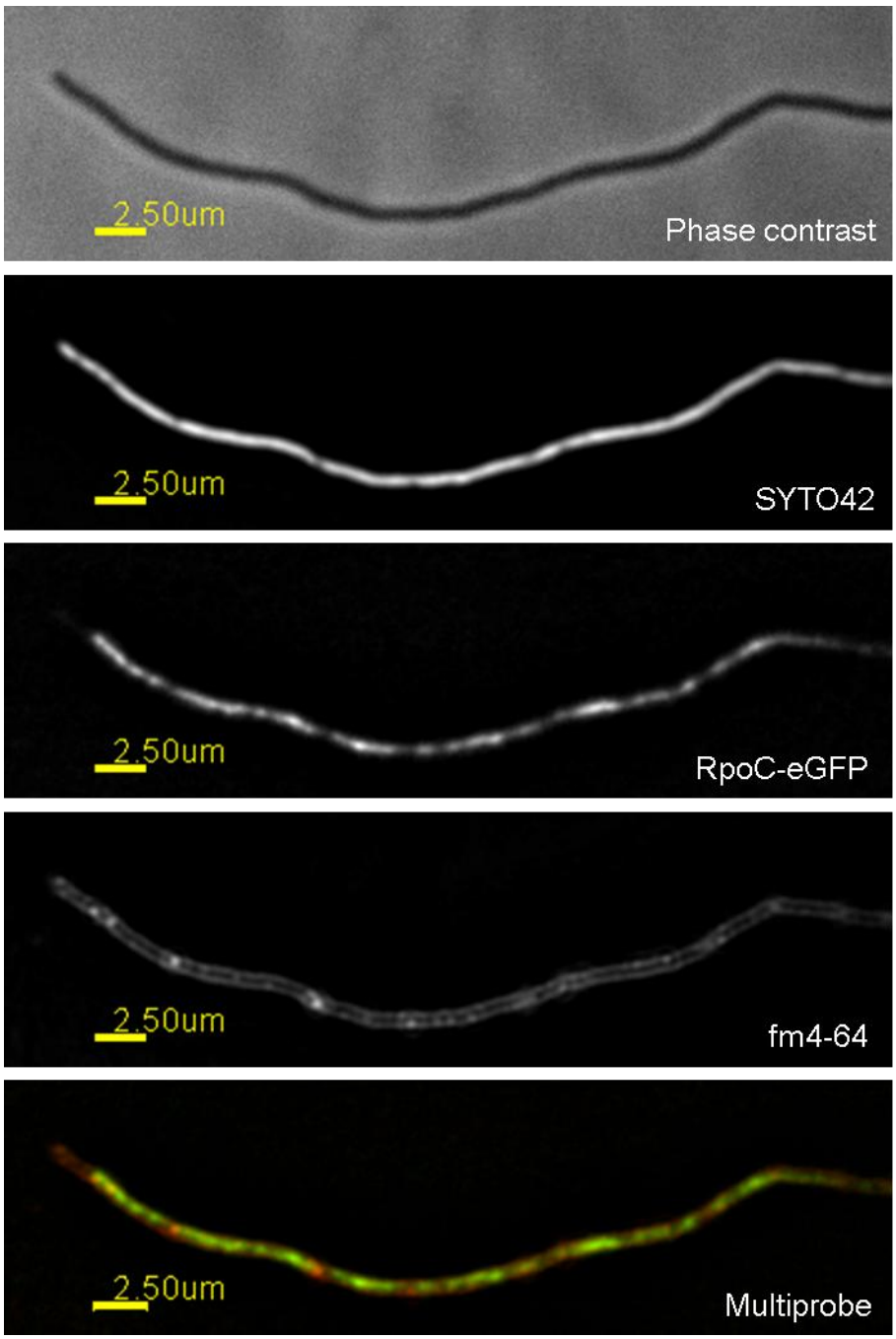

Figure 7.2: Localization of RpoC-eGFP at the hyphal tip. Fluorescence images of nucleic acids (SYTO42) and cell membranes (FM4-64) are shown. Multiprobe image illustrates the location of cell membranes (red) and RpoC-eGFP (green). Note that RpoC-eGFP is not located at the hyphal tip. Deconvolution was performed on z-section images and the used scale bar 2.5 µm.

To study the localization of RpoC-eGFP at the hyphal tips in live, actively elongating hypha, strain LN301 was observed under the microscope over a prolonged period of time (ca 5 hours). The bacteria were grown at 30°C, inside a microdisc, under two different growth conditions, minimal medium (MM) containing 5% (wt/vol) mannitol and nutrient agar (NA), to establish a low and high growth rates respectively. The measured growth rates were around 10.1 ± 3.6 μm/h (mean ± standard deviation, n = 12, CV% = 35) on MM with mannitol and around 18.9 μm/h ± 4.3 μm/h (mean ± standard deviation, n = 8, CV% = 23) on NA. Microscopic images were taken every 10 minutes and videos of the hyphal elongation were constructed using IPLab programme (see videos 1 and 2 on supplemented DVD). Still images of both growth conditions are shown in Figure 7.3. Through observation of the videos 1 and 2, it became evident that in many parts of the vegetative hyphae, the location of RpoC-eGFP was dynamic along the hyphae (see further analysis later on in this chapter), and that the RpoC-eGFP was never located at the hyphal tip. The length of the space between the hyphal tip and the eGFP fluorescence in actively elongating hyphae was then measured from the videos 1 and 2 (see Table 7.1). The average lengths ± standard deviations of this space in low and high growth rate experiments were 2.0 ± 0.4 μm and 1.7 ± 0.2 μm, respectively. The difference in space was statistically significant (p-value of 0.0053) between the two growth rates.

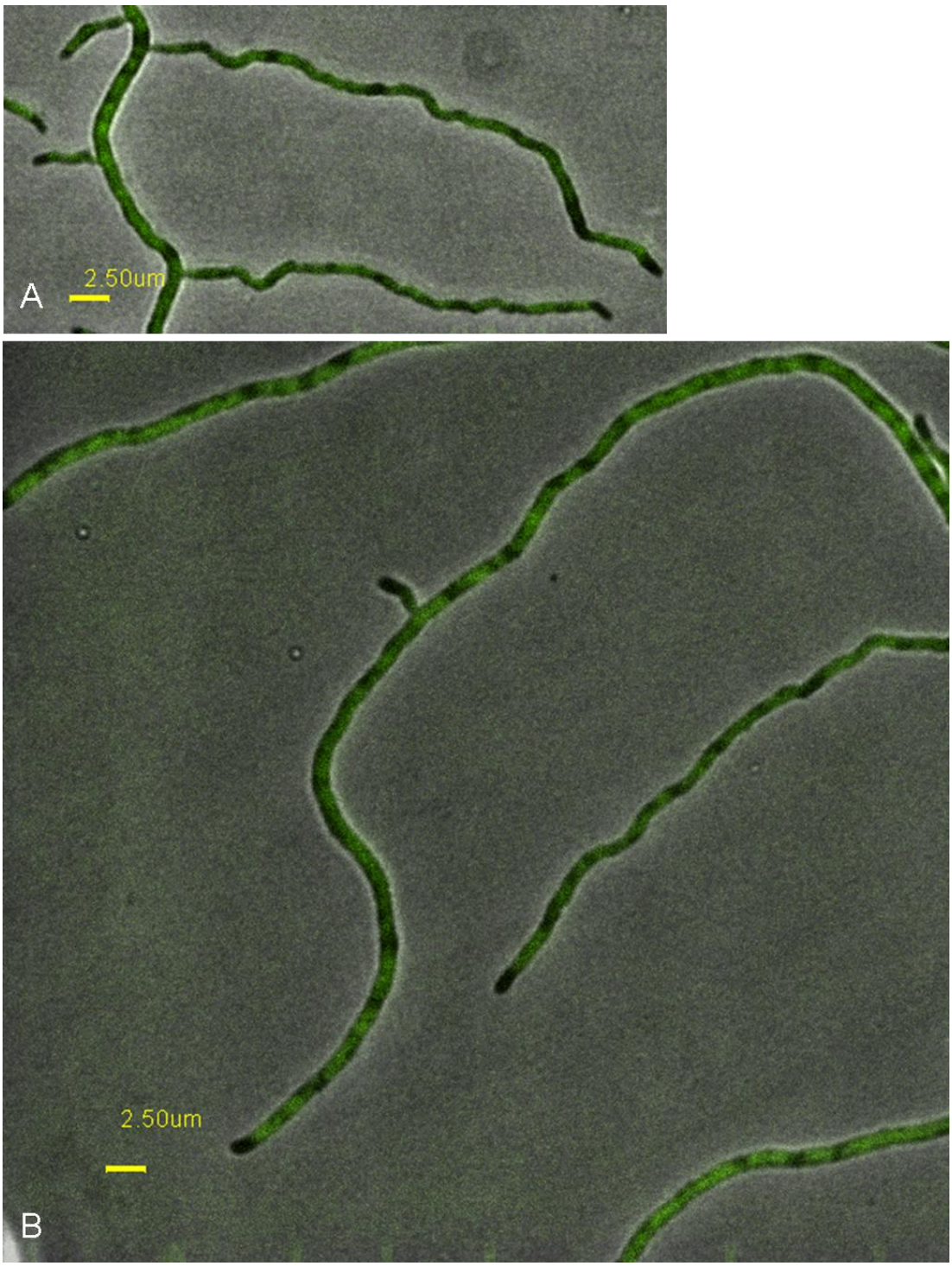

Figure 7.3: Location of transcription during low and high growth rates. Multiprobe images of hyphal growth are presented for low growth on minimal medium containing 5% mannitol (A) and high growth on nutrient agar (B) (see also videos 1 and 2). Green colour corresponds to RpoC-eGFP. The used scale bar is 2.5 µm.

Table 7.1: Distance between the tip to the nearest RpoC-eGFP in actively elongating hyphae. The bacteria were grown on minimal medium with 5% mannitol and nutrient agar to establish low and high growth rates, respectively (see videos 1 and 2).

	Low growth rate	High growth rate	Total measured†
Mean (µm)	2.0*	1.7*	1.8
Stdev	0.4	0.2	0.3
CV%	18.5	12.9	18.7
n	14	15	29

* Statistically significant difference (p-value 0.0053).

† Measurements from both low and high growth rate experiments combined.

To establish the relationship between the apical location of RpoC-eGFP and other macromolecules and proteins with known apical subcellular locations, we compared our data with values from the literature. Table 7.2 shows the known distance from the hyphal tip to DivIVA-eGFP, an indicator of an active tip and/or branching point (Flärdh, 2003), and to the nearest ParB-eGFP, an indicator of DNA *parS* sequences located near to the origin of replication (*oriC*; Jakimowicz *et al*., 2005; Jakimowicz *et al*, 2002), and to the DnaN-eGFP, an indicator of DNA replication machinery (Wolánski et al., 2011; Ruban-Ośmiałowska *et al*., 2006). The apical ParB-eGFP is located at ca 1.4 µm away from the tip. This distance is shorter than what we saw for the apical RpoC-eGFP (around 1.8 µm) and indicates that chromosomal DNA is present closer to the tip than where the apical fluorescent signal for transcription is detected. Some of this difference noticed in location could be down to the experimental set up and/or strain dependant elongation rate, however, our SYTO42 stained images of strain LN301 (see Figures 7.1 and 7.2) support the observation that the transcription complexes are located further away from the tip than nucleic acid. The fact that apical replisomes are located at around 5.32 µm (±2.0 µm) from the tip, as shown by DnaN-eGFP (Wolánski *et al*., 2011), poses an intriguing observation that these data, along with our fusion protein suggest that there is a well defined hierarchy at the hyphal tip that has different molecular processes spatially separated during apical growth.

Based on the results from the fluorescence microscopy in this study and previously published data shown in Table 6.2, we proposed the following model for tip hierarchy where the apical spatial order, starting from the hyphal tip, is nucleic acids, transcription complexes and DNA replication complexes (Figure 7.4). The space taken up by DivIVA is not included in the model. Subcellular organization of a tip exists for example in fungi where an apical cluster of vesicles, cytoskeletal elements and other proteins have previously been named as Spitzenkörper (Steinberg, 2007).

Table 7.2: Apical localization of known eGFP constructs.

Average apical distance ± standard deviation (µm)	eGFP construct	Reference
At the tip	DivIVA-eGFP	Flärdh, 2003
1.4 ± 0.3	ParB-eGFP*	Jakimowicz *et al*., 2005
1.8 ± 0.3	RpoC-eGFP	this study
5.3 ± 2.0	DnaN-eGFP†	Wolánski *et al*., 2011

* Marks *parS* sites that are located in close proxima to *oriC* (Jakimowicz *et al*., 2002).

† Marks the site of replisomes (Ruban-Ośmiałowska *et al*., 2006).

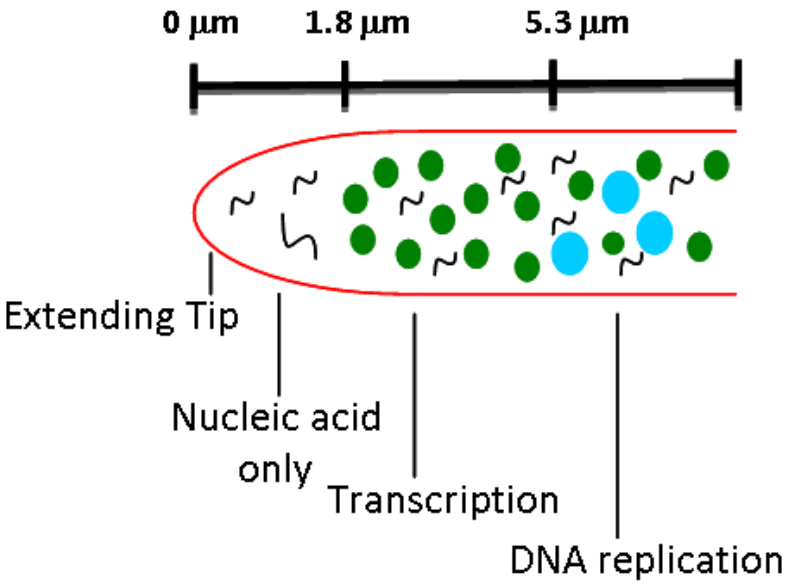

Figure 7.4: Model for apical localization of macromolecular syntheses. The transcription and replication are spatially separated at the hyphal tip. The apical spatial order of the molecular components is nucleic acids (black lines), transcription complexes (green dots) and DNA replication complexes (blue dots). The scale bar relates to the distances shown in Table 7.2.

The hypothesis of spatial separation of transcription and DNA replication at the hyphal tip was further tested experimentally. A strain DJ542 harboring translational fusion of DnaN to mCherry (a red fluorescent protein) was kindly provided by Dr Dagmara Jakimowicz, University of Wroclaw, Poland. The *rpoC-eGFP* fusion from Chapter five was conjugated in to the DJ542 strain in order to visualize both the transcriptional and DNA replication localization within the same hyphal tip. Fluorescence microscopy was performed on DJ542/RpoC-eGFP grown on minimal medium with 5% mannitol. The results in Figure 7.5 show four actively elongating, leading hyphae of strain DJ542/RpoC-eGFP. In three out of four cases the RpoC-eGFP localized at the same distance from the tip as the DnaN-mCherry. However, what was striking was the actually distance. The RpoC-eGFP was noticed to lag behind the tip at ca 3.5 μm distance, which is much longer than what had been seen before. The maximum tip to RpoC-eGFP distance, previously measured from actively elongating LN301 hypha grown on minimal medium with 5% mannitol, is only 2.6 μm (n=14, see above). This might imply that the tagging of both transcription and replication with fluorescent proteins may disrupt the normal growth of hyphae and alter the location of RNAP at the hyphal tip.

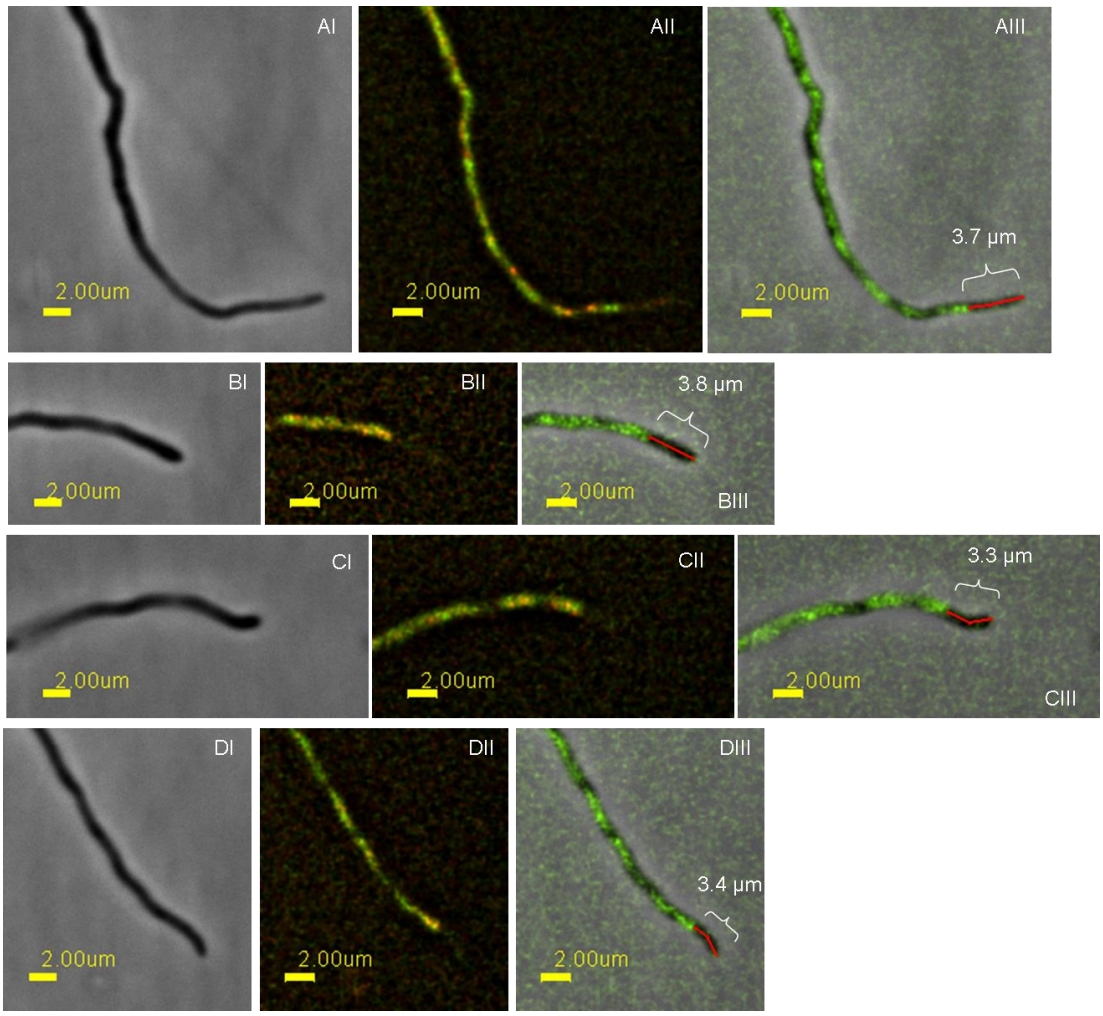

Figure 7.5: Apical localization of RpoC-eGFP and DnaN-mCherry in strain DJ542/RpoC-eGFP. Four actively elongating, leading hyphae are presented (A-D). The images show brightfield (I), multiprobe of RpoC-eGFP (green) together with DnaN-mCherry (red) (II), and multiprobe images of RpoC-eGFP (green) with brightfield (grey) where the tip to apical RpoC-eGFP distance is measured (red, µm) (III). The used scale bar is 2 µm (yellow). The strain was grown on minimal medium with 5% mannitol.

Dynamics of RNAP during vegetative growth

It was observed from the low and high growth rate videos 1 and 2, respectively (see supplemented DVD), that some transcription foci moved along the hyphae. To analyse the foci movement, measurements were made from apical (first foci from the hyphal tip) and subapical foci within hyphae (Table 7.3). The speed of foci were measured from hyphae grown on either nutrient agar or on minimal medium with mannitol. The speed of a subapical foci movement was difficult to measure due to the resolution of the microscopy images, however, measurements were made from a subapical foci adjacent to a distinctive space between two foci (during a time period of 20 - 30 min). The measured subapical foci were located at different distances (5 - 27 µm) behind their respective tips (note, that the measurements were made from actively elongating hyphae, and that there were no existing or emerging branches in the hyphal area between the tip and the foci at the time of measurement). It was observed that the speed of the subapical foci was around 33% less than the speed of its apical foci. No difference was observed in the apical foci speed and the extension rate of the hyphae (data not included). The speed of the subapical foci did not seem to be related to the tip-proximal distance the subapical foci were located at. Internal hyphal movement has previously been observed in replisomes where it has been reported that both hte apical and the subapical replisomes move along the hypha at a speed equivalent to the extension rate of the tip (Wolánski *et al*., 2011).

Table 7.3: The speed of RpoC-eGFP foci located within an apical area of hyphae. The measurements were made from strain LN301 grown on nutrient agar (NA) or minimal medium with mannitol (MM).

	Speed of apical foci (µm/h)	Speed of subapical foci (µm/h)	Distance between the tip and the subapical foci (µm)	Percentage of foci speed from the tip speed (%)
Hypha 1 (NA)	22	18	10	82
Hypha 2 (NA)	22	14	10	63
Hypha 3 (NA)	17	10	27	59
Hypha 4* (MM)	16	10	23	62
Hypha 4* (MM)	17	11	5	67

* same hypha, two, separate foci measurements were made at different time points.

The RpoC-eGFP fluorescence however was not uniformly distributed within foci. Moreover, in some older parts of hyphae the transcription foci were observed to have no movement. These stagnant areas were noticed to fluoresce at higher intensity at later time points. It can be speculated that these stagnant, high fluorescent areas are due to spatially increased autofluorescence as seen in Willemse and Wezel (2008). However, the exposure time (100 ms) used in this study is much lower than the exposure times used in Willemse and Wezel (2008) study (1 - 20 s). Moreover, our control strain, a fully grown wildtype M145 mycelium, showed no fluorescence under the used exposure time (100 ms). Figures 7.6 and 7.7 are a collection of still images from low and high nutrient medium reflecting low and high growth rate videos respectively.

We measured the length of the transcription foci in both low and high growth rate videos (see Table 7.3). No statistically significant difference was seen in the length of the RpoC-eGFP foci between the two growth conditions. The total of 116 measured transcription complexes had an average length of 2.5 µm with standard deviation of 1.6 (63.5 CV%) in actively elongating hyphae.

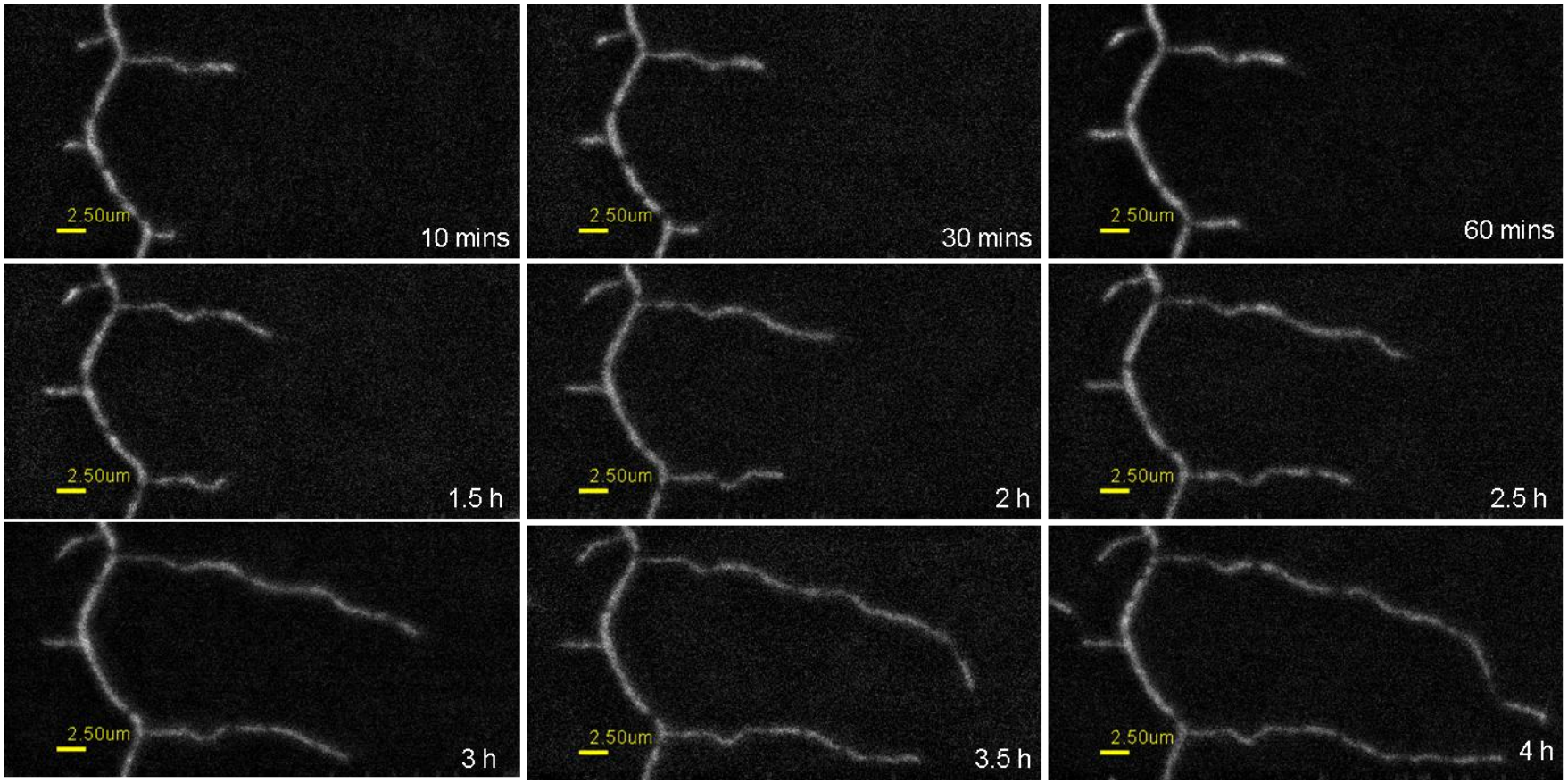

Figure 7.6: Time-lapse images showing the spatio-temporal localization of RpoC-eGFP during low growth rate experiment. Strain LN301 was grown on minimal medium containing 5% mannitol. Scale bar 2.5 µm.

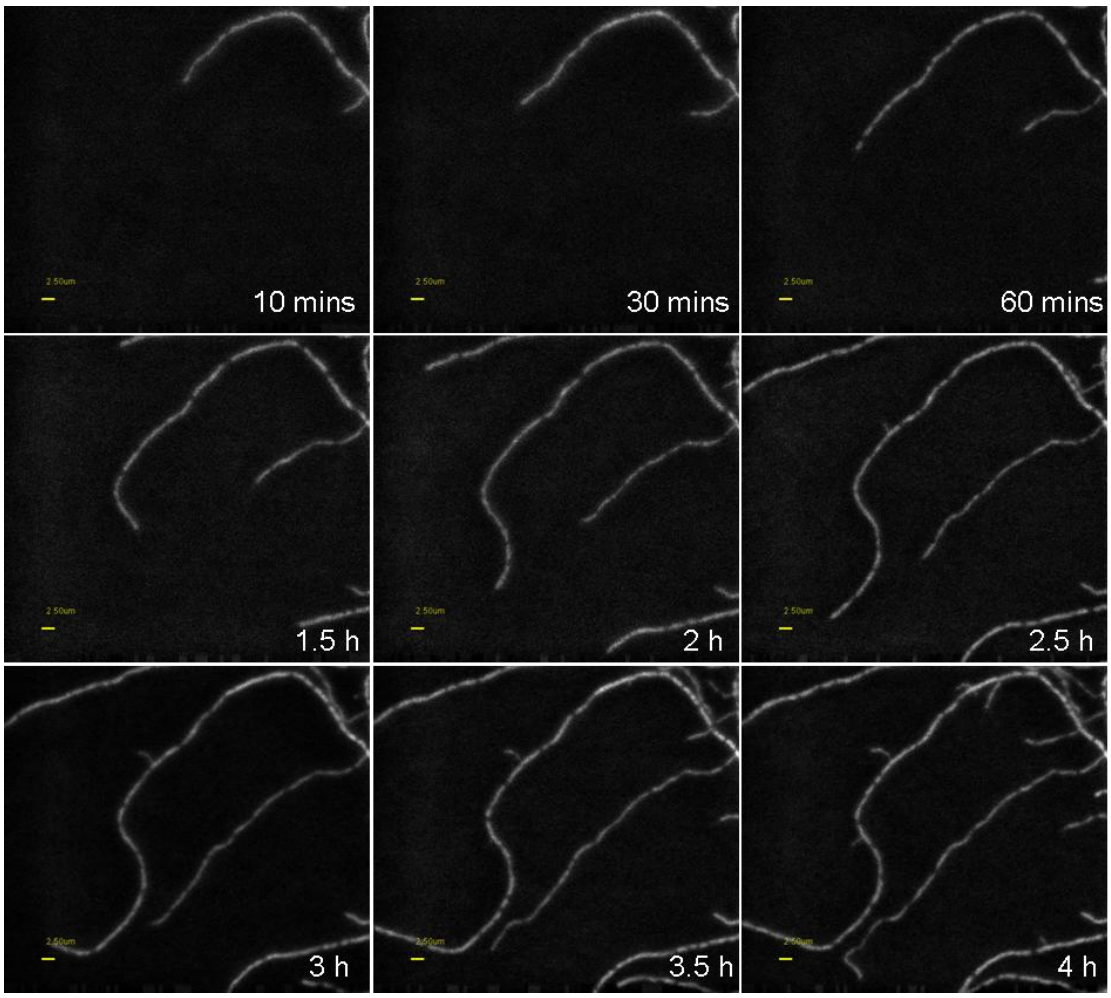

Figure 7.7: Time-lapse images showing the spatio-temporal localization of RpoC-eGFP during high growth rate experiment. Strain LN301 was grown in nutrient agar. The used scale bar is 2.5 µm.

Table 7.3: The length of RpoC-eGFP foci in elongating hyphae.

	Low growth rate (MM+Man)	High growth rate (NA)	Total measured*
Mean (μm)	2.5	2.5	2.5
Stdev	1.5	1.6	1.6
CV%	61.6	65.7	63.5
n	54	62	116

* Measurements from both low and high growth rate experiments together.

On nutrient agar (high growth rate) experiment, it was observed that the RpoC-eGFP foci seemed to be more condensed in older parts of hyphae compared to the apical regions. To see if this observation could be measured and analysed statistically, the average transcription foci lengths between the tip to the first branch and from first branch onwards were compared (see Table 7.4). The average length ± standard deviation of RpoC-eGFP foci was 2.9 ± 0.9 μm in apical locations and 2.7 ± 2.2 μm in interbranch locations. There is no statistically significant difference between the two locations.

Table 7.4: The length of RpoC-eGFP foci in apical (a) and interbranch (b) locations.

	a	b
Mean (μm)	2.9	2.7
Stdev	0.9	2.2
CV%	31.6	81.0
n	12	15

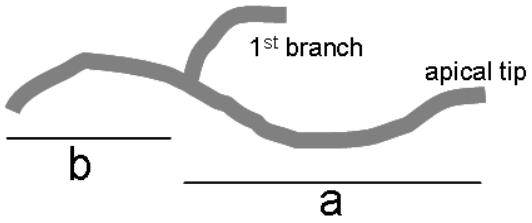

However, since measuring the RpoC-eGFP foci proved to be very challenging due to the difficulty in observing separate foci from each others, we did further data sorting where only measurements of equal to or less than 4 μm were included. The length 4 μm was chosen as a threshold since it had previously been measured that an average distance between replisomes was 4.01 ± 2.39 μm (Wolánski *et al*. 2011), therefore the likelihood to include only one nucleoid per transcription foci was thought to increase. In Table 7.5 the results from Tables 7.3 and 7.4 are presented after data sorting. The average length of RpoC-eGFP foci reduced to around 2 μm in both low and high growth rate experiments (Note, that these foci measurements include both the apical and interbranch locations). When the foci length measurements taken from either apical or interbranch locations on nutrient agar (high growth rate) were compared to each others after data sorting, it was noticed that the foci length reduced to around 2 μm in the interbranch locations, however, in the apical locations the average length of RpoC-eGFP foci stayed at around 2.7 μm. This time, the statistical analysis also showed that the tip to first branch foci measurements (apical) were significantly longer from the foci lengths in interbranch locations (p-value of 0.035).

Table 7.5: Data sorting of transcription foci length measurements. Only RpoC-eGFP foci that were equal to or less than 4 μm in length are included.

	Apical location †	Interbranch location †	Low growth rate (MM+Man)‡	High growth rate (NA) ‡
Mean (μm)	2.7*	2.0*	2.0	2.1
Stdev	0.8	0.6	0.6	0.8
CV%	28.4	28.1	31.5	38.3
n	10	13	47	55

* Statistically significant difference (p-value 0.035).

† Measured from nutrient agar (NA) grown culture. See Table 7.4 for comparison.

‡ See Table 7.3 for comparison. Data includes both apical and interbranch hyphal locations. MM+Man: minimal medium with mannitol

Localization of RNAP during *Streptomyces* development

S. coelicolor has a complex life cycle during which vegetative hyphae develop to form aerial hyphae and eventually, spore chains (Elliot *et al*., 2008). We observed the location of RNAP during the hyphal development by monitoring RpoC-eGFP localization in combination with fluorescence stains SYTO42 (nucleic acids) and FM4-64 (cell membranes). In Figure 7.8 the nucleic acids (II) and the cell membranes (IV) show a typical compartmentalized arrangement for aerial hyphae. Unsurprisingly, the RpoC-eGFP (III) was found inside the compartments together with the nucleic acids. However, as the fluorescence of SYTO42 was mainly confluent within the compartment, the RpoC-eGFP fluorescence was more concentrated to a certain area, sometimes showing a spot of higher intensity. Strain M145 was included in this experiment as a control. No autofluorescence was observed in the M145 under the used microscope settings for FITC filter set (eGFP) (Figure 7.9).

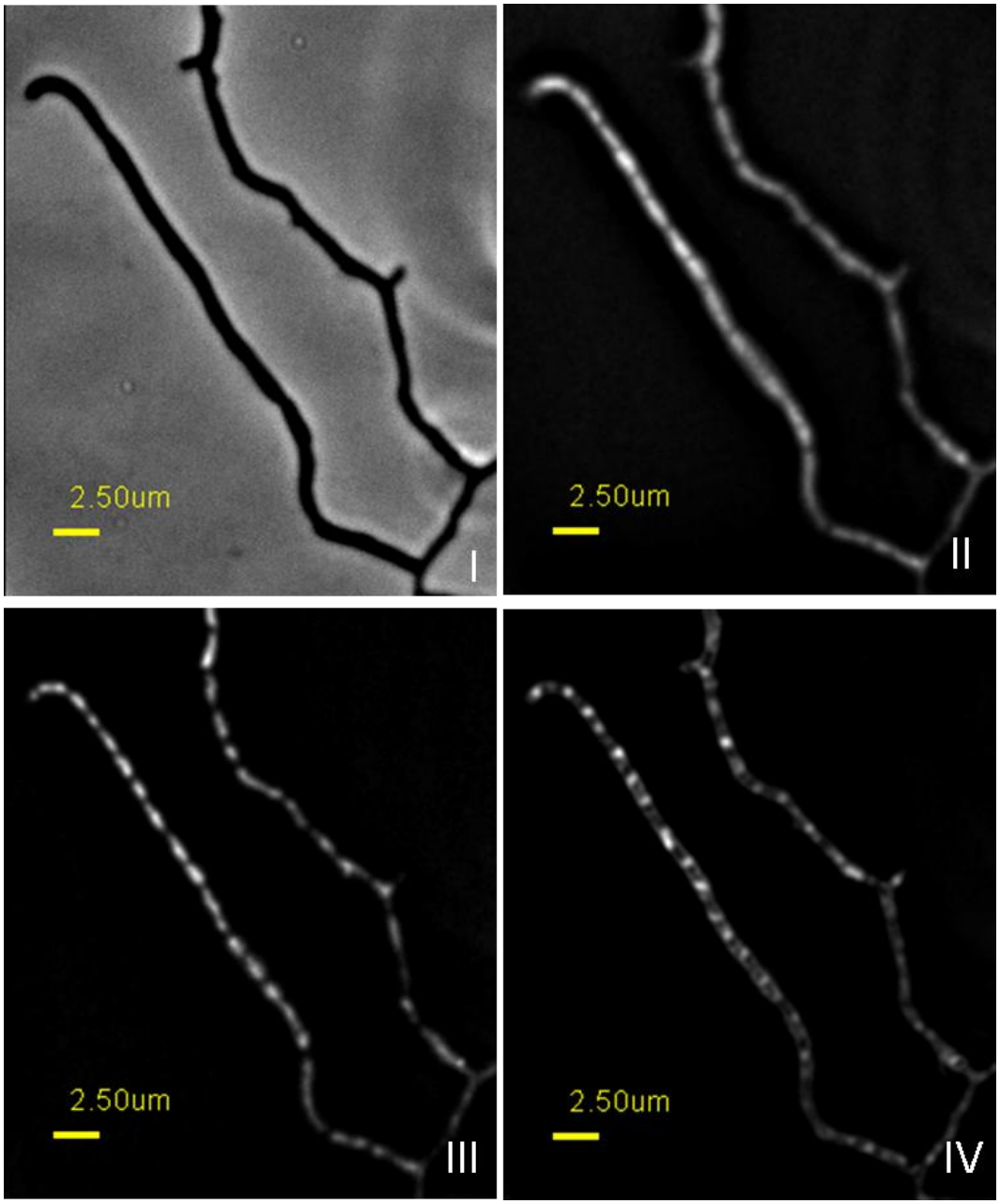

Figure 7.8: Location of RNAP in aerial hyphae of strain LN301. The images show aerial hyphae under bright field (I), nucleic acid as stained with SYTO42 (II), RpoC-eGFP (III) and cell membranes dyed with FM4-64 (IV). Deconvolution was performed on z-section images and the used scale bar is 2.5µm.

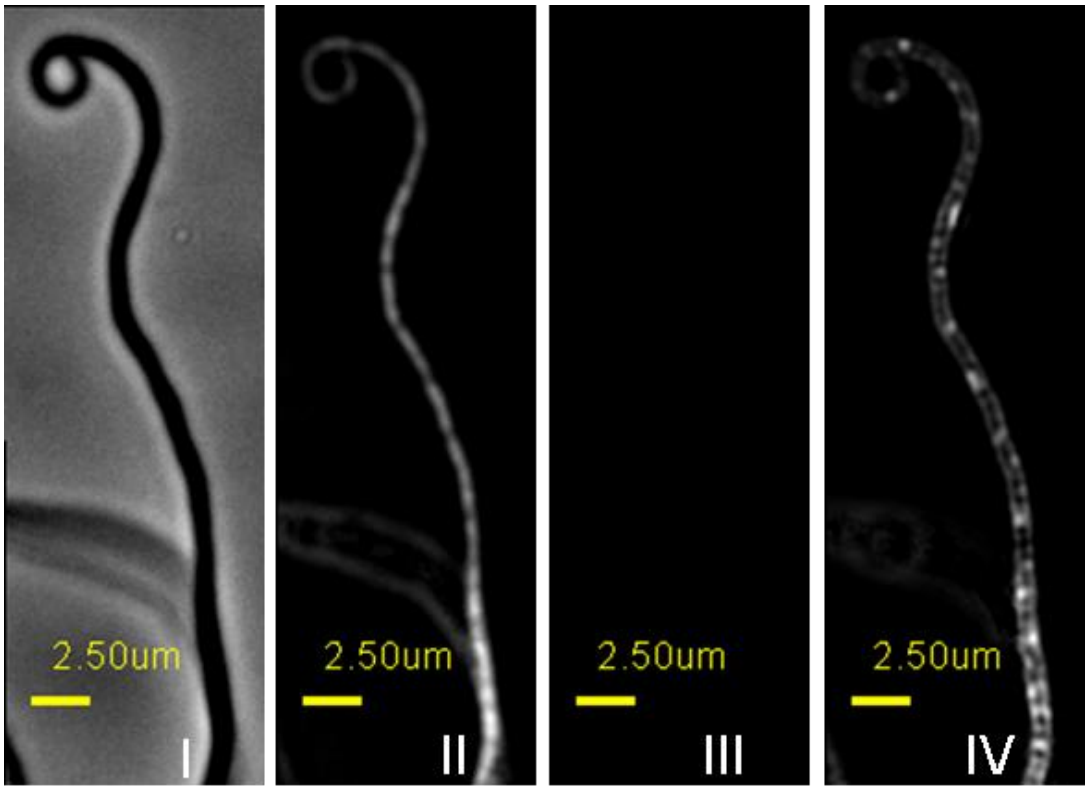

Figure 7.9: Aerial hyphae of control strain M145. Images illustrate the aerial hyphae under brightfield (I), and fluorescence filters for of nucleic acids (II, SYTO42), FITC filter (III, eGFP) and cell membrances (IV, FM4-64). Deconvolution performed on z-section images. No autofluorescence was observed under the used settings for the FITC filter set.

The above experiment was repeated to study RNAP localization in spore chains. A spore chain of LN301 is shown in Figure 7.10 and a control M145 showing no autofluorescence under FITC filter set is shown in Figure 7.11. RpoC-eGFP was found in each spore together with the nucleic acids (SYTO42). The fluorescence areas of the two were similar in size, unlike what had been observed in aerial hyphae. The cell membranes (FM4-64) were found at the edges of the spores. This also demonstrates the packaging of RNAP within the condensed nucleoids of spores.

Interestingly, a spore chain where fully formed spores occupied only half of the developed hypha, was spotted during the experiment (Figure 7.12). In the middle of this hypha, nucleic acids were observed to have formed a spore like structure (II, orange arrow). However, this putative spore lacked the well defined RpoC-eGFP fluorescence seen in the spores (III) and it showed no resemblance to other spores under brightfield imaging (I). Moreover, the cell membranes were noticed to have formed a plane in the middle of this putative spore that was not observed in the other spores (IV). Adjacent to the putative spore, there were matured spores at the top but a hyphal area of ca 2.5 µm in length, at the bottom that had high, location wise undefined, SYTO42 intensity, heterogenous RpoC-eGFP localization and low intensity from the FM4-64. This kind of relation between the different fluorescent levels had previously been observed in aerial hyphae (see above). It is tempting to make assumption that this hyphal area and the putative spore would evolve further in time and eventually form mature spores. In that case, the intensity levels seen at different stages of maturing spore would guide the understanding of spore development. However, more work is needed in order to confirm this kind of conclusion.

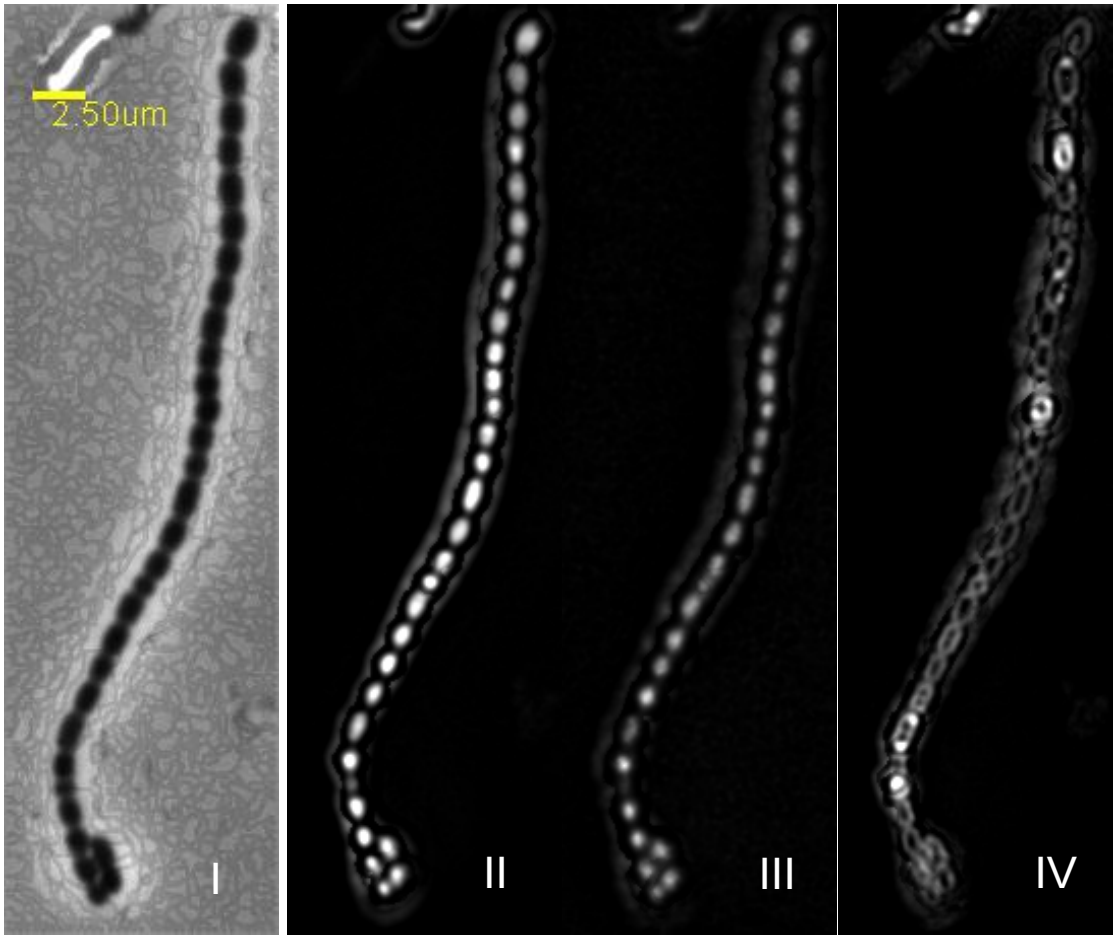

Figure 7.10: A mature spore chain of strain LN301. Brightfield (I), nucleic acids (II, SYTO42), FITC filter set (III, eGFP) and cell membranes (IV, FM4-64) are presented. Deconvolution was performed on z-section images.

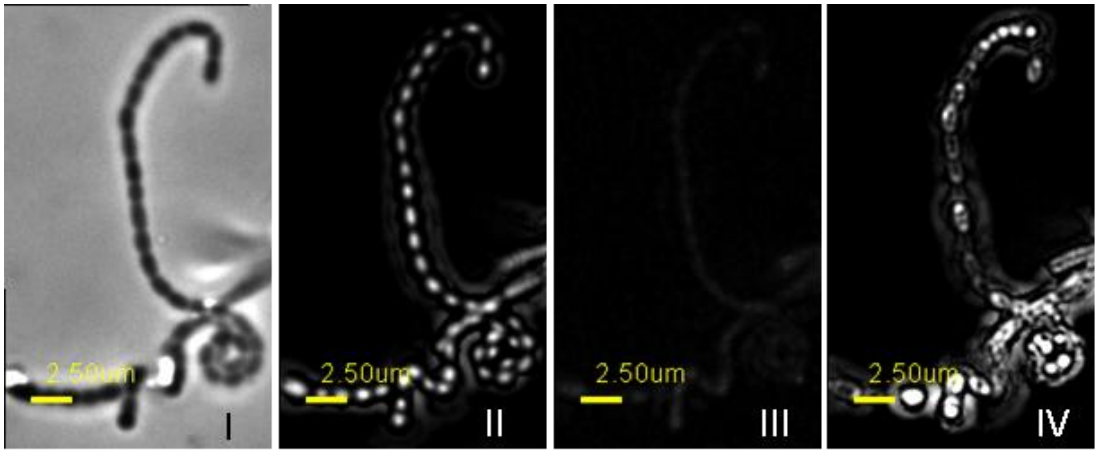

Figure 7.11: A spore chain of the control strain M145. Bright field (I) and fluorescent images are illustrated showing nucleic acids (II, SYTO42), FITC filter set (III, eGFP) and cell membrances (IV, FM4-64). Deconvolution was carried out on z-section images.

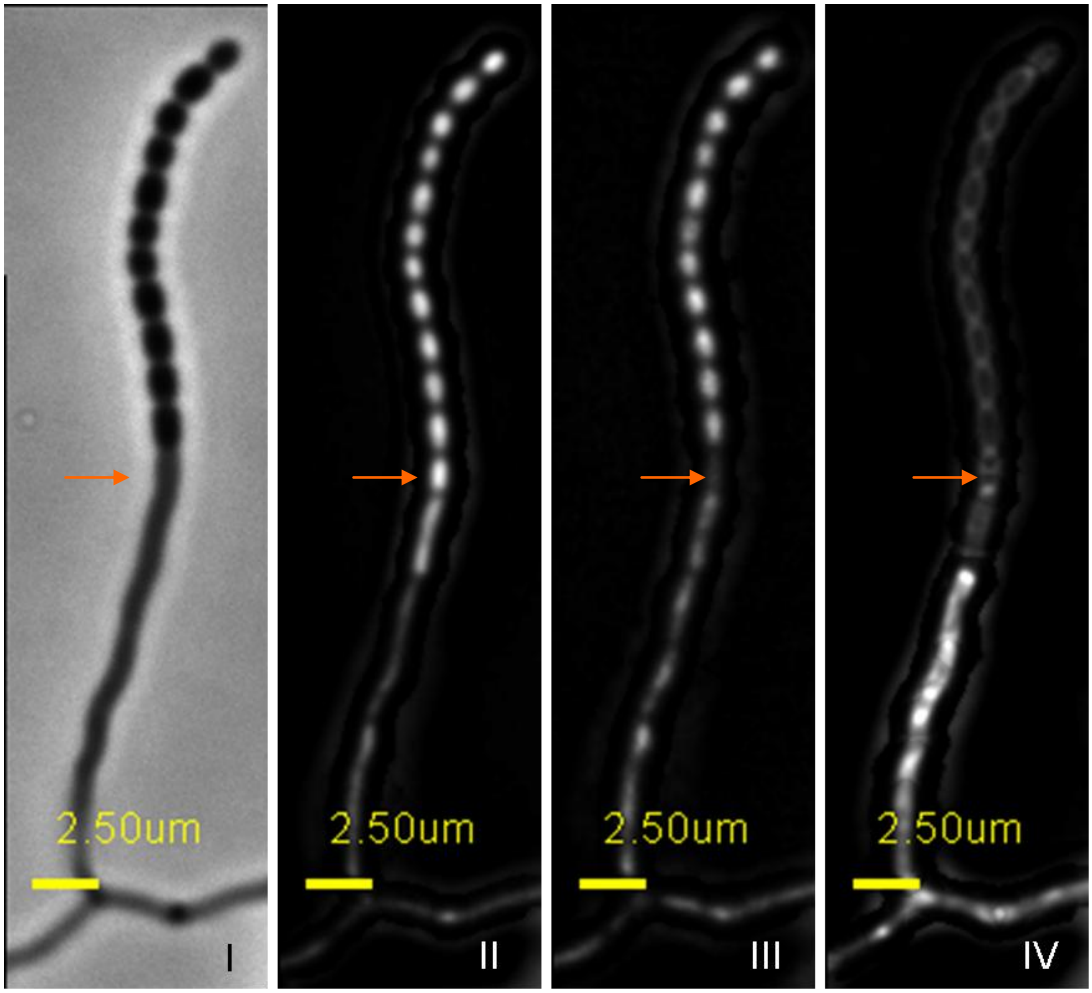

Figure 7.12: A half developed hypha of strain LN301. Images show brightfield (I), nucleic acids stained with SYTO42 (II), RpoC-eGFP (III) and cell membranes dyed with FM4-64 (IV). Z-section images were processed to achieve deconvolution. Orange arrow marks the site of a putative spore.

Localization of RNAP during hyphal development can also be studied in another way by taking advantage of the known developmental mutants of *S.coelicolor*. One such strain is J1681 (*ΔbldA*) that is deficient in the formation of aerial hyphae and sporulation. The gene *bldA* transcribes a rare tRNA with UUA codon that has been related to the expression of certain secondary metabolism genes (Leskiw *et al*., 1993). We created a translational fusion of RpoC-eGFP in J1681 strain and studied the localization of RNAP under fluorescent microscopy. In Figure 7.13, the images of J1681/RpoC-eGFP and LN301 are compared. No clear difference was observed in the RpoC-eGFP fluorescence between these two strains.

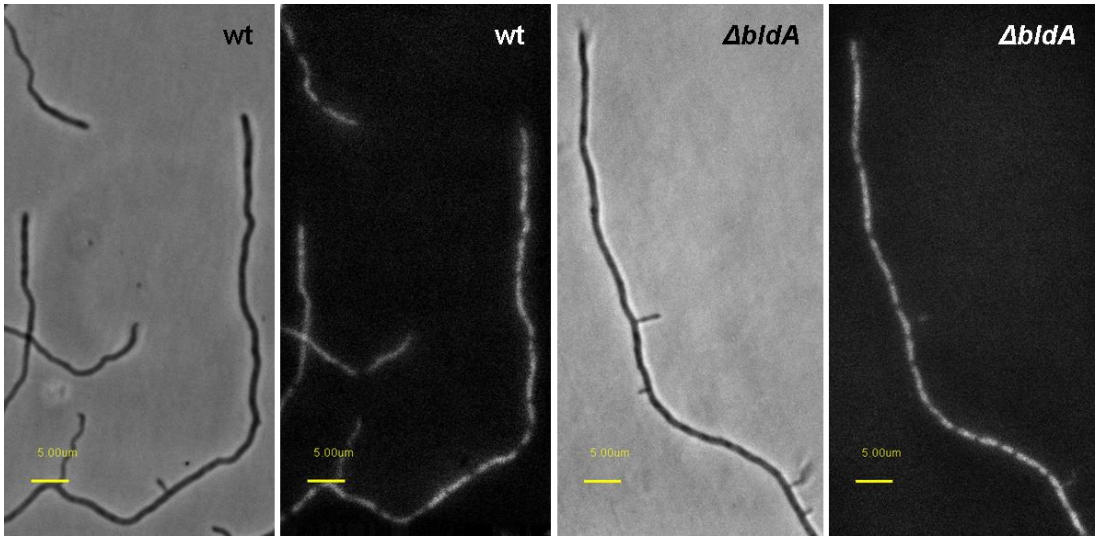

Figure 7.13: RNAP localization in developmental mutant strain J1681/RpoC-eGFP *(Δbld*A). Brightfield and FITC fluorescence images of RpoC-eGFP are presented. Strain LN301 (wt) was used as a control strain. The used scale bar is 5 µm.

RNAP is found in spores and in germ tubes

To test if *Streptomyces* stores RNAP in spores, we took several images of individual spores after long term storage (over a year) at -80 ˚C in 20% glycerol. Figure 7.14 shows a typical image of the spores of strain LN301. All the spores examined were found to fluoresce and therefore contain RNAP.

The localization of RpoC-eGFP in germ tubes of strain LN301 were examined together with the fluorescent dyes SYTO42 (nucleic acids) and FM4-64 (cell membranes). Unsurprisingly, RNAP was present in newly emerged hyphae at similar locations to the nucleic acids (Figure 7.15). However, in the germtubes, the fluorescence of the RpoC-eGFP was noticed at a very close proxima to the tip (< 1 μm). This occurred also in the second emerging germ tube even when the first emerged hypha had already reached a hyphal length of 44.6 μm and showed the lagging of RpoC-eGFP behind the tip at a standard length of 2.6 μm (Figure 7.16). This kind of close proxima of RpoC-eGFP to the hyphal tip has previously been seen in the rifampicin treated cultures (see further on in this chapter) when the distance to tip was measured to be ca 1 μm. Short tip-proximal distance has also been previously noticed in some hyphae that has stopped elongation. More work is needed in order to properly assess the transcription dynamics during the formation of germ tubes.

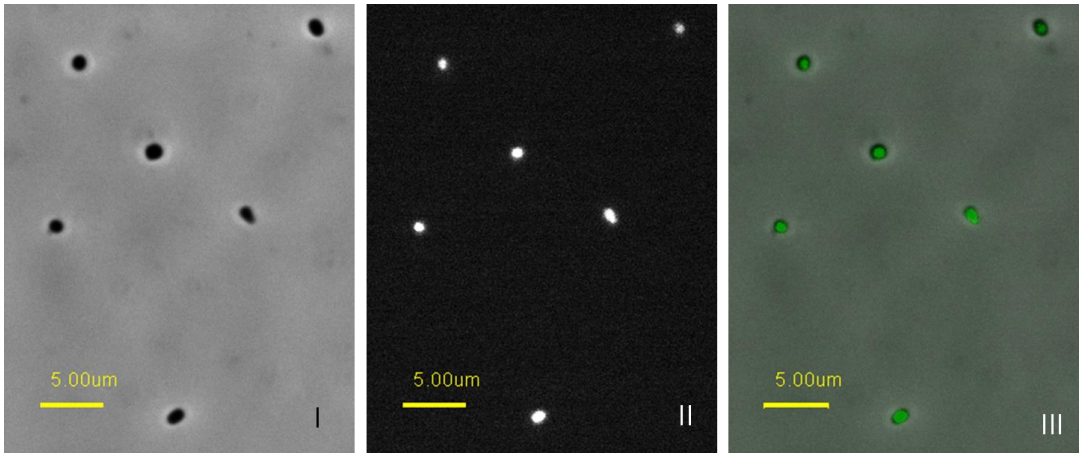

Figure 7.14: Spores of LN301 after long term storage. Brightfield (I), FITC filter set (II, eGFP) and multiprobe (III, where green corresponds to RpoC-eGFP) images are shown with the scale bar illustrating 5 µm in length.

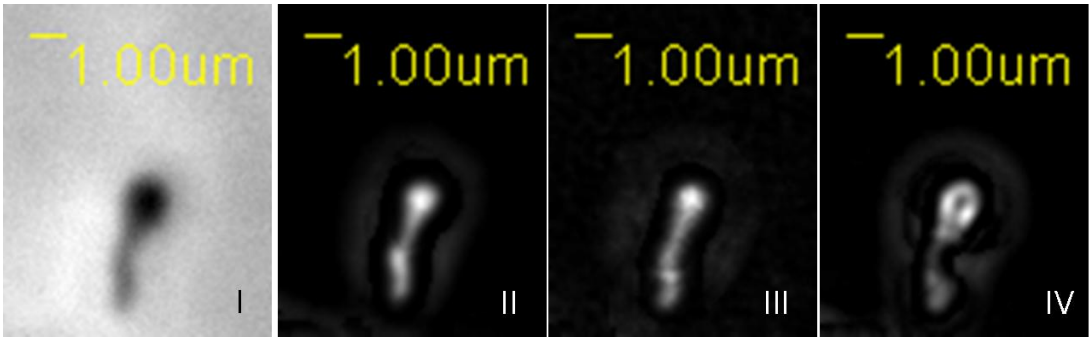

Figure 7.15: A typical germ tube of strain LN301. Brightfield (I) and eGFP (III, FITC filter set) images are presented together with fluorescent images for nucleic acids (II, stained with SYTO42) and cell membranes (IV, stained with FM4-64). Deconvolution performed on z-section images. Scale bar illustrates 1 µm.

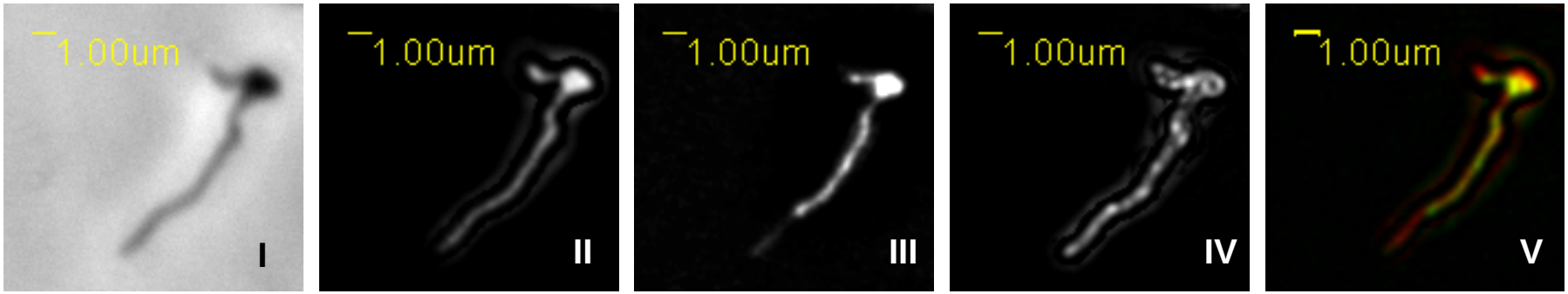

Figure 7.16: A germinated spore of strain LN301 showing both vegetative hypha and a germtube. The images illustrate brightfield (I, cells), SYTO42 (II, nucleic acids), eGFP (III, RpoC-eGFP), FM4-64 (IV, cell membranes) and multiprobe of SYTO42 and eGFP (V, RpoC-eGFP in green, nucleic acids falsely coloured in red for better contrast). Deconvolution was performed on z-section images and a scale bar of 1 µm is shown.

Localization of RNAP during nutritional stress

Visual inspection of RpoC-eGFP fluorescence images suggested that the foci are more intense/compact in high growth rate than in low growth rate. Another interesting observation was the level of the fluorescence within the foci that was not confluent and brighter areas were observed inside some of the foci. This variation in the intensity was suspected to be a consequence of various gene expression levels in different parts of a genome. It is known that a strategic order and orientation of genes exists within a bacterial genome in order to rapidly regulate gene expression in adaptation to environmental cues. One example of this is the duplication and origin-proximal location of rRNA operons to maximize their expression, ultimately maximizing the growth rate (Lewis *et al*., 2008). There are six rRNA operons in *Streptomyces coelicolor* genome and four of them are located at the left-hand end of the linear chromosome (Bentley *et al*., 2002), which might play a role in this compaction of the RpoC-eGFP foci. To test if the variation seen in the RpoC-eGFP intensity is down to the transcription foci formed around the rRNA operons, we took advantage of stringent response and mutagenesis. Under amino acid starvation, an uncharged tRNA binds to the acceptor site of translating ribosomes and causes the ribosomes to stall. This activates the stringent response and a ribosome-bound RelA is released to start synthesizing (p)ppGpp from ATP and GTP. The accumulation of alarmones, ppGpp and pppGpp, reduces the transcription of stable RNA genes (rRNA and tRNA) and increases the transcription of some amino acid biosynthetic operons (Ferullo and Lovett, 2008). In *S. coelicolor*, the ppGpp was also noticed to activate the *act*II-ORF4 transcription, a pathway-specific activator gene of actinorhodin biosynthesis (Hesketh *et al*., 2001).

Genes *relA*, ppGpp synthetase gene, and *rshA*, a *relA* homologue, are both involved in the stringent response in *S. coelicolor* (Chakraburtty and Bibb, 1997, Sun *et al*., 2001). At first, translational fusions of *rpoC-eGFP* were made in *S.coelicolor* knockout strains M570 (*ΔrelA*; Chakraburtty and Bibb, 1997), M680 (*ΔrshAΔrelA*; Sun *et al*., 2001) and M690 (*ΔrshA,* Andrew

Hesketh personal communication). The brightfield and fluorescence images of the three construct strains are shown in Figure 7.17. It has been reported that *Streptomyces coelicolor relA* null mutant, M570, is defective in the biosynthesis of ppGpp under nitrogen and carbon limitation (Chakraburtty and Bibb 1997, Yong-Gu *et al*., 2007), where as *rshA* gene has been related to ppGpp synthesis under phosphate limitation (Yong-Gu *et al*., 2007). To understand whether there was a specific transcription response to nitrogen availability, we grew *Streptomyces* strain M570/RpoC-eGFP, deficient in stringent response, under nitrogen limited conditions and observed the localization of RpoC-eGFP. If the different levels of fluorescence within foci were due to high ribosomal transcription, then we expected to see these brighter spots to disappear in the wild-type but keep existing in the mutant strain under nitrogen limitation. To perform the experiment, the strains were first grown on minimal medium with 5% mannitol and then transferred to minimal medium with 5% mannitol containing sodium nitrate instead of L-asparagine as the sole source of nitrogen in order to induce the stringent response (Karandikar *et al*., 1997). Imaging was started 10 minutes after induction and images of the strains LN301 and M570/RpoC-eGFP were taken every 10 min for ca 2 h period to monitor the spatio-temporal response of the RpoC-eGFP foci (see videos 3 and 4, respectively). The microscopy images of the experiment are shown in Figure 7.18. Hyphal growth continued under nitrogen-limited conditions in the same manner for both strains. Only a small slow down was noticed in elongation of some tips before and around one hour time point after induction. No clear shift in fluorescence pattern was observed.

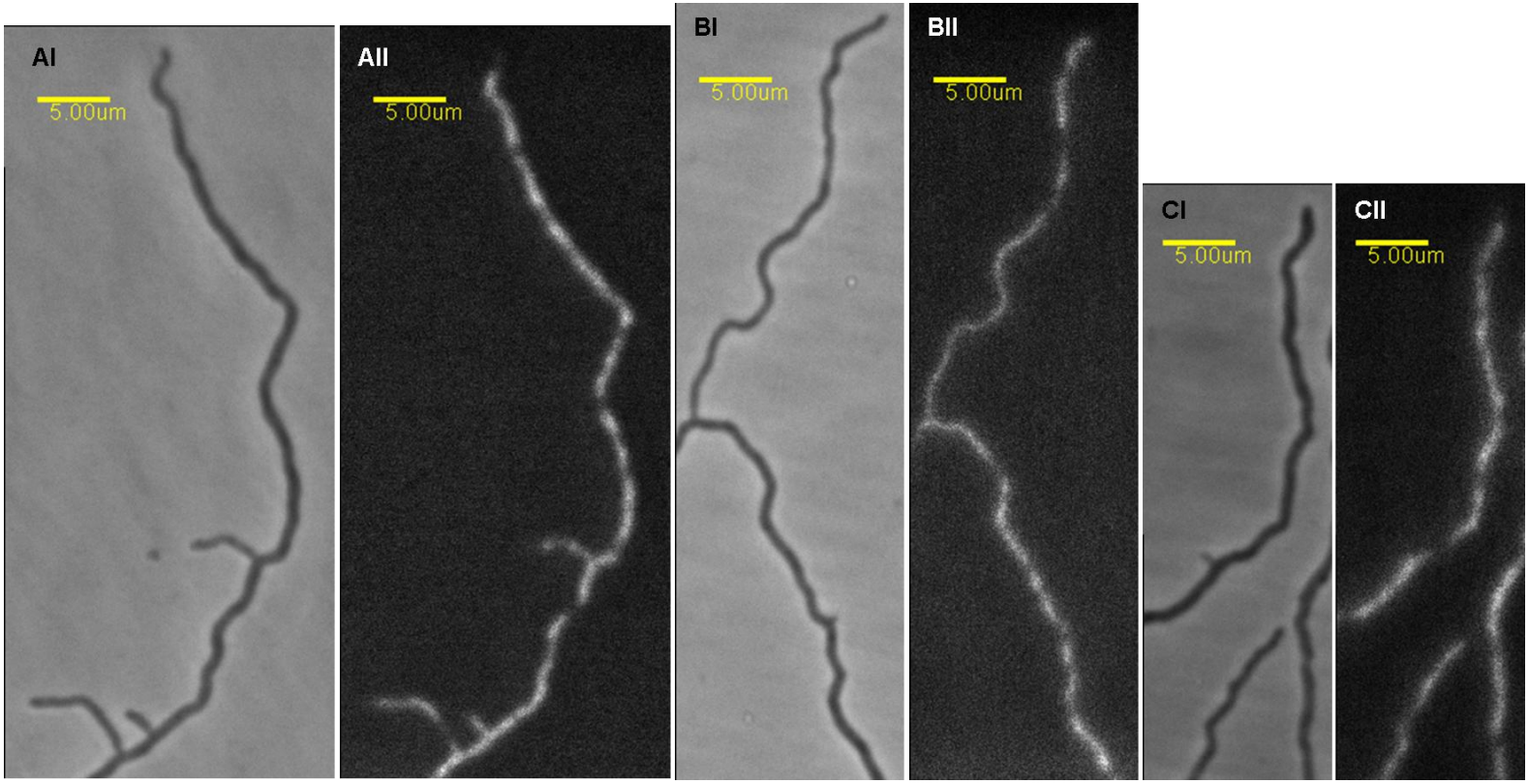

Figure 7.17: RpoC-eGFP translational fusion in strains deficient in producing ppGpp synthethases. Brightfield (I) and green fluorescence images (II) of strains M570/rpoC-eGFP (*ΔrelA,* A), M680/rpoC-eGFP (*ΔrshAΔrelA*, B) and M690/rpoC-eGFP (*ΔrshA*, C). The used scale bar is 5 µm.

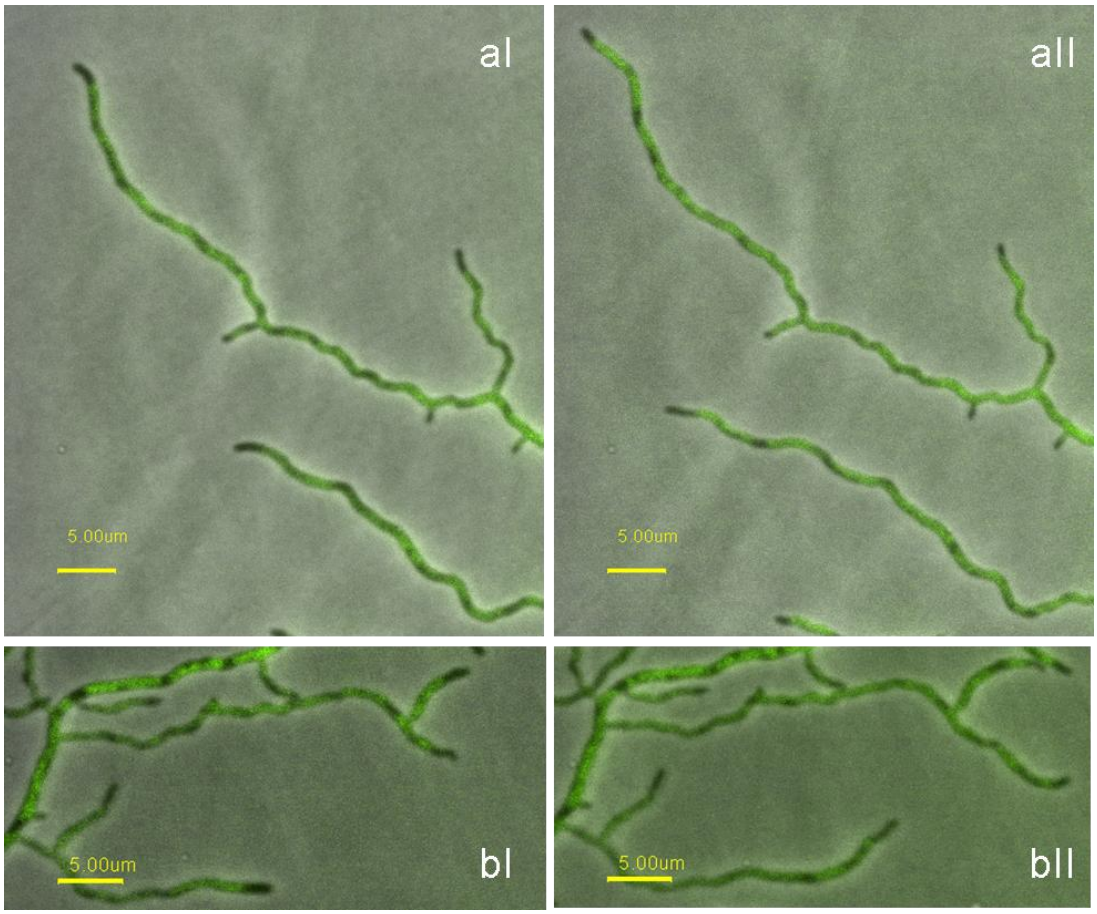

Figure 7.18: Localization of RpoC-eGFP during stringent response after low growth rate conditions. Strains LN301 (a) and M570/RpoC-eGFP (b, *ΔrelA*) were grown on minimal medium containing mannitol. Stringent response was induced by nitrogen down shift. Images taken at 10 min (I) and 1 hour (II) after induction. Multiprobe images show phase contrast (grey) and eGFP (green) with scale bar of 5 µm.

The number and intensity of transcription foci related to rRNA gene clusters transcription, has been reported to increase with increasing growth rate (Lewis *et al.* 2000, Cabrera and Jin 2003). To see if clearer response to stringent conditions could be achieved, the above experiment was repeated using high growth rate medium (nutrient agar) as starting conditions. To induce the stringent response, the culture was transferred from nutrient agar to nitrogen-limited minimal medium containing mannitol. Videos of the two strains LN301 and M570/RpoC-eGFP were taken after subjected to nitrogen down-shift (see videos 5 and 6, respectively). Individual, fluorescent images of the videos are shown in Figure 7.19. at 10 min, 1 h and 2 h after induced stringent response. This time a difference in RpoC-eGFP fluorescence was observed in LN301. Even though some brighter areas within foci as well as some black spaces between foci were still present in LN301 after induction of stringent response, the fluorescence of RpoC-eGFP generally evened out along the hyphae as time progressed. However, the two different nutrient conditions (i.e. nutrient agar and nitrogen-limited minimal medium with mannitol) affected the hyphal growth of LN301 in a surprising way that might influence the observed RpoC-eGFP localization. Figure 7.20 shows the multiprobe images (phase contrast in gray, eGFP in green) of the two strains at 10 min (I), 1 h (II), 2 h (III) and 3 h (IV) after induction. It was observed that the strain LN301 went through growth arrest in both apical elongation and branching. The growth was restored at first by branching (ca one hour after induction) and then by apical elongation (ca two hours after induction). It is noted that this unexpected growth arrest could have affected the concentration and localization of RpoC-eGFP and therefore, the shift seen in fluorescence pattern in strain LN301 could have been a secondary effect from the growth arrest. No difference was seen in the fluorescence of RpoC-eGFP foci in the *relA* knockout strain M570/RpoC-eGFP that also continued hyphal elongation undisturbed despite of the change in the nutrient availability.

It is noted that an alternative hypothesis for the heterogenous fluorescence of RpoC-eGFP in LN301 hyphae (i.e. bright fluorescence spots and more diffused fluorescence around the spots), other than the brighter areas being the location of highly transcribed genes, is that not all RpoC-eGFP is actively transcribing, so that the bright spots represented DNA bound RNAP (accumulation of active RNAP) and the diffused fluorescence areas unbound RNAP. However, studies in *E. coli* have indicated that there is no free RNAP in the *E. coli* cytoplasm (Shepherd *et al*., 2001).

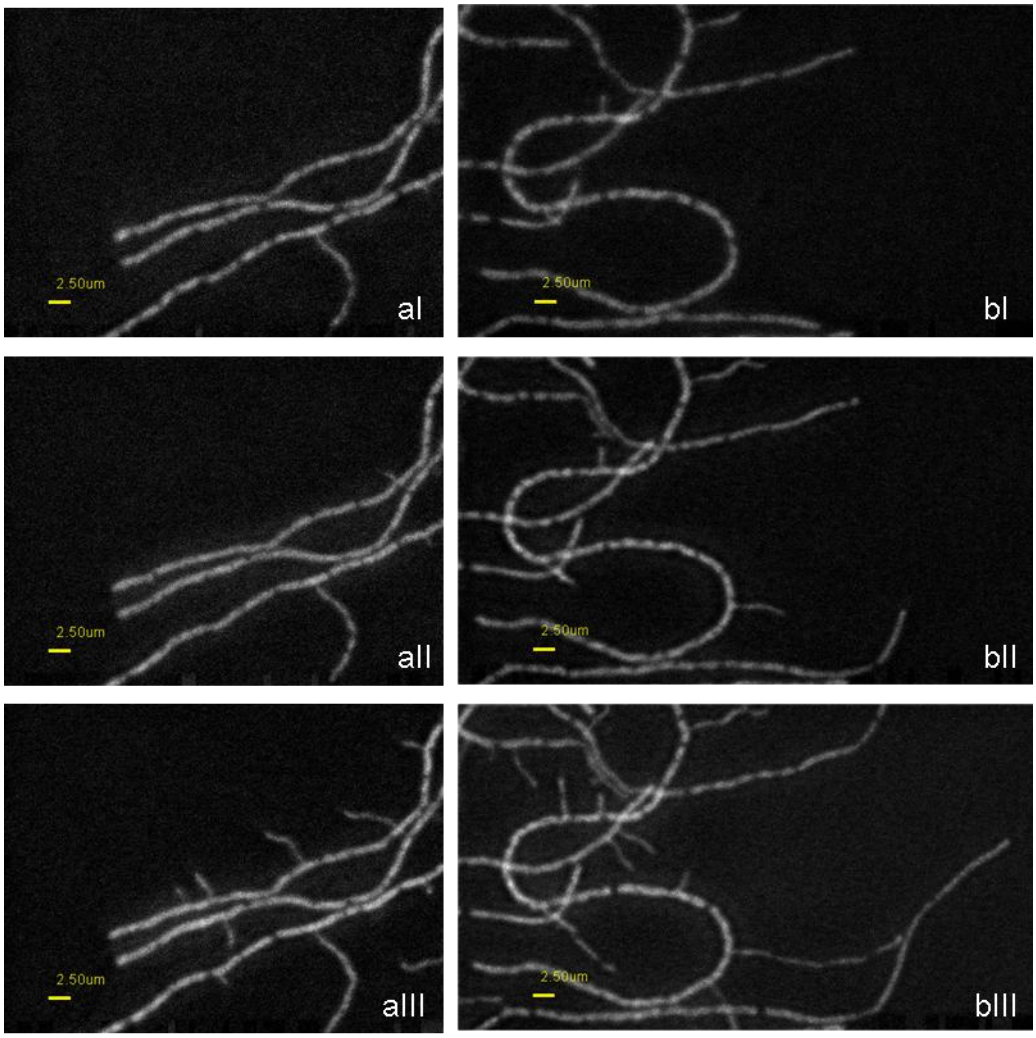

Figure 7.19: Localization of RpoC-eGFP during stringent response after high growth rate conditions. The bacteria were transferred from nutrient agar to nitrogen limited minimal medium containing mannitol in order to induce stringent response. Fluorescent images of strains LN301 (a) and M570/RpoC-eGFP (b, *ΔrelA*) are shown at 10 min (I), 1 h (II) and 2 h (III) after induction. The used scale bar is 2.5 µm.

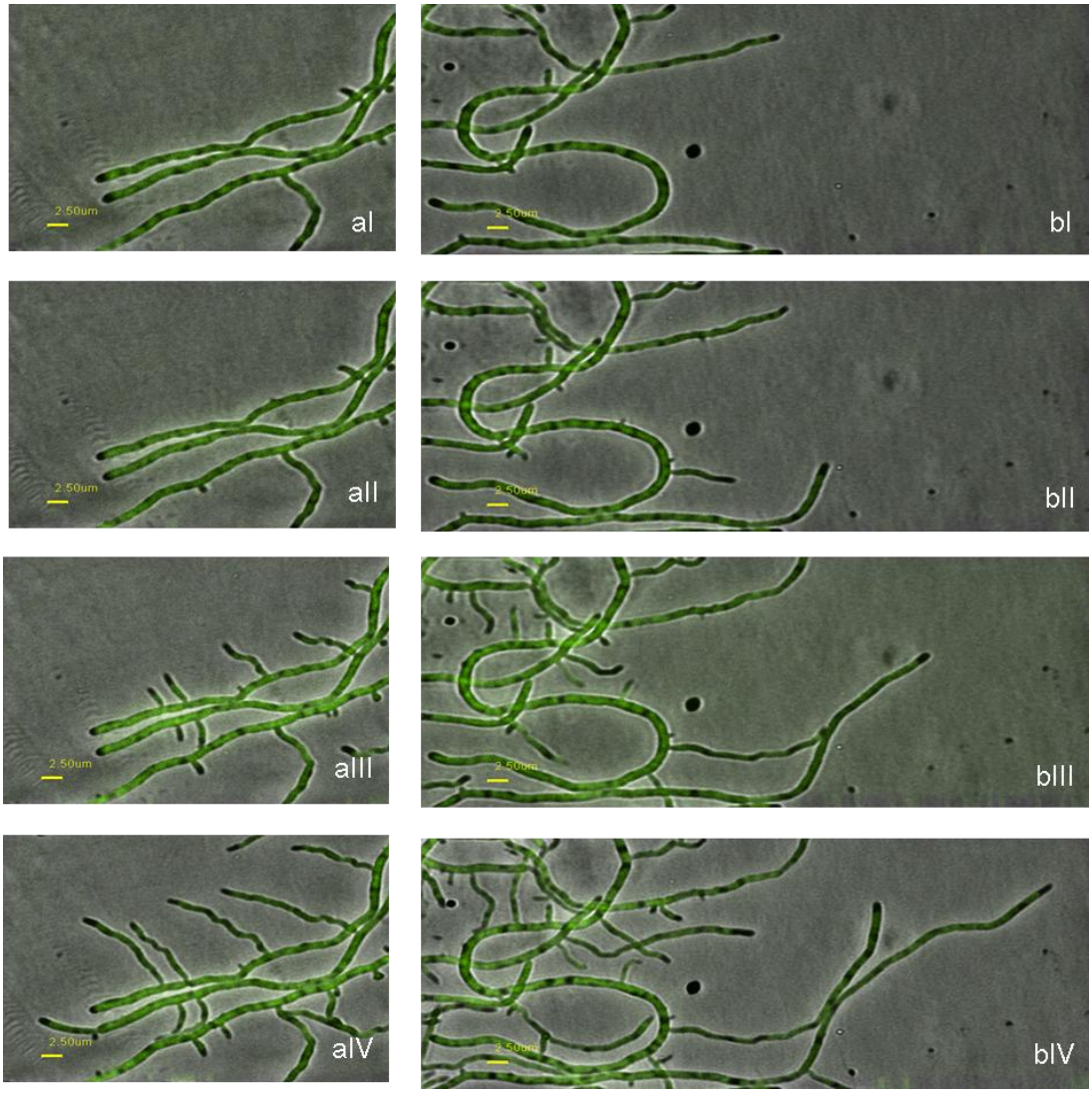

Figure 7.20: Multiprobe images (eGFP in green) of the localization of RpoC-eGFP during stringent response after high growth rate conditions. The stringent response was induced by transferred the bacteria from nutrient agar to nitrogen limited minimal medium containing mannitol. Images of strains LN301 (a) and M570/RpoC-eGFP (b, *ΔrelA*) are shown at 10 min (I), 1 h (II), 2 h (III) and 3 h (IV) after induction with the used scale bar of 2.5 µm.

Localization of RNAP during antibiotic treatments

To test what effect blocking transcription or translation have on localization of RNAP in *Streptomyces*, we took advantage of the molecular action of antibiotics rifampicin (RIF) and chloramphenicol (CHLOR), and observed the localization pattern of RpoC-eGFP under fluorescent microscope after adding the antibiotics to the growth medium. It is known that rifampicin inhibits transcription by binding to the β subunit (RpoB) of the RNAP (Wehrli 1983) and blocking the elongation at transcript lengths of 2 to 3 nucleotides (Campbell *et al*., 2001). Chloramphenicol, on the other hand, binds to bacterial ribosome and inhibits protein chain elongation during translation by blocking formation of the peptide bonds (Madigan *et al*., 2012).

The strain LN301 was grown at 30°C overnight on a cellophane that was placed on a plate containing minimal medium with 5% mannitol. The cellophane with the bacteria was then transferred inside a microdisc and a piece of agar (minimal medium with mannitol) was placed on the top of it. The microdisc was incubated in a heated (30°C) incubation chamber under the microscope for ca one hour. The growth of bacteria was confirmed by observing the elongation of hyphae under the microscope before changing the agar blob on the top of the culture to minimal medium with 5% mannitol supplemented with appropriate antibiotics. The used concentration of antibiotics was half of the previously reported, minimal inhibitory concentration (MIC) levels. For rifampicin, the MIC in *S. coelicolor* is between 32-64 µg/ml (Kim *et al.*, 2005). We tested the concentration levels of 15 and 32 µg/ml which both permitted slowed down hyphal elongation. The MIC for chloramphenicol in *S. coelicolor* A3(2) is 20 µg/ml (Shaw and Hopwood, 1976). The used chloramphenicol concentrations in our experiments were either 10 or 13 µg/ml that both inhibited the elongation of hyphae.

Figure 7.21 presents the images from the antibiotic experiments (see also video 1 for control, video 7 for RIF and video 8 for CHLOR) at 10 min, 1.5 h and 3 h time after the start of antibiotic treatment. Under rifampicin, the

RpoC-eGFP fluorescence of strain LN301 was noticed to spread along the hyphae more evenly than what had been observed in the untreated culture. At the hyphal tip, the RpoC-eGFP was first noticed to lag behind the slowly elongating tip at a greater distance than what had been seen in the untreated hyphae. After three hours incubation, the RpoC-eGFP was however located almost at the hyphal tip. In chloramphenicol treated culture, the RpoC-eGFP fluorescence was noticed to condensate at interhyphal areas.

Different lengths were observed for the space between the hyphal tip and the start of the RpoC–eGFP fluorescence. The tip to RpoC-eGFP distances were measured at three hour time point and the results are presented in Table 7.6. The difference in average length between untreated, rifampicin and chloramphenicol treated tips was statistically significant. Rifampicin treatment narrowed the space between the tip and the fluorescence to an average of 1.0 μm where as chloramphenicol treatment expanded this average to 4.5 μm. The length of the RpoC-eGFP foci within hyphae was also measured even though this had been proven to be challenging in previous experiments. The results are presented in Table 7.7. The average foci length was noticed to increase from 2.5 μm to 4.3 μm under rifampicin and to 8.6 μm under chloramphenicol treatments. To describe the observed fluorescence patterns in a numerical manner, we calculated the percentage of the foci that were beyond 4 μm in length at three hour time point. In untreated hyphae, 13% of the total of 54 foci measured were over 4 μm in length. This percentage increased to 47% and 58% in rifampicin and chloramphenicol treated hyphae, respectively.

Previous studies in *E. coli* have shown that RNAP-eGFP fluorescent coincides with the DAPI-stained DNA and its periphery regardless of the used growth and nutrient conditions (Cabrera and Jin, 2003). Although the structure of the bacterial nucleoid is not well understood, suggestions have been made that the nucleoid structure is determined by a balance of several compaction forces, such as DNA binding proteins (i.e. RNAP) and DNA

supercoiling, and one expansion force, named transertion. It is believed that during transertion, the coupled transcription and translation of membrane proteins and/or exported proteins pull and stabilize the transcribed nucleoid onto the cytoplasmic membrane of bacteria (Cabrera *et al.*, 2009; Woldringh *et al*., 1995). In support to this, it has been shown that the translation inhibitor, chloramphenicol, contracts the bacterial nucleoid into more round off structures (Zimmerman, 2002; Woldringh *et al.*, 1994) and that active transcription, especially from rRNA operons, is necessary for chloramphenicol-induced nucleoid compaction (Cabrera *et al*., 2009). In contrast, transcription inhibitor, rifampicin, has been noted to make the *E. coli* nucleoid less condensed and diminishing the intense fluorescent signals of RNAP-eGFP transcription foci (Cabrera and Jin, 2003).

Unfortunately, the parallel control experiment in this study, illustrating the DNA dynamics during antibiotic treatment by staining DNA with SYTO42 dye, were unsuccessful, possible due to interference by the cellophane. Nevertheless, the RpoC-eGFP fluorescent patterns observed in this study are in agreement with the previously reported dynamics of bacterial nucleoids under rifampicin (less condense) and chloramphenicol (more condense) treatments.

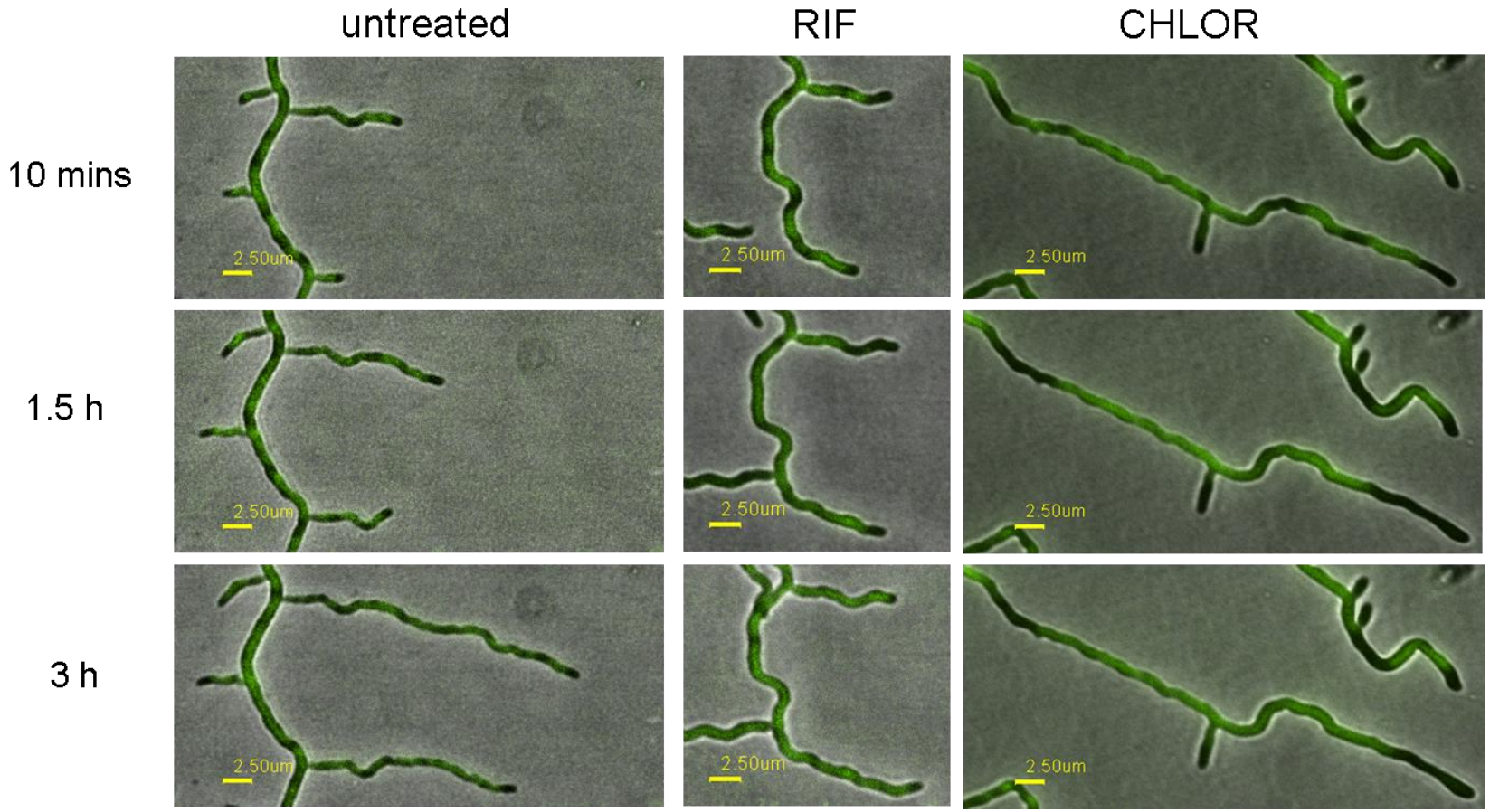

Figure 7.21: The localization of RpoC-eGFP in *Streptomyces* during antibiotic treatment. Strain LN301 was grown on minimal medium with 5% mannitol containing either rifampicin (RIF, 32 µg/ml) or chloramphenicol (CHLOR, 13 µg/ml). The multiprobe images show hyphae in grey and eGFP in green. The used scale bar is 2.5µm.

Table 7.6: The tip to RpoC-eGFP distance in untreated, rifampicin and chloramphenicol treated LN301 cultures after three hours of exposure.

	Untreated	Rifampicin treated	Chloramphenicol treated
Mean	2.0*	1.0*	4.5*
Stdev	0.4	0.4	2.4
CV%	18	35	53
n	14	17	15
Elongation stops	no	no	yes

* Statistically significant difference

Table 7.7: The length of the RpoC-eGFP foci in untreated, rifampicin and chloramphenicol treated hyphae at three hour time point after treatment.

	Untreated	Rifampicin treated	Chloramphenicol treated
Mean	2.5	4.3	8.6
Stdev	1.5	3.0	9.2
CV%	61.6	68.5	107.3
n	54	30	24

One application for the strain LN301 is to use it in *in vivo* spatio-temporal monitoring of transcription complexes during combination drug therapies. The administration of more than one drug can have diverse results ranging from synergistic to antagonistic. It has been reported that a DNA synthesis inhibitor used together with a protein synthesis inhibitor actually increases the growth rate of bacteria through balancing the use of metabolic resources (Bollenbach et al., 2009). To test what happens when a transcription and translation inhibitors are used together, we performed an experiment using rifampicin in combination with chloramphenicol at concentrations of 32 µg/ml and 13 µg/ml, respectively. Figure 7.22 shows the drug combination experiment where it was noticed that the hyphal elongation stopped and the transcription foci packed together at interhyphal regions as seen taken place under chloramphenicol treatment, perhaps representing the stalling of transcription and translation in the same region of the cell, thus compacting the foci. The results suggest that the combined use of rifampicin and chloramphenicol is not suppressive.

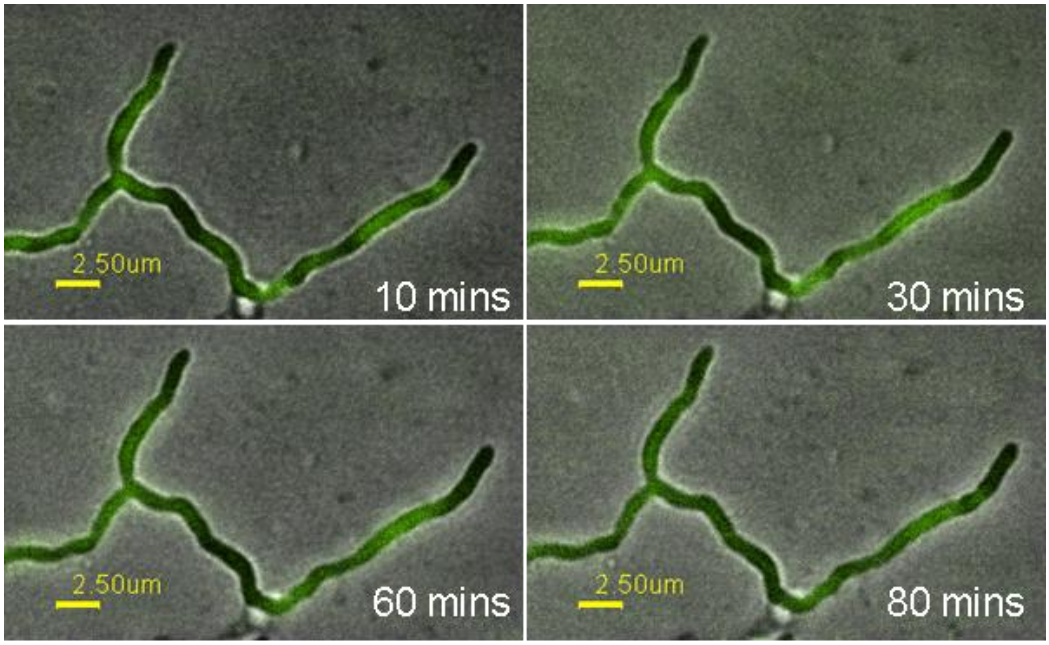

Figure 7.22: Localization of RpoC-eGFP during combined treatment with rifampicin and chloramphenicol. Multiprobe images of bright field (grey) and eGFP (green) show the effect of antibiotics to the growth of strain LN301 at 10, 30, 60 and 80 min after treatment. The images show a scale bar of 2.5 µm.

Summary and conclusions

We studied RNAP localization in live *S.coelicolor* by taking advantage of fluorescence microscopy and translationally fused RpoC-eGFP strains. The experiments revealed that the RNAP localized, as expected, at the sites of nucleic acids. Studies using antibiotics that are known inhibitors of transcription and translation suggested that the RNAP is DNA bound in vegetative hyphae. RNAP was noticed to be missing from the hyphal tips and the distance between the hyphal tip and the RNAP varied depending on the used growth conditions. The RNAP was observed to be dynamic along the hyphae although stagnant fluorescent areas were noticed at older parts of vegetative hyphae. The foci length of the RpoC-eGFP was noticed to differ when tip to first branch and interbranch hyphal areas were compared to each others. The fluorescent of the RpoC-eGFP foci was heterogenous. However, this was not explicitly proven to be the consequence of highly transcribed ribosomal genes during high growth rates. The RNAP localized in aerial hyphae and in spore chains in a similar manner to the DNA. The RNAP was also present in spores after a prolonged storage at -80°C. During germination, the RNAP was observed to be present in germ tubes. Interestingly, the tips of the germtubes did not show the typical localization of RpoC-EGFP as seen in mature vegetative hyphal tips.

Chapter 8: Discussion

How does the model described here compare to the existing literature?

This thesis describes the development of a new model for the study of *Streptomyces* growth in liquid culture and in particular to the formation and heterogeneity of mycelial pellets. Studying the models reviewed earlier in this thesis, I discussed how Meyerhoff *et al.*, (1995) included different types of hyphal morphology and hyphal metabolism in their model. The hyphal morphology described two types of compartments differing by the number of tips present. The hyphal metabolism was characterised between actively growing hypha, and hypha with only maintenance requirements for oxygen and glucose consumption. Cell lysis was also included in the model. In an earlier model by the same authors, there was no distinction between primary and secondary metabolism, however, Meyerhoff and Bellgardt (1995a) updated their model to include sub-apical antibiotic production once the glucose concentration dropped below critical level of 0.4 g/l. The modeling of antibiotic production also included a length increment subtraction from the tip. In a more recent single pellet model by Celler *et al*. (2012) a similar approach to metabolic differentiation was used, except that the hyphal length determining the metabolic state was tied to a certain arbitrary age of hypha.

The model framework suggested in this study took these previous models further by linking the secondary metabolism directly to the available substrate concentration without any hyphal length subtractions or age assumptions. The model does not restrict the hyphal growth to certain compartments or layers. Instead, the model includes explicit spatial heterogeneity within hyphae. Also, the hyphal elongation and branching both have a random aspect in them. The advantage of this model is also that all but a few of the parameters describing the hyphal growth and differentiation can be directly drawn from experimental data.

The vector based mathematical model of Meškauskas *et al*. (2004) is ideal for modeling growth on a solid surface. Although *Streptomyces spp.* do not produce complex fungal fruit bodies, different structures of spore chains are still known (Goodfellow, 2012). The main benefit of the Meškauskas *et al*. (2004) model is the extended control of which a user can have over the model. This kind of control would be helpful for running and analysing multiple simulations studies. Another key character of the Meškauskas *et al*. (2004) model is the use of external fields to create neighboring sensing feature. Lejeune *et al.* (1997) also modelled neighboring sensing by taking into account the porosity of the pellet at the site of new growth. Neighbor sensing is important character of *Streptomyces* growth, however, in our model the tips tended to grow outwards due to external substrate concentration. So, that hyphal extension limitations due to crowding effects was rarely observed. Since our model only simulates growth on 2D+, neighbour sensing was not regarded as significant for the purposes of this model and was therefore not incorporated into the model.

Nutrient levels affect pellet morphology

Stocks and Thomas (2001) highlighted that mid-growth phase and end-growth phase fragmentations are common phenomenon in actinomycetes grown in fermentors with either defined or complex media. The results presented in this study show that under the tested growth conditions, the phosphorus exhaustion started at mid-log phase (around 20 – 22 h). This coincided with the start of the slower growth rate seen in average pellet diameter and area measurements. Voelker and Altaba (2001) discussed that under phosphate exhaustion the teichoic acids of the cell wall get broken down to recover phosphate from the cell wall to continue growth. Stocks and Thomas (2001) studied the breaking force of hypha in nitrogen-limited fermentations. Their data shows that at mid-log phase when nitrate has been exhausted, both the hyphal diameter and the breaking force of hypha decreased. The growth still continued after nitrate exhaustion, although with a slower growth rate. Since there is metabolic control of phosphorus over

nitrate metabolism, discussed in the introduction of this study, it is tempting to speculate if the phosphorus exhaustion at mid-log phase results in alterations of the cell wall structure that would make the hyphae more vulnerable to the breaking forces of mechanical mixing used in fermentors and also result in slower pellet extension rate, ultimately causing mid-log phase fragmentation in fermentors.

Another interesting point during the growth curve experiment was the 16 – 18 h time period when the pellet volume increased less than initially expected. The same was not observed in the increase of the dry weight of the culture which almost tripled during the two hour time period. Interestingly, the timing of this coincided with the doubling of the average pellet intensity of SYTO9 stained DNA. Taken together, this data indicates that the main growth during this time occurred from branch formation that would increase the dry weight and create denser pellets with higher SYTO9 intensity without really increasing the pellet volume. Also, at this 16 -18 h time period the pH started to decrease possible reflecting interruptions in TCA cycle. Therefore, one hypothesis is that during this time (16-18 h) the hyphal elongation went through a minor growth arrest in order to rearrange the metabolic machinery for adaptation to depleting phosphate levels. A surprising support for this hypothesis came from the RpoC-eGFP studies where the strain was first grown on nutrient agar and then transferred to nitrogen limited minimal medium with mannitol. The resulting video of the bacterial growth under these conditions revealed that right after the transfer from rich to poor media, the elongation of hyphae stopped for a period of time and the growth restored first by almost simultaneous multi-branching and only after, by apical elongation of the leading hyphae.

The model presented in this thesis simulates the effect oxygen has on hyphal metabolism and pellet morphology. With a single substrate (oxygen), the model accurately predicts the time of the appearance of antibiotic producing cells and the size dimensions of the pellet at the end of exponential growth.

Most of the models reviewed in the introduction of this study take into account some kind of internal or external concentration gradient for subtrates such as glucose or oxygen. However, none of them considered external phosphate or nitrogen profiles. From the results presented in this study, it can be concluded that phosphorus has a major role over *Streptomyces* metabolism and that both phosphate and nitrogen concentration are important to take into account in any future models. The model platform constructed during this study allows an easy updating possibility for multiple external substrates.

Heterogenous metabolism within a pellet

The results of this study show that the nonviable regions of hyphae are first located mainly at the centre of the pellet. The appearance of nonviable mycelium already at the early stage of the growth curve (before the onset of antibiotic production) could be down to depleting external phosphate levels resulting in break down of the cell wall in order to release the polyphosphate storage, or down to the natural cell death occurring at the older parts of hypha or in case of fully formed pellets, down to the diffusion limitations within the pellet.

It has been proven that after being exposed to a less severe stress and consequently been stained red by PI, a small portion of a yeast population was still able to repair their membrane damage and to recover growth (Davey and Hexley, 2010). It has been discussed that perhaps in *Streptomyces* the PI stain is able to enter live cells but is immediately removed from the cell by efflux pumps (Stocks, 2004; Hoskisson P. A. and Smith M. C. M personal communication). Simple transport system across the cell membrane, capable of such an efflux, can be driven by proton motive force (PMF). The PMF, generating membrane potential, can be created during oxidative phosphorylation when oxygen serves as a final electron acceptor (Jormakka *et al*., 2003). In the absence of oxygen, the aerobic respiration cannot take place resulting in compromised membrane potential and eventually

dysfunction of the PMF driven efflux pumps. Therefore, the hypothesis is that under limited oxygen conditions, PI is not pumped out of the cell and it is, therefore, able to stain hyphae red. This might happen already before unrecoverable membrane damage and cell death occurs. The model presented in this study, predicts that at the green/red interphase the external media has ca half of the total carrying capacity of oxygen still present and even at the very core of the pellet the growth conditions are not totally anoxic. This leaves two questions; is this amount of oxygen sufficient enough for keeping the cells alive (maintenance requirements only) and if so, what portion (if any) of the PI stained pellet area is able to recover active metabolism under favorable growth conditions? Further work is needed in order to answer these questions.

Four metabolic states of hyphae are included in the model: active growth, antibiotic production, maintenance requirements only and dead. Regardless of which branching rule is used, the model predicts that the antibiotic production occurs underneath the pellet surface and that actively growing hyphae appears at the outskirts and maintenance requirements hyphae are located at the core of the pellet. The model predictions were tested using eGFP-tagged proteins as indicators for primary metabolism (Idh-eGFP), secondary metabolism (PstS-eGFP) and transcription (RpoC-eGFP). The results were analysed for the pellet growth before antibiotic production occurred and they showed that both the Idh-eGFP and RpoC-eGFP were located in all parts of the pellet, even at the core of the pellet which stained red with PI. The metabolic state of red stained hyphae is not fully understood and the eGFP-analysis described above might imply that at least some parts of the red stained hyphae are alive since they contain key primary metabolism protein. However, the fluorescent microscopy is not able to distinguish whether a protein is active or not. Since both Idh and RpoC are extremely important proteins for cell growth, it may be that their main regulation is not at the gene expression level, and since the half-life of these eGFP-fused proteins is not known, their existence in the red stained hyphae

cannot be taken as direct proof that the hyphae is still alive. The third eGFP-construct made during this study marked the location of secondary metabolism within a pellet. An initial, putative location for PstS-eGFP appeared right at the edges of the red stained pellet core. This result clearly implies that the active metabolism is located at the green stained hyphal parts. The only controversy left is the bright appearance of autofluorescence after the onset of antibiotic production that seems to cover the whole pellet, including the core (not hollow), but this might be an imaging related artifact.

Model analysis and applications

Mathematical modeling can guide biological understanding and produce quantitative predictions on processes that are almost impossible to obtain experimentally. We used the model to predict for example, the effect different branching rules and patterns have on pellet morphology and therefore on pellet metabolism. Taken together, the model simulations showed that the location of emerging branches is a more significant determinant to pellet morphology and metabolism than for example, the oxygen consumption rates of metabolically different cells. Using the mathematical model for data generation, regression lines can also be utilized for quantitative prediction purposes. However, when the model simulation of a pellet development over time was compared to the experimental data, it was noticed that in the model simulations the maintenance requirements only hyphae always appears after the onset of antibiotic production. Yet, in the experiments, active metabolism was observed to localize at the outskirt of the pellet before the initiation of antibiotic production. Therefore, even though the model has been validated for early hyphal growth and experimentally tested at the end of the exponential growth, there is a discrepancy between the model and the laboratory experiments as regards to the pellet development during the exponential growth phase. This discrepancy might be a result of more diffusion/substrate limitations present in the pellet than just oxygen. Therefore, in its current state, although useful for qualitative predictions, the model is not suitable for quantitative analysis of antibiotic production over

time and more work is needed to achieve this. Using genetic engineering approaches to alter branching patterns would offer an alternative to investigating better fermentation characteristics. Proteins known to be involved in cell division in streptomycetes, such as SsgA, have been shown to facilitate fragmentation and improve growth rates and enzyme production when overexpressed (Kawamoto *et al*., 1997; van Wezel *et al*., 2006).

Transcription

The dynamic localization of RNAP was studied using an RpoC-eGFP construct in order to understand the transcription within a pellet but also to generate experimental data for tagging RNAP movement in the mathematical model (Future work). RNAP was found to be located in almost all parts of *Streptomyces* growth (spores, vegetative hyphae, aerial hypha, spore chains). The heterogenous fluorescence of the RpoC-eGFP in vegetative hyphae proved to be difficult to measure although the microscopy revealed the absence of the RNAP at the hyphal tip. When the measures were compared to the other known eGFP locations at the hyphal tip, a hypothesis of spatial separation between the transcription and DNA replication at the hyphal tip was generated. This hypothesis was experimentally tested using a strain expressing both RpoC-eGFP and DnaN-mCherry. Unfortunately, the apical location of RNAP was changed in this strain. The apical RpoC-eGFP in other strains (M570, M680 and M690) did not show any alteration in the tip to RpoC-eGFP distance when compared to LN301 strain. Therefore, it is likely that the prolonged apical distance of RNAP in strain DJ542/RPoC-eGFP is a secondary effect from the fluorescent protein tagging of the two extremely important growth processes, transcription and replication. The theory of apical, spatial separation of these two processes remains unsolved and may serve as a starting point for future mathematical modelling.

Future work

The model highlighted the importance of branching. More specifically, the location of emerging branches is one of the key morphological properties affecting pellet structure and hyphal metabolism. The experimental validation of different branching rules might include studies with strains with mutagenetically altered branching frequencies, such as the penicillin binding protein (PBP) mutants of *Streptomyces* (Hoskisson P.A. and Hobbs G., personal communication). The experimental work using growth curves identified the need for more substrates in the model. Therefore, to develop the model to produce quantitative predictions, additional nutrients such as phosphate and nitrogen, should be added in to the model framework. It would be interesting to see how different branching rules and frequencies affect the pellet metabolism and morphology under for example, nitrogen or phosphate limitations. Promising results in determining the location of initiation of secondary metabolism were gained from this study with PstS-eGFP strain LN205. The validation of different branching rules under nutrient depletions might include the fusion of PstS-eGFP in these PBP mutant strains. Another aspect to rational strain design for industrial purposes is the use of fermenters. In a continuous culture, the substrate concentrations can be controlled and it would be beneficial for any future fermenter models to allow similar kind of control over external substrate levels (Hoskisson and Hobbs, 2005). Finally, modelling of the movement of proteins through hyphae and then scaling this to the level of the pellets could enhance our knowledge of *Streptomyces* biology and pellet formation. Similar to what has been achieved in this study, the close relationship between mathematical modelling and laboratory experiments should be maintained in all of the future model updates.

References

Allenby, N.E.E., E. Laing, G. Bucca, A.M. Kierzek, and C.P. Smith. 2012. Diverse Control of Metabolism and Other Cellular Processes in *Streptomyces coelicolor* by the PhoP Transcription Factor: Genome-wide Identification of *in vivo* Targets. Nucleic Acid Research. 40:9543-9556.

Baron, C. 2009. Visualising Transcription Complexes in the Differentiating Bacterium *Streptomyces coelicolor* A3(2). University of Strathclyde. Master's Thesis.

Bebber, D.P, J. Hynes, P.R. Darrah, L. Boddy, and M.D. Fricker. 2007. Biological Solutions to Transport Network Design. Proceedings of the Royal Society B: Biological Sciences. 274: 2307–2315.

Bentley, S.D., K.F. Chater, A.-M. Cerdeno-Tarraga, G.L. Challis *et al*. 2002. Complete Genome Sequence of the Model Actinomycete *Streptomyces coelicolor* A3(2). Nature. 417: 141-147.

Bezzi, M., and A. Ciliberto. 2004. Mathematical Modeling of Filamentous Microorganisms. 2004. Eprint arXiv:q-bio/042004. 1-29.

Bibb, M.J. 2005. Regulation of Secondary Metabolism in streptomycetes. Current Opinion in Microbiology. 8:208-215.

Birnboim, H. C., and J. Doly. 1979. Rapid Alkaline Extraction Procedure for Screening Recombinant Plasmid DNA. Nucleic Acids Research. 7:1513-1523.

Bishop, A., S. Fielding, P. Dyson, and P. Herron. 2004. Systematic Insertional Mutagenesis of a Streptomycete Genome: A Link between Osmoadaptation and Antibiotic Production. Genome Research. 14:893-900.

Bollenbach, T., S. Quan, R. Chait, and R. Kishony. 2009. Nonoptimal Microbial Response to Antibiotics Underlies Suppressive Drug Interactions. Cell. 139:707-718.

Boswell, G.P., H. Jacobs, F.A. Davidson, G.M. Gadd, and K. Ritz. 2002. Functional Consequences of Nutrient Translocation in Mycelial Fungi. Journal of Theoretical Biology. 217: 459–477.

Boswell, G.P., H. Jacobs, F.A. Davidson, G.M. Gadd, and K. Ritz. 2003a. Growth and Function of Fungal Mycelia in Heterogeneous Environments. Bulletin of Mathematical Biology. 65:447-447.

Boswell, G.P., H. Jacobs, K. Ritz, G.M. Gadd, and F.A. Davidson. 2007. The Development of Fungal Networks in Complex Environments. Bulletin of Mathematical Biology 69:605-634.

Browning, D.F., and S.J.W. Busby. 2004. The Regulation of Bacterial Transcription Initiation. Nature Reviews Microbiology. 2:1-9.

Cabrera, J.E., C. Cagliero, S. Quan, C.L. Squires, and D.J. Jin. 2009. Active Transcription of rRNA Operons Condenses the Nucleoid in *Escherichia coli*: Examining the Effect of Transcription on Nucleoid Structure in the Absence of Transertion. Journal of Bacteriology. 191:4180-4185.

Cabrera, E.J., and D.J. Jin. 2003. The Distribution of RNA Polymerase in *Escherichia coli* is Dynamic and Sensitive to Environmental Cues. Molecular Microbiology. 50:1493-1505.

Campbell, E.A., N. Korzheva, A. Mustaev, K. Murakami, S. Nair, A. Goldfarb, and S.A. Darst. 2001. Structural Mechanism for Rifampicin Inhibition of Bacterial RNA Polymerase. Cell 104:901-912.

Celler, K., C. Pcioreanu, M.C.M. van Loosdrecht, and G.P. van Wezel. 2012. Structured Morphological Modeling as a Framework for Rational Strain Design of *Streptomyces* species. Antonie van Leewenhoek. 102:409-423.

Chakraburtty, R., and M. Bibb. 1997. The ppGpp Synthetase Gene (*relA*) of *Streptomyces coelicolor* A3(2) Plays a Conditional Role in Antibiotic Production and Morphological Differentiation. Journal of Bacteriology. 179:5854-5861.

Chang-fa, C., Q. Xia-chang, Q. Jiang-chao, Z. Ying-ping, C. Ju, and Z. Si-liang. 2009. Effects of the Dissolved Oxygen on the Erythromycin Components of Recombinant Strain *Saccharopolyspora erythraea* ZL1004 Fermentation. Chinese Journal of Antibiotics. 11.

Chater, K.F. 2001. Regulation of Sporulation in Streptomyces coelicolor A3(2): a Checkpoint Multiplex? Current Opinion in Microbiology. 6:667-673.

Chater, K.F., and G. Chandra. 2006. The Evolution of Development in *Streptomyces* Analysed by Genome Comparisons. FEMS Microbiology Reviews. 30:651-672.

Chen, H.C., and F. Wilde. 1991. The Effect of Dissolved Oxygen and Aeration Rate on Antibiotic Production of Streptomyces fradiae. Biotechnology and Bioengineering. 15:591-595.

Claessen, D., R. Rink, W. de Jong, J. Siebring, P. de Vreugd, F. G. Hidde Boersma, L. Dijkhuizen, and H. A. B. Wösten. 2003. A Novel Class of Secreted Hydrophobic Proteins is Involved in Aerial Hyphae Formation in *Streptomyces coelicolor* by Forming Amyloid-like Fibrils. Genes and Development. 17:1714-1726.

Datsenko, K.A., and B.L. Wanner. 2000. One-step Inactivation of Chromosomal Genes in *Escherichia coli* K-12 using PCR Products. Proceedings of the National Academy of Sciences of the United States of America. 97:6640-6645.

Davey, H. M., and P. Hexley. 2010. Red but Not Dead? Membranes of Stressed *Saccharomyces cerevisiae* are Permeable to Propidium Iodide. Society for Applied Microbiology and Blackwell Publishing Ltd. Environmental Microbiology.

Delvigne, F., A. Lejeune, J. Destain, and P. Thonart. 2006. Modelling of the Substrate Heterogeneities Experienced by a Limited Microbial Population in Scale-Down and in Large-Scale Bioreactors. Chemical Engineering Journal. 120:157-167.

Dower, W.J., J.F. Miller, and C.W. Ragsdale. 1988. High-Efficiency Transformation of *Escherichia coli* by High-Voltage Electroporation. Nucleic Acids Research. 16:6127-6145.

Dunn, G.A., and A.F. Brown. 1987. A Unified Approach to Analysing Cell Motility. Journal of Cell Science – Supplement. 8:81-102.

Dupuy, L, P.J. Gregory, and A.G. Bengough. 2010 Root Growth Models: Towards a New Generation of Continuous Approaches. Journal of Experimental Botany. 61: 2131–2143.

Elander, R.P. 2003. Industrial Production of β-lactam Antibiotics. Applied Microbiology and Biotechnology. 61:385-392.

Elliot, M.A., N. Karoonuthaisiri, J. Huang, M.J. Bibb, S.N. Cohen, C. M. Kao, and M.J. Buttner. 2003. The Chaplins: a Family of Hydrophobic Cell-surface

Proteins Involved in Aerial Mycelium Formation in *Streptomyces coelicolor*. Genes and Development. 17:1727-1740.

Elliot, M.A., M.J. Buttner, and J.R. Nodwell. 2008. Myxobacteria: Multicellularity and Differentiation. ASM Press, Washington, DC. 419-438.

El-Mansi, E.M.T., C.F.A. Bryce, A.L. Demain, and A.R. Allman. 2007. Fermentation Microbiology and Biotechnology. CRC Press Taylor & Francis Group. Boca Raton, Florida. pg.131-133.

Fawcett, J.K. and J.E. Scott. 1960. A Rapid and Precise Method for the Determination of Urea. Journal of Clinical Pathology. 13:156–160.

Ferullo, D.J. and S.T. Lovett. 2008. The Stringent Response and Cell Cycle Arrest in *Escherichia coli*. PLoS Genetics. 4:e1000300.

Flärdh, K. 2003. Essential Role of DivIVA in Polar Growth and Morphogenesis in *Streptomyces coelicolor* A3(2). Molecular Microbiology 49:1523-1536.

Flärdh, K. and M.J. Buttner. 2009. *Streptomyces* Morphogenetics: Dissecting Differentiation in a Filamentous Bacterium. Nature Reviews Microbiology. 7:36-49.

Giegerich, R., F. Meyer, and C. Schleiermacher. 1996. GeneFisher--software Support for the Detection of Postulated genes. Proceedings of the International Conference on Intelligent Systems for Molecular Biology. 4:68-77.

Goodfellow, M., *et al*. 2012. Bergey's Manual of Systematic Bacteriology. Volume 5. The *Actinobacteria*. Springer. New York.

Goriely, A., and M. Tabor. 2003. Biomechanical Models of Hyphal Growth in Actinomycetes. Journal of Theoretical Biology. 222:211-218.

Gottschalk, G. 1986. Bacterial Metabolism. 2nd Edition. Springer-Verlag New York Inc.

Gow, N.A.R., and G.M. Gadd. 1995. The Growing Fungus. Chapman & Hall, London. pg. 301-335.

Grant, S.G.N., J. Jessee, F.R. Bloom, and D. Hanahan. 1990. Differential Plasmid Rescue form Transgenic Mouse DNAs into *Escherichia coli* Methylation-Restriction Mutants. Proceedings of the National Academy of Sciences of the United States of America. 87:4645-4649.

Gust, B., T. Kieser, and K. F. Chater. 2002. REDIRECT Technology: PCR-Targeting System in *Streptomyces coelicolor*. John Innes Centre, Norwich, UK.

Gust, B., G. Chandra, D. Jakimowicz, T. Yuqing, C.J. Bruton and K.F. Chater. 2004. λ Red-mediated Genetic Manipulation of Antibiotic-producing *Streptomyces*. Advances in Applied Microbiology. 54:107-128.

Hesketh, A., J. Sun and M. Bibb. 2001. Induction of ppGpp Synthesis in *Streptomyces coelicolor* A3(2) Grown under Conditions of Nutritional Sufficiency Elicits *act*II-ORF4 Transcription and Actinorhodin Biosynthesis. Molecular Microbiology. 39:136-144.

Hickey, P.C., D.J. Jacobson, N.D. Read, and N.L. Glass. 2002. Live-cell Imaging of Vegetative Hyphal Fusion in *Neurospora crassa*. Fungal Genetics and Biology. 37:109-119.

Higham, D. J., and P.E. Kloeden. 2008. An Introduction to the Numerical Simulation of Stochastic Differential Equations. Lecture Notes for the Scottish Mathematical Sciences Training Centre.

Hopwood, D.A. 1967. Genetic analysis and genome structure in *Streptomyces coelicolor*. Bacteriology Review. 31:373-403.

Hoskisson, P.A., and G. Hobbs. 2005. Continuous Culture – Making a Comeback? Microbiology. 151:3153-3159.

Hoskisson, P.A., and G. Hobbs. 2006. One Size Doesn't Fit All. Microbiology. 152:1891.

Hoskisson, P.A., S. Rigali, K. Fowler, K. C. Findlay, and M.J. Buttner. 2006. DevA, a GntR-like Transcriptional Regulator Required for Development in *Streptomyces coelicolor*. Journal of Bacteriology. 188:5014-5023.

Ishhorowicz, D., and J.F. Burke. 1981. Rapid and Efficient Cosmid Cloning. Nucleic Acids Research. 9:2989-2998.

Jakimowicz, D., K. Chater, and J. Zakrzewska-Czerwińska. 2002. The ParB Protein of *Streptomyces coelicolor* A3(2) Recognizes a Cluster of *parS* Sequences within the Origin-proximal Region of the Linear Chromosome. Molecular Microbiology. 45:1365-1377.

Jakimowicz, D., B. Gust, J. Zakrzewska-Czerwinska, and K. F. Chater. 2005. Developmental-stage-specific Assembly of ParB Complexes in *Streptomyces coelicolor* Hyphae. Journal of Bacteriology. 187:3572-3580.

Jones, P.F., and B.D. Sleeman. 2006. Angiogenesis - Understanding the Mathematical Challenge. Angiogenesis 9:127–138.

Jormakka, M., B. Byrne and S. Iwata. 2003. Protonmotive Force Generation by Redox Loop Mechanism. FEBS Letters. 545:25-30.

Jyothikumar, V., E.J. Tilley, R. Wali, and P.R. Herron. 2008. Time-Lapse Microscopy of *Streptomyces coelicolor* Growth and Sporulation. Applied and Environmental Microbiology. 74:6774-6781.

Karandikar, A., G.P. Sharples, and G. Hobbs. 1997. Differentiation of *Streptomyces coelicolor* A3(2) under Nitrate-limited Conditions. Microbiology 143:3581-3590.

Kawamoto, S., H. Watanabe, A. Hesketh, J.C. Ensign, and K. Ochi. 1997. Expression Analysis of the *ssgA* Gene Product, Associated with Sporulation and Cell Division in *Streptomyces griseus*. Microbiology 143:1077-1086.

Kelemen, G.H., and M.J. Buttner. 1998. Initiation of Aerial Mycelium Formation in *Streptomyces*. Current Opinion in Microbiology. 1: 656-662.

Kieser, T., M.J. Bibb, M.J. Buttner, K.F. Chater, and D.A. Hopwood. 2000. Practical *Streptomyces* Genetics. The John Innes Foundation.

Kim, H.B., C.P. Smith, J. Micklefield, and F. Mavituna. 2004. Metabolic Flux Analysis for Calcium Dependent Antibiotic (CDA) Production in *Streptomyces coelicolor*. Metabolic Engineering. 6:313-325.

Kim, H., S-H. Kim, Y-H. Ying, H-J. Kim, Y-H. Koh, C-J. Kim, S-H. Lee, C-Y. Cha, Y-H. Kook, and B-J. Kim. 2005. Mechanism of Natural Rifampicin Resistance of *Streptomyces* spp. Systematic and Applied Microbiology. 25:398-404.

King, R. 1998. Mathematical Modelling of the Morphology of *Streptomyces* Species. Advances in Biochemical Engineering/Biotechnology. 60:95-124.

Kodani, S., M.E. Hudson, M.C. Durrant, M.J. Buttner, J.R. Nodwell, and J.M. Willey. 2004. The SapB Morphogen is a Lantibiotic-like Peptide Derived from the Product of the Developmental Gene *ramS* in *Streptomyces coelicolor*. PNAS. 101:11448-11453.

Labeda, D.P. 2011. Multilocus Sequence Analysis of Phytopathogenic Species of the Genus Streptomyces. International Journal of Systematic and Evolutionary Microbiology. 61:2525-2531.

Lejeune, R., J. Nielsen, and G.V. Baron. 1995. Morphology of *Trichoderma reesei* QM 9414 in Submerged Cultures. Biotechnology and Bioengineering. 47:609-615.

Lejeune, R., and G.V. Baron. 1997. Simulation of Growth of a Filamentous Fungus in 3 Dimensions. Biotechnology and Bioengineering. 53:139-150.

Leskiw, B.K., R. Mah, E.J. Lawlor, and K.F. Chater. 1993. Accumulation of *bldA*-specified tRNA is Temporally Regulated in *Streptomyces coelicolor* A3(2). Journal of Bacteriology. 175:1995-2005.

Lewis, M.E. 2006. Dissolved Oxygen. U.S. Geological Survey Techniques of Water-Resources Investigations. accessed 21 June 2010 from http://pubs.water.usgs.gov/twri9A6/.

Lewis, P.J., S.D. Thaker, and J. Errington. 2000. Compartmentalization of Transcription and Translation in *Bacillus subtilis*. The EMBO Journal. 19:710-718.

Lewis, P.J., G.P. Doherty, and J. Clarke. 2008. Transcription Factor Dynamics. Microbiology. 154:1837-1844.

Li, W., J. Wu, W. Tao, C. Zhao, Y. Wang, X. He, G. Chandra, X. Zhou, Z. Deng, K.F. Chater, and M. Tao. 2007. A Genetic and Bioinformatic Analysis of *Streptomyces coelicolor* Genes Containing TTA Codons, Possible Targets for Regulation by a Developmentally Significant tRNA. FEMS Microbiology Letters. 266:20-28.

Lucas, M., Y. Guédon, C. Jay-Allemand, C. Godin, and L. Laplaze. 2008. An Auxin Transport-based Model of Root Branching in Arabidopsis thaliana. PLoS ONE. 3:e3673.

MacNeil, D.J., K.M. Gewain, C.L. Ruby, G. Dezeny, P.H. Gibbons, and T. Macneil. 1992. Analysis of *Streptomyces avermitilis* Genes Required for Avermectin Biosynthesis Utilizing a Novel Integration Vector. *Gene*. 111:61-68.

Madigan, M., J. Martinko, D. Stahl and D. Clark. 2012. Brock Biology of Microorganisms. 13th Edition. Pearson Education Inc. San Francisco, USA.

Manteca, A., R. Alvarez, N. Salazar, P. Yague, and J. Sanchez. 2008. Mycelium Differentiation and Antibiotic Production in Submerged Cultures of *Streptomyces coelicolor*. Applied and Environmental Microbiology. 74:3877-3886.

Merrick, M.J. 1976. A Morphological and Genetic Mapping Study of Bald Colony Mutants of *Streptomyces coelicolor*. Journal of General Microbiology. 96:299-315.

Meškauskas, A., L.J. McNulty, and D. Moore. 2004a. Concerted Regulation of All Hyphal Tips Generates Fungal Fruit Body Structures: Experiments with Computer Visualizations Produced by a New Mathematical Model of Hyphal Growth. Mycological Research. 108:341-353.

Meškauskas, A., M.D. Fricker, and D. Moore. 2004b. Simulating Colonial Growth of Fungi with the Neighbour-Sensing Model of Hyphal Growth. Mycological Research. 108:1241-1256.

Meyerhoff, J., V. Tiller, and K.-H. Bellgardt. 1995a. Two Mathematical Models for the Development of a Single Microbial Pellet – Part I. Bioprocess Engineering. 12:305-313.

Meyerhoff, J., V. Tiller, and K.-H. Bellgardt. 1995b. Two Mathematical Models for the Development of a Single Microbial Pellet – Part II. Bioprocess Engineering. 12:315-322.

Meyerhoff, J., and K.-H. Bellgardt. 1995. A Morphology-Based Model for Fed-Batch Cultivation of *Penicillium chrysogenum* Growing in Pellet Form. Journal of Biotechnology. 38:201.217.

Nieminen, L., S. Webb, M.C.M. Smith, and P.A. Hoskisson. 2013. A Flexible Mathematical Model Platform for Studying Branching Networks: Experimentally Validated Using the Model actinomycete, *Streptomyces coelicolor*. PLoS ONE. 8:e54316.

Nieselt, K., F. Battke, A. Herbig, P. Bruheim, A. Wentzel, O. M. Jakobsen, H. Sletta, M. T. Alam, M. E. Merlo, J. Moore, W. A. M. *et al*. 2010. The Dynamic Architecture of the Metabolic Switch in *Streptomyces coelicolor*. BMC Genomics. 11:10.

Ozergin-Ulgen, K., and F. Mavituna. 1998. Oxygen Transfer and Uptake in Streptomyces coelicolor A3(2) Culture in a Batch Bioreactor. Journal of Chemical Technology and Biotechnology. 73:243-250.

Paget, M.S., L. Chamberlin, A. Atrih, S.J. Foster, and M.J. Buttner. 1999. Evidence that the Extracytoplasmic Function Sigma Factor *sigmaE* is

Required for Normal Cell Wall Structure in *Streptomyces coelicolor* A3(2). Journal of Bacteriology. 181:204–211.

Pamboukian, C.R.D., L.M. Guimarães, and M.C.R. Facciotti. 2002. Applications of Image Analysis in the Characterization of *Sreptomyces olindensis* in Submerged Culture. Brazilian Journal of Microbiology. 33:17-21.

Peel, J.L., and B.C. Loughman. 1957. Some Observations on the Role of Copper Ions in the Reduction of Phosphomolybdate by Ascorbic Acid and their Application in the Determination of Inorganic Orthophosphate. Biochemical Journal. 65:709-716.

Plummer, D.T. 1987. An Introduction to Practical Biochemistry. 3rd Edition. McGraw-Hill Book Company. London.

Prosser, J.I., and A.J. Tough. 1991. Growth Mechanisms and Growth Kinetics of Filamentous Microorganisms. Critical Reviews in Biotechnology. 10:253-274.

Redenbach, M., H.M. Kieser, D. Denapaite, A. Eichner, J. Cullum, H. Kinashi and D.A. Hopwood. 1996. A Set of Ordered Cosmids and a Detailed Genetic and Physical Map for the 8 Mb *Streptomyces coelicolor* A3(2) Chromosome. Molecular Microbiology. 21:77-96.

Reid, R.C., J.M. Praunsnitz, and T.K. Sherwood. 1977. The Properties of Gases and Liquids. Third Edition. McGraw-Hill. NY. p. 578.

Richards, D.M., A.M. Hempel, K. Flärdh, M.J. Buttner, and M. Howard. 2012. Mechanistic Basis of Branch-Site Selection in Filamentous Bacteria. PLoS Computational Biology. 8:e1002423.

Robinson, J.A., and J.M. Tiedje. 1983. Nonlinear Estimation of Monod Growth Kinetic Parameters from a Single Substrate Depletion Curve. Applied and Environmental Microbiology. 45:1453-1458.

Rodríguez-García, A., A. Sola-Landa, K. Apel, F. Santos-Beneit, and J.F. Martín. 2009. Phosphate Control over Nitrogen Metabolism in *Streptomyces coelicolor*: Direct and Indirect Negative Control of *glnR*, *glnA*, *glnII* and *amtB* Expression by the Response Regulator PhoP. Nucleic Acids Research. Doi:10.1093/nar/gkp162.1-13.

Rosen, H. 1957. A Modified Ninhydrin Colorimetric Analysis for Amino Acids. Archives of Biochemistry and Biophysics. 67:10-15.

Ruban-Ośmiałowska B., D. Jakimowicz, A. Smulczyk-Krawczyszyn, K.F. Chater and J. Zakrzewska-Czerwińska. 2006. Replisome Localization in Vegetative and Aerial Hyphae of *Streptomyces coelicolor*. Journal of Bacteriology. 188:7311-7316.

Ryu, Y.-G., E.-S. Kim, D.-W. Kim, S.-K. Kim, and K.J. Lee. 2007. Differential Stringent Responses of *Streptomyces coelicolor* M600 to Starvation of Specific Nutrients. Journal of Microbiology and Biotechnology. 17:305-312.

Sambrook, J., E.F. Fritsch, and T. Maniatis. 1989. Molecular Cloning a Laboratory Manual. Cold Spring Harbour Laboratory Press.

Sangal, V., N. P. Tucker, A. Burkovski and P.A. Hoskisson. 2012. The Draft Genome Sequence of *Corynebacterium diphteriae* by *mitis* NCTC 3529 Reveals Significant Diversity between the Primary Disease-Causing Biovars. Journal of Bacteriology. 194:3269.

Sarrà, M., C. Casas, and F. Gòdia. 1996. Continuous Production of a Hybrid Antibiotic by *Streptomyces lividans* TK21 Pellets in a Three-Phase Fluidized-Bed Bioreactor. Biotechnology and Bioengineering. 53:601-610.

Shaw, W.V., and D.A. Hopwood. 1976. Chloramphenicol Acetylation in *Streptomyces*. Journal of General Microbiology. 94:159-166.

Shepherd, N., P. Dennis, and H. Bremer. 2001 Cytoplasmic RNA Polymerase in *Escherichia coli*. Journal of Bacteriology. 183:2527–2534.

Sievers, F., A. Wilm, D.G. Dineen, T.J. Gibson, K. Karplus, W. Li, R. Lopez, H. McWilliam, M. Remmert, J. Söding, J.D. Thompson, and D.G. Higgins. 2011. Fast, Scalable Generation of High-Quality Protein Multiple Sequence Alignments Using Clustal Omega. Molecular Systems Biology. 7:539 doi:10.1038/msb.2011.75.

Smith, M., J. Bruhn, and J. Anderson. 1992. The Fungus Armillaria-Bulbosa is among the Largest and Oldest Living Organisms. Nature. 356:428-431.

Sola-Landa, A., R.S. Moura, and J.F. Martin. 2003. The Two-Component PhoR-PhoP System Controls both Primary Metabolism and Secondary Metabolite Biosynthesis in *Streptomyces lividans*. PNAS. 100:6133-6138.

Steinberg, G. 2007. Hyphal Growth: a Tale of Motors, Lipids and the Spitzenkörper. Eukaryotic Cell. 6:351-360.

Stocks, S.M., and C.R. Thomas. 2001. Viability, Strenght, and Fragmentation of *Saccharopolyspora erythraea* in Submerged Fermentation. Biotechnology and Bioengineering. 75:702-709.

Stocks, S.M. 2004. Mechanism and Use of the Commercially Available Viability Stain, *Bac*Light. Cytometry Part A 61A:189-195.

Stokes, C.L., D.A. Lauffenburger, and S.K. Williams. 1991. Migration of Individual Microvessel Endothelial Cells: Stochastic Model and Parameter Measurement. Journal of Cell Science. 99:419-430.

Stokes, C.L., and D.A. Lauffenburger. 1991. Analysis of the Roles of Microvessel Endothelial Cell Random Motility and Chemotaxis in Angiogenesis. Journal of Theoretical Biology. 152:377-403.

Sun, J., A. Hesketh, and M. Bibb. 2001. Functional Analysis of *relA* and *rshA*, Two *relA/spoT* Homologues of *Streptomyces coelicolor* A3(2). Journal of Bacteriology 183:3488-3498.

Taylor, G.T., and S.J. Pirt. 1977. Nutrition and Factors Limiting the Growth of a Methanogenic Bacterium (*Methanobacterium thermoautotrophicum*). Archives of Microbiology. 113:17-22.

Taylor, R.D. 1992. Purification and Characterisation of the Isocitrate Dehydrogenase from *Streptomyces coelicolor* and Cloning of its Gene. University of Glasgow. PhD Thesis.

Thomas, L., D. A. Hodgson, A. Wentzel, K. Nieselt, T. E. Ellingsen, J. Moore, E.R. Morrissey, R. Legaie, The STREAM Consortium, W. Wohlleben, A. Rodriguez-García, J.F. Martín, N.J. Burroughs, E.M.H. Wellington, and M.C.M. Smith. 2012. Metabolic Switches and Adaptations Deduced from the Proteomes of *Streptomyces coelicolor* Wild Type and *phoP* Mutant Grown in Batch Culture. Molecular Cell Proteomics. 11: M111.013797.

Transparency Market Research, 2012, Antibiotic Market – Global Size, Share, Trends, Analysis and Forecast, 2012 - 2018. Press Release 10.03.2012. accessed 20 May 2013 http://www.sbwire.com/press-

releases/antibiotic-market-global-industry-size-share-trends-analysis-and-forecast-2012-2018-168346.htm.

Uhlenbeck, G.E., and L.S. Ornstein. 1930. On the Theory of the Brownian Motion. Physical Review. 36:823-841.

van Veluw, G.J., M.L.C. Petrus, J. Gubbens, R. de Graaf, I.P. de Jong, G.P. van Wezel, H.A.B. Wösten, and D. Claessen. 2012. Analysis of Two Distinct Mycelial Populations in Liquid-Grown *Streptomyces* Cultures Using a Flow Cytometry-Based Proteomics Approach. Applied Microbiology and Biotechnology. DOI 10.1007/s00253-012-4490-5.

van Wezel, G.P., P. Krabben, B.A. Traag, B.J.F. Keijser, R. Kerste, E. Vijgenboom, J.J. Heijnen, and B. Kraal. 2006. Unlocking *Streptomyces* spp. for Use as Sustainable Industrial Production Platforms by Morphological Engineering. Applied and Environmental Microbiology. 72:5283-5288.

van Wezel, G.P., J. White, G. Hoogvliet, and M.J. Bibb. 2000. Application of *redD*, the Transcriptional Activator Gene of the Undecylprodigiosin Biosynthetic Pathway, as a Reporter for Transcriptional Activity in *Streptomyces coelicolor* A3(2) and *Streptomyces lividans*. Journal of Molecular Biotechnology. 2:551-556.

Viollier, P.H., W. Minas, G.E. Dale, M. Folcher, and C.J. Thompson. 2001. Role of Acid Metabolism in *Streptomyces coelicolor* Morphological Differentiation and Antibiotic Biosynthesis. Journal of Bacteriology. 183:3184-3192.

Voelker, F., and S. Altaba. 2001. Nitrogen Source Governs the Patterns of Growth and Pristinamycin Production in '*Streptomyces pristinaespiralis*'. Microbiology. 147. 2447-2459.

Weast, R.C. (ed.) 1969. CRC Handbook of Chemistry and Physics, 50th Edition. p.F-36.

Wehmeier, S., A.S. Varghese, S.S. Gurcha, B. Tissot, M. Panico, P. Hitchen, H.R. Morris, G.S. Besra, A. Dell, and M.C.M. Smith. 2009. Glycosylation of the Phosphate Binding Protein, PstS, in *Streptomyces coelicolor* by a Pathway that Resembles Protein 0-Mannosylation in Eukaryotes. Molecular Microbiology. 71:421-433.

Wehrli, W. 1983. Rifampicin: Mechanism of Action and Resistance. Reviews of Infectious Diseases. 5:S407-S411.

Welty, J.R., C.E. Wicks, and R.E. Wilson. 1984. Fundamentals of Momentum, Heat, and Mass Transfer. Third Edition. John Wiley & Sons, NY. p. 803.

Willemse, J. and G.P. van Wezel. 2008. Imaging of *Streptomyces coelicolor* A3(2) with Reduced Autofluorescence Reveals a Novel Stage of FtsZ Localization. PLoS ONE 4 e4242:1-5.

Willey, J.W., J. Schwedock, and R. Losick. 1993. Multiple Extracellular Signals Govern the Production of a Morphogenetic Protein Involved in Aerial Mycelium Formation by *Streptomyces coelicolor*. Genes and Development. 7:895–903.

Wolánski, M., R. Wali, E. Tilley, D. Jakimowicz, J. Zakrzewska-Czerwińska and P. Herron. 2011. Replisome Trafficking in Growing Vegetative Hyphae of *Streptomyces coelicolor* A3(2). Journal of Bacteriology. 193:1273-1275.

Woldringh, C.L., A. Zaritsky and N.B. Grover. 1994. Nucleoid Partitioning and the Division Plane in *Escherichia coli*. Journal of Bacteriology. 176:6030-6038.

Woldringh, C.L., P.R. Jensen and H.V. Westerhoff. 1995. Structure and Partitioning of Bacterial DNA: Determined by a Balance of Compaction and Expansion Forces? FEMS Microbiology Letters. 131:235-242.

Yang, H., U. Reichl, R. King, and E.D. Gilles. 1992a. Measurement and Simulation of the Morphological Development of Filamentous Microorganisms. Biotechnology and Bioengineering. 39:44-48.

Yang, H., R. King, U. Reichl, and E.D. Gilles. 1992b. Mathematical Model for Apical Growth, Septation, and Branching of Mycelial Microorganisms. Biotechnology and Bioengineering. 39:49-58.

Zhang, B.-B., P. Wang, A. Wang, W.-C. Wang, W-G. Tang, and G-P. Zhu. 2013. Expression and Characterization of a Novel Isocitrate Dehydrogenase from *Streptomyces diastaticus* No. 7 Strain M1033. Molecular Biology Reports. 40:1615-1623.

Zimmerman, S. B. 2002. Toroidal Nucleoids in *Escherichia coli* Exposed to Chloramphenicol. Journal of Structural Biology. 138:199-206.

Appendix 1

Appendix 1

Table 1 shows a summary of the mathematical models reviewed in the introduction of this thesis and Table 2 highlights the main differences between the models.

Table 1. Summary of reviewed models

Author(s)	Model organism	Model based on	Modeling
Yang *et al*. (1992a)	*Streptomyces tendae*	Deterministic kinetics	Model for tip growth and branching direction
Yang *et al*. (1992b)	*Streptomyces tendae*	Yang *et al*. (1992a)	Mathematical model for tip growth, septation and branching
Meyerhoff *et al*. (1995)	*Penicillium chrysogenum*	Yang *et al*. (1992b)	Model for pellet growth
Meyerhoff and Bellgardt (1995a)	*Penicillium chrysogenum*	Meyerhoff *et al*. (1995)	Model for pellet growth in fed-batch cultivation
Meyerhoff and Bellgardt (1995b)	*Penicillium chrysogenum*	Meyerhoff and Bellgardt (1995a)	Simplified model of pellet growth for process simulations
Lejeune *et al*. (1995)	*Trichoderma reesei*	Deterministic kinetics	Model for early growth and branching
Lejeune and Baron (1997)	*Trichoderma reesei*	Lejeune and Baron (1995)	Random walk 3D model for filamentous growth
Stokes *et al.* (1991)	Microvessel endothelial cells	Dunn and Brown (1987), Uhlenbeck and Ornstein (1930)	Biased random walk 2D model for motility and chemotaxis of a cell
Stokes and Lauffenburger (1991)	Microvessel endothelial cells	Stokes *et al.* (1991)	Biased random walk 2D model for motility and chemotaxis of cells
Meškauskas *et al*. (2004a)	Fungi	Hyphal growth kinetics	Vector-based neighbour sensing model of hyphal growth
Meškauskas *et al*. (2004b)	*Phanerochaete velutina*	Meškauskas *et al*. (2004a)	Model for growth on semi-solid substrata

Boswell *et al*. (2007)	*Rhizoctonia solani*	Boswell *et al*. (2003a), Boswell *et al*. (2002)	Hybrid cellular automaton model
Lucas *et al*. (2008)	*Arabidopsis thaliana*	Stochastic data	Hidden markovian model for plant root formation
Delvigne *et al*. (2006)	*Saccharomyces cerevisiae*	Stochastic modeling methodology	Biased random walk model based on Markov chain for monitoring bioreactors
Celler *et al*. (2012)	*Streptomyces coelicolor*	Yang *et al*. (1992a), Meyerhoff *et al*. (1995), Lejeune and Baron (1997)	Combined morphological and structured model of 3D pellet formation
Richards *et al*. (2012)	*Streptomyces coelicolor*	Experimental data	Tip-focus splitting mechanism

Table 2. A detailed comparison of reviewed models

Author(s)	**Growth**	**Branching**	**Hyphal morphology**	**Hyphal metabolism**	**Antibiotic production**	**Pellet formed as**	**Neighbour sensing**	**Space**	**Concentration gradient**	**Shear forces**	**Simulation**
Yang *et al*. (1992a)	Section-wise at hyphal extension rate	Normally distributed	Compartment (0 or 1 tip) of constant diameter	-	-	Discrete hyphae	-	3D	-	-	3.6 μm germ tube – pellet (14 h)
Yang *et al*. (1992b)	Section-wise, extension rate proportional to internal growth component	Normally distributed around septa	Compartment (0 or 1 tip) of constant diameter	Key growth component formation and diffusion	-	Discrete hyphae	-	3D	Internal key component for growth	-	3.6 μm germ tube – pellet (13 h)
Meyerhoff *et al*. (1995)	Section-wise, extension rate proportional to internal growth component	Normally distributed around septa	Type 1 and 2 compartments (0, 1 or 2 tips) with constant diameter	Actively growing hypha, hypha with only maintenance requirements, lysis	-	Discrete hyphae, subdivided into spherical layers	-	3D	Internal growth component, external glucose and oxygen (Monod kinetics)	Included for outer regions of hyphae	two compartments – pellet (110 h)
Meyerhoff and Bellgardt (1995a)	Section-wise until 150-300 tips formed, then layer-wise	Truncated Gauß-distribution, stiff chain model	Type 1 compartments only (0 or 1 tip) with constant diameter	Actively growing hypha, hypha with only maintenance requirements, lysis	-	Spherical layers	-	3D	External glucose and oxygen (Monod kinetics)	Included for outer regions of hyphae	Oxygen and glucose profiles for a single pellet (216 h)

- = Not included in the model

Table 2. A detailed comparison of reviewed models (continued)

Author(s)	**Growth**	**Branching**	**Hyphal morphology**	**Hyphal metabolism**	**Antibiotic production**	**Pellet formed as**	**Neighbour sensing**	**Space**	**Concentration gradient**	**Shear forces**	**Simulation**
Meyerhoff and Bellgardt (1995b)	Section-wise until 150-300 tips formed, then layer-wise	Truncated Gauß-distribution, stiff chain model	Type 1 compartments only (0 or 1 tip) with constant diameter	Actively growing hypha, hypha with only maintenance requirements, lysis	Included at glucose level (<0.4 g/L), only in actively growing hypha, not produced by tips	Spherical layers	-	3D	External glucose and oxygen (Monod kinetics)	Stochastic breaking of pellets (over 200 µm in diameter) into 8 identical pieces	Total biomass, glucose and product conc. of 100 developing pellets (190 h)
Lejeune *et al*. (1995)	Saturation type kinetics	Stochastic in respect to total hyphal length	-	-	-	-	-	-	-	-	Lenght of hypha, number of tips (21 h)
Lejeune and Baron (1997)	Random walk of tips with oxygen dependant extension rate	Stochastic in respect to total hyphal length	Cylindrical shape with constant diameter and density	-	-	Discrete hyphae	Porosity of pellet	3D fractal dimension by box counting method	External oxygen (Monod kinetics)	-	Pellet development (27 h)

- = Not included in the model

Table 2. A detailed comparison of reviewed models (continued)

Author(s)	Growth	Branching	Hyphal morphology	Hyphal metabolism	Antibiotic production	Pellet formed as	Neighbour sensing	Space	Concentration gradient	Shear forces	Simulation
Stokes *et al.* (1991)	Random walk (Ornstein-Uhlenbeck process)	-	Cell path	-	-	-	-	2D	Attractant for chemotaxis	-	Single cell migration (41 h)
Stokes and Lauffenburger (1991)	Random walk (Ornstein-Uhlenbeck process)	Stochastic	Cell path	-	-	-	Anastomosis	2D	Attractant for chemotaxis	-	Cells migration from parent vessel
Meškauskas *et al*. (2004a)	Growth vector of tip, growth kinetics	Stochastic or density dependent	Growth vector	-	-	Discrete hyphae	Mycelium surrounding of six fields	3D	Gravity, light, chemicals	-	Fungal fruit bodies, gravitropism
Meškauskas *et al*. (2004b)	Growth vector of tip, growth kinetics	Stochastic or density dependent	Growth vector	-	-	Discrete hyphae	Mycelium surrounding of six fields	3D	Gravity, light, chemicals	-	Colony development on semi-solid surface

- = Not included in the model

Table 2. A detailed comparison of reviewed models (continued)

Author(s)	**Growth**	**Branching**	**Hyphal morphology**	**Hyphal metabolism**	**Antibiotic production**	**Pellet formed as**	**Neighbour sensing**	**Space**	**Concentration gradient**	**Shear forces**	**Simulation**
Boswell *et al*. (2007)	biased random walk of tips on the vertices of a triangular lattice embedded within the hexagonal lattice of substrate	Linear branching rate with respect to the amount of internal substrate	Hyphal tips and active or inactive hyphae	Internal substrate levels affect the viability of hyphae and the uptake of external substrate	-	Discrete hyphae over hexagonal substratae	anastomosis	-	Translocation of nutrient reallocation within hyphae, heterogeneous environment, acidification	-	hypha to mycelium in various environments
Lucas *et al*. (2008)	Hidden Markovian chain based on classical likelihood maximization procedure	-	Zones and segments with six different developmental states	Auxin flux	-	-	-	-	Internal auxin	-	-
Delvigne *et al*. (2006)	Biased random walk of microorganism	-	-	-	-	-	-	3D	External particle movement according to Markov chain	Drift coefficient for flow caused by recirculation pump	Tracer curves for bioreactors

- = Not included in the model

Table 2. A detailed comparison of reviewed models (continued)

Author(s)	**Growth**	**Branching**	**Hyphal morphology**	**Hyphal metabolism**	**Antibiotic production**	**Pellet formed as**	**Neighbour sensing**	**Space**	**Concentration gradient**	**Shear forces**	**Simulation**
Celler *et al*. (2012)	as per Yang *et al*. (1992a)	at chosen branching intervals in response to oxygen concentration	Three compartments (apical, subapical and hyphal)	All compartments consume oxygen at same level as per Monod kinetics	Assumed to occur from hyphal compartment	Discrete hyphae	Collision detection	3D	External oxygen	Fragmentation to occur at cross-walls next to branching sites in low biomass density area	Pellet development (36 h)
Richards et al. (2012)	Length increment at each time step	By tip-focus splitting mechanism with trimming rule	-	DivIVA production	-	-	-	1D arrays	-	-	Histograms of hyphal length using different trimming lengths

- = Not included in the model

Appendix 2

Appendix 2

Used media

Mannitol soya flour medium (MS medium)

D-Mannitol (Fisher, UK) 16 g/L

Soya Bean flour 16 g/L

Agar technical No.3 (Oxoid, UK) 20 g/L

Autoclaved at 120°C for ca 30 min.

L-Broth medium (LB)

Tryptone (Oxoid, UK)10 g/L

Yeast extract (Oxoid, UK) 5 g/L

NaCl (Fisher, UK) 5 g/L

pH adjusted to ca 7.0 with NaOH

Autoclaved at 120°C for ca 15 min.

2 x YT

Tryptone (Oxoid, UK) 16 g/L

Yeast extract (Oxoid, UK) 10 g/L

NaCl (Fisher, UK) 5 g/L

Autoclaved at 120°C for ca 15 min.

SOB (according to Hanahan 1983)

Tryptone (Oxoid, UK) 20 g/L

Yeast extract (Oxoid, UK) 5 g/L

NaCl (Fisher, UK) 10 mM

KCl (Sigma, UK) 2.5 mM

Autoclaved at 120°C for ca 15 min and allowed to cool down before adding:

MgCl (Fisher, UK) 10 mM (sterile filtered)

$MgSO_4$ (Fisher, UK) 10 mM (sterile filtered)

YEME no sucrose

Yeast extract (Oxoid, UK) 3 g/L

Peptone (Fisher, UK) 5 g/L

Malt extract (Oxoid, UK) 3 g/L

D-Glucose (Fisher, UK) 10 g/L

Autoclaved at 120°C for ca 15 min and allowed to cool down before adding:

MgCl (Fisher, UK) 5 mM

Used reagents

Phosphorus assay

Ammonium molybdate (Fisher, UK) 50 g/L

Copper acetate buffer pH 4

Copper sulphate (Fisher, UK) 25 g/L

Sodium acetate (Sigma, UK) 46 g/L

Dissolved in 1 L of 2 M acetic acid (Riedel-de-Haen)

Reducing agent

p-methylaminophenol sulphate (METOL) (Fluka, UK) 20 g/L

Sodium sulfite (Fluka, UK) 100 g/L

Stored in dark bottle

Ammonia assay

Sodium phenate

Phenol (Sigma, UK) 250g/L

Sodium hydroxide 0.3 M

Stable for 1 month at + 4 °C

Sodium nitroprusside (Fisher, UK) 0.1 % (w/v)

Stable for 1 month at + 4 °C

Sodium hypochlorite (Sigma-Aldrich, UK)

Diluted 1:5 prior to use

DNA extraction by alkaline lysis method

Solution 1 – resuspension solution for cell pellet

50 mM glucose

25 mM Tris-Cl (pH 8.0)

10 mM EDTA (pH 8.0)

Solution 2 – lysis solution

0.2 N NaOH

1% SDS

Solution 3 – neutralization solution

60 ml of 5 M potassium acetate

11.5 ml of glacial acetic acid

28.5 ml dH_2O

TE buffer – resuspension solution for DNA pellet

10 mM Tris-Cl (pH 8.0)

1 mM EDTA (pH 8.0)

Southern blot analysis

Stock solutions for pre-hybridisation and hybridisation

20x SSC	175.3 g NaCl
	388.2 g Sodium citrate
	Make up to 1 litre with dH_2O
	Adjust to pH 7.0 with HCl
10% SDS	10 g SDS in 100 ml dH_2O
	Heat to 68 ºC to dissolve
	Adjust to pH 7.2 with HCl

10% N-laurylsarcosine	5 g in 50 ml dH_2O
Maleic acid buffer	22.2 g Maleic acid
	17.6 g NaCl
	Make up to 1 litre with dH_2O
	Adjust to pH 7.5 with solid NaOH
10% blocking solution	10 g blocking reagent
	100 ml maleic acid buffer
	Microwave to dissolve
Detection buffer	3.63 g Tris-HCl
	1.753 g NaCl
	Make up to 300 ml with dH_2O
	Adjust to pH 9.5

Hybridisation

Standard hybridisation buffer (SHB)	5x SSC
	0.1% w/v N-laurylsarcosine
	0.02% w/v SDS
	1% v/v blocking solution

Stringency washes

Stringency buffer A	2x SSC
	0.1% SDS
Stringency buffer B	0.2x SSC
	0.1% w/v SDS

Detection

Washing buffer	1x Maleic acid buffer
	0.3% w/v Tween 20
Blocking solution	1x Blocking solution in maleic acid buffer
Antibody solution	Dilute anti-DIG-AP 1:5000 in 1% blocking solution

Colour substrate solution	One NBT/BCIP tablet in 10 ml dH_2O

Appendix 3

Appendix 3

The results of this thesis were published in PLoS ONE journal with the following title: “A Flexible Mathematical Model Platform for Studying Branching Networks: Experimentally Validated Using the Model actinomycete, *Streptomyces coelicolor*”. The publication is attached to this thesis.

OPEN ACCESS Freely available online

PLOS ONE

A Flexible Mathematical Model Platform for Studying Branching Networks: Experimentally Validated Using the Model Actinomycete, *Streptomyces coelicolor*

Leena Nieminen[1,2], Steven Webb[3]*, Margaret C. M. Smith[4], Paul A. Hoskisson[1]*

1 Strathclyde Institute of Pharmacy and Biomedical Sciences, University of Strathclyde, Glasgow, United Kingdom, **2** Department of Mathematics and Statistics, University of Strathclyde, Glasgow, United Kingdom, **3** MRC Centre for Drug Safety Science, University of Liverpool, Liverpool, United Kingdom, **4** Department of Biology, University of York, York, United Kingdom

Abstract

Branching networks are ubiquitous in nature and their growth often responds to environmental cues dynamically. Using the antibiotic-producing soil bacterium *Streptomyces* as a model we have developed a flexible mathematical model platform for the study of branched biological networks. *Streptomyces* form large aggregates in liquid culture that can impair industrial antibiotic fermentations. Understanding the features of these could aid improvement of such processes. The model requires relatively few experimental values for parameterisation, yet delivers realistic simulations of *Streptomyces* pellet and is able to predict features, such as the density of hyphae, the number of growing tips and the location of antibiotic production within a pellet in response to pellet size and external nutrient supply. The model is scalable and will find utility in a range of branched biological networks such as angiogenesis, plant root growth and fungal hyphal networks.

Citation: Nieminen L, Webb S, Smith MCM, Hoskisson PA (2013) A Flexible Mathematical Model Platform for Studying Branching Networks: Experimentally Validated Using the Model Actinomycete, *Streptomyces coelicolor*. PLoS ONE 8(2): e54316. doi:10.1371/journal.pone.0054316

Editor: Alissa M. Weaver, Vanderbilt University Medical Center, United States of America

Received November 26, 2012; **Accepted** December 10, 2012; **Published** February 18, 2013

Funding: The authors would like to thank the Scottish Universities Life Science Alliance (SULSA) for PhD studentship funding to LN (http://www.sulsa.ac.uk/). The funders had no role in study design, data collection and analysis, decision to publish, or preparation of the manuscript.

Competing Interests: The authors have declared that no competing interests exist.

* E-mail: steven.webb@liverpool.ac.uk (SW); Paul.hoskisson@strath.ac.uk (PAH)

Introduction

Branched morphological networks are ubiquitous in biology and have received much attention in theoretical and experimental studies in a range of biological systems. Branched networks are highly scalable from bacterial hyphal structures in the μm to mm spatial range and minutes to hours timescales through to colonies of *Armillaria bulbosa* occupying 150,000 square metres over thousands of year timescales [1]. These scales represent a significant challenge to the modeling of such dynamic recursive structures, yet modeling these systems has been valuable in revealing many emergent properties of branched networks, yielding important details regarding angiogenesis in organs and tumors [2–6], transport networks in fungi [1,7–9] and amoebae [2–6,10] and the development of root systems in plants [11,12]. Often however such models are system specific and lack flexibility. Thus an adaptable and flexible model platform that responds to external factors and can give an output in terms of the network heterogeneity that can be applied to many branched networks would be highly desirable.

The saprophytic soil bacterium *Streptomyces* is commercially exploited for the production of antibiotics, immunosuppressive, anticancer agents and other bioactive metabolites. *Streptomyces* are unusual bacteria in their growth form; they grow by apical extension of an individual hypha, achieving exponential growth by the addition of new hyphal tips through branching [13]. In their natural soil environment the hyphae access resources in a heterogeneous environment via this exploratory apical extension. In liquid culture, such as the conditions used commercially to produce bioactive metabolites, these apically extending and branching hyphae become entangled and form large hyphal aggregates, whose morphology can significantly affect the efficiency of industrial scale fermentations. These mycelial aggregates (or pellets) are physiologically heterogeneous – often metabolically active at the edges, yet nutrient starved and anoxic at the centre [14,15]. It is known that the nutritional status of *Streptomyces* cells has a profound effect on the formation of secondary metabolites such as antibiotics [16], such that much of the biomass in an industrial fermentation may be non-productive in terms of the desired metabolite. Measuring the heterogeneity of these pellets is difficult experimentally and understanding the heterogeneity could have significant value in the manipulation of industrial organisms in terms of their morphology and their fermentation characteristics. This is particularly important through the application of molecular biology and genetics to alter the morphology of industrial strains for improved fermentation characteristics. Studies in the literature show that there is a critical pellet size for the production of the antibiotic erythromycin in *Saccharopolyspora erythrea* [17]. Similarly strain variants with altered branching frequency showed more desirable fermentation characteristics such as increased antibiotic production [18,19]. Increasing fragmentation of strains through the manipulation of key cell division genes such as *ssgA* in *Streptomyces* has also shown that engineering of production strains offers great potential for improved fermentation efficiency and yield [18,19]. The application of a robust modeling platform to

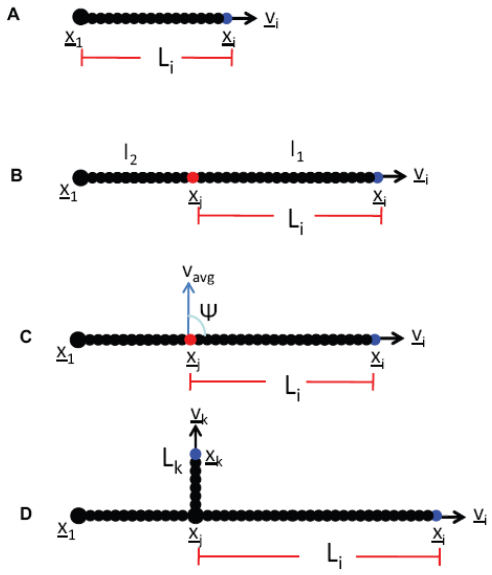

Figure 1. Branching events in the model. A. Hypha grows with velocity ($\underline{v}_i$) from its original position ($\underline{x}_1$). The total length of the hyphae is (L_i). **B.** By a probability drawn from a normal distribution, a branching point $\underline{x}_j$ is identified away from a starting point $\underline{x}_1$ at an average inter-branch distance of l_2, derived from experimentally observed values. **C.** A new hyphae emerges from the branching point position $\underline{x}_j$ with branching angle ϕ and average velocity v_{avg}. The branching angle is taken from the parent hyphae using a bimodal probability distribution derived from experimental data. The average velocity (v_{avg}) is measured from early hyphal growth experiments. **D.** Both the new and the parent hypha continue to elongate with their own velocities ($\underline{v}_k$ and $\underline{v}_j$ respectively). The length L_i of the parent hyphae is now reset to be the distance between the latest branching point $\underline{x}_j$ and its tip position $\underline{x}_i$, whereas the length of the new hyphae L_k initiates from zero and increases as the new hyphae extends.
doi:10.1371/journal.pone.0054316.g001

this process should therefore yield key information regarding the production of secondary metabolites and how this can be manipulated.

Previously there has been a great deal of interest in modelling both fungal and bacterial hyphal growth [20–23]. Lattice-based modelling has been applied to fungal hyphal growth [9,24] and recent modelling attempts of *Streptomyces* include a genome wide metabolic model reconstruction [25], a mechanistic based model of branching [26] and a morphological model of pellet growth [27], all of which have built upon earlier work modelling work focussed on filamentous fungi in particular [14,28–30].

Here we present a discrete-continuum stochastic differential equation model platform that is applicable to many of the branched networks found in biology. The advantage of our model is that it uses relatively few parameters, of which most are directly derived from experimental data. We have validated and parameterised the model using experimental data and used the resulting model outputs to make biologically important inferences regarding the growth dynamics, physiological heterogeneity and antibiotic production in the industrially important bacterium *Streptomyces*. Using oxygen as a growth limiting substrate, we evaluate the influence of hyphal extension and branching on pellet formation and gain insight into the areas of the pellet producing antibiotics. This is important for applications where an optimal branching rate can influence production. The model can make predictions that are difficult or impossible to measure using experimental methods. We have used the model to gain quantitative insight into pellet growth characteristics, predicting quantities such as the hyphal growth unit (HGU) and the localisation of maximal branching. The flexibility of this modelling platform means that it can be applied to a wide range of branched biological networks such as plant root growth, angiogenesis and fungal mycelium.

Table 1. Parameters used for modelling early hyphal growth.

Parameter	Symbol	Value
Simulation time interval	T	4 h
Number of Brownian steps	_	100
Diffusion coefficient	α	10
Drift coefficient	β	10
Average apical length	l_1	28.5 μm
Average interbranch length	l_2	7.3 μm
Standard deviation of apical length	l_1sd	8.5 μm
Standard deviation of interbranch length	l_2sd	3.9 μm
Average branching angle	ϕ	±84.0 deg
Standard deviation of branching angle	ϕ_{sd}	23.0 deg
Average hyphal velocity	v_{avg}	6.3 μm/h

doi:10.1371/journal.pone.0054316.t001

Results

Mathematical Description and Experimental Validation of the Model

Elongation of network. To describe the elongation of an individual tip within the network, we constructed a 2D random walk model. The location of a tip over time is defined by an ordinary differential equation, where the i^{th} hyphal tip has a position ($\underline{x}_i \in \mathbb{R}^2$) that varies over time (t) according to its velocity ($\underline{v}_i \in \mathbb{R}^2$), namely;

$$\frac{d\underline{x}_i(t)}{dt} = \underline{v}_i(t) \tag{1}$$

Equation 1 was solved using Euler's method. The direction of the tip movement is described by its velocity using a stochastic differential equation similar to that used by Stokes *et al.*, [2]. We further amend the model to include the average speed of extension (v_{avg}) and normal velocity $\hat{\underline{v}}_i(t)$ as shown in (2), where the velocity depends on the current value plus a random component which is unbiased and uncorrelated:

$$d\underline{v}_i(t) = \beta(v_{avg}\hat{\underline{v}}_i(t) - \underline{v}_i(t))dt + \sqrt{\alpha}d\underline{W}_i(t) \tag{2}$$

where,

$$\hat{\underline{v}}_i(t) = \frac{\underline{v}_i(t)}{\|\underline{v}_i(t)\|} \tag{3}$$

and $\beta(v_{avg}\hat{\underline{v}}_i(t)-\underline{v}_i(t))dt$ describes the tendency of the tip to move at the average elongation rate, and $\sqrt{\alpha}d\underline{W}_i(t)$ describes random fluctuations in tip speed and direction incorporating white noise into the model, where β is the drift coefficient and α is the diffusion coefficient.

The velocity of an individual tip is impossible to measure in liquid cultures and thus no speed distribution can be directly derived from experimental data. We assume that even when the hyphal network has grown to form a large pellet, the environment where the tips elongate and branches are formed, being at the extremities of the pellet, is still similar to the early hyphal growth (i.e. no growth limiting factors are minimal). Therefore, our assumption is that the velocity is unlikely to change dramatically during a pellet lifetime. The randomness incorporated in to the velocity is validated by model comparison against corresponding experimental observations of hyphal growth spread.

The model allows tip paths to cross over creating a 2D+ effect where we make the assumption that the overlapping tip paths are in different 3D planes. Therefore, the model is trying to capture 3D effects in 2D framework. This means that crowding is not explicitly included in the model, however it is intrinsically introduced via the growth limiting effects of an external substrate. The model has been rigorously validated and tested using laboratory studies to overcome any geometrical limitations of the 2D+ framework.

Branching. We mimic the natural process and model the branching of the network to occur behind the apically growing tip. The tip-to-branch distance is drawn from a cumulative probability distribution function with an average and standard deviation obtained from experimentally determined branching frequency distributions. The probability of branching increases with increasing apical length of an elongating tip. The length of a hypha (L_i) is defined as:

$$\frac{dL_i(t)}{dt}=\|\underline{v}_i(t)\| \tag{4}$$

At each time step, a new position for each growing tip is calculated, the hyphal length updated and the probability of branching determined. The probability of branching is obtained from an experimentally derived cumulative distribution function (average l_1+l_2, standard deviation $l_1$sd+$l_2$sd) and is compared to a random number in the unit interval drawn from a uniform distribution. If the branching probability is higher than the randomly generated number, branching occurs and a branch point is created (note that we only allow branching to occur if the external substrate levels are high enough for active growth), therefore only growing cells can branch. The position of this new branching point is calculated from the start of the hyphae at an average interbranch distance (l_2), which is experimentally derived. The branching angle (ϕ) is determined from a bimodal probability distribution derived from experimental data. The new tip first emerges from the branching point with an average velocity (v_{avg}), measured from experimental data, and then continues to elongate on its own velocity independent from the parent hypha's velocity. The length of the new hypha increases from zero from the branching point and the length of the parent hypha is reset to be the distance between its tip position and the new branching point. The sub-apical branching event is depicted in **Fig. 1**. Information about the branching procedure is given in the Fig. 1 legend.

Validation of early network growth. At this stage, the model can be used to simulate early network growth where there are no rate limiting growth factors on the individual tips, e.g. such as substrate depletion. Out of total of eleven parameters used, only three cannot be measured directly from laboratory experiments in our model system, *Streptomyces* (see Table 1 for a full list of parameters). The first one of these parameters, the number of Brownian steps, was set to be 100 for a 4 h time interval. We found this sufficient for convergence of the Euler-Maruyama scheme used to numerically solve the stochastic differential equation (2). The most accurate values for the other two parameters, diffusion and drift coefficients, were determined using comparisons of simulations to equivalent experimental measurements of early *Streptomyces* hyphal growth experiments, where the external nutrient environment is constant and not limiting to growth.

The simulation results for different diffusion α and drift β coefficient values are shown in **Fig. 2**, where subplots A– show the diffusion coefficient α varying from 0.1–000, when the drift coefficient β is taken to be constant. The bottom row subplots E– illustrate the difference between the drift coefficient values when they range from 0.01–100, whilst the diffusion coefficient stays constant. For experimental validation purposes the following conclusion can be drawn – the greater the diffusion coefficient the larger the random noise whereas with a large drift coefficient the resistance to random fluctuation is higher. Comparison of these simulations to microscopy images of early hyphal growth (Fig. 2 I), allows us to estimate the most appropriate alpha and beta values for this model organism. We confirmed this morphological observation by numerical calibration to the maximum pellet diameter and the number of tips in the **α** and **β** simulations to the corresponding experimental results. Simulations were run for values **α** (0.1–0) and **β** (0.01–000) (**Fig. 3**) and a comparison is made for each **α** and **β** value to the hyphal growth network shown in Fig. 2. From the comparison of the maximum pellet diameter it can be seen that the low **α** and high **β** values reduce the variation between the minimum and maximum values. To keep the minimum and maximum values within the scope of experimental standard deviations and still maintain as high a random variation as possible, only the **α** values of 1 and 10 and respective **β** values of 0.01–10 and 0.01–10 are taken forward. When comparing the effect **α** and **β** have to the number of the tips in the simulations, it is shown that with the value 10 for both **α** and **β** simulation output is closest to the average from the biological data, and with the variation between simulations staying within acceptable observed biological variation. From hereon in, we take $\alpha=\beta=10$ (indicated by the dashed box in **Fig. 2**).

External environment

Streptomyces is grown in liquid cultures for the production of antibiotics, where the growing hyphae form dense pellets. Despite continuous mixing in these cultures nutrient and oxygen gradients can be generated inside pellets due to consumption, diffusion and mass transfer constraints, cell lysis and degradation processes [31]. We model a concentration of external substrate, $c(\underline{x},t)$ (mmol/l) where $\underline{x}=[x,y]$, using a reaction-diffusion equation where the diffusion term is described by Fick's law [32]:

$$\frac{\partial c}{\partial t}=\nabla^2 cD_c-d_c c \tag{5}$$

where D_c is the diffusion coefficient ($\mu m^2/h$) and d_c is the rate of consumption (h^{-1}). For our experiments and simulations, the growth rate of the hyphae (hours) defines the time scale of interest. Compared to this time scale, over the length scale of a hyphal pellet the diffusion rate is fast and the consumption (d_c) rate is also fast (order of seconds). We make use of these differences and

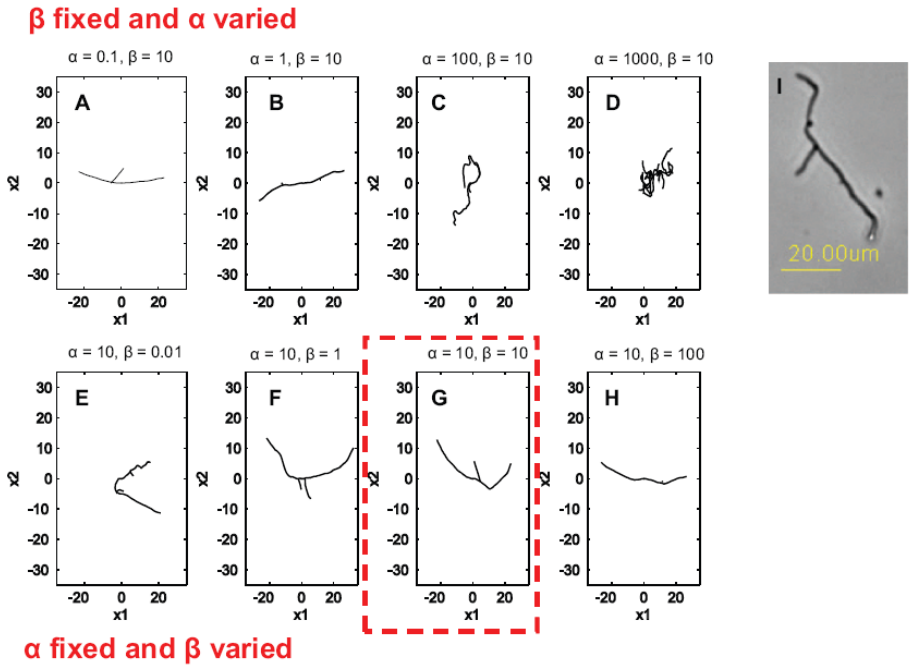

Figure 2. Simulation results for early network growth using different diffusion and drift coefficient values. A–D. Diffusion coefficient α varying from 0.1–1000, drift coefficient β is constant at 10. **E–H.** Drift coefficient β ranging from 0.01–100 when diffusion coefficient α stays constant 10. The remaining parameters are as per **Table 1**. **I.** A phase contrast image of *S. coelicolor* early hyphal growth for comparison. The dashed box shows the simulation results for α and β values used in further simulations.
doi:10.1371/journal.pone.0054316.g002

assume a quasi-steady substrate concentration, to give the leading order expression:

$$0 = \nabla^2 c - \overline{d_c} c \tag{6}$$

where $\overline{d_c} = d_c / D_c$. To solve this equation we subdivide the 2-D domain into a (NxN) regular square grid and discretize the laplacian using finite differences to give N^2 coupled algebraic equations. Unless otherwise stated, we take $N = 200$ and a square domain of size 200×200 μm^2.

We set the boundary conditions as being fixed to the substrate concentration that is detected in media in the absence of any cells. Initially a homogenous concentration is assumed throughout the grid. The tip paths are related to the underlying grid using a least squares interpolation. The hyphal consumption rate (d_c) is then taken to be a function of hyphal occupancy density in the presence of cells. The density can then be calculated by interpolating each of the hyphal branches to the underlying square grid and counting the number of hyphae in different metabolic states in each grid square.

Cell metabolism

We incorporate four different metabolic states of the hyphal aggregate into the model. We assume that as the external substrate concentration depletes due to diffusion limitation and cellular consumption, the hyphae switch from an active growth state (tip elongation and branching) to secondary metabolism state (the antibiotic producing state) as substrate limits growth [16]. As the substrate concentration depletes further the hyphae either die directly, or go through a state where only maintenance energy requirements are met, the cell is therefore alive but not growing or making antibiotic. From this state the hyphae are still able to recover active growth or antibiotic production states depending on the fluctuating external substrate concentration levels, or will then die. The consumption of substrate is assumed to decrease as the metabolism of hyphae change from actively growing to antibiotic producing and further to the maintenance state. Once the hypha dies, no substrate is consumed and it is not possible for the hypha to recover to previous metabolic states.

With the above assumptions, the substrate consumption rate in each square grid cell (i,j), i,j = 1…N is defined as

$$d_c^{i,j} = d_c^a A^{i,j} + d_c^p P^{i,j} + d_c^m M^{i,j} + d_c^e E^{i,j} \tag{7}$$

where $A^{i,j}$, $P^{i,j}$, $M^{i,j}$ and $E^{i,j}$ are the numbers of actively growing, antibiotic producing, maintenance energy only and dead hyphae, respectively, in the grid cell (i,j). The parameters d_c^a, d_c^p, d_c^m and d_c^e are taken to be the consumption rates for different metabolic states of hyphae. Note that $\overline{d_c^a}$, $\overline{d_c^p}$, $\overline{d_c^m}$ and $\overline{d_c^e}$ denote the corresponding rescaled (by D_c) consumption rates. Note that $\overline{d_c^e}$ is zero for the simulations presented in this paper, however, if chemical oxygen demand for cell degradation processes are taken into account, this parameter can be adjusted accordingly.

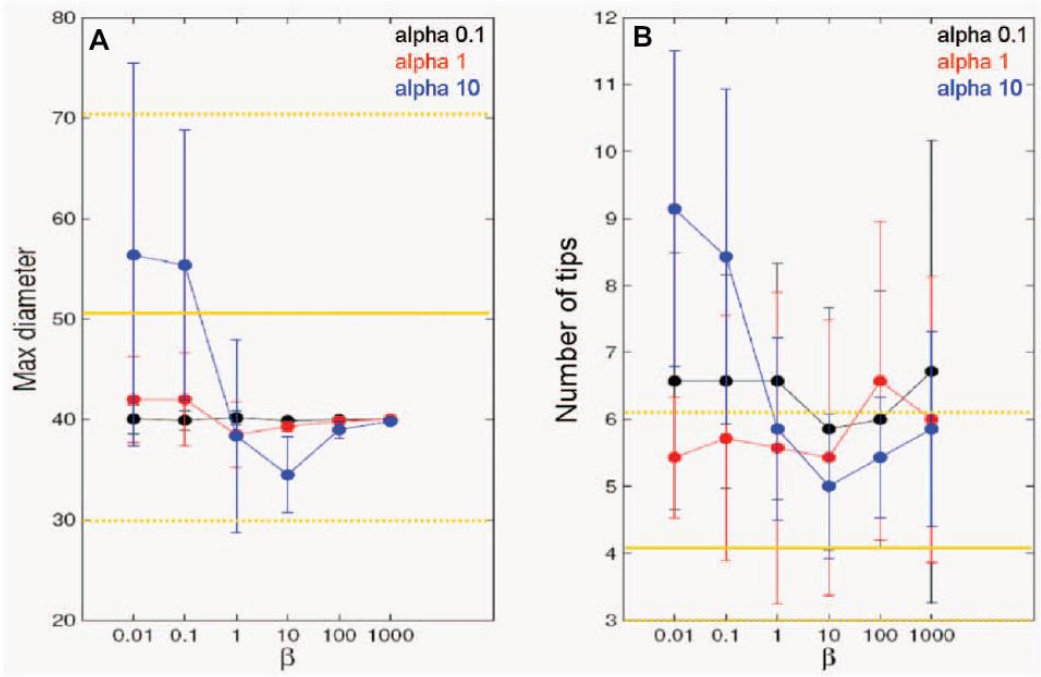

Figure 3. Numerical validation of early network growth. A. Comparison of maximum pellet diameter between the model and experimental data (n = 41). **B.** Comparison of number of tips between the model and experimental data (n = 44). The simulation results are presented as average with error bars showing the minimum to maximum values. The results from laboratory experiment are shown as yellow lines for mean (continuous line) and standard deviation (dashed line).
doi:10.1371/journal.pone.0054316.g003

Validation of the model using oxygen as an external substrate

In our simulations, we use oxygen as an external substrate. We calculate the rescaled consumption rate ($\overline{d_c^a}$) by taking into account the single cell dry weight, volume of a grid voxel (8 μm^3 with the typical N and domain values indicated above, allowing the 2D+ effect of overlapping tip paths, as described above), the external oxygen concentration (c), the oxygen consumption rate (d_c) and the oxygen diffusion coefficient (D_c; Table 2). Since the mass of an average cell of *Streptomyces* is not known, mainly since the cell dimensions in filamentous organisms are hard to define [33], we make assumptions of the cell dry mass based on the *Escherichia coli* cell dry weight. To calculate the hypothetical cell volume for *Streptomyces coelicolor*, we exploit the fact that a single nucleus is associated with 1.9 μm hyphal length in vegetative hyphae and a hyphal diameter is known to vary between 0.5–1 μm [13]. Therefore, the *Streptomyces* single cell dimensions are assumed to be cylindrical with length of 1.9 μm and diameter of 1 μm. Then by assuming that an *E. coli* cell of the same volume weighs the same as a *Streptomyces* 'cell', we calculate a *Streptomyces* cell dry weight utilizing published *E. coli* cell dry weight measurements [34].

Table 2. Typical parameters used for external oxygen concentration and diffusion.

Parameter	Symbol	Value
O_2 diffusion coefficient[1]	D	9.216×10^6 μm^2/h
O_2 concentration (in absence of cells)	c	0.1975 mmol/l
O_2 consumption rate[2] – active growth	$\overline{d}_c^a$	1×10^{-5} μm^{-2}
O_2 consumption rate – antibiotic production	$\overline{d}_c^p$	70% of $\overline{d}_c^a$
O_2 consumption rate – maintenance requirements only	$\overline{d}_c^m$	50% of $\overline{d}_c^a$
O_2 consumption rate – dead	$\overline{d}_c^e$	0

[1]Calculated using [45].
[2]Consumption rate rescaled by diffusion rate.
doi:10.1371/journal.pone.0054316.t002

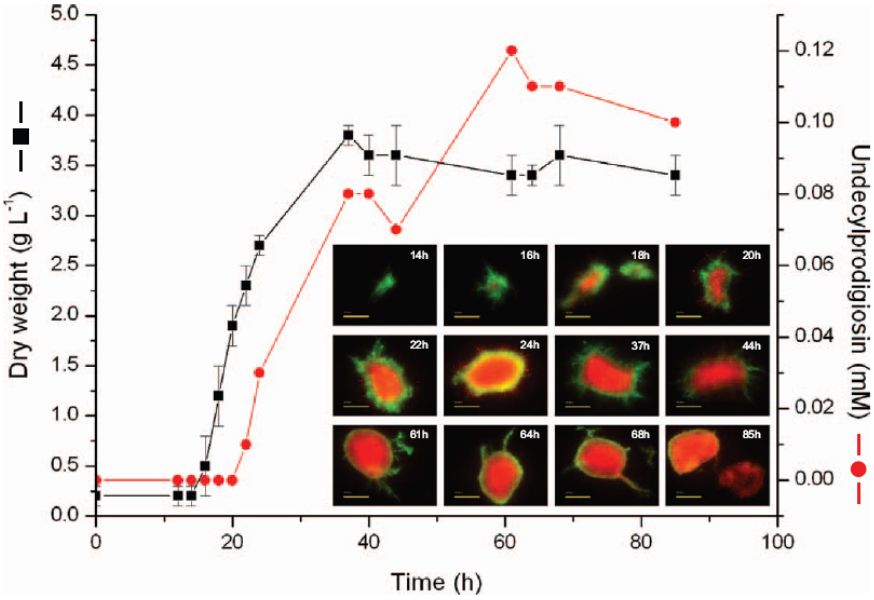

Figure 4. One generation of pellet development where BacLight live/dead staining highlights the cell heterogeneity within a pellet. As pellets grow in size, the red area spread from the core of the pellet to eventually covering the whole pellet. Green fluorescence (SYTO9) is associated with live cells; Red fluorescence propidium iodide (PI) stains dead cells. Bar = 100 μm. Bacterial growth was monitored by dry weight weight (black squares). Antibiotic production is shown as undecylprodigiosin concentration (red circles). The error bars illustrate the standard deviation (n = 3).
doi:10.1371/journal.pone.0054316.g004

The consumption rate of oxygen is estimated to be around 6.5 mmol g^{-1} h^{-1} for actively growing hyphae [35]. According to Melzoch *et al.* [35] continuous culture studies, at this rate, *Streptomyces coelicolor* M145 does not produce antibiotics, yet it is actively growing. By applying the above values to the rescaled oxygen consumption rate calculations ($\overline{d_c} = d_c/D_c$), we are able to come to a value of ca 1×10^{-6} μm^{-2}. It turns out, however, that this estimate produces a very dense pellet that is fully metabolically active with the core of the pellet consisting of antibiotic producing hyphae and no hyphae with only maintenance requirements. Our live/dead staining data suggest that the core of the pellet is likely to be inactive. Therefore simulations using the rescaled consumption rate of 1×10^{-5} μm^{-2} gave the most realistic comparison between our simulations and the experimentally data. We found this difference in the model parameter acceptable since the single cell dry weight is based on the above assumptions, and some of the data used in the calculations are derived from 3-dimensional studies (continuous culture studies), yet our model only takes into account 2-dimensional growth.

We estimated the varying levels of external oxygen concentration needed to change the metabolic states of the hypha based on the work of Melzoch *et al.* [35]. We made the assumptions that at 90–100% of initial oxygen concentration, all hyphae are assumed to be actively growing. When oxygen levels drop due to metabolic consumption, the probability of hyphae switching from an actively growing state to an antibiotic producing state increases. When the external oxygen levels are between 50–60% of the initial concentration, all the hypha are assumed to produce antibiotics. Antibiotic production stops when less than 40% of the initial oxygen concentration is present and the cells are only able to stay alive, but are non-growing between 15–46% oxygen. The cells die when less than 15% of the initial oxygen concentration level is available. It is noted that these parameters can be difficult to establish. We therefore performed a parameter sensitivity analysis on these parameters (omitted for brevity) and found no qualitative difference in the results.

Pellet development

Streptomyces grow by forming multigenomic, apically extending filamentous hyphae. Growth is initiated from a single spore and as growth proceeds in liquid cultures, the individual filaments get tangled together forming hyphal clumps and eventually dense pellets. Due to substrate diffusion limitations, the cells within a pellet are assumed to be heterogeneous in their metabolism. To illustrate this cell heterogeneity in a developing pellet, a *Streptomyces* growth curve is shown in **Fig. 4**, where growth is monitored by dry cell mass and cell pellets are stained using BacLight live/dead staining. Green areas correspond to the fluorescent dye, SYTO9 that stains cells with an intact membrane potential (Live cells). Red areas show hyphae that are stained with propidium iodide (PI), indicating cells with impaired membrane potential that are likely to be dead or at the very least metabolically inactive. Initial pellet development appears fully green implying that all the cells are live and active. Once the pellets develop further, the red areas appear first at the core of the pellet and eventually spread over the whole pellet, indicating a decrease in membrane potential and cell death. Some red staining hyphae are present throughout growth, likely representing natural variance in the system. Antibiotic production (the cell associated, red pigmented antibiotic, undecylprodigiosin [16]) was observed at 22–24 h onwards (**Fig. 4**). The cultures were

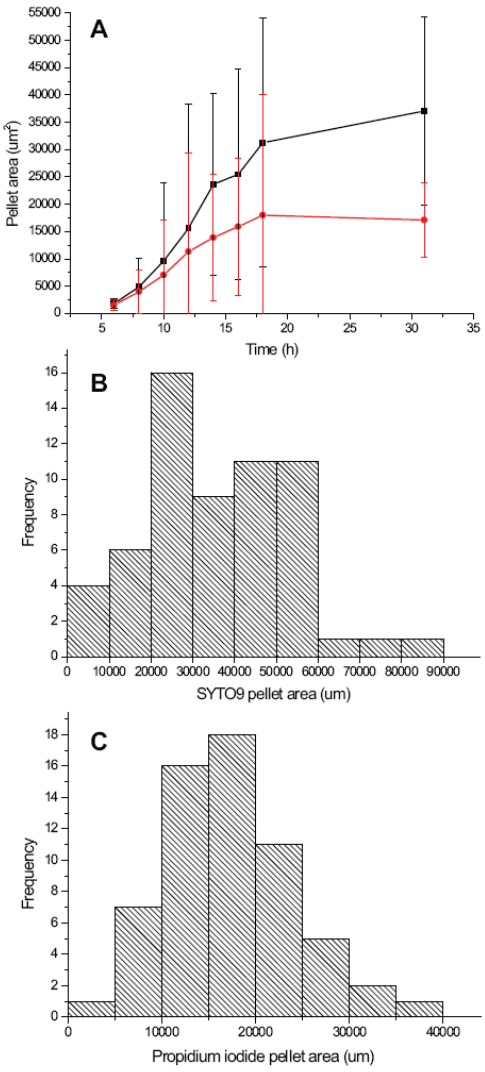

Figure 5. Results from automated image analysis of *Streptomyces coelicolor* pellets using live/dead staining. A. The mean area of SYTO9 (black squares) and PI (red diamonds) stained pellets over time. The total number of images included in the analysis was 892. The error bars correspond to the standard deviation of the data. At each time point, between 28 to 71 pellets were measured. Time scale adjusted to the modeling time line by deducting a 6 h germination period from the start of the growth curve. **B.** A frequency histogram of SYTO9 pellet areas at the end of the exponentially growing phase. The total number of pellets measured was 60. C. A frequency histogram at the end of the exponentially growing phase of pellet areas stained with PI. The number of pellets included was 61.
doi:10.1371/journal.pone.0054316.g005

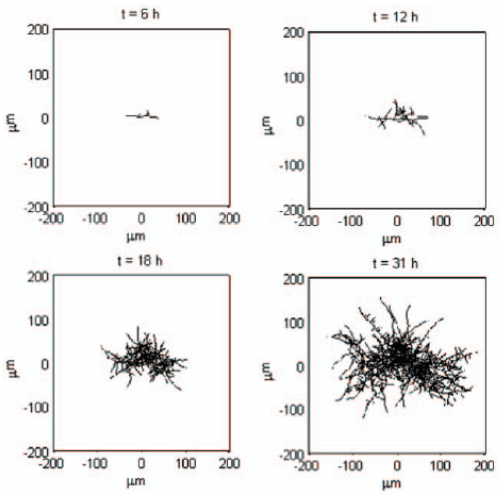

Figure 6. Example model simulation of network growth from a single cell to a dense network. The time points shown are 6 h, 12 h, 18 h and 31 h after germination. Details of the simulation procedure is given in the main text. Initially, two hyphal tips are considered to emerge from the origin $(x,y) = (0,0)$, both with initial velocities v_{avg} and random initial orientations.
doi:10.1371/journal.pone.0054316.g006

largely comprised of dead cells from 61 hrs onwards and at the end of the growth curve, only the hyphal fragments, released from the edges of old pellets, remained active.

Automated image analysis

To gain insight into the pellet development, automated image analysis was performed on BacLight stained fluorescence images. During the rapid growing phase, the pellet area increased in size in both SYTO9 and PI stained hyphal parts (**Fig. 5**). At the end of the rapid growing phase (31 h), both the SYTO9 and PI pellet areas had relatively high coefficient variation (CV) of 46% and 39% respectively. From the frequency histograms presented in

Table 3. The ratio of maximum pellet diameter in SYTO9 fluorescence images compared to phase-contrast images (manual measurements).

Time after germination[1] (h)	Ratio of max pellet diameter (%)	n
6	67.2	31
8	64.9	53
10	66.3	10
12	63.8	10
14	74.4	10
16	76.6	10
18	75.4	10
31	76.7	10

[1]Germination time 6 h.
doi:10.1371/journal.pone.0054316.t003

Table 4. Comparison of simulation results to experimentally determined values.

Measurement[1]	Model simulation	Experiment (from min to max)[2]
max pellet diameter (μm)	380	90–50
pellet area (μm^2)	60,000	250–90,000[3]
pellet perimeter (μm)	1250	260–3600

1 Measured at 31 h after germination.
2 Measured from SYTO9 fluorescence images, n = 60.
3 See histogram in Fig. 5.
doi:10.1371/journal.pone.0054316.t004

Fig. 5, it was observed that only few pellets out of ca 60 measurements contributed to this large distribution.

The average maximum pellet diameter was 270 μm for the SYTO9 fluorescence image analysis at the end of the exponential growth phase. By comparing manual measurements between SYTO9 fluorescence and phase-contrast images, it was seen that the average maximum pellet diameter in SYTO9 dyed images were 65.6% (CV 20.5) and 75.8% (CV 8.1) of the average maximum pellet diameter in phase-contrast images for time points 6–12 h and 14–31 h after germination respectively (Table 3). Consequently, the average maximum pellet diameter measured from SYTO9 fluorescence images gives results that are 35% and 24% smaller than the actual pellet for 6–12 h and 14–31 h after germination respectively. If the average value of 270 μm is corrected to represent the actual maximum pellet diameter, then the average maximum pellet diameter would be around 356 μm. The difference observed in fluorescence measurements and the phase contrast images of pellet development may be explained by the density of the pellets, such that the fluorescence from the pellet centre is higher than the fluorescence from the individual tips resulting in reduced detection of individual tips.

Comparison of Simulations to Experiments

We model the hyphal growth from a single cell to pellet formation and show an example of the simulated hyphal morphologies at 6 h, 12 h, 18 h and 31 h after germination (**Fig. 6**). Since no time lag is incorporated into the model for spore germination, the time shown is from the emergence of a germ tube, which in experiments was following approximately 6 hours of incubation. The simulation is clearly representative of the experimentally observed features. For example, when comparing pellet size (measured as the maximum pellet diameter) the pellet area and pellet perimeter, at the end of the simulation (31 h), it was noted that the simulations very accurately represent the biological variation observed at the end of rapid growth in the automated image analysis (**Table 4**). The corrected value for the average maximum pellet diameter is 356 μm, and the corresponding value from the simulations is 380 μm; Therefore, the model correlates very accurately to the experimental data when comparing pellet diameters. The experimental data for pellet area gives a mode of between 20,000–30,000 and an average of 37,000. If this average is corrected to represent the phase contrast images of pellets (+24%) then it rescales to 46,000. This is still smaller than the 60,000 estimated from the simulations, but is likely to reflect additional complexities in the experiment such as additional growth limiting factors. It is noted that the antibiotic producing cells emerge in the simulations at around 16 h after germination. This corresponds to the timing observed for the production of undecylprodigiosin in our growth curve experiments.

Exploiting Model Simulations

Cell heterogeneity and oxygen limitation. Now that we have a validated model framework, we use simulations to predict the cell and pellet heterogeneity in filamentous growth (**Fig. 7**). The simulation (**Fig. 7C**) indicates the switch from active to inactive hyphae at the interface of green/red areas of pellet. Part D in **Fig. 7** shows specific locations of the metabolic switch from primary to secondary metabolism where actively growing hyphae

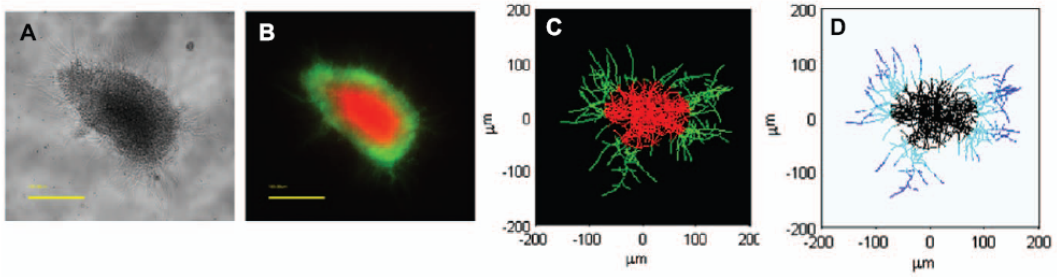

Figure 7. Microscopy images of *Streptomyces coelicolor* pellet compared to model simulations. A. Phase-contrast image of a pellet. **B.** Fluorescence image of the pellet using green SYTO9 (live cells) and red propidium iodide (likely dead cells) nucleic acid stains. **C.** Model simulation of a live/dead pellet at the end of the exponentially growing phase. Green colour corresponds to live cells with high consumption rate for oxygen 70% or more, and red colour illustrates the cells surrounded by less than ca 50% of the external oxygen present at the start of the incubation. **D.** The different metabolic states of the hyphae within the pellet at the end of the exponentially growing phase. Blue colour at the outskirts of the pellet marks the actively growing hyphae. Cyan colour corresponds to hyphae producing antibiotics. Black colour, at the core of the pellet, illustrates metabolically inactive hyphae with only maintenance demands for oxygen.
doi:10.1371/journal.pone.0054316.g007

Table 5. The average area of propidium iodide stained cells in experimental data (1.71×10^4 μm^2) is used to predict the oxygen concentration level at the interface of live/dead stained cells.

External O_2 concentration[1] at the interface of green/red areas in the simulations (%)	Average red (PI) area in simulations ($\times 10^4$ μm^2)
40%	0.62
45%	1.04
50%	1.53
51%	1.45
52%	1.56
53%	1.66
53.5%	1.78
54%	1.81
55%	1.89
60%	2.48
65%	2.89

[1]Percentage scaled to the total carrying capacity of oxygen in media.

doi:10.1371/journal.pone.0054316.t005

are predicted to be at the outskirts of the pellet (blue). More centrally are the parts of the hyphae that produce antibiotics (cyan). Within the simulation time scale no dead hyphae (light blue) are seen, instead at the core of the pellet the hyphae are still alive, however, they are not actively growing nor are they producing antibiotics, yet they still have maintenance requirements for oxygen (black).

To predict the external oxygen concentration surrounding cells located at the interface of live/dead stained areas, a number of simulations were run using different values of external oxygen concentration for the switch from green (live) to red (likely to be dead) areas and measuring the resulting red area. The red areas in simulations are then compared to the average red area seen in experimental data, where the average PI area were observed to be 1.71×10^4 μm^2 at the end of log phase. Using this comparison the model predicts that the shift seen in experiments from green to red occurs when external oxygen concentration drops to ca 50–55% (**Table 5**).

Network morphology. To find the effect that different branching patterns have on network morphology, oxygen consumption and metabolism, we ran simulations with varying parameters for apical (first branch point) and inter-branch distances as previously published for *S coelicolor* [36], [37] (see Table S1 for parameter values used). As observed in Fig. 8, increasing branching frequency in the model affects pellet morphology (**Fig. 8: A–H**). Interestingly, the model prediction

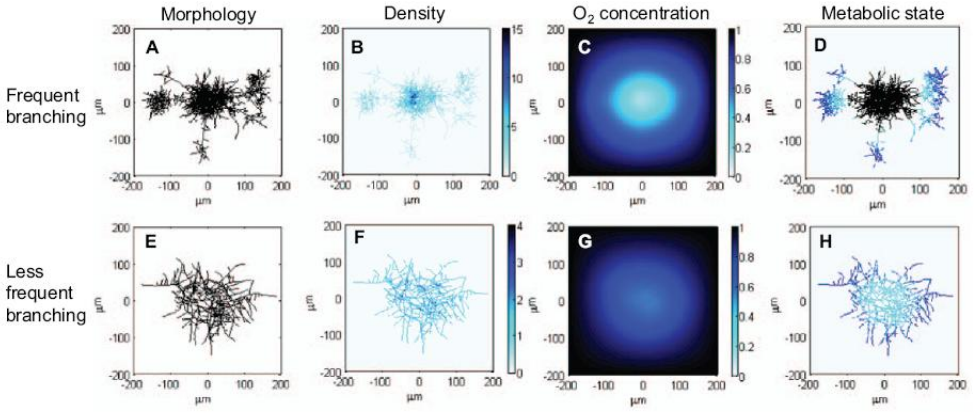

Figure 8. The effect of different branching patterns on pellet morphology, density, oxygen consumption and metabolism. In simulations **A–D** a frequent branching pattern using the previously measured apical and inter-branch distances of Jyothikumar et al. [36]. **E–H** illustrate less frequent branching pattern using the previously determined parameters of Allan and Prosser [37]. **B** and **F** show the hyphal density within a pellet and **C** and **G** show the rate of consumption of external oxygen. In **D** and **H** the metabolic state of hyphae is shown where blue colour corresponds to actively growing hyphae, cyan colour illustrates antibiotic producing hyphae, and black colour marks metabolically inactive hyphae with only maintenance demand for oxygen. The highest oxygen consumption is observed where the hyphae are densest. Less frequent branching produces larger, less dense pellets that demand less oxygen and are metabolically active across the whole pellet. See Table S1. for parameter values.

doi:10.1371/journal.pone.0054316.g008

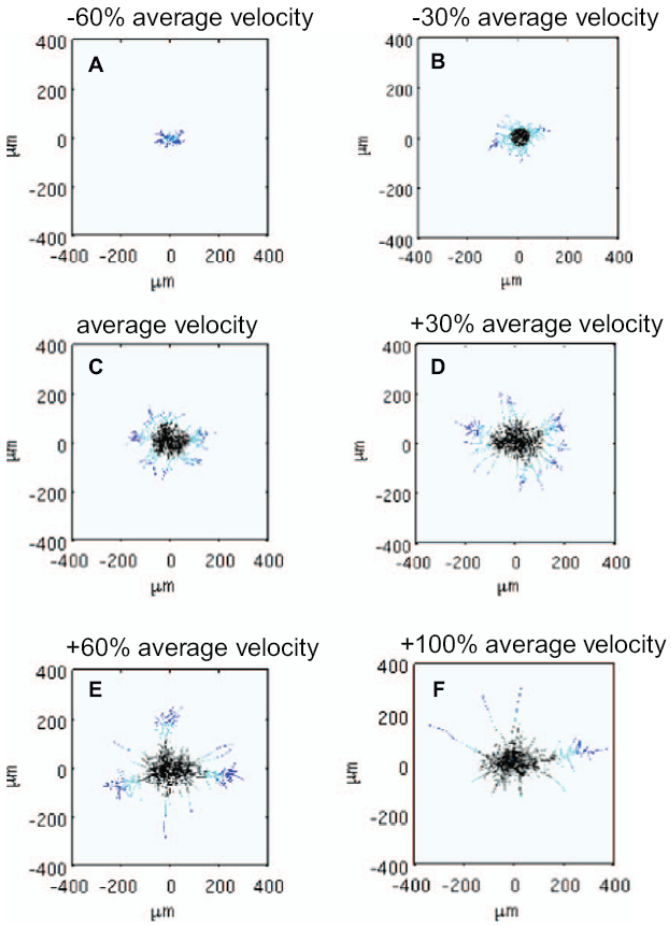

Figure 9. Increasing hyphal elongation velocity affects the network morphology. Simulation results show the shape of a network using an average tip elongation rate that is −60% (**A**), −30% (**B**), 0% (**C**), +30% (**D**), +60% (**E**) and +100% (**F**) of the experimentally observed value (6.3 µm/h). Note that to accommodate the increased velocities, the domain size was increased to 500 µm×500 µm, 600 µm×600 µm, 800 µm×800 µm in (**D**), (**E**) and (**F**), respectively. Note: the images were manually adjusted to show 400 µm×400 µm coordinates to allow a comparison between the different cases.
doi:10.1371/journal.pone.0054316.g009

of pellet morphology using frequent branching parameters shows the appearance of satellite pellets that are likely to break off from the original pellet under experimental conditions. A reassuring conclusion about the good fit between the model and the empirical work can be affirmed by observing the apparent that high hyphal density co-localises with increased branching frequency (**Fig. 8: B** and **F**). The oxygen concentration for both of the cases is shown in **Fig. 8: C and G**, where dense pellet areas have higher oxygen consumption. Images in **Fig. 8: D and H** show prediction of the metabolic state of hyphae suggesting that less frequent branching creates larger and less dense pellets that consume less oxygen and stay fully metabolically active.

Average hyphal velocity. In our model the hyphae elongate during the rapid growth phase according to an average velocity of 6.3 µm/h, based on experimental values. To determine the effect of different elongation rates and to test the effects of domain size on growth characteristics, we ran multiple simulations using average velocity values of 2.5 µm/h (−60%), 4.4 µm/h (−30%), 8.2 µm/h (+30%), 10 µm/h (+60%) and 12.6 µm/h (+100%), where the value in brackets corresponds to a percentage difference from our original assumed average velocity (see Table 1). In simulations, we observe that the decreased velocity results in smaller pellets with delayed antibiotic production. Increasing the velocity significantly affects overall morphology, with the pellet growing quicker with antibiotic producing cells appearing earlier. However, as the main body of the pellet stays approximately at the same size a few long, unbranched hyphae emerge from the main body forming sub-pellets (**Fig. 9**). This simulation outcome reveals two unexpected aspects of pellet development in our model. Firstly, within the simulation time the spatial domain needed to be

increased such that the hyphal tips did not hit the simulated domain boundary as a result of rapid extension. Since oxygen has a limited diffusion distance, as the domain boundary is enlarged the oxygen distribution is affected. This artefact only affects the high velocity simulations where the oxygen does not diffuse through the space sufficiently such that the oxygen concentration at the pellet interior will be low. The lack of oxygen near the pellet surface makes it impossible for most of the hypha to continue elongating, and the long hypha seen in the simulations, are a result of the only few hyphal tips still reaching the area where adequate oxygen concentration for growth is present. Secondly, elongating hyphae appear unbranched even though the branching frequency is assumed to increase with increasing hyphal length. Our assumption in the model is that once the branching event occurs, the new branching point is calculated from the previous branching point. Since the previous branching point does not significantly change, the new branching point will emerge at the average interbranch distance of l_2. Since this new position is already in the area of inadequate external oxygen concentration for growth, the branching event is most likely going to be unsuccessful. Therefore, it was noted that the model is favouring unsuccessful branching events when oxygen concentration is limited.

Insight into branching. The model also allows us to gain quantitative insight into processes that are very difficult or impossible to obtain experimentally. Using the standard parameters for *Streptomyces* (see table 1), we can use the model to measure the hyphal growth unit (HGU) and the total number of tips inside a pellet (**Fig. 10: A & B**) – measurements that are almost impossible to make by microscopy. HGU is routinely used as a metric for growth of hyphal organisms. It is defined as total length of the hyphae divided by the number of tips and is a useful measure of the growth behaviour of a hyphal population. In our simulations the HGU is close to the HGU data previously measured by Allan and Prosser [37] where the HGU initially oscillated and subsequently reached a constant value. Similarly, the total numbers of tips in our simulations increase throughout the growth curve. The model also allows us to track the frequency of successful (blue) and unsuccessful (red) branching events during simulations (**Fig. 10 C**). At the start of the growth curve, most of the branching events are successful with increasing frequency, with successful branching, declining rapidly following the onset of antibiotic production.

Using the data from the different branching pattern simulations (**Fig. 8**) we can draw further biological insight into the HGU and the hyphal area for antibiotic producing cells at the end of log phase (**Fig. 11 A & B**). In Figure 11 the HGU (A) and area of antibiotic producing cells (B) for the apical and inter-branch lengths associated with the less frequent branching patterns (**I**) observed in the study of Allan and Prosser [37], (**III**) is for parameter values associated with the frequent branching study of Jyothikumar *et al*. [36] and (**II**) is for branch lengths as measured in this study at a 10 h time point of the growth curve experiment, in which we see a long apical branch distance and short inter-branch distance (which we will refer to as the standard parameters, see Table 1 for the model parameter values for this case). As expected, increasing branching frequency in the model reduces the HGU (**Fig. 11 A**). This monotonic form, however, is not repeated in **Fig. 11 B**, which shows that the area of antibiotic producing cells maximizes for standard parameters (**II**), indicating that both apical and inter-branch lengths are crucial determinants of antibiotic production.

Data from the velocity simulations (**Fig. 9**) can be similarly used infer additional insight. For example, plotting HGU at the end of log phase versus average tip velocity (**Fig. 11 C**) and the time of maximum successful branching versus these calculated HGUs (**Fig. 11 D**) shows congruence, as would be expected when exponential growth is underway (i.e. fast extension rate, rapid branching). Again, using these calculated HGUs, we can also observe the relationships between end diameters and areas of the different metabolic regions versus HGU (see **Fig. 12 A, B**). Note that the different states of metabolism resemble growth curve characteristics with lag phase, exponential growth and stationary/death phases. We also plot the maximum rates of oxygen consumption in these simulations versus the calculated HGUs (see **Fig. 12 C**). Not only can these plots be used for prediction purposes but also they highlight that an optimal value of average tip velocity for exponential growth exists and can be utilised in the design of industrial processes through the application of rational process design.

Discussion

Branched networks are found throughout biology. The ability to achieve exponential network growth through branching has been adopted by many systems across a range of organisms either as a strategy [38,39] or as an emergent property of apical growth [10,40]. Here, we present a model that allows the visualisation of pellet development in *Streptomyces* and the estimation of difficult or impossible to obtain experimental measures, such as Hyphal Growth Units (HGU), pellet density, the prediction of metabolic status versus time across a pellet and the precise identification of antibiotic producing cells.

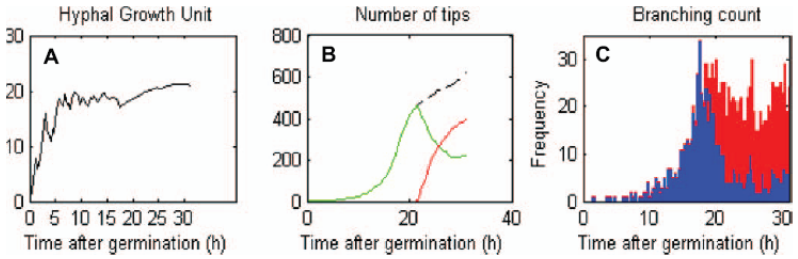

Figure 10. Additional insight into network characteristics. The model provides information on the hyphal growth unit (**A**), number of tips (**B**) and branching count (**C**) inside a dense network. In the simulation **B**, the black, dashed curve corresponds to the total number of tips, and green and red curves illustrate the total number of live and dead tips respectively. In **C**, the blue bars show the frequency of successful branching events and the red bars, the frequency of unsuccessful ones.
doi:10.1371/journal.pone.0054316.g010

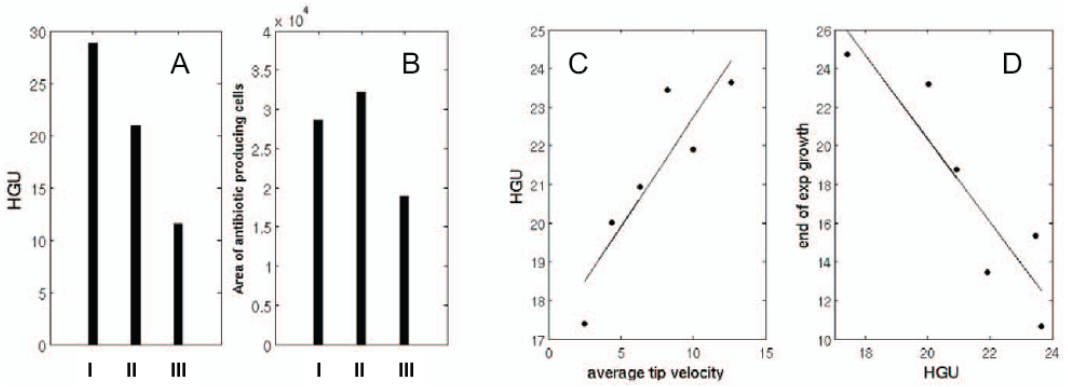

Figure 11. Model predictions using different branching patterns. Three different branching patterns for less frequent (I), standard (II) and frequent (III) branching affect the HGU (**A**) and the area of the antibiotic producing cells (**B**) at the end of log phase. Regression lines utilized to determine the HGU and the time of maximum succesful branching (**C** and **D** respectively) based on average tip velocities of 2.5 μm/h (−60%), 4.4 μm/h (−30%), 6.3 μm/h (±0), 8.2 μm/h (+30%), 10 μm/h (+60%) and 12.6 μm/h (+100%).
doi:10.1371/journal.pone.0054316.g011

The model is able to predict the physiological heterogeneity within a pellet showing that the hypothesis of substrate-limitation within each pellet is significant in causing cessation of growth and cell death in the centre of pellets. The ability to test the model prediction through our use of BacLight fluorescent staining and also to compare the results to other studies of cell pellets [41] and to oxygen measurements [42] means that we can validate our modelling framework. Accurately predicting this behaviour from our model with verification through experimental testing allows further layers of complexity to be tested by the model. Antibiotic production (and other secondary metabolites) are often regulated by the availability of nutrients, and the ability of the model to predict those cells producing a product in an industrial setting will have great utility in assessing the morphology of pellets and the nutrient concentrations likely for optimised production. It is clear from the model that some of the inefficiency observed in fermentations may be the result of less than 50% of the biomass within a process producing the desired product, such that through manipulation of morphology, productivity can be enhanced. Several mutants are known to affect pellet formation, through fragmentation and also significantly enhance the production of a desired product [18,19]. This should provide a rational framework for the rapid characterisation of cell division mutants that may be useful in an industrial process.

Interestingly, the number of tips in the model increases throughout, as would be expected, given that branching is a requirement for exponential growth in hyphal organisms. The model demonstrates that the number of successful branching events drops at the onset of antibiotic production, correlating with the decrease in growth rate that is observed in experiments at this time, indicating that our model can link the cessation of exponential growth and nutrient limitation to the production of antibiotics. The relatively few, easily measured parameters allow

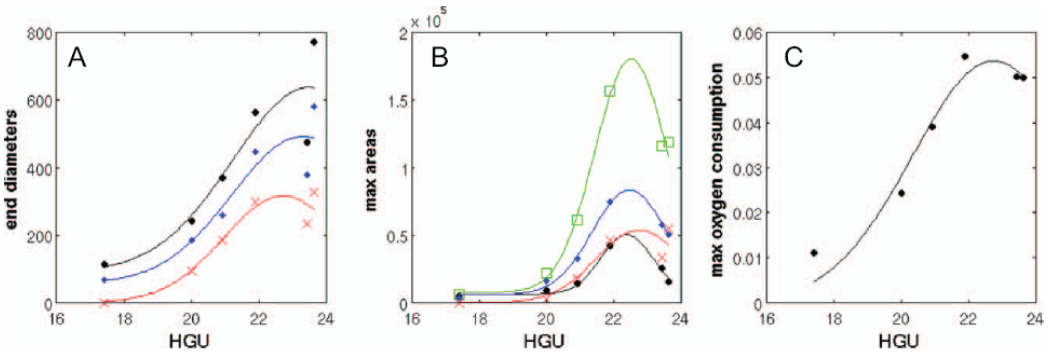

Figure 12. Model predictions using different average tip velocities. The relationships between end diameters and areas of the different metabolic regions using average tip velocities of 2.5 μm/h (−60%), 4.4 μm/h (−30%), 6.3 μm/h (±0), 8.2 μm/h (+30%), 10 μm/h (+60%) and 12.6 μm/h (+100%) versus HGU (**A** and **B**, respectively). The metabolic state of the network is indicated for actively growing cells (black circles), antibiotic producing cells (blue diamonds), maintenance requirements only cells (red crosses) and the total area of network (green rectangles). In (**C**), we plot the maximum rates of oxygen consumption in these simulations versus the calculated HGUs.
doi:10.1371/journal.pone.0054316.g012

significant biological and functional information to be gathered from simulations.

To understand the hyphal elongation or pellet formation of filamentous organisms, several mathematical models have previously been constructed [14,15,26,28–30,42,43]. Some of these models do take into account external substrate and metabolic state of cells, however only very few include antibiotic production. Our discrete model framework is able to predict the location of antibiotic producing cells in a pellet without having to compromise on the structure of a single hypha. Our model has the advantage that it is constructed from a few parameters that can be determined from experimental data. This tight link between mathematics and biology and the low number of unknown parameters makes the model very powerful. Thus ensures that we have a well-validated framework which we can use as a solid platform for further modelling applications. The model can be extended for future studies on biological processes such as the internal movement of proteins, DNA in hyphae and can be broadened to encompass any form of branched network structure. Additionally the information derived form these processes can be incorporated in to rational design of bioprocesses.

Materials and Methods

Bacterial strain and culturing

Streptomyces coelicolor strain M145 [44] was used in this study. The bacteria were routinely cultured and maintained following standard procedures [44]. Growth curve experiments were carried out at 30°C in Yeast Extract Malt Extract (YEME) media lacking sucrose [44] in two-litre Erlenmeyer flask without baffles or springs, shaking at 220 rpm. Cultures were inoculated with 1×10^5 cfu/ml bacterial spores in 400 ml of media. Biomass concentration was determined in triplicate by vacuum-filtering 5 mL of culture onto pre-weighed, glass microfiber filters (GF/C, Whatman, UK). The filters and biomass were washed twice with 5 mL of distilled water and dried to a constant mass. The concentration of oxygen in media was determined using a dissolved oxygen probe (Mettler Toledo, UK).

Microscopy and image analysis

Bacterial viability was estimated by microscopy using Live/dead® BacLight™ bacterial viability kit (Molecular Probes, L7007, Invitrogen Detection Technologies, Leiden, The Netherlands). The maximum excitation/emission for SYTO9 and PI are 480/500 nm and 490/635 nm respectively. Microscopic slides were prepared in the dark by mixing 15 µl of culture with 15 µl of 0.0334 mM SYTO9 and 0.20 mM PI stain in distilled water. Images were observed using a Nikon TE2000S inverted fluorescence microscopy at x200. Images were captured using a Hamamatsu Orca-285 Firewire digital charge-coupled device camera. Exposure times were 20 ms for phase-contrast and fluorescence imaging throughout the growth curve analysis. For PI the initial exposure time was 50 ms for 12 h to 24 h time points and 20 ms for 37 h to 85 h time points. Pictures were analysed using IPLab scientific imaging software version 3.7 (Scanalytics, Inc., Rockville, USA) and an automated image analysis was performed for fluorescence images using iterative mode as per the software manufacturer's instructions. The resulting segmentation of the pellets was manually verified to cover the area of the pellet. Statistical analysis of the hyphal and pellet measurements was performed using Microsoft Office Excel software. Hyphal growth unit was calculated as the total length of hyphae divided by the total number of tips [13].

Supporting Information

Table S1 Parameter values for frequent and less frequent branching patterns used in Fig. 8.
(DOC)

Acknowledgments

We would like to thank Ioannis Voulgaris, University of Strathclyde, for assistance with determining dissolved oxygen concentrations. Thanks to Paul R Herron for microscopy assistance.

Author Contributions

Conceived and designed the experiments: PAH LN SW MS. Performed the experiments: LN SW PAH. Analyzed the data: LN SW PAH. Contributed reagents/materials/analysis tools: LN PAH SW. Wrote the paper: PAH LN SW MS.

References

1. Smith M, Bruhn J, Anderson J (1992) The Fungus Armillaria-Bulbosa Is Among the Largest and Oldest Living Organisms. Nature 356: 428–431.
2. Stokes CL, Lauffenburger DA, Williams SK (1991) Migration of individual microvessel endothelial cells: stochastic model and parameter measurement. J Cell Sci 99: 419–430.
3. Jones PF, Sleeman BD (2006) Angiogenesis – understanding the mathematical challenge. Angiogenesis 9: 127–138.
4. Peirce SM (2008) Computational and Mathematical Modeling of Angiogenesis. Microcirculation 15: 739–751.
5. Mantzaris NV, Webb S, Othmer HG (2004) Mathematical modeling of tumor-induced angiogenesis. J Math Biol 49: 111–187.
6. Plank MJ, Sleeman BD (2004) Lattice and non-lattice models of tumour angiogenesis. Bull Math Biol 66: 1785–1819.
7. Davidson F (1998) Modelling the qualitative response of fungal mycelia to heterogeneous environments. Journal of Theoretical Biology 195: 281–292.
8. Boswell GP, Jacobs H, Davidson FA, Gadd GM, Ritz K (2002) Functional consequences of nutrient translocation in mycelial fungi. Journal of Theoretical Biology 217: 459–477.
9. Boswell GP, Davidson FA (2012) Modelling hyphal networks. Fungal Biology Reviews 26: 30–38.
10. Bebber DP, Hynes J, Darrah PR, Boddy L, Fricker MD (2007) Biological solutions to transport network design. Proc Biol Sci 274: 2307–2315.
11. Dupuy L, Gregory PJ, Bengough AG (2010) Root growth models: towards a new generation of continuous approaches. J Exp Bot 61: 2131–2143.
12. Bastian P, Chavarría-Krauser A, Engwer C, Jäger W, Marnach S, et al. (2008) Modelling in vitro growth of dense root networks. Journal of Theoretical Biology 254: 99–109.
13. Prosser J, Tough A (1991) Growth Mechanisms and Growth-Kinetics of Filamentous Microorganisms. Crit Rev Biotechnol 10: 253–274.
14. Meyerhoff J, Bellgardt K (1995) A morphology-based model for fed-batch cultivations of Penicillium chrysogenum growing in pellet form. Journal of Biotechnology 38: 201–217.
15. Meyerhoff J, Tiller V, Bellgardt KH (1995) Two mathematical models for the development of a single microbial pellet. Bioprocess and Biosystems Engineering 12: 305–313.
16. Bibb MJ (2005) Regulation of secondary metabolism in streptomycetes. Curr Opin Microbiol 8: 208–215.
17. Wardell JN, Stocks SM, Thomas CR, Bushell ME (2002) Decreasing the hyphal branching rate of Saccharopolyspora erythraea NRRL 2338 leads to increased resistance to breakage and increased antibiotic production. Biotechnol Bioeng 78: 141–146.
18. Traag BA, Seghezzi N, Vijgenboom E, van Wezel GP (2007) Characterization of the Sporulation Control Protein SsgA by Use of an Efficient Method To Create and Screen Random Mutant Libraries in Streptomycetes. Applied and Environmental Microbiology 73: 2085–2092.
19. van Wezel GP, Krabben P, Traag BA, Keijser BJF, Kerste R, et al. (2006) Unlocking Streptomyces spp. for Use as Sustainable Industrial Production Platforms by Morphological Engineering. Appl Environ Microbiol: 72: 5283–5288.

20. Prosser JI, Trinci AP (1979) A model for hyphal growth and branching. J Gen Microbiol 111: 153–164.
21. Obert M, Pfeifer P, Sernetz M (1990) Microbial growth patterns described by fractal geometry. J Bacteriol 172: 1180–1185.
22. Nielsen J (1993) A Simple morphologically structured model describing the growth of filamentous microorganisms. Biotechnol Bioeng 41: 715–727.
23. Birol G, Undey C, Parulekar SJ, Cinar A (2002) A morphologically structured model for penicillin production. Biotechnol Bioeng 77: 538–552.
24. Boswell GP (2008) Modelling mycelial networks in structured environments. Mycol Res 112: 1015–1025.
25. Alam MT, Merlo ME, stream TSC, Hodgson DA, Wellington EM, et al. (2010) Metabolic modeling and analysis of the metabolic switch in Streptomyces coelicolor. BMC Genomics 11: 202.
26. Richards DM, Hempel AM, Flärdh K, Buttner MJ, Howard M (2012) Mechanistic Basis of Branch-Site Selection in Filamentous Bacteria. PLoS Comput Biol 8: –. doi:10.1371/journal.pcbi.1002423.
27. Celler K, Picioreanu C, van Loosdrecht MCM, van Wezel GP (2012) Structured morphological modeling as a framework for rational strain design of Streptomyces species. Antonie Van Leeuwenhoek 102: 409–423.
28. Yang H, King R, Reichl U, Gilles ED (1992) Mathematical model for apical growth, septation, and branching of mycelial microorganisms. Biotechnol Bioeng 39: 49–58.
29. Yang H, Reichl U, King R, Gilles ED (1992) Measurement and simulation of the morphological development of filamentous microorganisms. Biotechnol Bioeng 39: 44–48.
30. Lejeune R, Baron GV (1997) Simulation of growth of a filamentous fungus in 3 dimensions. Biotechnol Bioeng 53: 139–150.
31. Tough AJ, Prosser JI (1996) Experimental verification of a mathematical model for pelleted growth of Streptomyces coelicolor A3(2) in submerged batch culture. Microbiology 142: 639–648.
32. Murray JD (2003) Mathematical Biology. Springer Verlag.
33. Shahab N, Flett F, Oliver SG, Butler PR (1996) Growth rate control of protein and nucleic acid content in Streptomyces coelicolor A3(2) and Escherichia coli B/r. Microbiology 142: 1927–1935.
34. Loferer-Krössbacher M, Klima J, Psenner R (1998) Determination of bacterial cell dry mass by transmission electron microscopy and densitometric image analysis. Applied and Environmental Microbiology 64: 688–694.
35. Melzoch K, de Mattos MJ, Neijssel OM (1997) Production of actinorhodin by Streptomyces coelicolor A3(2) grown in chemostat culture. Biotechnol Bioeng 54: 577–582.
36. Jyothikumar V, Tilley EJ, Wali R, Herron PR (2008) Time-lapse microscopy of Streptomyces coelicolor growth and sporulation. Applied and Environmental Microbiology 74: 6774–6781.
37. Allan EJ, Prosser JI (1983) Mycelial Growth and Branching of Streptomyces coelicolor A3(2) on Solid Medium. Microbiology 129: 2029–2036.
38. Fricker MD, Lee JA, Bebber DP, Tlalka M, Hynes J, et al. (2008) Imaging complex nutrient dynamics in mycelial networks. J Microsc 231: 317–331.
39. Heaton L, Obara B, Grau V, Jones N (2012) Analysis of fungal networks. Fungal Biology Reviews 26: 12–29.
40. Tero A, Takagi S, Saigusa T, Ito K, Bebber DP, et al. (2010) Rules for Biologically Inspired Adaptive Network Design. Science 327: 439–442.
41. Manteca A, Alvarez R, Salazar N, Yague P, Sanchez J (2008) Mycelium Differentiation and Antibiotic Production in Submerged Cultures of Streptomyces coelicolor. Applied and Environmental Microbiology 74: 3877–3886.
42. Hille A, Neu TR, Hempel DC, Horn H (2005) Oxygen profiles and biomass distribution in biopellets of Aspergillus niger. Biotechnol Bioeng 92: 614–623.
43. Lejeune R, Nielsen J, Baron GV (1995) Morphology of Trichoderma reesei QM 9414 in submerged cultures. Biotechnol Bioeng 47: 609–615.
44. Kieser T, Bibb MJ, Buttner MJ, Chater KF, Hopwood DA (2000) Practical Streptomyces Genetics. John Innes Foundation.
45. Wilke C, Chang P (1955) Correlation of diffusion coefficients in dilute solutions. AIChE J 1: 264–270.